CHEMICALLY DEPOSITED REDUCED GRAPHENE OXIDE (rGO)/ CONDUCTING POLYMER COMPOSITE THIN FILMS FOR SUPERCAPACITOR APPLICATION

THESIS SUBMITTED TO

D. Y. PATIL EDUCATION SOCIETY
(DEEMED TO BE UNIVERSITY),
KOLHAPUR

FOR THE DEGREE OF

DOCTOR OF PHILOSOPHY
IN
PHYSICS

BY

Ms. DIVYA CHANDRAKANT PAWAR

M. Sc.

UNDER THE SUPERVISION OF

Prof. CHANDRAKANT D. LOKHANDE

M. Sc., Ph. D.

DEAN AND RESEARCH DIRECTOR,
CENTRE FOR INTERDISCIPLINARY RESEARCH,
D. Y. PATIL EDUCATION SOCIETY
(DEEMED TO BE UNIVERSITY),
KOLHAPUR- 416 006, MAHARASHTRA, (INDIA)

2025

"CHEMICALLY DEPOSITED REDUCED GRAPHENE OXIDE (rGO)/ CONDUCTING POLYMER COMPOSITE THIN FILMS FOR SUPERCAPACITOR APPLICATION"

A THESIS SUBMITTED TO

D. Y. PATIL EDUCATION SOCIETY (DEEMED TO BE UNIVERSITY), KOLHAPUR

FOR THE DEGREE OF

DOCTOR OF PHILOSOPHY

IN

PHYSICS

UNDER THE FACULTY OF
INTERDISCIPLINARY STUDIES

BY

Ms. DIVYA CHANDRAKANT PAWAR

M. Sc.

UNDER THE SUPERVISION OF

Prof. CHANDRAKANT. D. LOKHANDE

M. Sc., Ph. D.

DEAN AND RESEARCH DIRECTOR,
CENTRE FOR INTERDISCIPLINARY RESEARCH,
D. Y. PATIL EDUCATION SOCIETY (DEEMED TO BE UNIVERSITY), KOLHAPUR
416 006, MAHARASHTRA, (INDIA)

2025

DECLARATION

I am **Divya Chandrakant Pawar**, hereby declare that the thesis entitled **"CHEMICALLY DEPOSITED REDUCED GRAPHENE OXIDE (rGO)/CONDUCTING POLYMER COMPOSITE THIN FILMS FOR SUPERCAPACITOR APPLICATION"** submitted for the degree of **Doctor of Philosophy (Ph.D.)** in **Physics**, Faculty of Interdisciplinary Studies, under the guidance of **Prof. C. D. Lokhande**, **Centre for Interdisciplinary Research (CIR), D. Y. Patil Education Society (Deemed to be University), Kolhapur** is completed and written by me, has not before made the basis for the award of any other higher education institute in India or any other country. To the best of my knowledge and belief, the thesis contains no material previously published or written by another person except where due reference is made. Further, I declare that I have not violated any of the provisions under the copyright and piracy/cyber/IPR Act amended from time to time.

Research Student

Place: Kolhapur
Date: 16/01/2025

Ms. Divya Chandrakant Pawar

CERTIFICATE OF GUIDE

This is to certify that the thesis entitled **"CHEMICALLY DEPOSITED REDUCED GRAPHENE OXIDE (rGO)/CONDUCTING POLYMER COMPOSITE THIN FILMS FOR SUPERCAPACITOR APPLICATION"** which is being submitted herewith for the award of the Degree of **Doctor of Philosophy (Ph.D.)** in **Physics, Faculty of Interdisciplinary Studies**, under the guidance of **Prof. C. D. Lokhande, Centre for Interdisciplinary Research (CIR), D. Y. Patil Education Society (Deemed to be University), Kolhapur**, is the result of the original research work completed by **Ms. Divya Chandrakant Pawar** under my supervision and guidance and to the best of my knowledge and belief, the work embodied in this thesis has not formed earlier the basis for the award of any degree or similar title of this or any other university or examining

Research Guide

Place: Kolhapur

Date: 16 | 01 | 2025

Prof. C. D. Lokhande
Dean and Research Director
Centre for Interdisciplinary Research,
D. Y. Patil Education Society,
(Deemed to be University),
Kolhapur – 416 006

Prof. C. D. LOKHANDE
Dean
Centre For Interdisciplinary Studies
D. Y. Patil Education Society
(Institution Deemed to be University)
869, 'E', Kasaba Bawada
KOLHAPUR- 416006

ACKNOWLEDGEMENT

This was a beautiful journey, a journey of expanding the boundaries of knowledge, a journey of finding your strengths and weaknesses, a journey of becoming mentally and emotionally strong. It became more beautiful and interesting because of the people I met along the way. I would like to take this opportunity to acknowledge those fascinating people.

I would like to express my first profound thanks and respect towards my cherished guide ***Prof. Chandrakant D. Lokhande*** *(Dean and Research Director, Centre for Interdisciplinary Research, D. Y. Patil Education Society, Kolhapur) for his keen awareness, valuable guidance, encouragement, and support. I am always amazed by his enthusiasm for science and how effectively he has shaped the young minds of two generations. I am very thankful to him for choosing me as his PhD student and I feel very fortunate to be part of CDL group.*

I would like to express my sincere thanks to President ***Dr. Sanjay D. Patil Saheb****, Vice President* ***Mr. Satej D. Patil Saheb****, Vice-Chancellor* ***Prof. R. K. Mudgal****, and the Registrar* ***Dr. V. V. Bhosale*** *for the inspiration and support. I thank* ***Dr. R. S. Patil, Dr. J. L. Gunjakar****,* ***Dr. U. M. Patil****,* ***Dr. Vishwajeet Khot, and Dr. Sharad Patil*** *who helped me to analyze the results with all their empathy and cooperative mind. I also thank* ***Dr. A. C. Lokhande****,* ***Dr. V. C. Lokhande****,* ***and Dr. D. B. Malavekar*** *for providing me important sample characterization data during entire research work.*

In addition, I acknowledge the funding support from the Ministry of Science and Technology India, ***Department of Science and Technology-Innovation in Science Pursuit for Inspired Research (DST-INSPIRE)****, through research project sanction No.* ***DST/INSPIRE Fellowship/2020/IF200234****.*

I would like to express sincere thanks to my seniors ***Shivaji Ubale****,* ***Prity Bagwade, Sambhaji Khot, Vikas Magdum, Ketaki Kadam, Ranjit Nikam, Yogesh Chitare, Shraddha Bhosale, and Sambhaji Kumbhar*** *for insightful guidance, scientific discussions and valuable suggestions on the present work.*

I would like to acknowledge my colleagues at Centre for Interdisciplinary Research, ***Ajinkya Bagde, Jyoti Thorat, Dilip Patil, Suraj Sankpal, Sujata Patil, Shraddha Pawar, Shweta Talekar, Gouri Khot, Prashant Sawant, Kuldip Belekar, Tamseen Nejakar, Najiya Mulla, Nadiya Patel, Sohel Shaikh, and Sumita Patil*** *for their wonderful collaboration. I want to thank them for their support and valuable suggestions during research work.*

I am thankful to ***Mrs. Namrata, Mr. Ramdas, Mr. Onkar, and Mrs. Savita*** *of the Centre for Interdisciplinary Research (CIR) and D. Y. Patil Education Society for co-operation in many ways during PhD.*

My heartfelt appreciation goes out to my father ***Chandrakant****, my mother* ***Manjusha****, my lovely brother* ***Prathmesh,*** *and all of the family members who depite their hard times and sufferings, continuously supported and encouraged me to complete my research.*

~Divya

Place: Kolhapur

LIST OF PATENTS, PUBLICATIONS AND CONFERENCES ATTAINED

Patents: (Granted 01, Published 06)

1. Method of synthesizing reduced graphene oxide/polyaniline coating for energy storage application thereof, Prof. C. D. Lokhande, **Miss. D. C. Pawar**, Mr. A. G. Bagde, Mr. S. R. Sankapal, Grant number: **542485**.

2. Porous reduced graphene oxide/ruthenium oxide coating for energy storage application, Prof. C. D. Lokhande, Mr. A. G. Bagde, **Miss. D. C. Pawar**, Mrs. J. P. Thorat, Dr. A. C. Lokhande, Application no: 202321038525.

3. A Method of synthesizing reduced graphene oxide-Nickel Cobalt oxide (rGo-$NiCO_2O_4$) composite coating on solid surface for energy storage application, Prof. C. D. Lokhande, Mrs. J. P. Thorat, Mr. A. G. Bagde, **Miss. D. C. Pawar**, Mr. S. D. Khot, Dr. V. C. Lokhande, Application no: 202321047985.

4. A chemical method of reduced graphene oxide/polypyrrole coating for energy storage, Prof. C. D. Lokhande, **Miss. D. C. Pawar**, Dr. V. C. Lokhande, Mrs. J. P. Thorat, Mr. A. G. Bagde, Application no: 202421002872.

5. Synthesizing method of copper vanadate oxide coating for energy storage application, Prof. C. D. Lokhande, Mr. S. R. Sankapal, Mr. A. G. Bagde, **Miss. D. C. Pawar**, Mrs. J. P. Thorat, Dr. V. C. Lokhande, Application no: 202421017358.

6. Method of synthesizing reduced graphene oxide/dysprosium sulfide composite coating for energy storage application thereof, Prof. C. D. Lokhande, Mr. S. D. Khot, Mr. A. G. Bagde, **Miss. D. C. Pawar**, Mr. S. B. Shaikh, Dr. V. C. Lokhande, Application no: 202421063773.

7. A chemical synthesis method for rGO/$NiCo_2O_4$ composite thin films electrocatalyst for oxygen evolution reaction, Prof. C. D. Lokhande, Mrs. J. P. Thorat, **Miss. D. C. Pawar**, Mr. S. R. Sankapal, Application no: 202421064202.

Papers Published in International Journals: (06)

1. **D. C. Pawar**, D. B. Malavekar, A. C. Lokhande, C. D. Lokhande, Facile synthesis of layered reduced graphene oxide/polyaniline (rGO/PANI) composite electrode for flexible asymmetric solid-state supercapacitor, J. Energy Storage, 79, (2024), 110154-110170, https://doi.org/10.1016/j.est.2023.110154 **(I.F.- 8.9)**.

2. **D. C. Pawar**, A. G. Bagde, J. P. Thorat, C. D. Lokhande, Synthesis of reduced graphene oxide (rGO)/polyaniline (PANI) composite electrode for energy storage:

Aqueous asymmetric supercapacitor, Eur. Polym. J., 218, (2024), 113366-113378, https://doi.org/10.1016/j.eurpolymj.2024.113366 **(I.F.- 5.8)**.

3. **D. C. Pawar**, D. B. Malavekar, J. H. Kim, C. D. Lokhande, Chemically deposited reduced graphene oxide/polypyrrole (rGO/Ppy) composite thin films for flexible solid-state supercapacitor: Effect of rGO composition, Electrochim. Acta, 514, (2025), 145671-145685 **(I.F.- 5.5)**

4. **D. C. Pawar**, D. B. Malavekar, S. D. Khot, A. G. Bagde, C. D. Lokhande, Performance of chemically synthesized polyaniline film-based asymmetric supercapacitor: Effect of reaction bath temperature, Mater. Sci. Eng. B, 292, (2023), 116432-116448, https://doi.org/10.1016/j.mseb.2023.116432 **(I.F.- 3.9)**.

5. A. G. Bagde, D. B. Malavekar, **D. C. Pawar**, S. D. Khot, C. D. Lokhande, Pseudocapacitive performance of amorphous ruthenium oxide deposited by successive ionic layer adsorption and reaction (SILAR): Effect of thickness, J. Phys. Chem. Solids, 179, (2023), 111386-111397, https://doi.org/10.1016/j.jpcs.2023.111386 **(IF-4.3)**.

6. D. Malavekar, **D. Pawar**, A. Bagade, S. Khot, S. Sankapal, S. Bachankar, S. Patil, C. Lokhande, J. Kim, Advancements in 2D carbon composite materials: A comprehensive review on synthesis, characterization, and supercapacitive charge storage, J. Chem. Eng., 501, (2024), 157533- 157576 **(I.F.- 13.3)**.

Paper/Poster Presented at National/International Conferences: (03)

1. Presented poster in international conference on **''Advanced Material Synthesis, Characterizations, and Applications''** (AMSCA-2022), 18th to 20th October 2022, Department of Physics, Savitribai Phule University, Pune.
2. Presented research paper in Three days International Conference on **"Nano Composite for Aerospace Applications"**, 2th to 4th February 2023, Department of Basic Science and Electronics and Communication Engineering, Cambridge Institute of Technology, Bengaluru.
3. Presented poster in Three days International Conference on **"Nanotechnology Addressing the Convergence of Materials Science, Biotechnology and Medical Science (IC-NACMBM-2024)"**, 12th to 14th February 2024, organized by CIR, D. Y. Patil Education Society, Kolhapur.

Conference/Seminar/Workshop Participation: (08)

1. Workshop and hands-on training on **"BIO-ATOMIC FORCE MICROSCOPY (BIO-AFM)"**, 4th and 5th January 2022, Shivaji University, Kolhapur.
2. National Conference on **"Emerging Trends in Chemistry"**- 10th February 2022, SMM Akluj.

3. Workshop on **''Intellectual Property Rights''** under National IPR Awareness Mission, 12th August 2022, D. P. Bhosale College, Koregaon.

4. International Conference on **"Emerging Trends in Material Science"**- 9th and 10th November 2022, D. P. Bhosale College, Koregaon.

5. National seminar on **"Emerging Nano Materials for Renewable Energy"**, 26th December 2022, Sanjay Ghodawat University, Kolhapur.

6. One Day National Conference on "**Physical, Chemical and Biological Strategies, Tools and Ideas for Promising Future"**, 10th March 2023, K. N. Bhise Arts, Commerce and Vinayakrao Patil Science College, Vidyanagar, Bhosare (Kurduwadi), Solapur.

7. One Day international Conference **on "Recent Trends in Fabrication of Nanomaterials and Their Applications (ICRTFNA-2023)"**, 15th March 2023, Rajarshri Chhatrapati Shahu College, Kolhapur.

8. One Day National Conference on **"Emerging Trends in Basic Science (NCETBS-2023)"**, 20th March 2023, Madhavrao Patil Arts, Commerce and Science college, Palam.

CONTENTS

LIST OF FIGURES

LIST OF TABLES AND CHARTS

LIST OF ABBREVIATIONS

AC	Activated carbon
Ag/AgCl	Silver/Silver chloride
APS	Ammonium persulfate
AR	Analytical grade
ASC	Asymmetric supercapacitor
BET	Brunauer- Emmett-Teller
BJH	Barrett-Joyner-Halenda
C_s	Specific capacitance
CBD	Chemical bath deposition
CC	Carbon cloth
CE	Counter electrode
CNT	Carbon nanotubes
CPs	Conducting polymers
CV	Cyclic voltammetry
CVD	Chemical vapour deposition
DDW	Double distilled water
EDLC	Electrochemical double layer capacitors
EIS	Electrochemical impedance spectroscopy
FT-IR	Fourier transform infrared spectroscopy
FWHM	Full width at half maximum
GCD	Galvanostatic charge-discharge
HCl	Hydrochloric acid
Hg/Hg_2SO_4	Mercury/Mercurous sulfate
HSCs	Hybrid supercapacitors
H_2SO_4	Sulphuric acid
IP	Ionic product
IUPAC	International Union of Pure and Applied Chemistry
KCl	Potassium chloride
KNO_3	Potassium nitrate
KOH	Potassium hydroxide
LBL	Layer-by-layer
LEDs	Light emitting diodes
LIBs	Lithium-ion batteries
LiCl	Lithium chloride
Na_2SO_4	Sodium sulfate
P	Adsorptive pressure
PANI	Polyaniline
Ppy	Polypyrrole
Pt	Platinum plate
PT	Polythiophene
PVA	Polyvinyl alcohol
PVDF	Polyvinylidene fluoride
Q	Constant phase element
rGO	Reduced graphene oxide
R_{ct}	Charge transfer resistance
R_s	Equivalent series resistance
RE	Reference electrode
RF	Radio frequency
S_E	Specific energy
SILAR	Successive ionic layer adsorption and reaction
S_P	Specific power
SP	Solubility product
SS	Stainless steel
SSC	Symmetric supercapacitor
t_d	Discharge time
ΔV	Potential window
W	Warburg
WE	Working electrode
WO_3	Tungsten oxide
XPS	X-ray photoelectron spectroscopy
XRD	X-ray diffraction

CHAPTER – I

Introduction of supercapacitor and literature review

CHAPTER – I

Introduction of supercapacitor and literature review

1.1 Energy storage systems:

In the previous decade, increasing industrialization, the human population and degradation of environment, as well as the depletion of fossil resources, have become the biggest pressing issues for both current and next generations **[1]**. Additionally, in a global ecology, natural resources are limited. To address these problems, there is a pressing necessity for development of secure and environmentally friendly renewable energy sources **[2, 3]**. In the past few years, renewable energy sources including solar, wind, and hydropower have become increasingly advantageous for the conversion of energy systems. It is more important to use these renewable energy sources to continuously produce energy rather than relying on fossil fuels. But the main drawback is that these resources are unreliable. Energy storage is a vital component that can help solve the issues. This accelerates research in the energy storage field involving academics and company to produce an electricity storage device. Furthermore, inexpensive, portable, lightweight, and high performance energy storage devices are essential needs to satisfy the demands for energy of the next generation. The energy storage device known as the supercapacitor (ultracapacitor) offers significant potential for use in a variety of applications **[4-6]**. Due to its useful characteristics including enhanced cycle stability, a quick charge-discharge process, and high power density, supercapacitors are used in a variety of applications, including hybrid automobiles, memory backup systems, and portable electronic gadgets **[7, 8]**. Like batteries, it can store and distribute electrical energy, however, they use a variety of electrochemical processes. Energy storage system performance may be described in relation of energy and power density.

The Ragone plot as seen in **Fig. 1.1** showing the "charge" times for various energy storage and combustion devices. The different materials that are available for the manufacture of various energy storage device components, including as an electrode, electrolytes, materials for packaging, and manufacturing processes, are some of the crucial factors that affect the device costs. In order to alter manufacturing processes, boost energy storage capacity, and improve electrochemical stability, several electrode materials have been thoroughly investigated. The choice of electrolyte has an impact on the stability and charge storage capacity of electrode materials. Researchers have mostly concentrated on developing cheap, non-toxic electrode materials **[9]**.

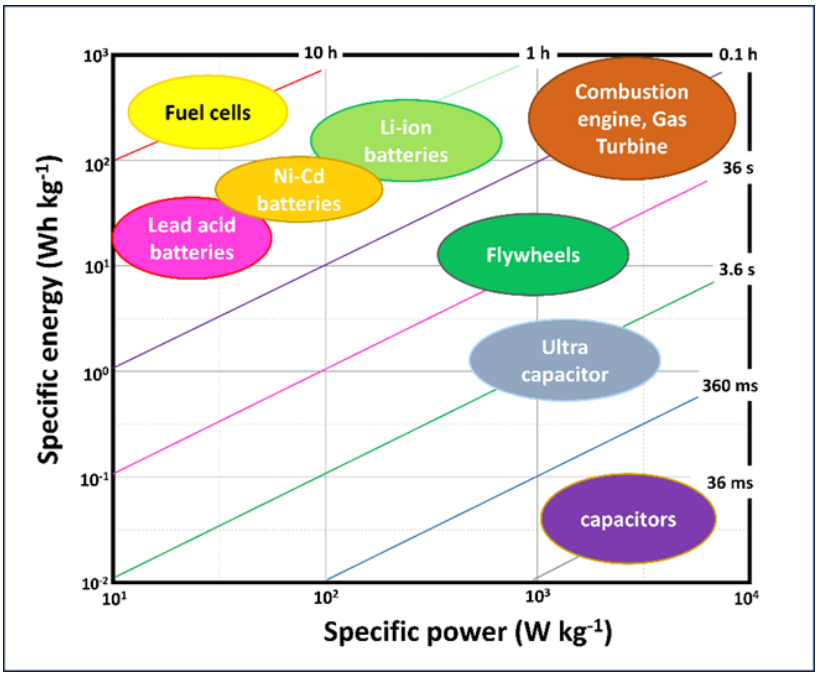

Fig. 1.1: Ragone plot for several energy storage and combustion devices along with their "charge" periods **[10]**.

An suitable, flexible energy storage device with a long lifetime is needed for the growing uses of lightweight and portable electronics. For energy storage devices, supercapacitors and lithium-ion batteries (LIBs) are useful in portable electronics. They both hold energy in distinct ways, the first stores energy by bulk redox processes, whereas the latter stores energy through electrostatic reactions (for carbon materials) or reversible redox reactions at the electrode surface (transition metal chalcogenides, oxides, and conducting polymers) **[11, 12]**.

Supercapacitors play a crucial role in the Ragone plot since they bridge the gap among batteries and traditional capacitors. Compared to regular capacitors, they have a higher energy density and greater power capacity. They have a greater power density and can deliver a substantial amount of energy. They also exceed batteries in terms of stability and have higher capacitance compared to traditional capacitors and lower equivalent series resistance (R_s). Hence supercapacitors offer a viable solution for more functioning electronics to meet rising power demands **[13]**.

1.2. Supercapacitors:

1.2.1 Basic working principle:

A supercapacitor stores energy by forming an electric double-layer at the electrode/electrolyte interface, in contrast to a typical capacitor, which stores energy

over electrode surfaces separated by a dielectric substance. The schematic of an electrochemical capacitor is displayed in **Fig. 1.2.** The specific capacitance (C_s) of supercapacitor devices is primarily influenced by the electrode plates specific surface area as well as the spacing across the two plates. The electrochemical capacitors capacitance is determined using the formula,

$$C = \frac{\varepsilon A}{d} \qquad (1.1)$$

where, 'C' is the capacitance of electrochemical capacitor, 'ε' is dielectric constant of the vacuum, 'A' denotes the specific surface area of the active electrodes, and 'd' is spacing. The following formulas can be used to calculate the specific energy (S_E) and specific power (S_P) of electrochemical capacitors:

$$S_E = \frac{C_S \times V^2}{7.2} \qquad (1.2), \text{ and}$$

$$S_P = \frac{3600 \times S_E}{t} \qquad (1.3)$$

where 'C_s' stands for specific capacitance, 'V' is a supercapacitor potential window, and 't' stands for discharge time.

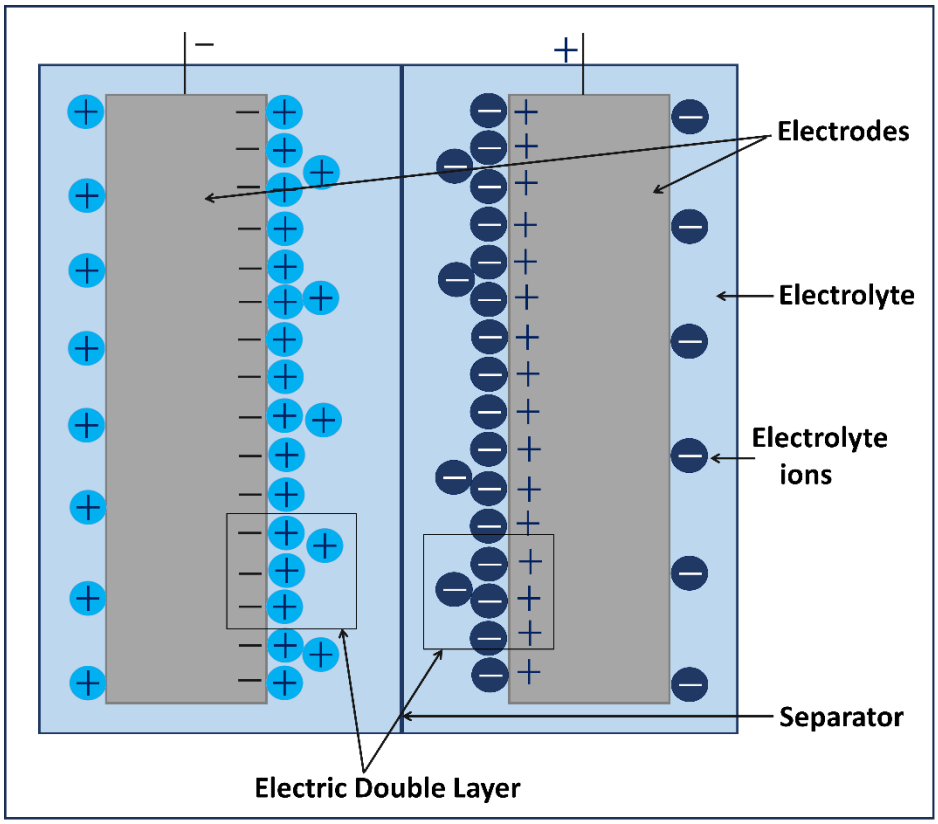

Fig. 1.2: Schematic of an electrochemical capacitor.

1.2.2 Taxonomy of supercapacitor:

Taxonomy of supercapacitor are classified into three primary groups based on the material and charge storage process used: electrochemical double layer capacitors (EDLC), faradic capacitors (also known as pseudocapacitors), and hybrid capacitors. In order to achieve exceptional charge storage capacity, the electrode materials must meet several requirements, including low synthesis cost, environmental friendliness, high electrical conductivity, chemical and thermal stability within the electrolyte, and a large specific surface area with appropriate pore size for electrochemical redox reactions.

Carbon-based materials are commonly used for EDLC type supercapacitor due to their thermal and chemical stability, as well as excellent conductivity. Pseudocapacitive materials, including conducting polymers, and metal hydroxides, nitrides, chalcogenides, carbides, silicates are used as pseudocapacitors because to their reversible redox processes and capacity of storing higher charges than EDLC materials **[14, 15]**. **Chart 1.1** depicts the categorization of supercapacitors into various types and subtypes.

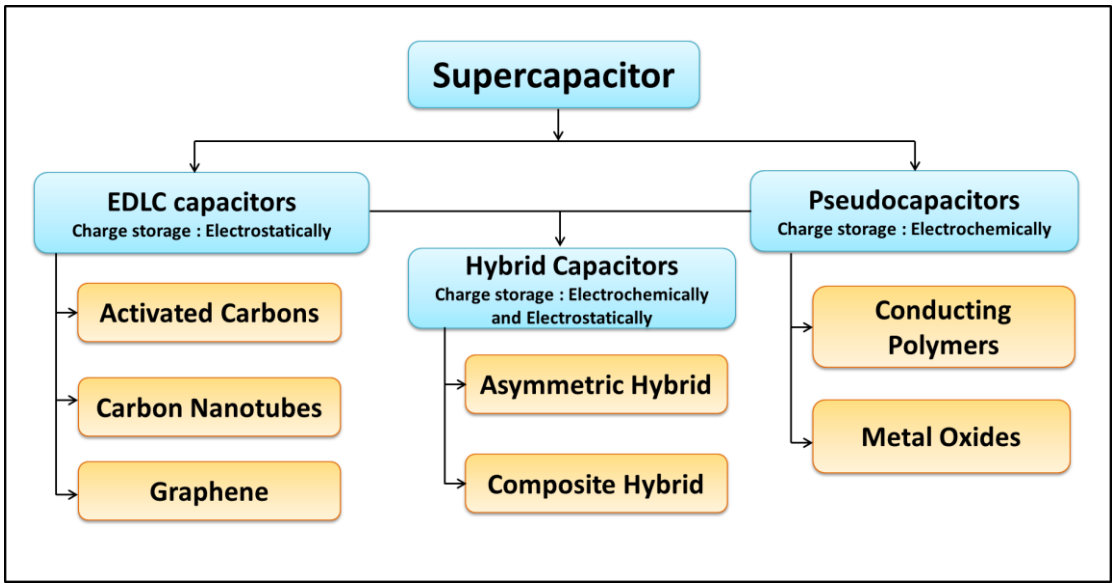

Chart 1.1: Supercapacitors classification with several types and subtypes.

1.2.2.1 Electrochemical double layer capacitors (EDLCs):

An electrochemical capacitor known as an EDLC stores charges at the electrode/electrolyte interface, causing it to store charges non-faradically. In addition to having a higher power capacity than batteries, they are also very promising

possibilities with an extended charge/discharge life due to their effectively reversible charge storage and release mechanism. In order to get high performance electrode material, a great deal of research has been done on carbon allotropes like carbon aerogels, activated carbons, graphene, graphite paper, graphene oxide (GO), reduced graphene oxide (rGO), and carbon nanotubes increased thermal and electrochemical stability, as well as better conductivity, across the board in electrolytes. Increased C_s compared to traditional capacitors can be achieved because both electrodes employ double-layer charge storage. In EDLC supercapacitors, carbon-based materials with significantly larger surface area (up to 3000 m^2 g^{-1}) and very thin double layer thicknesses, as opposed to traditional capacitors that use electrode distance **[16, 17]**. The charge storing mechanism of EDLC is shown in **Fig. 1.3a**.

1.2.2.2 Pseudocapacitors:

Pseudocapacitor is another type of supercapacitors. Pseudocapacitors store energy via transferring charges between electrode and electrolyte through quick, reversible surface redox processes. The pseudocapacitor schematic with a redox process is shown in **Fig. 1.3b**. The surfaces of pseudocapacitive electrodes undergo oxidation and reduction when a voltage is applied. In order to store higher charges and energy, supercapacitors primarily employ pseudocapacitive materials. Pseudocapacitive materials are crucial for attaining high S_E and S_P, which is the primary goal of recent energy storage systems. There are two types of pseudocapacitive materials such as conducting polymers and metal oxides.

1.2.2.3 Hybrid capacitors:

Carbon-based electrode materials are preferred for EDLCs because to their greater surface area compared to pseudocapacitive materials. The EDLCs have less S_E and a comparatively smaller C_s. In contrast to EDLCs, the pseudocapacitor has a higher S_E; nevertheless, it is not as stable because of its redox processes and has several drawbacks, including electrical conductivity and lower S_P. The development of a new supercapacitor type known as hybrid capacitors allowed for the minimising of the drawbacks of EDLCs and pseudocapacitors. Combining EDLC and pseudocapacitor materials, the hybrid capacitor stores charges by both redox and electrostatic processes **[18-20]**. The charge storing mechanism of hybrid capacitor is shown in **Fig. 1.3c**. High capacitance pseudocapacitive or faradic electrodes in hybrid

capacitor systems yield high S_E, whereas larger S_P are achieved possible by the electrostatic EDLC electrode. Hybrid capacitor offer superior capacitance, cyclic stability, S_E and S_P in comparison to EDLCs and pseudocapacitors. Researchers are trying to produce new hybrid electrode materials for supercapacitors with a significant C_s, electrochemical stability, S_E and S_P. etc. Combining the advantages of different materials to form composites should be an effective approach to optimizing each component for enhancing their supercapacitor performance.

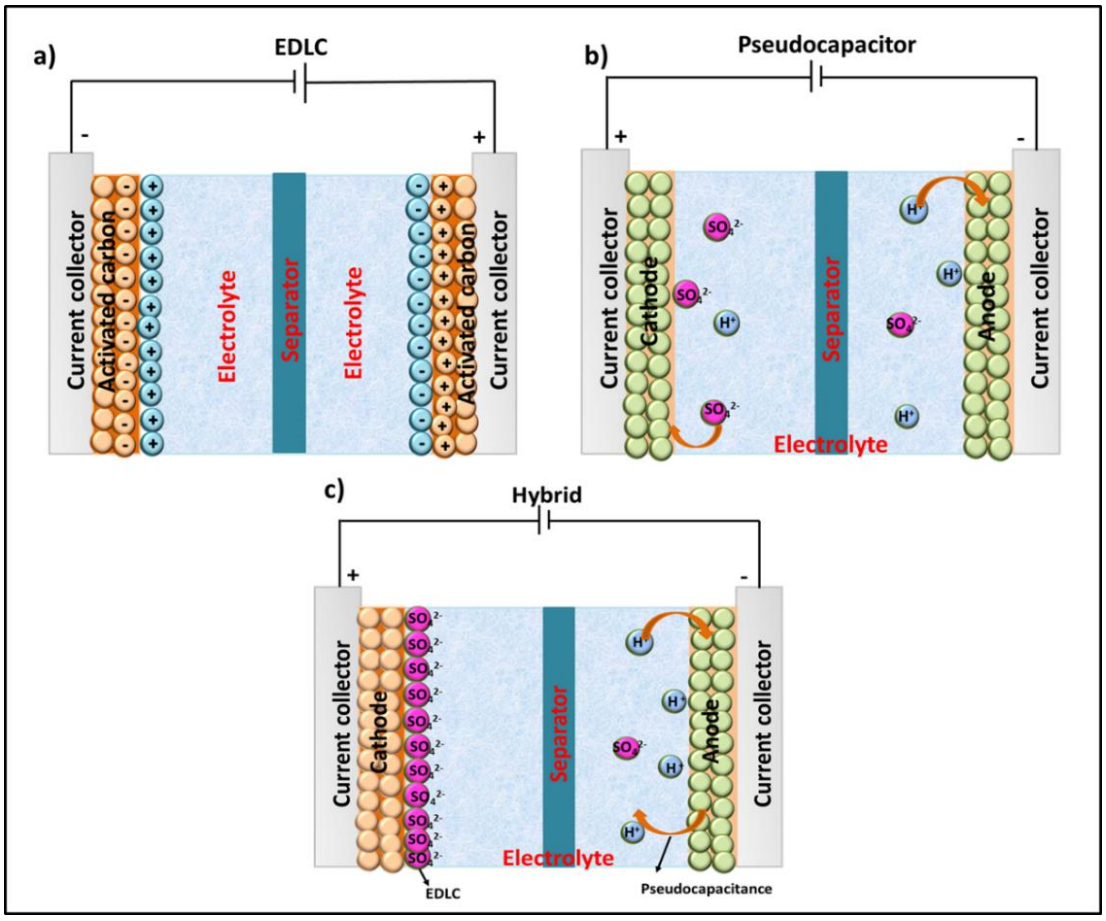

Fig. 1.3: Schematic of charge storage mechanisms a) EDLC, b) pseudocapacitor, and c) hybrid capacitor.

1.3 Electrode materials for supercapacitors:

It is well known that the performance and characteristics of supercapacitors are significantly influenced by the electrode materials used. In order to fabricate excellent performance supercapacitors, the following are essential requirements for electrode material:

- To obtain the highest C_s use a high specific surface area.

- Ion intercalation may be easily facilitated by controlled porosity.
- Non-toxic and inexpensive materials are required. To enhance electrochemical performance, a number of active sites is needed.
- Excellent electrical conductivity is necessary for S_P and rate capabilities.
- An easy and inexpensive synthesis method for the production of electrodes.

1.3.1 Carbon-based materials:

Carbon-based materials are ideal for electrochemical energy storage due to their distinct physical and chemical features. These features include a broad availability of the electrochemically active sites, great chemical stability, superior corrosion resistance, outstanding electric conductivity, huge specific surface area, and tunable pore size **[21]**. To improve the supercapacitive characteristics of EDLCs, electrode materials based on carbon, such as carbon aerogel, carbon nanotubes, and activated carbon, are regularly utilized.

1.3.1.1 Activated carbon (AC):

Activated carbons (ACs) are commonly used in supercapacitor electrodes due to their enormous surface area (>1000 m^2 g^{-1}), chemical stability, superior electrical conductivity, and low prices **[22]**. For the production of ACs, a variety of carbonaceous materials can be utilised as precursors, such as wood, coal, nutshells, and charcoal. ACs are produced from low porosity materials by the use of appropriate activation techniques, such as physical, chemical, and hybrid activation. The ACs improves supercapacitor performance by controlling surface area, pore distribution, pore length, and size **[23]**. Although capacitance is affected by surface area, the experimental results indicate that ACs whole surface area is not contributing to the device capacitance.

1.3.1.2 Carbon nanotubes (CNTs):

Carbon nanotubes (CNTs) are cylindrical hollow nanostructures made up of carbon allotropes. The synthesis of supercapacitor electrodes has attracted special attention to CNTs because of their exceptional qualities, which include high conductivity, strong thermal and chemical stability, highly pores structures, etc. Due to their unique open tubular shape, high aspect ratio, and exceptional mechanical

stability, CNTs provide good substrates for other materials. Research on CNTs have shown interest for replacing carbon electrodes in a number of applications, including supercapacitors, sensors, batteries, hydrogen storage, and semiconductors. There are three types of carbon nanotubes: multi-walled (MWNTs), single-walled (SWNTs), and double-walled (DWNTs). CNTs are commonly employed as electrode materials in high S_P devices due to their relatively low resistance **[24, 25]**. There are several ways of producing CNTs, including chemical vapour deposition (CVD), arc discharge, and laser ablation. CNTs frequently serve as electrodes in supercapacitors due to their reduced R_s compared to AC electrodes, resulting in S_E and S_P **[26]**.

1.3.1.3 Graphene:

In emerging materials, the two-dimensional and sp^2 hybridized carbon material known as graphene has emerged as a promising choice for supercapacitor electrode material. This is because graphene sheets have a huge accessible surface area (2630 $m^2\ g^{-1}$), facilitating large double-layer capacitance. In addition, covalent sp^2 bonds between carbon atoms have a unique physical structure that promotes high electrical conductivity, which significantly lowers resistance of material **[27, 28]**. In practical applications, rGO is typically another choice for graphene. The structure of rGO changes due to small changes in reduction methods. However, GO sheets have reduced electrical conductivity due to increased disorder and oxygen containing groups **[29]**. Graphene is a very attractive material because of its rapid electron transfer kinetics, wide surface area, and extended stability when compared to other carbon-based materials like AC and CNTs **[30]**. To achieve superior electrochemical performance, special focus has been given to improving extremely efficient graphene methods for production.

1.3.2 Pseudocapacitive materials:

Pseudocapacitive materials gained importance because to their high S_E, C_s, and quick, reversible faradic reactions. Supercapacitors primarily uses pseudocapacitive materials to store larger amounts of charges. Pseudocapacitance is the term used to describe these materials ability to retain charge through rapidly reversible redox processes at the electrode surface. In comparison to batteries, these pseudocapacitive materials undergo redox processes more quickly. There are two types of pseudocapacitive materials: conducting polymers and metal oxides.

1.3.2.1 Conducting polymers (CPs):

Since conducting polymers (CPs) have a large voltage window, large pores, and excellent conductivity, they are suitable electrode materials for supercapacitors **[31, 32]**. Redox processes take place both on the surface and within conducting materials. Ions are absorbed from the electrolyte to polymer surfaces during charging and released upon discharge. Due to the lack of phase transition in CPs, redox processes are extremely reversible. CPs get positively or negatively charged during oxidation or reduction processes, which causes them to exhibit conducting behaviour. These oxidation and reduction reactions are commonly referred to as doping. CPs only have conductive properties when they are doped. In supercapacitor electrode materials, polyaniline (PANI) **[33]**, polypyrrole (Ppy) **[34]**, and polythiophene (PT) **[35]** are the most often utilized CPs. An ideal working potential window is crucial for polymers. Improper potential windows cause CPs to deteriorate and decrease in conductivity. Consequently, optimal supercapacitor performance of CPs depends greatly on potential range.

1.3.2.2 Metal oxides:

Metal oxides have a high C_s, a high S_E, and improved cycle stability, making them appealing and viable electrode materials for supercapacitors. Metal oxides can have many oxidation states within a single phase. Metal oxides can change their state of oxidation during the charging and discharging process, allowing for ion intercalation and deintercalation in the active material. Transition metal oxides, including manganese dioxide (MnO_2) **[36]**, tungsten trioxide (WO_3) **[37]**, ruthenium oxide (RuO_2) **[38]**, vanadium pentoxide (V_2O_5) **[39]**, and cobalt oxide (Co_3O_4) **[40]**, have been evaluated as electrode materials for supercapacitors. Among them, RuO_2 is one of these transition metal oxides that is commonly used as the active electrode material in supercapacitors because of its excellent electrical conductivity, broad potential window, and large theoretical C_s **[41, 42]**. Nevertheless, ruthenium precursors are too costly and hazardous to be used further for commercial purposes.

1.4 Literature review:

The remarkable physical and electrical features of CPs have garnered significant interest for their potential uses in optoelectronic, optical, and electronic

devices **[43]**. Recently, CPs are considered as promising electrode materials due to their large surface area, relatively low resistance, stability, and other unique features. Typically, polymers form three-dimensional structures with significant porosity and roughness. This provides a huge surface area that is ideal for accelerating the electrochemical process. The PANI and Ppy are the excellent materials among CPs and have been studied recently due to its strong environmental stability, various redox states, and a significant doping dedoping rate during charging and discharging. Furthermore, it is inexpensive and simple to produce into a variety of nanostructures **[44, 45]**. **Table 1.1** provides a literature review of PANI and Ppy electrode materials for energy storage applications.

1.4.1 Literature review of conducting polymers:

CPs involve PANI, Ppy, and PT, have also been largely composited and studied for supercapacitor applications due to their prominent energy storage properties **[46]**. CPs have special and significant characteristics, especially the capacity to transition between redox states and strong electrical conductivity like metals. Here few reports describe preparation of CPs thin films using different deposition methods. **Table 1.1** summarizes the literature study on CPs electrode materials for supercapacitor applications.

Soudagar et al. **[47]** reported PANI on the surface of stainless steel (SS) prepared by chemical bath deposition (CBD) method and achieved a C_s of 670 F g^{-1} at a 5 mV s^{-1} scan rate in a 1 M H_2SO_4 electrolyte. Zhou et al. **[48]** reported PANI electrode synthesized by microwave assisted chemical oxidative polymerization method and exhibited a C_s of 1034 F g^{-1}. Zeng et al. **[49]** reported an templet free chemical polymerization method to prepare PANI with a C_s of 584 F g^{-1}. Anbalagan and Sawant **[50]** reported porous PANI electrode and achieved a C_s of 662 F g^{-1}. For the synthesis of PANI nanofibers, Zhou et al. **[51]** reported a in-situ polymerization method and exhibited a C_s of 636 F g^{-1}. Hou et al. **[52]** reported deposition of PANI by electrodeposition method, which exhibited a maximum C_s of 149.3 mF cm^{-2}. Chemical coprecipitation method for developing sea cucumber-shape of PANI on SS substrate was reported by Sun et al. **[53]**, and a C_s of 408 F g^{-1} was achieved. Erdogan et al. **[54]** reported PANI synthesized via electrodeposition method, which showed C_s of 833 F g^{-1}. Zhang et al. **[55]** reported that electropolymerization synthesized PANI,

which showed C_s of 1342 C g^{-1}. Lakshmi et al. **[56]** reported C_s of 106 F g^{-1} for PANI thin film synthesized using solar irradiation method. Mooss et al. **[57]** reported PANI electrode on grafoil paper prepared by Chemical oxidation method, which exhibited C_s of 523 F g^{-1}. Bhalerao et al. **[58]** reported that chemical precipitation method for synthesized Ppy electrode and exhibited C_s of 931 F g^{-1}. Bo et al. **[59]** used the tube-inversion method to produce Ppy thin films on a CC glass substrate. The C_s value for the nanoparticles Ppy electrode was 328 F g^{-1}. Zhao et al. **[60]** prepared nanowires structure of Ppy using chemical oxidative polymerization method and achieved C_s of 420 F g^{-1}. Wang et al. **[61]** reported C_s of 313 F g^{-1} for Ppy electrode synthesized via modified vapor phase polymerization method. Rajesh et al. **[62]** synthesized cauliflower-like Ppy nanostructures with a C_s of 297 F g^{-1}. Li and Yang **[63]** used chemical oxidative polymerization method for preparation of Ppy on nickel foam with C_s of 576 F g^{-1}. Chen et al. **[64]** reported Ppy nanoparticles prepared through a simple interfacial polymerization method, which exhibited C_s of 736.1 mF cm^{-2}. Dubal et al. **[65]** reported C_s of 604 F g^{-1} of Ppy nanofibers thin film prepared by reactive template route. Electrodeposition method for developing horn-like Ppy was reported by Sun et al. **[66]**, and a C_s of 420 mF cm^{-2} was achieved.

Conclusions:

The literature survey shows that, different methods have been used to synthesis several CPs materials. Electropolymerization produced the maximum C_s value (1342 C g^{-1}) for a PANI electrode in 1 M H_2SO_4 electrolyte **[55]**.

Table 1.1: The literature review of conducting polymer thin films for supercapacitor application.

Sr. No.	Material	Synthesis method	Substrate	Surface morphology	Electrolyte	Specific capacitance ($F\ g^{-1}$)	Potential window	Stability (%) (cycles)	Ref. No.
1	PANI	Chemical bath deposition (CBD)	SS	Nanotubes	1M H_2SO_4	670	-0.2 to 0.8 V/SCE	67 (5,00)	47
2	PANI	Microwave assisted chemical oxidative polymerization	CC	Honeycomb-like nanosheet	1 M H_2SO_4	1034	-0.4 to 1.0 V/SCE	92 (5,000)	48
3	PANI	Templet free chemical polymerization	Glassy carbon (GC)	Nanobelt	1 M H_2SO_4	584	-0.2 to 0.8 V/Ag/AgCl	77 (2,000)	49
4	PANI	Polymerization	GC	Porous	0.5 M H_2SO_4	662	0 to 0.8 V/Ag/AgCl	60 (1,000)	50
5	PANI	In-situ polymerization	GC	Nanofibers	1 M H_2SO_4	636	-0.2 to 0.8 V/SCE	83 (10,000)	51
6	PANI	Electrodeposition	Graphite paper	Nanofibrous	1 M HCl	149.3 $mF\ cm^{-2}$	-0.5 to 0.5 V/SCE	93 (5,000)	52
7	PANI	Chemical coprecipitation	SS	Sea cucumber-shape	1 M H_2SO_4	408	-0.6 to 0.1 V/Hg/Hg_2SO_4	96 (5,000)	53
8	PANI	Electrodeposition	Graphite	Nanoparticles	Ethaline ionic liquid	833	-0.5 to 0.6 V/Ag wire	87 (10,000)	54
9	PANI	Electropolymerization	CC	Formicary-like	1 M H_2SO_4	1342 $C\ g^{-1}$	-0.2 to 0.8 V/Ag/AgCl	57 (2,000)	55

10	PANI	Solar irradiation	Fluorine doped tin oxide (FTO)	Nanorod	0.5 M H_2SO_4	106	-0.2 to 1.0 V/SCE	66 (1,000)	56
11	PANI	Chemical oxidation	Grafoil paper	Interconnected nano-bridge	0.5 M H_2SO_4	523	-0.4 to 0.4 V/Hg/Hg_2SO_4	88 (10,000)	57
12	Ppy	Chemical precipitation	Ni foam	Spherical	3 M KOH	931	-0.1 to 0.5 V/SCE	89 (5,000)	58
13	Ppy	Tube-inversion	CC	Nanoparticles	1 M H_2SO_4	328	0 to 0.8 V/Ag/AgCl	90 (3,000)	59
14	Ppy	Chemical oxidative polymerization	Nickel foam	Nanowires	1 M Na_2SO_4	420	-0.2 to 0.5 V/SCE	97.9 (8,000)	60
15	Ppy	Modified vapor phase polymerization	SS foil	Pore-rich	1 M Na_2SO_4	313	-0.6 to 0.4 V/Ag/AgCl	-	61
16	Ppy	Electropolymerization	SS	Cauliflower	1 M H_2SO_4	297	-0.2 to 0.8 V/Ag/AgCl	91 (4,000)	62
17	Ppy	Chemical oxidative polymerization	Nickel foam	Nanotubes	1 M KCl	576	0.1 to 0.7 V/SCE	82 (1,000)	63
18	Ppy	Interfacial polymerization	Air-laid paper	Nanoparticles	1 M HCl	736.1 mF cm^{-2}	0 to 0.7 V/Ag/AgCl	87 (10,000)	64
19	Ppy	Reactive template route	CC	Nanofibers	1 M H_2SO_4	604	0 to 0.8 V/Ag/AgCl	91 (1,000)	65
20	Ppy	Electrodeposition	Carbonized cotton fabric	Horn-like	1 M Na_2SO_4	420 mF cm^{-2}	-0.5 to 0.5 V/Ag/AgCl	96 (4,000)	66

1.4.2 Literature review of reduced graphene oxide/conducting polymers:

The surface morphology, C_s, stability values of several rGO based composite CPs materials synthesized with different chemical methods and electrolyte solutions are shown in **Table 1.2**. Ciplak et al. **[67]** prepared rGO-AuNPs/PANI composite using in-situ polymerization method and achieved a C_s of 441 F g^{-1}. Khawas et al. **[68]** synthesized rGO/MnO_2/PANI composite thin film using polymerization method and achieved C_s of 762 F g^{-1} in 1 M H_2SO_4 electrolyte. Shabani-Nooshabadi and Zahedi **[69]** prepared ERGO/PANI composite via electrodeposition method, which showed C_s of 184 F g^{-1}. Zheng et al. **[70]** developed MSG/PANI nano-arrays by in-situ polymerization method and observed C_s of 912 F g^{-1}. Using a hydrothermal method, Chen et al. **[71]** created worm-like nanorods of PANI/rGO composite electrode and achieved a C_s of 524 F g^{-1} in 1 M H_2SO_4 electrolyte. Vighnesha et al. **[72]** studied electrochemical performance of rGO/PANI composite electrode deposited via chemical blending process which exhibited C_s of 72 F g^{-1} in 0.1 M HCl electrolyte. For the synthesis of rGO/PANI, Liu et al. **[73]** reported a electrodeposition method and achieved a C_s of 853 F g^{-1}. Liu et al. **[74]** synthesized H-NrGO/PANI composite electrode via in-situ chemical oxidation polymerization method and obtained 746 F g^{-1} C_s in 1 M H_2SO_4. Chen et al. **[75]** used co-electrodeposition method for preparation of rGO/Ppy platelet-shaped with C_s of 411 mF cm^{-2}. Moyseowicz and Gryglewicz **[76]** used a hydrothermal method to produce Ppy/rGO, with a C_s of 186 mAh g^{-1}. Shu et al. **[77]** used electropolymerization method for preparation of rGO-Ppy nodule-like morphology with C_s of 440 mF cm^{-2}. Chen et al. **[78]** synthesized rGO/Ppy by pulsed electrochemical on Ti foil which exhibited a C_s of 419 mF cm^{-2}. Hao et al. **[79]** synthesized MoS_2/Ppy-rGO on Ni foam by hydrothermal method with C_s of 1942 F g^{-1} in 3 M KOH electrolyte. Alves et al. **[80]** prepared Ppy/rGO via chronoamperometry method with C_s of 213 F g^{-1} in 1 M KCl electrolyte. Zhang et al. **[81]** developed microspheres of GO/Carbon dots/Ppy, which revealed C_s of 582 F g^{-1} in 1 M H_2SO_4 electrolyte.

Table 1.2: The literature review of reduced graphene oxide (rGO)/conducting polymer composite thin films for supercapacitor application.

Sr. No.	Material	Synthesis method	Substrate	Surface morphology	Electrolyte	Specific capacitance ($F\ g^{-1}$)	Potential window	Stability (%) (cycles)	Ref. No.
1	rGO-AuNPs/PANI	In-situ polymerization	SS	Sub-micron polymeric particles	1 M H_2SO_4	441	0 to 0.8 V/Ag/AgCl	86 (5,000)	67
2	rGO/MnO_2/PANI	Polymerization	GC	Tubular wiregrass sedge and spherical cactus	1 M H_2SO_4	762	-0.2 to 0.8 V/Ag/AgCl	75 (10,000)	68
3	ERGO/PANI	Electrodeposition	GC	Spherical	1 M H_2SO_4	184	-0.2 to 0.6 V/Ag/AgCl	89 (1,000)	69
4	MSG/PANI	In-situ polymerization	Nickel foam	Nano-arrays	1 M H_2SO_4	912	-0.2 to 0.8 V/SCE	89 (10,000)	70
5	PANI/rGO	Hydrothermal	SS	Worm-like nanorods	1 M H_2SO_4	524	-0.2 to 0.7 V/SCE	81 (2,000)	71
6	rGO/PANI	Chemical blending	SS	Granular	0.1 M HCl	72	-0.2 to 0.8 V/SCE	95 (100)	72
7	rGO/PANI	Electrodeposition	CC	Tiny granules	1 M H_2SO_4	853	-0.2 to 0.8 V/Ag/AgCl	90 (8,000)	73
8	H-NrGO/PANI	In-situ chemical oxidation	Carbon current	Nanopores	1 M H_2SO_4	746	-0.2 to 0.8 V/SCE	97 (2,000)	74

		polymerization	collector						
9	rGO/Ppy	Co-electrodeposition	Ti	Platelet-shaped	1 M KCl	411 mF cm^{-2}	-0.5 to 0.5 V/SCE	80 (5,000)	75
10	Ppy/rGO	Hydrothermal	-	Spherical nanoparticles	1 M H_2SO_4	186 mAh g^{-1}	-0.65 to 0.25 V/Hg/Hg_2SO_4	96 (2,500)	76
11	rGO-Ppy	Electropolymerization	-	Nodule-like	1 M H_2SO_4	440 mF cm^{-2}	0 to 1.0 V/Ag/AgCl	81 (5,000)	77
12	rGO/Ppy	Pulsed electrochemical	Ti foil	Porous	1 M KCl	419 mF cm^{-2}	-0.5 to 0.5 V/SCE	95.7 (10,000)	78
13	MoS_2/Ppy-rGO	Hydrothermal	Nickel foam	Curled and crossed lamellas	3 M KOH	1942	-0.2 to 0.7 V/SCE	78 (3,000)	79
14	Ppy/rGO	Chronoamperometry	Carbon fiber	Granular and porous	1 M KCl	213	-0.5 to 0.5 V/Ag/AgCl	-	80
15	GO/Carbon dots/Ppy	In-situ polymerization	Nickel sheet	Microspheres	1 M H_2SO_4	582	-0.2 to 0.8 V/SCE	92.9 (5,000)	81

AuNPs: Gold nanoparticles, MnO_2: Manganese dioxide, ERGO: Electrochemical reduced graphene oxide, MSG: Multi-growth site graphene, H-NrGO: Holey nitrogen-doped reduced graphene oxide, MoS_2: Molybdenum disulfide, Ti: Titanium.

Conclusions:

A brief overview of current research on rGO composites with CPs is given in this literature review. In a 3 M KOH electrolyte, MoS_2/Ppy-rGO thin film over nickel foam produced by a hydrothermal method showed a maximum C_s of 1942 F g^{-1} **[79]**. These results reveal that, in comparison to pristine CPs thin films, rGO composited CPs thin films show better C_s and cyclic stability.

1.4.3 Literature review of reduced graphene oxide/conducting polymers composite based asymmetric supercapacitor (ASC) device:

The supercapacitor S_E is determined by their operating potential window and C_s value. Consequently, producing electrolytes with a wide potential window and electrode materials with high C_s, or combining both of them, can improve the S_E. Hence, to optimise supercapacitor performance, high performing active materials must be combined with appropriate electrolytes. In order to improve the supercapacitor devices S_E, an asymmetric configuration of supercapacitors is more desirable over a symmetric one. Asymmetric supercapacitor (ASC) devices provide a broad working potential window and additional benefits due to the configuration of various materials, such as pseudocapacitive and EDLCs. Therefore, electrodes with various charge storage mechanisms and operating potential windows were combined to form ASC devices.

Several studies report the use of CPs as a cathode in ASCs to accomplish S_E and S_P are displayed in **Table 1.3**. Lee et al. **[82]** fabricated AC//PANI-M90 ASC device and reported C_s of 73 C g^{-1} and capacitive retention of 80% for 3,000 cycles. The device showed S_E of Wh kg^{-1} at 0.378 kW kg^{-1} S_P. He et al. **[83]** fabricated $NiCo_2S_4$/PANI//AC ASC device with C_s of 152 F g^{-1} and S_E of 54.06 Wh kg^{-1} at 0.79 kW kg^{-1} S_P. After 5,000 cycles, device retained 84.5% of its capacitance. Iqbal et al. **[84]** prepared ASC device using AC and MOF/PANI electrode and reported C_s of 104 C g^{-1} with S_E of 23.11 Wh kg^{-1} and S_P of 1.60 kW kg^{-1}. Omar et al. **[85]** prepared PANI-$ZnCo_2O_4$//AC ASC device and showed C_s of 64 C g^{-1} in 2 M KOH electrolyte with 90% cyclic retention after 3,000 cycles. It delivered S_E of 13.25 Wh kg^{-1} at 0.375 kW kg^{-1} S_P. Rashti et al. **[86]** assembled a $NiCo_2O_4$-PANI-rGO//AC device with PVA-KOH gel electrolyte, achieving C_s of 262 F g^{-1} and 78% cyclic stability after 3,500 cycles. Additionally, it showed a high S_E of 45.6 Wh kg^{-1} with an S_P of 0.610

kW kg^{-1}. Zhang et al. **[87]** prepared rGOH//Ppy/rGOH solid-state ASC device. In PVA-KNO_3 electrolyte, the device demonstrated C_s of 131 F g^{-1} and improved cyclic stability of 94% after 10,000 cycles. It delivered S_E of 46.9 Wh kg^{-1} at 0.8 kW kg^{-1} S_P. Zhu et al. **[88]** studied electrochemical performance of Ppy/rGO//NCs ASC device in PVA/LiCl electrolyte with C_s of 43.2 F g^{-1}. It showed 88.7% cyclic stability for 10,000 cycles. The device showed high S_E of 15.8 Wh kg^{-1} at a S_P of 0.14 kW kg^{-1} with potential window 0 to 1.6 V. Li et al. **[89]** prepared ASC device in the configuration of V_2O_5/Ppy/CF//MnO_2/Ppy/CF. The device showed 51 F g^{-1} C_s in PVA/LiCl gel electrolyte and S_E of 26.8 Wh kg^{-1} at a S_P of 0.200 kW kg^{-1}. Ding et al. **[90]** prepared PGR//RGO ASC device. The electrochemical behaviour of device is studied in PVA/H_2SO_4 gel electrolyte. Device achieved C_s of 99 F g^{-1} with 91% electrochemical cyclic stability over 3,000 cycles. The device revealed the S_E of 19.32 Wh kg^{-1} at a 9.62 kW kg^{-1} S_P.

Conclusions:

This literature review gives a summary of recent research on aqueous and solid ASC devices that use CPs electrodes as the cathode electrode. In all devices, $NiCo_2O_4$-PANI-rGO//AC ASC solid-state device achieved the greatest C_s of 262 F g^{-1} in PVA-KOH gel electrolyte **[86]**. The advantages of polymer gel electrolytes over liquid electrolytes include flexible supercapacitor structures, exceptional electrochemical stability across a wider range, leakage-free systems, and effective ionic separators.

Table 1.3: Reduced graphene oxide (rGO)/conducting polymers composite based asymmetric supercapacitor devices.

Sr. No.	Device Configuration	Electrolyte	Potential (V)	Specific capacitance ($F\ g^{-1}$)	Energy density ($Wh\ kg^{-1}$)	Power density ($kW\ kg^{-1}$)	Stability (%) (cycles)	Ref. No.
1	AC//PANI-M90	1 M KOH	0 to 1.5	73 C g^{-1}	14.7	0.378	80 (3,000)	82
2	$NiCo_2S_4$/PANI//AC	PVA-KOH	0 to 1.6	152	54.06	0.79	84.5 (5,000)	83
3	AC//MOF/PANI	1 M KOH	0 to 1.6	104 C g^{-1}	23.11	1.60	-	84
4	PANI-$ZnCo_2O_4$//AC	2 M KOH	0 to 1.5	64 C g^{-1}	13.25	0.375	90 (3,000)	85
5	$NiCo_2O_4$-PANI-rGO//AC	PVA-KOH	0 to 1.5	262	45.6	0.610	78 (3,500)	86
6	rGOH//Ppy/rGOH	PVA-KNO_3	0 to 1.6	131	46.9	0.8	94 (10,000)	87
7	Ppy/rGO//NCs	PVA/LiCl	0 to 1.6	43.2	15.8	0.14	88.7 (10,000)	88
8	V_2O_5/Ppy/CF//MnO_2/Ppy /CF	PVA/LiCl	0 to 2.0	51	28.6	0.200	89 (20,000)	89
9	PGR//RGO	PVA/H_2SO_4	0 to 1.2	99	19.32	9.62	91 (3,000)	90

PANI-M90: Polyaniline-manganese phosphate, $NiCo_2S_4$: Nickel cobalt sulfide, PANI-$ZnCo_2O_4$: Polyaniline-zinc cobaltite, $NiCo_2O_4$: Nickel cobaltite, rGOH: Reduced graphene oxide hydrogel, NCs: Nitrogen-doped carbon nano-sheets, V_2O_5: Vanadium pentoxide, PGR: Polypyrrole based graphene hydrogel.

1.5 Title and objectives of the research:

Title:

"Chemically deposited reduced graphene oxide (rGO)/conducting polymer composite thin films for supercapacitor application".

Objectives:

1) To prepare graphene oxide by modified Hummer's method and reduced graphene oxide by chemical reduction method. To synthesis reduced graphene oxide (rGO)/conducting polymer (PANI and Ppy) composite thin films on solid substrate using SILAR and CBD methods.
2) To characterize reduced graphene oxide (rGO)/conducting polymer (PANI and Ppy) composite electrodes using different physico-chemical techniques.
3) To study supercapacitive properties of reduced graphene oxide (rGO)/conducting polymer (PANI and Ppy) composite electrodes using cyclic voltammetry (CV), galvanostatic charge-discharge (GCD) and electrochemical impedance spectroscopy (EIS) studies and to form asymmetric device and study supercapacitive performance evaluation.

1.6 Purpose of the research:

Over the past few decades, many attempts have been performed on improving the electrochemical properties and fabricate the supercapacitors to power portable and flexible electronic devices effectively. The electrolyte and electrode in supercapacitors generate R_s, which limits the device ability to reach greater S_P. Numerous methods have been used and are still being researched to lower R_s, including the electroactive materials grow directly on the current collector. Efficient supercapacitors have a large surface area and quick, reversible redox processes due to their active materials, which contribute to total performance. The development of novel electrode materials with greater conductive properties, larger redox potentials, and greater surface areas with porous electrodes will be essential to improve the performance of supercapacitors. The supercapacitors are widely used due to their inexpensive cost, high electrochemical performance, and extended cycle life. It is important to remember that the electrode material and electrolyte used in the supercapacitors will affect its performance and can be utilised to improve it. As a

result, there are several opportunities for developing active materials and electrolytes for supercapacitor.

Recently, CPs are widely used in various fields including solar cell, sensor, energy storage devices and bioelectronics due to their unique physical and chemical properties. CPs have high conductivity, good redox reversibility and environmental friendliness. In all CPs, PANI and Ppy have received a lot of attention, especially for its affordable price, environmental friendliness, and simplicity of preparation. Yet, because of weak structural stability in the charging and discharging processes, it has weak cycling and rate capability. An efficient way to improve electrochemical cycle stability is provided by EDLC materials combined with pseudocapacitive materials. The rGO sheets are composited with PANI and Ppy to boost the capacitance performance because of the special synergistic impact of the two materials. The rGO is characterized by layer structure with oxygen functional group. It is highly conductive, high theoretical specific surface area (>1000 $m^2 g^{-1}$), excellent mechanical strength (tensile strength 1 Gpa and young's modulus 1 Tpa). The rGO offers a robust scaffold for the polymer matrix, favorable lightweight excellent conductivity and electrochemical stability. Functional groups like -OH, -COOH, -CHO, etc. of rGO offer superior defect sites for the development of PANI and Ppy over rGO sheets.

Use of rGO controls pore structure in electrode, enhances effective surface area and lowers R_s. Hence the composition of rGO in CPs, improves the cycling stability of CPs. Thus, rGO offers high surface area and stability while CPs offer distinct redox activity and higher reduction potential of CPs provide large potential window and effectively improves C_s, S_E, S_P, and charge-discharge stability of composite thin films. Hence, the problem of poor stability and S_P of CPs materials can be solved employing rGO and it is as a backbone material for pseudocapacitive CPs.

However, there is still a problem with the synthesis of the composite electrode without using a binder on the conductive substrate. The stacking of rGO sheets is one of the issues for composition. However, the majority of these articles reported the production of rGO and CPs composite as powder, and the electrode preparation for supercapacitors in those reports used typical binder-assisted coating processes, including polyvinylidene fluoride (PVDF). On the other hand, present study examines the direct synthesis of PANI and rGO/PANI composite thin films on SS substrate using CBD method, as well as Ppy and rGO/Ppy composite thin films using simple successive ionic layer adsorption and reaction (SILAR) method. It is considered to be

a more effective strategy for improving interfacial contact than binder-enriched coating approaches.

These methods are simple, low energy consumption, and thereby, low-cost methods, useful for preparing uniform, well adherent and large area thin films. The CBD method relies on a compound solubility product to develop in the bath. The development of nucleation is essential for the formation of precipitates. The result of nucleation in solution is that the molecular clusters produced quickly decompose, and particles combine to grow the film to a particular thickness. The controlled precipitation of the desired compound from a solution of its constituents is the fundamental principle of CBD method. The SILAR method is a modification of CBD method that reduces material wastage.

As the initial part of the work, CBD and SILAR methods are used to produce rGO/PANI and rGO/Ppy thin films. Optimising preparation parameters such as solution concentration, bath temperature, pH, deposition time, number of SILAR cycles are crucial for achieving high quality film deposit. Using X-ray diffraction (XRD) technique, the phase formation and crystallite size are examined. Fourier transform infrared spectroscopy (FT-IR) and Raman spectroscopy are used to examine the chemical bonding and verify phase development of material. The field emission scanning electron microscopy (FE-SEM) method is used to examine the surface morphology of the thin film. The oxidation states of the material constituent elements are determined by X-ray photoelectron spectroscopy (XPS) technique. Contact angle measurement is used to study the wettability of films with electrolytes. Using Brunauer-Emmett-Teller (BET) and Barrett-Joyner-Halenda (BJH) techniques are used to determine the specific surface area and pore size distribution details. The electrochemical properties of rGO/PANI and rGO/Ppy electrodes are examined using cyclic voltammetry (CV), galvanostatic charge-discharge (GCD), and electrochemical impedance spectroscopy (EIS) techniques. The electrochemical supercapacitive analysis is conducted in a standard three-electrode setup includes a platinum plate, a saturated calomel electrode (SCE) as a counter, and a reference electrode, respectively and rGO/PANI, or rGO/PANI composite electrodes as a working electrode. An aqueous 1 M H_2SO_4 solution serves as the electrolyte. Finally, their supercapacitive performances are evaluated to find out C_s, resistive parameters, and cyclic stability.

The next stage involves fabrication of flexible solid-state ASC devices using rGO/PANI and rGO/Ppy electrodes as a cathode and PVA-H_2SO_4 gel as an

electrolyte. Fabrication of solid-state devices are used to explore electrode material performance and electrolyte usefulness. The devices supercapacitive performances are examined in terms of C_s, S_E, S_P, and cyclic stability. Furthermore, the impact of bending on electrochemical properties of the ASC devices are examined to verify its suitability for use in a variety of portable electronic devices.

References:

[1] C. Zhong, Y. Deng, W. Hu, J. Qiao, L. Zhang, J. Zhang, Chem. Soc. Rev., 44, (2015), 7484-7539.

[2] H. Huang and J. Zhu, Analyst., 144, (2019), 6789-6811.

[3] D. Dubal, N. Chodankar, D. Kim, P. Romero, Chem. Soc. Rev., 47, (2018), 2065-2129.

[4] L. Hou, H. Hua, S. Liu, G. Pang, C. Yuan, New J Chem, 39, (2015), 5507-5512.

[5] M. Jayalakshmi and K. Balasubramanian, Int. J. Electrochem. Sci., 3, (2008), 1196-1217.

[6] G. Wu, X. Wu, X. Zhu, J. Xu, N. Bao, ACS Nano., 16, (2022), 10130-10155.

[7] Q. Chen, Y. Meng, C. Hu, Y. Zhao, H. Shao, N. Chen, L. Qu, J. Power Sources, 247, (2014), 32-39.

[8] Y. Qian, R. Liu, Q. Wang, J. Xu, D. Chen, G. Shen, J. Mater. Chem. A, 2, (2014), 10917-10922.

[9] W. Low, P. Khiew, S. Lim, C. Siong, E. Ezeigwe, J. Alloys Compd., 775, (2019,) 1324-1356.

[10] S. Moura, J. Siegel, D. Siegel, H. Fathy, A. Stefanopoulou, IEEE Vehicle Power and Propulsion Conference, (2010), 1-6.

[11] P. Pazhamalai, K. Krishnamoorthy, S. Sahoo, V. Mariappan, S. Kim, Chem. Eng. J., 359, (2019), 409-418.

[12] N. Maile, S. Shinde, K. Patil, A. Fulari, A. Shahzad, D. Lee, V. Fulari, SN Appl. Sci., 1, (2019), 1333-1343.

[13] R. Rakhi, N. Alhebshi, D. Anjum, H. Alshareef, J. Mater. Chem. A, 2, (2014), 16190-16198.

[14] Q. Ke, C. Guan, X. Zhang, M. Zheng, Y. Zhang, Y. Cai, H. Zhang, J. Wang, Adv. Mater., 29, (2017), 1604164-1604171.

[15] P. Yu, Z. Zhang, L. Zheng, F. Teng, L. Hu, X. Fang, Adv. Energy Mater., 6, (2016), 1601111-1601122.

[16] D. Dubal, J. Kim, Y. Kim, R. Holze, C. Lokhande, W. Kim, Energy Technol., 2, (2014), 325-341.

[17] J. Wei, Y. Li, D. Dai, F. Zhang, H. Zou, X. Yang, Y. Ji, B. Li, X. Wei, ACS Appl. Mater. Interfaces, 12, (2020), 5786-5792.

[18] T. Chen and Y. Elabd, Electrochim. Acta, 229, (2017), 65-72.

[19] X. Li, W. Zhao, R. Yin, X. Huang, L. Qian, Eng. Sci., 3, (2018), 89-95.

[20] T. Ko, J. Seong, S. Radhakrishnan, C. Kwak, M. Khil, H. Kim, B. Kim, J. Ind. Eng. Chem., 73, (2019), 1-7.

[21] R. Dubey and V. Guruviah, Ionics, 25, (2019), 1419-1445.

[22] V. Dodevski, B. Jankovi, M. Stojmenovi, S. Krsti, J. Popovi, M. Pagnacco, M. Popovi, S. Pasali, Colloids Surf. A: Physicochem. Eng. Aspects, 522, (2017), 83-96.

[23] A. Pandolfo and A. Hollenkamp, J. Power Sources, 157, (2006), 11-27.

[24] C. Xiong, T. Li, T. Zhao, A. Dang, H. Li, X. Ji, W. Jin, S. Jiao, Y. Shang, Y. Zhang, Compos. B Eng., 116, (2017), 7-15.

[25] W. Liu, Y. Tang, Z. Sun, S. Gao, J. Ma, L. Liu, Carbon, 115, (2017), 754-762.

[26] S. Ramesh, S. Khandelwal, K. Rhee, D. Hui, Compos. B Eng., 138, (2018), 45-54.

[27] Z. Yang, J. Tian, Z. Yin, C. Cui, W. Qian, F. Wei, Carbon, 141, (2019), 467-480.

[28] H. Fan, N. Zhao, H. Wang, J. Xu, F. Pan, Mater. Chem. A, 2, (2014), 12340-12348.

[29] I. Jung, D. Dikin, R. Piner, R. Ruoff, Nano Lett., 8, (2008), 4283-4287.

[30] L. Zhang, R. Zhou, X. Zhao, J. Mater. Chem., 20, (2010), 5983-5992.

[31] K. Namsheer and C. Rout, RSC Adv., 11, (2021), 5659-5697.

[32] A. Majeed, L. Mohammed, O. Hammoodi, S. Sehgal, M. Alheety, K. Saxena, S. Dadoosh, I. Mohammed, M. Jasim, N. Salmaan, Int. J. Polym. Sci., 2022, (2022), 9047554-9047573.

[33] A. Eftekhari, L. Li, Y. Yang, J. Power Sources, 347, (2017), 86-107.

[34] S. Ji, J. Yang, J. Cao, X. Zhao, M. Mohammed, P. He, R. Dryfe, I. Kinloch, ACS Appl. Mater. Interfaces, 12, (2020), 13386-13399.

[35] A. Tawade, S. Tayade, D. Dubal, S. Mali, C. Hong, K. Sharma, J. Chem. Eng., 492, (2024), 151843-151877.

[36] D. Wu, X. Xie, Y. Zhang, D. Zhang, W. Du, X. Zhang, B. Wang, Front. Mater. Sci., 7, (2020), 2-16.

[37] V. Lokhande, A. Lokhande, G. Namkoong, J. Kim, T. Ji, Results Phys., 12, (2019), 2012-2020.

[38] Q. Zhang, D. Gu, H. Li, Z. Xu, H. Sun, J. Li, L. Wang, L. Shen, Electrochim. Acta, 367, (2021), 137455-137463.

[39] W. Bi, J. Wang, E. Jahrman, G. Seidler, G. Gao, G. Wu, G. Cao, Small, 15, (2019), 1901747-1901755.

[40] X. Wang, A. Hu, C. Meng, C. Wu, S. Yang, X. Hong, Molecules, 25, (2020), 269-305.

[41] S. Korkmaz, I. Kariper, O. Karaman, C. Karaman, Ceram. Int., 47, (2021), 34514-34534.

[42] R. Arunachalam, R. Prataap, R. Pavul Raj, S. Mohan, J. Vijayakumar, L. Peter, M. Al Ahmad, Surf. Eng., 35, (2019), 102-110.

[43] S. Kulkarni, U. Patil, I. Shackery, J. Sohn, S. Lee, B. Park, S. Jun, J. Mater. Chem. A, 2, (2014), 4989-4998.

[44] S. Cho, K. Shin, J. Jang, ACS Appl. Mater. Interfaces, 5, (2013), 9186-9193.

[45] G. Wang, N. Jiang, Y. Xu, Z. Zhang, G. Wang, K. Cheng, J. Colloid Interface Sci., 630, (2023), 817-827.

[46] C. Wang, Y. Yang, R. Li, D. Wu, Y. Qin, Y. Kong, Chem. Commun., 56, (2020), 4003-4009.

[47] N. Soudagar, V. Pandit, R. Pujari, K. Chorghade, C. Lokhande, S. Joshi, Int. J. Eng. Res., 10, (2017), 587-594.

[48] C. Zhou, S. He, H. Yang, J. An, L. Yang, P. Yan, H. Zhang, Electrochim. Acta, 390, (2021), 138818-138829.

[49] F. Zeng, Y. Xiao, Y. Shen, X. Xu, Z. Qin, Electrochim. Acta, 386, (2021), 138516-138526.

[50] A. Anbalagan and S. Sawant, Polymer, 87, (2016), 129-137.

[51] K. Zhou, Y. He, Q. Xu, Q. Zhang, A. Zhou, Z. Lu, L. Yang, Y. Jiang, D. Ge, X. Liu, H. Bai, ACS Nano, 12, (2018), 5888-5894.

[52] L. Hou, X. Zhi, W. Zhang, H. Zhou, J. Electroanal. Chem., 863, (2020), 114064-114073.

[53] Z. Sun, J. Zhang, F. Ye, W. Wang, G. Wang, Z. Zhang, S. Li, Y. Zhou, J. Cai, J. Power Sources, 443, (2019), 227246-227254.

[54] P. Erdogan, H. Zengin, A. Yavuz, Solid State Ion., 352, (2020), 115362-115372.

[55] M. Zhang, A. Nautiyal, H. Du, Z. Wei, X. Zhang, R. Wang, Electrochim. Acta, 376, (2021), 138037-138049.

[56] M. Lakshmi, S. Wabaidur, Z. Alothman, D. Ragupathy, Synth. Met., 270, (2020), 116591-116600.

[57] V. Mooss, V. Vijayakumar, S. Kurungot, A. Athawale, Polym. J., 212, (2021), 123169-123180.

[58] A. Bhalerao, R. Bulakhe, P. Deshmukh, J. Shim, K. Nandurkar, B. Wagh, S. Prabhakar Vattikuti, C. Lokhande, J. Mater. Sci. Mater. Electron., 29, (2018), 15699-15707.

[59] J. Bo, X. Luo, H. Huang, L. Li, W. Lai, X. Yu, J. Power Sources, 407, (2018), 105-111.

[60] J. Zhao, J. Wu, B. Li, W. Du, Q. Huang, M. Zheng, H. Xue, H. Pang, Prog. Nat. Sci.: Mater., 26, (2016), 237-242.

[61] T. Wang, Y. Wang, D. Zhang, X. Hu, L. Zhang, C. Zhao, Y. He, W. Zhang, N. Yang, Z. Ma, ACS Appl. Mater. Interfaces, 13, (2021), 17726-17735.

[62] M. Rajesh, C. Raj, B. Kim, B. Cho, J. Ko, K. Yu, Electrochim. Acta, 220, (2016), 373-383.

[63] M. Li and L. Yang, J. Mater. Sci.: Mater. Electron., 26, (2015), 4875-4884.

[64] Y. Chen, K. Cai, C. Liu, H. Song, X. Yang, Adv. Energy Mater., 21, (2017), 1701247-1701258.

[65] D. Dubal, Z. Caban-Huertas, R. Holze, P. Gomez-Romero, Electrochim. Acta, 191, (2016), 346-354.

[66] C. Sun, X. Li, Z. Cai, F. Ge, Electrochim. Acta, 296, (2019), 617-626.

[67] Z. Ciplak, A. Yildiz, N. Yildiz, J. Energy Storage, 32, (2020), 101846-101857.

[68] K. Khawas, P. Kumari, S. Daripa, R. Oraon, B. Kuila, ChemistrySelect, 2, (2017), 11783-11792.

[69] M. Shabani-Nooshabadi and F. Zahedi, Electrochim. Acta, 245, (2017), 575-586.

[70] X. Zheng, H. Yu, R. Xing, X. Ge, H. Sun, R. Li, Q. Zhang, Electrochim. Acta, 260, (2018), 504-517.

[71] N. Chen, Y. Ren, P. Kong, L. Tan, H. Feng, Y. Luo, Appl. Surf. Sci., 392, (2017), 71-80.

[72] K. Vighnesha, D. Sangeetha, M. Selvakumar, Surf. Eng. Appl. Electrochem., 54, (2018), 359-366.

[73] Z. Liu, Z. Zhao, A. Xu, W. Li, Y. Qin, J. Alloys Compd., 875, (2021), 159931-159942.

[74] J. Liu, P. Du, Q. Wang, D. Liu, P. Liu, Electrochim. Acta, 305, (2019), 175-186.

[75] J. Chen, Y. Wang, J. Cao, Y. Liu, Y. Zhou, J. Ouyang, D. Jia, ACS Appl. Mater. Interfaces, 9, (2017), 19831-19842.

[76] A. Moyseowicz and G. Gryglewicz, Electrochim. Acta, 354, (2020), 136661-136698.

[77] K. Shu, C. Wang, C. Zhao, Y. Ge, G. Wallace, Electrochim. Acta, 212, (2016), 561-571.

[78] J. Chen, Y. Wang, J. Cao, L. Liao, Y. Liu, Y. Zhou, J. Ouyang, D. Jia, M. Wang, X. Li, Z. Li, Electrochim. Acta, 361, (2020), 137036-137048.

[79] J. Hao, H. Liu, S. Han, J. Lian, ACS Appl. Nano Mater., 4, (2021), 1330-1339.

[80] A. Alves, R. Koizumi, A. Samanta, L. Machado, A. Singh, D. Galvao, G. Silva, C. Tiwary, P. Ajayan, Nano Energy, 3, (2017), 225-232.

[81] X. Zhang, J. Wang, J. Liu, J. Wu, H. Chen, H. Bi, Carbon, 115, (2017), 134-146.

[82] C. Lee, F. Omar, A. Numan, N. Duraisamy, K. Ramesh, S. Ramesh, J. Solid State Electrochem., 21, (2017), 3205-3213.

[83] X. He, Q. Liu, J. Liu, R. Li, H. Zhang, R. Chen, J. Wang, J. Chem. Eng., 325, (2017), 134-143.

[84] M. Iqbal, M. Faisal, S. Ali, S. Farid, A. Afzal, Electrochim. Acta, 346, (2020), 36039-36085.

[85] F. Omar, A. Numan, N. Duraisamy, S. Bashir, K. Ramesh, S. Ramesh, J. Alloys Compd., 716, (2017), 96-105.

[86] A. Rashti, B. Wang, E. Hassani, F. Farshad., X. Zhang, T. Oh, Energy Fuel, 34, (2020), 6448-6461.

[87] X. Zhang, J. Zhang, Y. Chen, K. Cheng, J. Yan, K. Zhu, K. Ye, G. Wang, L. Zhou, D. Cao, J. Colloid Interface Sci., 536, (2019), 291-300.

[88] J. Zhu, T. Feng, X. Du, J. Wang, J. Hu, L. Wei, J. Power Sources, 346, (2017), 120-127.

[89] L. Li, S. Peng, H. Chen, X. Han, F. Cheng, M. Srinivasan, S. Adams, S. Ramakrishna, J. Chen, Nano Energy, 19, (2016), 307-324.

[90] J. Ding, P. Chen, B. Wang, X. Chen, K. Guo, Small Structures, 2, (2021), 2100073-2100096.

CHAPTER – II

Theoretical background of thin film, synthesis methods, characterization techniques and supercapacitor

CHAPTER – II

Theoretical background of thin film, synthesis methods, characterization techniques and supercapacitor

2.1 General introduction:

This chapter introduces thin films and gives a theoretical basis on chemical deposition methods. This chapter provides a detailed discussion of chemical bath deposition (CBD), successive ionic layer adsorption and reaction (SILAR) methods and thin film characterization techniques for the investigation of surface morphology, wettability, and structure. Additionally, this chapter concludes with an explanation of the electrochemical supercapacitor properties.

2.2 Introduction to thin films:

Thin film technology has received a lot of interest lately owing to its distinct optical, magnetic, and electrical properties, which are utilized in a variety of thin film applications. The technique is applied based on certain characteristics of film materials that are easily controlled by changing preparative parameters. A thin film is defined as a surface enclosed by two parallel planes that extend infinity in two directions but have a restricted dimension in the third direction. Its thickness ranges from nanometer to less than one micrometre.

Thin films can be synthesized using either physical or chemical methods. **Chart 2.1** displays a broad classification of thin film deposition methods. The two main subclasses of physical thin film deposition methods are vacuum evaporation **[1]** and sputtering **[2]**. These may be further divided into electron beam evaporation **[3]**, laser evaporation **[4]**, radio frequency (RF) sputtering **[5]**, and magnetron sputtering **[6].**

Sputtering is a method that uses plasma to remove one or two atoms at a time from a target. The target is constantly maintained at a lower temperature since the evaporation rate is extremely low at low temperatures. Physical methods need high vacuum level and a higher working temperature, as well as being expensive, needing the deposition chamber to be cleaned after each deposition, and requiring small area deposition. Chemical methods may be broadly divided into two phases i.e. gas and liquid phase **[7, 8]**. There are several methods used in the gas phase, such as chemical vapour deposition (CVD), metal organic chemical vapour deposition (MO-CVD), plasma photochemical vapour deposition (PC-CVD), plasma enhanced chemical vapour deposition (PE-CVD), and laser chemical vapour deposition (L-CVD) **[9-13]**. Liquid phase methods include, CBD, SILAR **[14-16]**, electrodeposition **[17]**, spray

pyrolysis **[18]**, liquid phase epitaxy **[19]**, dip coating **[20]**, hydrothermal **[21]**, and spin coating etc **[22]**. Chemical deposition is more effective than physical deposition for synthesizing thin films with large surface area. Chemical methods for the deposition of CPs thin films are cost-effective, easy, environmentally friendly, require minimal material waste, and can be done at room temperature.

2.3 Theoretical background of chemical methods:

2.3.1 Chemical bath deposition (CBD) method:

The CBD method is a cost-effective, easy, and binder-free way to prepare thin films. It relies on the two primary reaction mechanisms: homogeneous and heterogeneous and does not require a vacuum system or other expensive equipment. This method allows for precise control over preparative parameters, resulting in superior thin film thickness. Malavekar et al. **[23]** provide a detailed explanation of CBD method reaction mechanism, including the impact of preparative parameters on the development of films. A number of review papers on CBD method of thin film production are available in the literature **[24, 25]**. **Fig. 2.1** shows a schematic of CBD method for production CP thin films.

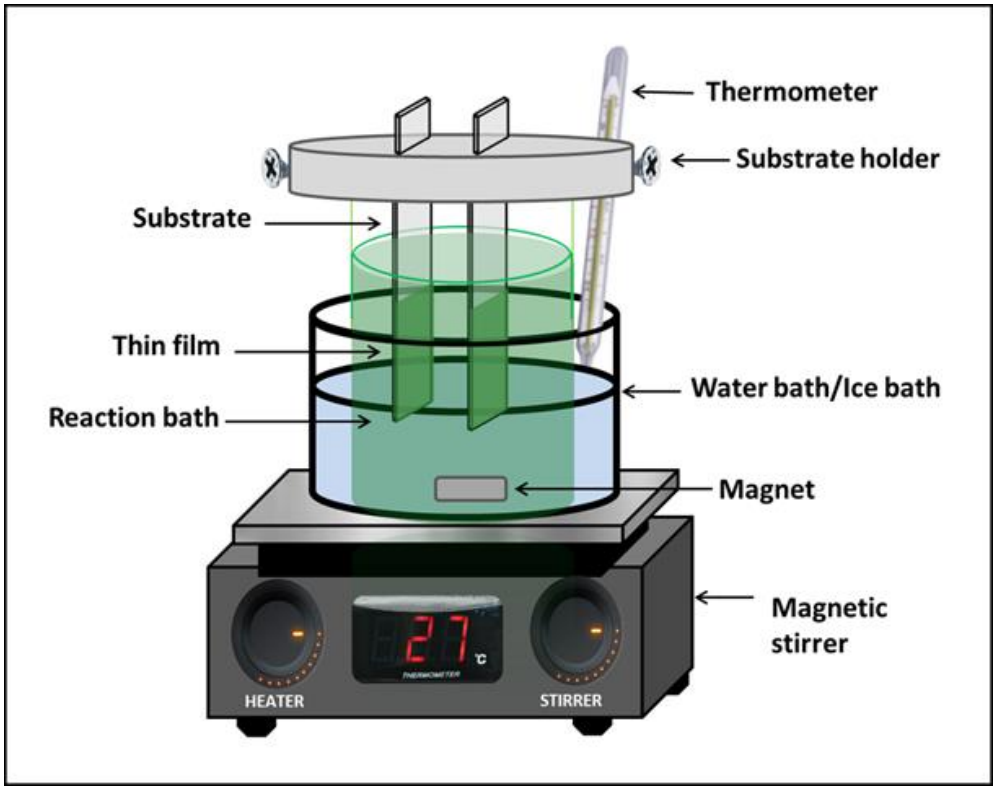

Fig. 2.1: The schematic of CBD method.

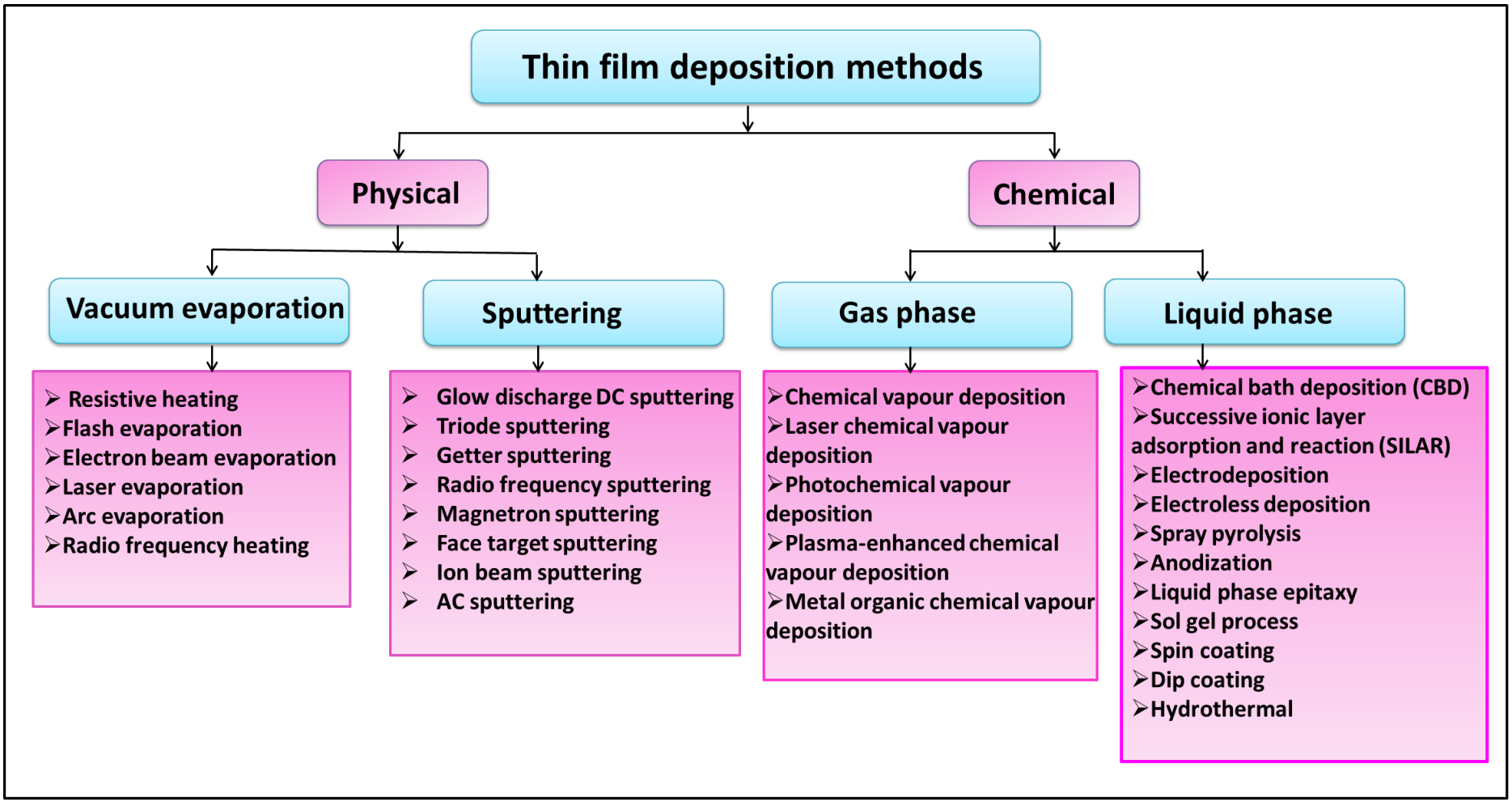

Chart 2.1: The broad classification of thin film deposition methods.

2.3.1.1 Basic principle of CBD:

The controlled precipitation of the desired compound from a solution of its constituents is the fundamental principle of CBD method. The development of nucleation is essential for the formation of precipitates. The result of nucleation in solution is that the molecular clusters produced quickly decompose, and particles combine to grow the film to a particular thickness. The formation of precipitates in CBD method requires that the ionic product must be greater than the solubility product **[24]**. The terms of ionic product and solubility product are explained here; when a sparingly soluble salt AB is introduced into water. A completely saturated solution with A^+ and B^- ions comes into contact with undissolved solid AB, and equilibrium is formed between the solid phase and the ions in the solution.

$$AB\,(S) \rightarrow A^+ + B^- \qquad (2.1)$$

According to the law of mass action and the equilibrium condition,

$$M = C_A^+ . C_B^- / C_{AB}(S) \qquad (2.2)$$

where, 'C_A^+' is concentrations of A^+, 'C_B^-' is concentrations of B^-, and 'C_{AB}' concentration of AB ions in the solution.

In a pure solid phase, the concentration remains constant i. e. C_{AB} (S) = constant = M'

$$M = C_A^+ . C_B^- / M' \qquad (2.3)$$

$$MM' = C_A^+ . C_B^- \qquad (2.4)$$

Due to the constants M and M', the product MM', or M_s, is also constant. Consequently, the previous equation becomes,

$$M_s = C_A^+ . C_B^- \qquad (2.5)$$

The solubility product (SP) is Ms, whereas the ionic product (IP) is denoted by $(C_A^+ . C_B^-)$. The IP and SP of ions are the same in a saturated solution. However, IP is greater than SP, or IP/SP = S > 1, precipitation occurs, the solution becomes supersaturated, and ions combine to produce homogeneous and heterogeneous nuclei in the solution and on the substrate **[26]**.

2.3.1.2 Theoretical background of nucleation and growth:

Thin films that are uniformly adherent can be deposited using chemical methods. Growth in chemical processes is achieved by either ion-by-ion or hydroxide cluster mechanism processes.

i) Ion-by-ion growth mechanism:

In the ion-by-ion growth process, a significant degree of saturation is necessary for homogeneous nucleation. A degree of heterogeneity is introduced by the free particle present on the surface, which promotes nucleation. Therefore, deposition proceeds via an ion-by-ion process. The substrates surface serves as a catalyst to initiate nucleation.

ii) Hydroxide cluster mechanism:

Usually, it refers to the development of metal chalcogenide films. The hydroxide cluster mechanism is quite easy, while metal hydroxide exists already in the solid phase and method simply involves replacing the hydroxide with chalcogenide on that solid phase.

Advantages of CBD method:

i. In comparison to other chemical processes, it is quite simple and cheap method.
ii. It is possible to synthesize thin films at low/room temperatures.
iii. It is not necessary to use a vacuum or a costly equipment at any step.
iv. A variety of substrates can be utilized.
v. Stoichiometric synthesis uses ions as the primary building components, rather than atoms.
vi. This method ensures pinhole-free and homogeneous preparations by keeping the solution in contact with the substrate.
vii. There is no evolution of the hazardous gases.
viii. Film thickness may be simply changed by adjusting preparative parameters includes concentration of solution, reaction bath temperature, pH of solution, and deposition time.

2.3.1.3 Preparative parameters of CBD:

The rate of chemical reaction determines the adhesion and uniformity of thin films deposited via CBD method. The solution supersaturation and the presence of nucleation centres determine thickness of film and rate of deposition. The film growth kinetics are influenced by several parameters, including pH, temperature, and complexing agents, etc. The impact of preparative parameters on the film formation is explained below.

i) pH of solution:

The pH of a solution is determined by the negative logarithm of H^+ ions concentration, which may be adjusted by a complexing agent. The supersaturation state regulates the speed of deposition and reaction. The availability of free metal ions is compromised when a metal ion complex becomes more stable due to a rise in the pH of the reaction solution. This affects the speed of reaction and may cause a change in the film thickness.

ii) Complexing agent:

The complexing agent function is to accept the metal cation while preventing precipitation of the substances to be generated. The cations are gradually released to react with the anions in the bath throughout the film developing process. Metal ion concentration decreases along with rising complexing agent concentration. This reduces the speed of reaction and precipitation, resulting in a slower deposition of film.

iii) Temperature:

Another factor that affects the rate of reaction is the bath temperature. As solution temperature rises, complexes dissolve more effectively, leading to increased kinetic energy and improved ion interactions. Temperature dependent supersaturation has an impact on the thin film terminal thickness.

iv) Substrate:

The rate of deposition and film thickness are largely dependent on the substrate that will be utilized for producing the thin films. On surface of the substrate,

nucleation centres facilitate nucleation and subsequent growth. Therefore, in order to achieve good thin film deposition, substrate cleaning is crucial. The lattice properties of the substrate have a significant impact on film growth. When they match the deposited material, the rate of deposition and resulting thickness increase.

2.3.2 Successive ionic layer adsorption and reaction (SILAR) method:

2.3.2.1 Basics of SILAR method:

The SILAR method enables adhesion, uniformity, and thin film formation with optimal properties. Thin film production occurs in CBD method if IP is greater than SP. However, precipitate formation in the solution is unavoidable. The SILAR, a modified variant of CBD method, reduces material loss and inefficient precipitation. Metal chalcogenide thin films were synthesised in the middle of the 1980s using SILAR method **[27]**. A SILAR method was first described by Ristov and coworkers **[28]** as an adaptable chemical immersion method. The name SILAR was selected by Nicolau and Menard **[29]**. A variety of chemical compounds and composite films may be deposited using this method. The SILAR method is often referred to as the improved CBD method. The SILAR method typically includes adsorption, reaction, and rinsing steps. A schematic of SILAR deposition method is shown in **Fig. 2.2**.

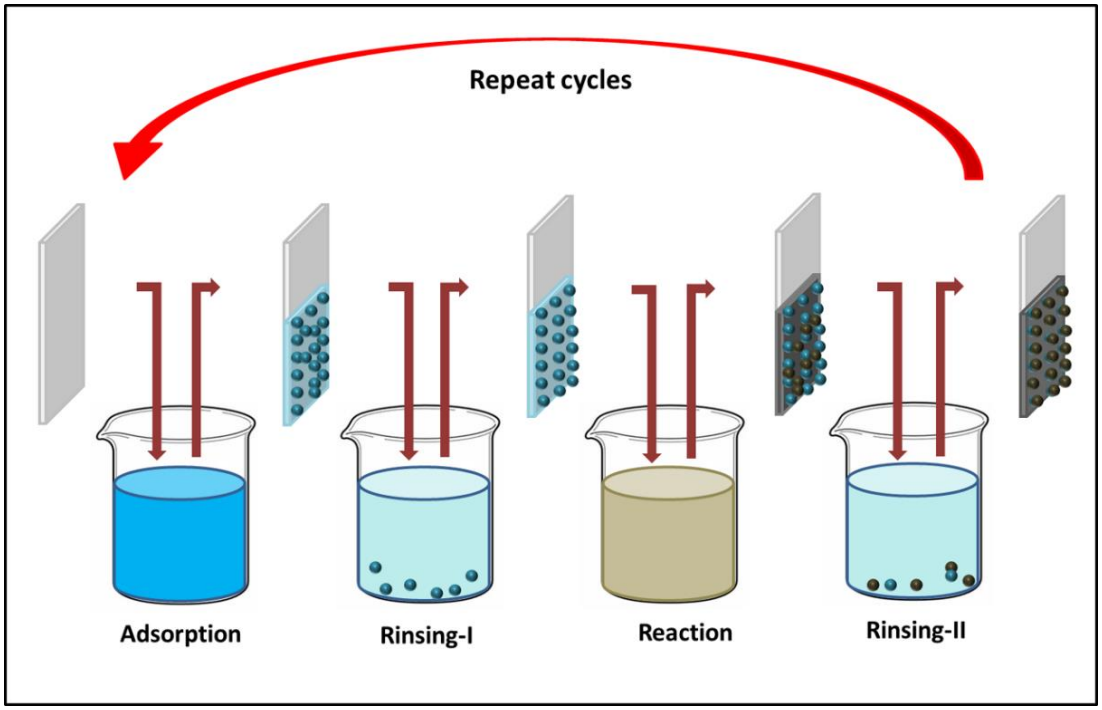

Fig. 2.2: The schematic of SILAR deposition method.

i) Adsorption:

Adsorption is the initial stage in SILAR method. Adsorption of cations on the surface of substrate results in the formation of a Helmholtz electric double layer, which is constituted of two layers due to Van der Waals forces. Inner electric layers are formed by positively charged cations. The second layer consists of negatively charged anions and a counter layer of cations.

ii) Rinsing-I:

Rinsing-I removes cations that have been loosely or unboundedly adsorbed on a surface. Rinsing significantly affects the size of particles, morphology, crystallinity, and adhesion of thin film to the substrate. Film material is usually rinsed with double distilled water (DDW).

iii) Reaction:

Anions from the anionic precursor solution combine with cations that have already been adsorbed to produce molecules or compounds.

iv) Rinsing-II:

This rinsing-II involves removing the unreacted and excess species as well as byproducts of the reaction. DDW is typically utilized for rinsing, similar to in step two.

The key variable influencing thin film deposition is film thickness, which may be varied by adjusting a number of preparatory parameters including bath temperature, anions and cations concentrations, complexing agent, number of SILAR cycles.

Advantages of SILAR method:

The following are the advantages of SILAR method:

i. It is an easy, convenient, environmentally friendly, binder-free method for the large area thin films deposition.
ii. It is simple to control the deposition rate.
iii. This procedure is performed out at room temperature.
iv. Any kind of substrate can be utilized.

v. High-quality targets or vacuum are not required during the process.
vi. It is easy to adjust the film thickness by adjusting the deposition conditions.

2.3.2.2 Effect of preparative parameters:

The SILAR method growth mechanisms are dependent on several factors, including temperature, complexing agent, adsorption and reaction time, and number of cycles. The impacts of various parameters are given below.

i) Concentration:

The precursor concentration is the primary factor that determines the film thickness in all chemical reactions. Proper concentration of the precursor is known to provide optimal film thickness, which in turn influences the material performance. Increasing the cationic precursor concentration causes a raise in adsorption rate, which leads to an excessive rise in film thickness and when the concentration of anionic precursor exceeds the rate of reaction, the particle size rapidly rises, affecting the material performance. For thickness dependent applications, the concentration of precursors can be used to adjust film thickness **[30]**.

ii) pH:

A solution pH has a significant impact on film formation. If the pH is higher, the reaction rate changes quickly. When the pH is lower, the metal ions concentration falls to a point where the metal and chalcogenide IP is smaller than the SP, which prevents the formation of a film. A complexing agent can be used to change the cationic solution pH value.

iii) Temperature:

By adjusting the temperature of bath, it is possible to vary the thickness of film. Temperature affects both complex anion formation and dissociation. At high temperature, there is a larger dissociation, which increase the rate of deposition. Film formation occurs slowly at lower (room) temperature. An increase in temperature causes an exponential rise in film thickness.

iv) Complexing agent:

Concentrations of metal ion can be adjusted by introducing complexing agents dropwise. Metal ion concentrations decrease when the concentration of complexing agents increases. Consequently, there is a decrease in the speed of reaction and precipitate production, which results in a thicker terminal thickness. Only the adsorption process is responsible for the thin film deposition. Chalcogenide sources are combined with metal ions from the metal ions complex to generate thin films. Certain common complexing agents include oxalic acid (OA), tartaric acid (TA), triethanolamine (TEA), citric acid (CA), and ethylenediaminetetraacetic (EDTA).

v) Number of cycles:

It is commonly known that when a SILAR reaction is conducted with more cycles, the film thickness rises. Consequently, in order to get improved performance, the cycle number must be optimized. A lower number of cycles causes the material to develop irregularly and unevenly, while a larger number of cycles can lead to the formation of clusters and peeling off thin film.

vi) Adsorption and reaction time:

The thin films formation is significantly influenced by the adsorption and reaction times. When adsorption time exceeds reaction time, film formation occurs through assorted reactions, resulting in a significant terminal thickness. The constant reaction produced by the same adsorption and reaction times leads to the uniform and adherent the formation of films.

2.4 Thin film characterization techniques:

2.4.1 X-ray diffraction (XRD):

X-ray diffraction (XRD) is a widely used and important characterization technique in the field of materials science that provides information on the crystal structure and atomic spacing of various materials in varying states **[31]**. The dimensions of the unit cells are also provided by this technique. Additionally, the crystallite size, lattice parameters, and phase analysis are also determined by this technique.

Working principle:

XRD analysis relies on crystalline materials and monochromatic X-rays that interfere constructively. In materials, the interplanar spacing (d) is around a few Angstroms (Å), which is equivalent to the X-rays wavelength (energy ranging from 3 to 8 keV). As a result, X-rays expose on crystalline material and produce both constructive and destructive interference pattern. A diffraction pattern can be generated by estimating the intensity of the diffracted X-rays as a function of the angle of scattering. If the wavelength of X-rays (λ) equals the path difference ((AC+CB)-AB), diffracted X-rays exhibit constructive interference. Mathematically, the Bragg's condition may be expressed as **[32]**,

$$d\sin\theta + d\sin\theta = n\lambda \quad \text{or} \quad 2d\sin\theta = n\lambda \qquad (2.6)$$

where, 'd', 'θ', and 'n' stand for the interplanar spacing, Bragg's angle, and order of diffraction, respectively.

Working of instrument:

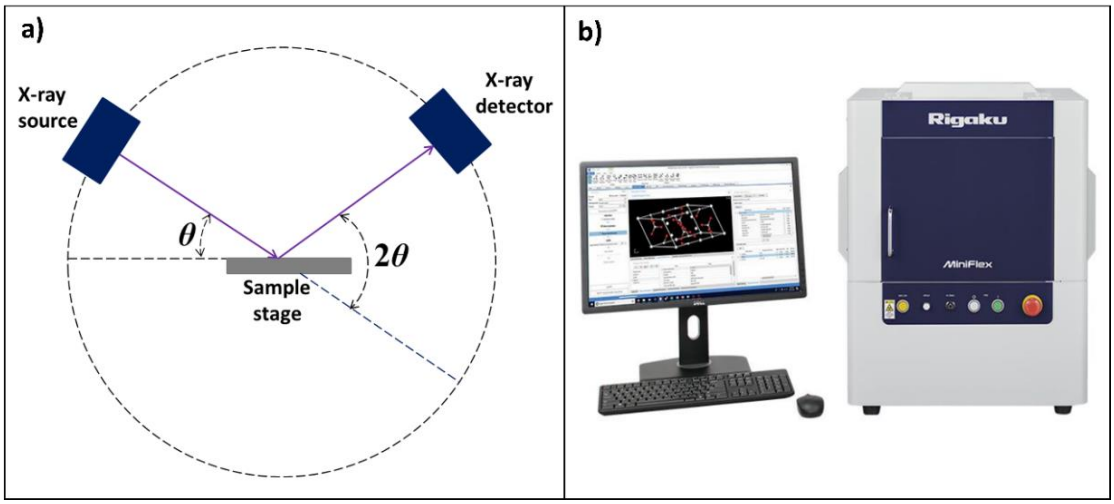

Fig. 2.3: a) Schematic of X-ray instrument **[33]**, and b) picture of Rigaku Miniflex-600 diffractometer **[34]**.

A monochromatic X-ray source is the basic component of the X-ray diffractometer, followed by a specimen holder and an X-ray detector. The cathode ray tube, also known as the X-ray generator, is composed of a cathode, a target material, and a monochromator, that are vacuum sealed inside a ceramic and glass container. To produce electrons, the cathode typically a tungsten filament is heated. By using a

significant amount of voltage, these electrons accelerate towards the target material (Fe, Cu, Mo, and Cr). When electrons possess sufficient energy to push out the electrons in the inner shell of target element, the outer electrons of target element come into inner shells, compensating for the imbalance of energy by emitting radiation. Radiation containing the K_α and K_β lines is released when copper is used as the target material.

Monochromatic X-rays are produced by filtering these radiations. Copper radiation has a wavelength of 1.5406 Å (CuK_α). Monochromatic X-rays are focused and pointed towards the desired material for characterisation. If Bragg's condition is satisfied, peaks in the X-ray intensity are observed while the detector and specimen are rotating. **Fig. 2.3a** depicts the schematic of an X-ray instrument. The detector records the signals, converts them to a count rate, and then transmits the information to a computer for further analysis.

Three methods exist for determining the materials crystal structure are Laue method, powder method, and rotating crystal method. The earliest approach for determining crystal structure is Laue method, which uses a fixed angle of incidence and a constant X-ray spectrum. This method uses monochromatic X-rays and produces quicker diffraction than other methods. Consequently, it is utilized to monitor dynamic processes in crystal structures. Rotating crystal method refers to using a constant incidence angle and a different wavelength. A monochromatic X-ray beam is permitted to fall on the sample while it rotates at a uniform rotational velocity in the rotating crystal method. The powder method is primarily used to easily analyse the material crystal structure. When utilizing the powder method, the wavelength is regarded fixed, while the angle of incidence is adjustable. **Fig. 2.3b** shows a picture of the Rigaku Miniflex-600 diffractometer. Scherer's equation is used to determine the material average crystalline size (D) **[35]**,

$$D = \frac{K \times \lambda}{\beta \times Cos\theta} \qquad (2.7)$$

where, 'β' represents the diffraction peak full width at half maximum (FWHM), while 'θ' represents its position in radians.

2.4.2 Raman spectroscopy:

The highly adaptable Raman spectroscopy method provides an easy, quick, and non-destructive way to analyse organic and inorganic materials **[36]**. It analyse

characteristics of material through light interaction. It monitors several modes of molecules, including vibrations, rotations, and low frequency mode **[37]**.

Working principle:

The Raman scattering mechanism involves two photons. Electrons are characterized by significant energy differences and vary in vibrational levels **(Fig. 2.4)**. The interaction between an electron in the sample and monochromatic light results in the electron absorbing photon energy and acquiring a virtual energy state. Electrons lose energy and return to an initial energy level. The electron returns to its original level and loses one photon when the energy lost is equivalent to the energy of the incident photon. Consequently, there are no Raman active modes in the molecule. Rayleigh scattering takes place when the incident photon and the secondary photon possess a similar frequency.

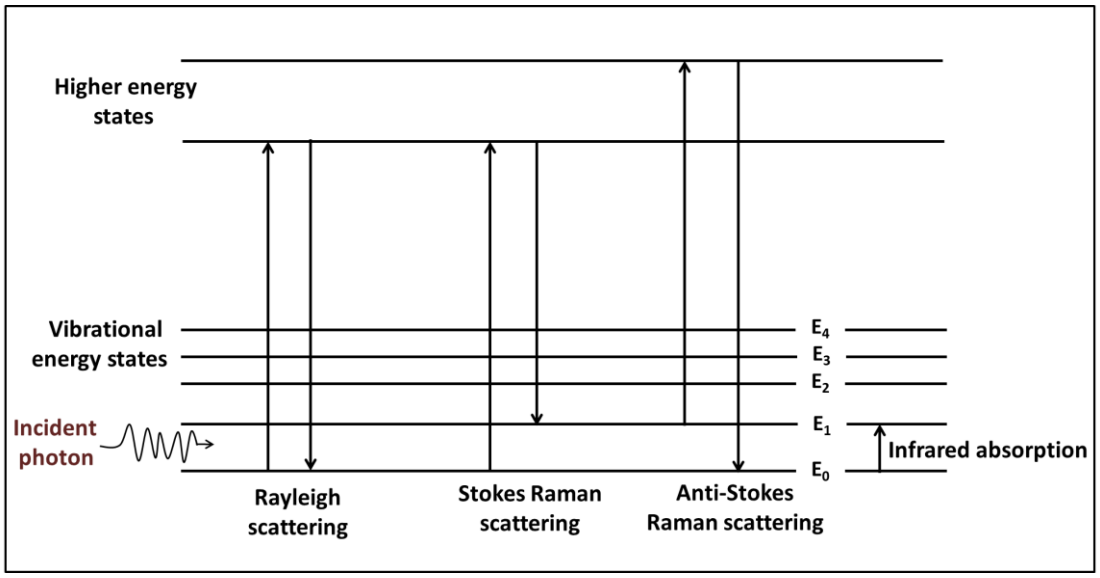

Fig. 2.4: Diagram of energy levels illustrating the states present in the Raman spectrum.

When electrons lose energy in the virtual state, they may return to a distinct vibrational level. In this instance, the energy that the electron loses and the energy gained from the coming photon are not equal. Thus, the resulting energy difference between the incident and emitted photons. Consequently, the frequency of the released photon differs from that of the incident photon. This produces Raman scattering. Based on the final vibrational state of the electron, Raman scattering is divided into stokes and antistokes lines. Stokes lines are defined as radiation with less

energy than the incident radiation and antistokes lines as radiation with more energy than the incident radiation **[38]**.

For stokes lines, the Raman shift (Δv) is positive, whereas for antistokes lines, it is negative. The molecular fingerprint is provided by the Raman spectrum, and it varies depending on the particular molecule. A specific molecule rotational levels can be determined by examining the Raman spectra. This is useful in the qualitative analysis of the sample.

Working of instrument:

Three main parts constitute a Raman spectrometer: a detector, a sampling equipment, and an excitation source. **Fig. 2.5** depicts the fundamental block diagram of a Raman spectrometer. A monochromatic excitation source is utilized in Raman spectroscopy. Usually, a laser with narrow and consistent bandwidth is utilized as the light source for excitation. A small form factor, low power consumption, narrow line width, constant power output, and dependable wavelength output are all desirable features for the laser source. It is crucial to move the laser wavelength into the near infrared for organic molecules in order to reduce fluorescence without going above the limitations of charge-coupled devices (CCDs), spectral detection. The 785 nm diode lasers are increasingly used due to their affordability and ability to reduce fluorescence without compromising spectral range or resolution. The ideal laser to use with very fluorescent or brightly coloured materials is the 1064 nm laser. The 532 nm laser is the ideal option for inorganic molecules because it has higher sensitivity. The second part of the fibre optic probe system is the sample interface. Typically, it provides a flexible interface for sampling. The versatility of fibre optics enables the probe to be submerged in liquids or slurries in both industrial and laboratory applications, in addition to the probe being inserted into a solid sample.

It is also compatible with microscopes and cuvette holders. The third component is the spectrometer, which has the ability to detect extremely weak Raman scattering due to its minimal noise, compact form factor, minimal power usage, and excellent resolution **[39]**. Furthermore, depending on the kind of excitation laser being utilized, the suitable detector is required. CCDs, are typically employed as the detector in Raman spectroscopy. In order to further improve the spectrometers

sensitivity for extremely low concentrations or weak Raman scatters, a back-thinned CCD may be required **[40, 41]**.

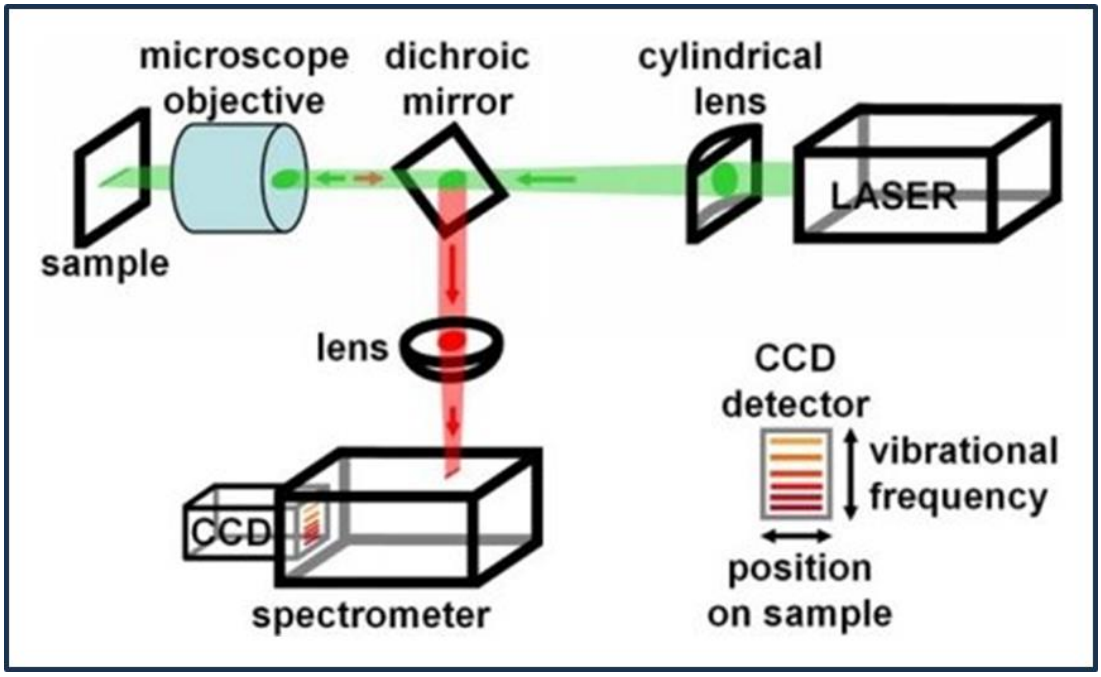

Fig. 2.5: The fundamental block diagram of a Raman spectrometer.

2.4.3 X-ray photoelectron spectroscopy (XPS):

X-ray photoelectron spectroscopy (XPS) is utilized to study the surface elemental composition and oxidation states of materials. Only samples with a depth of 1-10 nm may be analyzed by XPS. The basis of the XPS process is electrons are released from a substance when it is exposed to electromagnetic radiation, a phenomenon known as the photoelectric effect. These released electrons are commonly known as photoelectrons.

Working principle:

When a specimen is hit by an X-ray with the appropriate amount of energy, it ejects inner shell electrons from the atoms **(Fig. 2.6)** and records their kinetic energy. The following relation may be used to determine the binding energy of the ejected electrons if the incident X-rays energy is known.

$$E_{binding} = E_{photon} - (E_{kinetic} + \phi) \qquad (2.8)$$

where, 'ϕ' represents the element work function.

The number of photoelectrons exiting the specimen is measured, and the elements composition and chemical states are ascertained based on their kinetic energy.

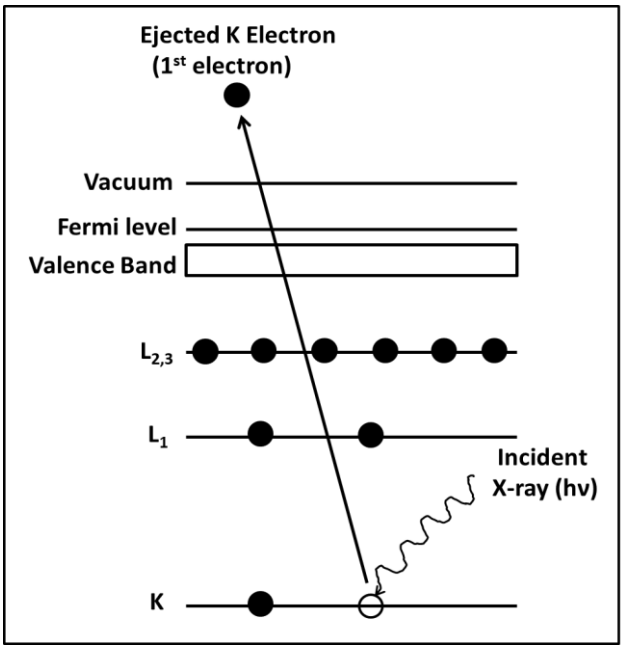

Fig. 2.6: An atomic representation of XPS operating principle.

Working of instrument:

In XPS, monochromatized X-rays of usually MgK_α or AlK_α are released using a monochromator. The monochromatized X-rays interact with the material, ejecting photoelectrons and detecting their quantity and kinetic energy using electron detectors. The electron kinetic energy gets converted into its binding energy by the software that is attached to the XPS machine. The data is shown as a spectrum of electron counts based on their binding energy. Each element in the compound has a unique binding energy, thus based on the binding energy displayed by the results, one may identify the element that is present. The XPS, K_α XPS equipment of Thermo Fisher Scientific, U.K. is utilised in this work.

2.4.4 Field emission scanning electron microscopy (FE-SEM):

An essential tool for determining surface morphology at high resolution is the field emission scanning electron microscopy (FE-SEM). For the imaging process, electrons are used rather than photons. These electrons are released using a field emission source. At magnifications ranging from 10 to 300,000X, the FE-SEM offers elemental and topographical information with a nearly infinite field depth.

Working principle:

The FE-SEM uses a high energy electron beam to raster scan over a surface of sample in order to capture image of it. The electric field accelerates the primary electrons that are emitted from a field emission source and these electrons are concentrated using electromagnetic lenses to produce a narrow beam. The beam is permitted to hit the sample. Primary electrons lose energy as they interact and different types of electrons are expelled from the sample, as seen in **Fig. 2.7**. Therefore, secondary electrons are released from the sample. As a result of the electrons interactions with the sample atoms, secondary electrons are created that carry information about the composition and topography of the surface. The detector produces an electric signal by analyzing these electrons, and after that, this signal is amplified and transformed into a picture.

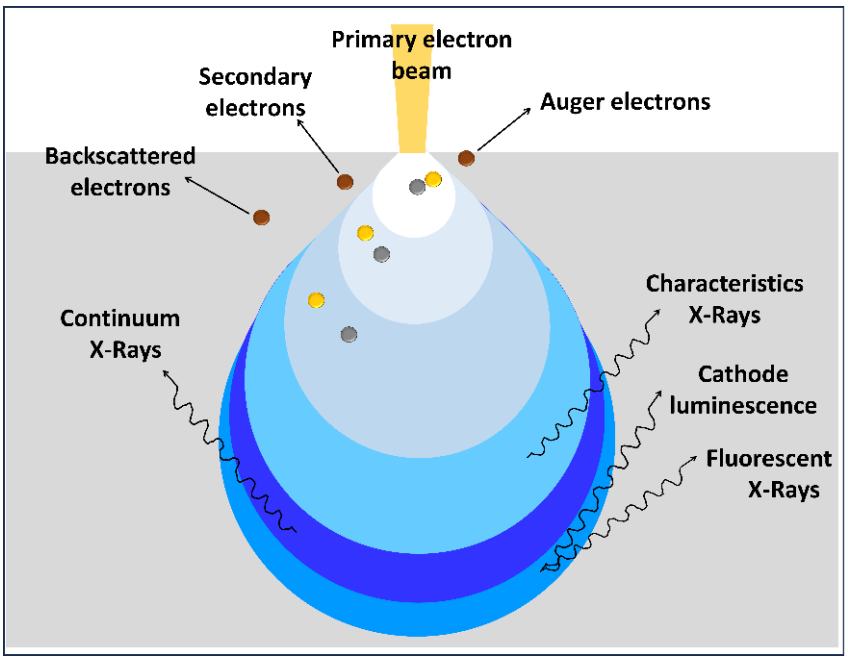

Fig. 2.7: Ray diagram showing the various types of electrons emitted during the interaction between sample and primary electrons from the source.

Working of instrument:

The schematic diagram of FE-SEM instrument is displayed in **Fig. 2.8a**. The primary components of a FE-SEM instrument are an electron guns, magnetic lenses, a sample holder, an anode (accelerator), and a detector. The complete system is attached to the desk. The gun head, specimen, and column chamber must be emptied

in order to operate. The column chamber valve closes in response to the vent command, permitting nitrogen (N_2) gas to pass via the vent valve and into the specimen chamber. An additional aspect of the FE-SEM study is preparation of sample. The sample should be electrically conductive. A thin layer of conductive metal, such as platinum (Pt), gold (Au), gold/palladium (Au/Pd), iridium (Ir), chromium (Cr), or silver (Ag) is applied to the samples in order to mount them on a holder **[42]**. The sample conductive metal covering reduces heat damage, avoids charging and enhances secondary electrons, resulting in a higher signal to noise ratio.

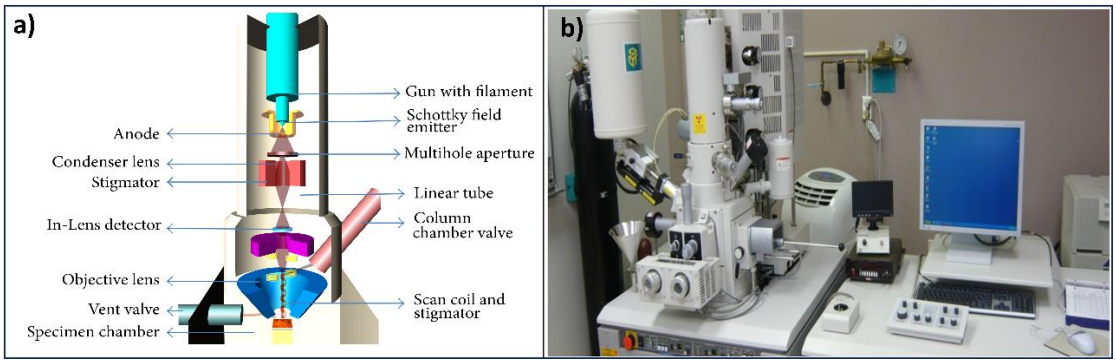

Fig. 2.8: a) Schematic of FE-SEM **[43]**, and b) photograph of FE-SEM instrument **[44]**.

The FE-SEM produce high energy electrons, also known as primary electrons produced by subjecting a tungsten filament shaped into a sharp point and placed into strong electrical potential gradient (cathode). Electrons that are produced might accelerate in the direction of the sample due to voltage differential between the anode and cathode. The microscope column maintains a high vacuum of around 10^{-6} Pa while the voltage ranges from 0.5 to 30 kV. The electron beam is focused into a narrow, precise region by the electromagnetic lenses. The magnification is adjusted by the condenser lens. Through the objective lens, electron beam is focused onto the sample. The electrostatic and electromagnetic lenses are used as objective lenses. With a deflection system, the beam of electron is moved in a point-to-point scan pattern using a series of scan coils. The focused electron beam interacts in many ways with the sample once it bombards its surface and permeates it up to a few microns **[45]**. Electron scattering and interaction volume are determined by atomic number, atom concentration, and primary electron energy. The interaction volume and scattering mechanism are enhanced by the significant primary electron energy.

However, the scattering and interaction volume will be reduced by the large atomic concentration and atomic number. A detector is used to collect all of these signals, which are then divided according to their energy values. Secondary and backscattered electrons are transformed and amplified to produce image of the sample. **Fig. 2.8b** displays the photograph of the FE-SEM instrument.

2.4.5 Brunauer-Emmett-Teller (BET) analysis:

Basically, this method may be used to calculate the specific surface area and pore volume for a given material. This is performed by using N_2 gas to the material surface at various relative pressures. The gas is eventually removed after sometime, the difference between the amount of gas sent inside and reverted is measured. The surface area of sample is given by the result in $m^2\ g^{-1}$.

Working principle:

The surface area determinations are based on two distinct principles: volumetric and gravimetric. In both the procedures, the sample is first placed within the chamber, heated to the necessary temperature, and then different relative pressures of N_2 gas are injected into it. When using the volumetric approach, the measurement of the relative pressure variation occurs in relation to the reading taken without material being placed within the chamber. The surface area and pore volume are calculated using the gravimetric approach, which measures the quantity of N_2 adsorbed onto surface and difference between the amount of N_2 supplied inside and recovered **[46]**. The plot of quantity adsorbed against the adsorptive pressure is called an isotherm. The pressure is represented as the adsorptive pressure (P) divided by the saturated vapour pressure (P_0). Volumetric measurement is commonly utilized because of its low cost and easy method.

Yet, volumetric analysis unclear conclusions limit its broad use. In this instance, gravimetric analysis provides more precision and accuracy. Six distinct isotherms exist, depending on the way adsorbent and adsorbate interact. Six distinct types of isotherms in the BET analysis are shown in **Fig. 2.9**.

1. Type I isotherm- physisorption or chemisorption on a material with tiny pores.
2. Type II isotherm- non-porous or microporous materials have a high adsorption energy.

3. Type III isotherm- non-porous or microporous materials have a low adsorption energy.
4. Type IV isotherm- the mesoporous materials have a high adsorption energy.
5. Type V isotherm- the mesoporous materials have a low adsorption energy.
6. Type VI isotherm- the materials include multiple pore sizes.

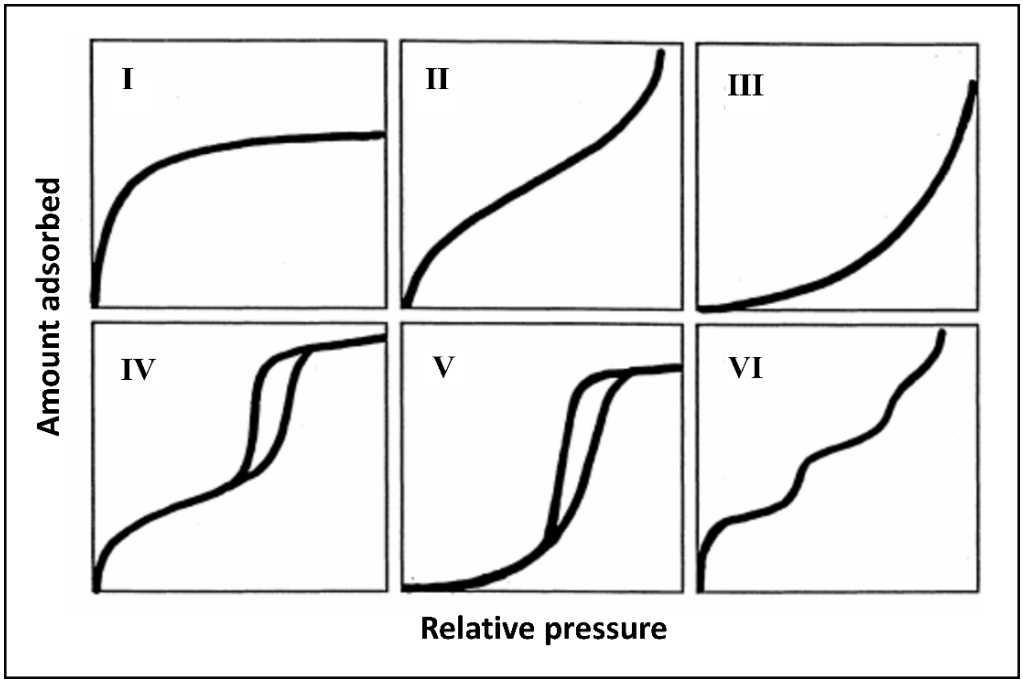

Fig. 2.9: Isotherm types in BET analysis **[47]**.

The BET theory is an extension of the Langmuir theory, which is a theory that applies monolayer molecule adsorption to multilayer adsorption with the following hypotheses:

a) Gas molecules physically adsorb on the solid surface.
b) There is no interaction among each adsorption layer.
c) The Langmuir theory can be implemented to each layer.

The BET technique is widely used in surface science to evaluate solid surface areas by the physical adsorption of gas molecules. In order to calculate the specific surface area from the number of moles of adsorbate in a monolayer (n_m) and the cross-sectional area of the adsorbate molecule (a),

$$\text{Specific surface area} = n_m N_A a \qquad (2.9)$$

where, '$a = (M/\rho)^{2/3}N_A^{1/3}$', 'M' stands for molar mass (g mol^{-1}), 'ρ' represents the liquid density (gm^{-3}), and 'N_A' is Avogadro's number (6.022×10^{-23} mol^{-1}).

Working of instrument:

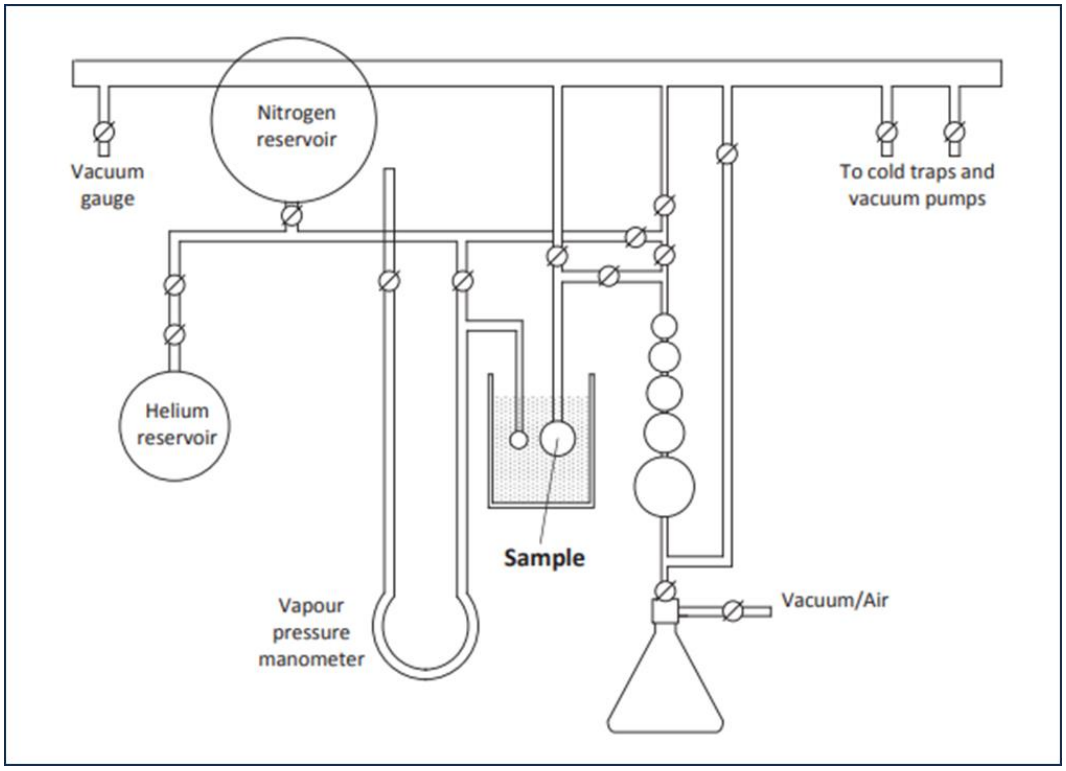

Fig. 2.10: A schematic representation of the dynamic flow method system **[48]**.

Specific surface area can be calculated using the volumetric approach of BET analysis, which uses a variety of instruments to quantify the adsorption of gas (usually N_2) onto a solid sample. In order to measure specific surface area of sample, initially, the sample is put in the sample holder, and the vacuum pump is used to evacuate the system to ensure there is no air or impurities in the chamber. After that, helium gas is pumped into the chamber to remove all remaining residual gas. This is done because helium is inert and does not adsorb on the surface, allowing for precise measurements of N_2 adsorption. After the chamber is vacuumed and purged, N_2 gas from the nitrogen reservoir is added at various pressures. The pressure is measured using a vacuum gauge and a manometer. As N_2 enters the system, the manometer monitors the pressure within the chamber. After allowing the gas adsorb on the samples surface, the pressure is changed until a number of readings at different pressures are obtained (typically, an order of increasing and then decreasing pressures). The data from changing pressures (P and P_0) is utilized to generate an adsorption isotherm. The

amount of N_2 adsorbed at each pressure is calculated, allowing the development of a BET plot. The specific surface area of the sample can be calculated using the BET equation and the volume of gas adsorbed at various pressures **[49]**. The schematic representation of the dynamic flow method system used for the measuring specific surface area is depicted in **Fig. 2.10**.

2.4.6 Contact angle measurement:

The wettability of the surface is determined by measuring the contact angle. This method can also be used to calculate the surface free energy. A thin film material wettability refers to its capacity to interact with liquid. The photograph of Rame-Hart contact angle meter is shown in **Fig. 2.11a**. **Fig. 2.11b** shows a liquid sample contact angle image on a surface of solid thin film. The angle measured within the liquid that connects a solid surface to a tangent drawn on its surface is known as the contact angle. A film surface is regarded as hydrophobic and less wettable if its contact angle is larger than 90°. A surface is considered super hydrophobic if the contact angle is more than 170°. Super hydrophilic nature is characterized by a very wettable surface and a contact angle of less than or equal to 5°. More wettability and hydrophilicity are associated with a contact angle of less than 90° **[50, 51]**. Net force is zero when all three phases are in an equilibrium state. Young's equation is used to compute the contact angle (θ) **[52]**,

$$\gamma_{S,V} = \gamma_{S,L} + \gamma_{L,V}\cos\theta \qquad (2.10)$$

where the solid-liquid, solid-vapour, and liquid-vapour interfacial energies are represented by the variables $\gamma_{S,L}$, $\gamma_{S,V}$, and $\gamma_{L,V}$, respectively.

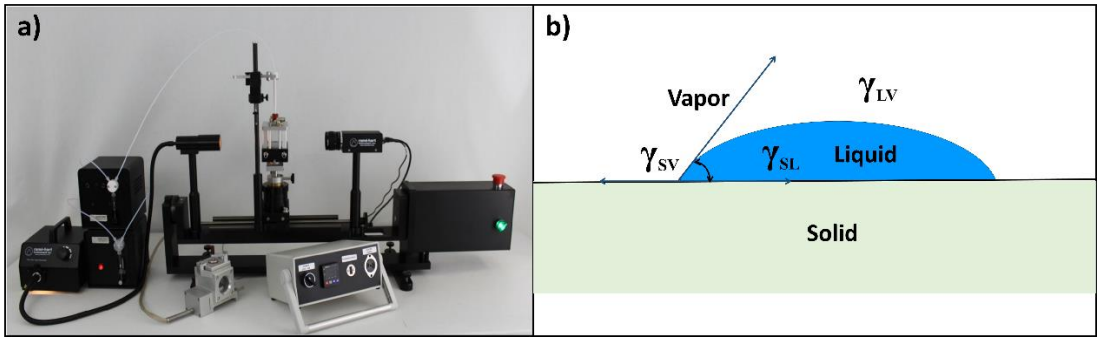

Fig. 2.11: a) A photograph of a Rame-Hart NRL contact angle meter **[53]**, and b) contact angle between a liquid and a solid sample.

2.5 Theoretical background of supercapacitor:

Supercapacitors are electrochemical capacitors that store and release energy more quickly than normal capacitors and have a higher S_P than batteries. The supercapacitor offers advantages over regular capacitor and battery. The supercapacitor exhibits long term cyclic stability, large C_s, and S_E. In contrast to a battery, it is harmless. Therefore, it is utilized in a variety of applications, including hybrid electric cars, telecommunications, backup for uninterruptible power supplies, and light-weight power sources for tiny aircraft.

2.5.1 Supercapacitor device:

Supercapacitor device types are displayed in **Fig. 2.12**. Supercapacitors may be classified into three categories such as symmetric, asymmetric, and hybrid devices. Both symmetric and asymmetric supercapacitive cell configurations have been the focus of several research publications, and it is important to establish common terms used to describe these devices **[54]**. Additionally, these words symmetric, asymmetric, and hybrid only apply to devices, not electrodes. Batteries are large energy devices with poor S_P, whereas capacitors are high power devices with limited energy storage capability. It is expected that the two systems working together will provide a high performing single device.

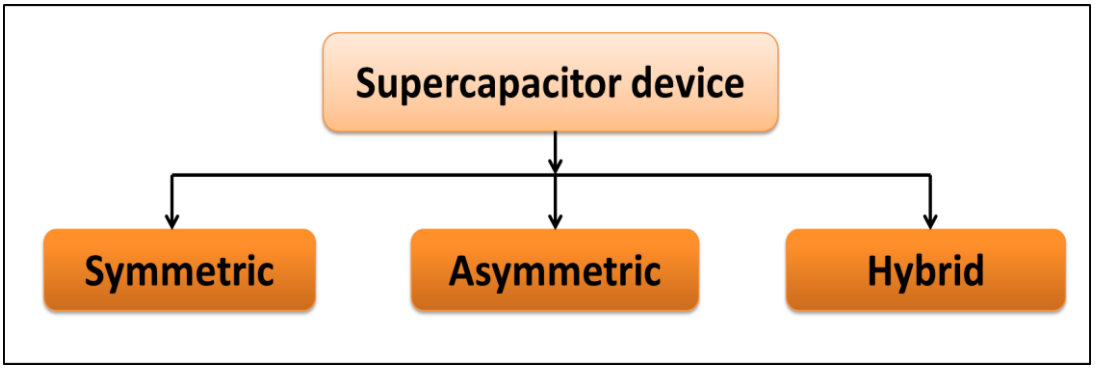

Fig. 2.12: Types of supercapacitor device.

Both comparable electrodes from the same charge storage mechanism can be used to develop a symmetric supercapacitor (SSC) system. Examples of SSC devices include AC//AC and MnO_2//MnO_2 **[55]**. Because both electrodes are made of similar materials, charge balancing is simple to establish in this case.

Asymmetric supercapacitors (ASCs) are a novel type of device that consists of two distinct electrode materials with different mechanisms for storing charge or

electroactive materials with variable ratios of redox active sites. Typically, electrodes based on EDLC and pseudocapacitive charge storage processes are built together. The ASCs have a high operating voltage, extended electrochemical stability, and high current rates with high S_E. The term ASC may be applied to a cell assembly consisting of two EDLC electrodes, one EDLC and one pseudocapacitive electrode, or both pseudocapacitive electrodes. A few examples of the ASCs devices are AC//CNTs, AC//MnO_2 **[56]**, and PANI//WO_3 **[57]**. The operating voltages of each electrode determine the final voltage of ASCs **[58]**. The balance of the charges stored (q) on the two component electrodes is required to reach the maximum operating potential and S_E i.e. $q_- = q_+$ **[59]**. Typically, the charges stored are correlated with the electrode material electroactive mass (m), C_s, and potential window (V). The electrodes optimal mass ratio is determined using the following relation,

$$\frac{m_+}{m_-} = \frac{C_{s-} \times \Delta V_-}{C_{s+} \times \Delta V_+} \qquad (2.11)$$

where 'ΔV' (V) is a potential window, 'm' (g) is the mass of active material, 'C_s' (F g^{-1}) is the specific capacitance, and +/− denotes electrodes with a positive and negative charges, respectively.

The term hybrid supercapacitors (HSCs) refers to the configuration of energy storage devices that combine two electrode types-one capacitive (carbon-based) and the other battery-type (NiO) **[60]**. The supercapacitor capacity to store energy is increased in this device by using its operating potential window to attain the faradic potential battery-like electrode. Due to hybridization, the hybrid device exhibits higher capacitive performance **[61, 62]**.

2.5.2 Cyclic voltammetry (CV):

This technique is highly effective in comprehending the electrochemical reactions involved in supercapacitive at the electrode and electrolyte interface. It is commonly used to assess reversible faradic reaction and ascertain the electrode or device operating potential window. Applying a constant initial and final voltages to an electrode or device and simultaneously estimating the consequent current is the basis of the CV concept **[63]**. In CV, a single cycle is completed by linearly varying the electrode potential between two constant potentials and then returning to the initial potential. These potential cycles are repeated several times. The current

is measurement based on the applied potential rate and the resulting graph is called a cyclic voltammogram. The CV data allows us to understand **[64]**,

I. Qualitative and pseudo-quantitative analyses,
II. Kinetic analysis using a broad range of scan rates, and
III. Estimate of the potential window.

Typically, two or three electrode configurations are used to perform the CV measurements. While measuring CV with three electrodes consisting a reference electrode (RE), a counter electrode (CE), and a working electrode (WE). The electrode operating potential is assessed in CV measurement with respect to the RE. **Fig. 2.13** presents the typical CV curve. The CV graph is used to compute the C_s of electrodes using the following equation:

$$C_s = \frac{1}{m \times \nu \times \Delta V} \int_{V_0}^{V_1} I(V) dV \qquad (2.12)$$

where, $\int_{V_0}^{V_1} I(V) \mathrm{d}V$ shows the half of total area covered by a single CV cycle, 'V_0' stands for initial potential and 'V_1' as final potential, 'm' is mass of active material (g), 'ν' denotes scan rate (V s^{-1}), 'ΔV' stands for potential difference (V), and 'I' is applied current density (A).

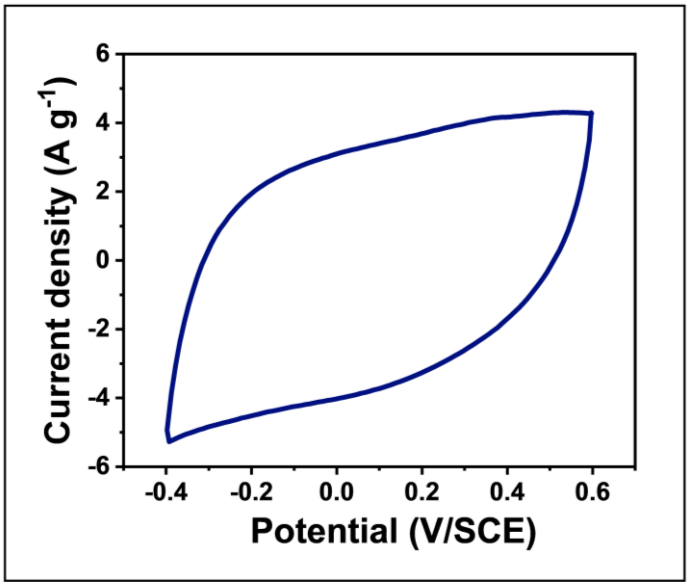

Fig. 2.13: The typical CV curve.

2.5.3 Galvanostatic charge discharge (GCD):

The GCD technique is often utilized to evaluate C_s of electrodes and devices as well as the stability of electrochemical cycles. According to the GCD principle, the

WE receives a constant current and as a function of time, the related potential is determined with respect to the RE. Initially, potential drops create a rapid change, followed by smaller changes **[65]**. **Fig. 2.14** shows a typical GCD curve.

Potential drops while discharging because of the solution and interfacial resistance; it can be avoided by using a steady potential offset. The sample electrode charge storage process is confirmed by the charging and discharging curve. The charge discharge curves symmetric shape indicates that the double layer process is primarily responsible for storing charge. If not, charge is stored through the pseudocapacitive mechanism **[66, 67]**. The following relation is used to calculate C_s from discharge curves,

$$C_s = \frac{I \times t}{m \times \Delta V} \tag{2.13}$$

where, 'm' is mass of active material (g), 'ΔV' stans for potential difference (V), 'I' is applied current density (A), and 't' is the discharge time (s). Furthermore, the S_E and S_P of the supercapacitor can be determined using GCD analysis.

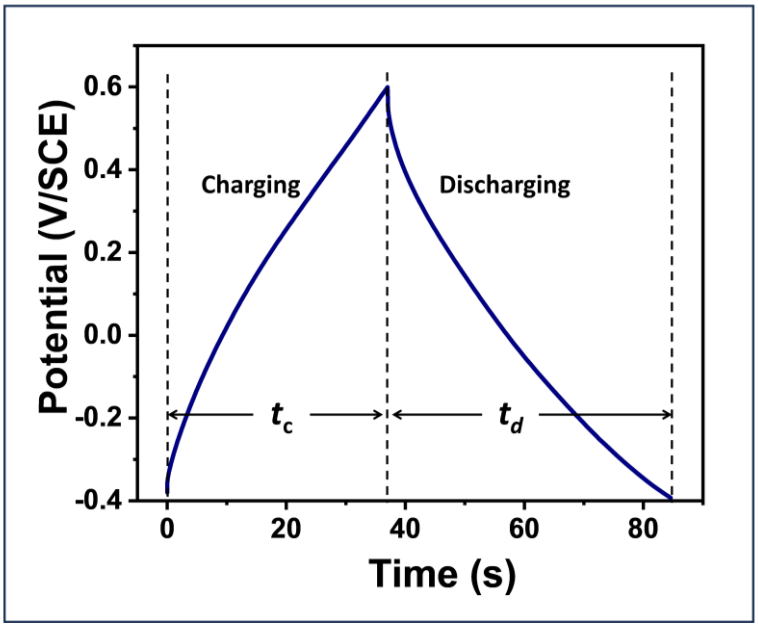

Fig. 2.14: The typical GCD curve.

2.5.4 Electrochemical impedance spectroscopy (EIS):

The EIS technique, also referred to as AC impedance spectroscopy, is one of the most effective ways to comprehend the impedance behaviour of supercapacitor at the electrode and electrolyte interface. For EIS, a little AC signal with frequencies

that vary between several mHz to kHz is used to charge the supercapacitor cell. Responding to applied AC signals, the output signals represent the current. The Nyquist plot refers to the imaginary impedance vs real impedance graph **[68, 69]**. The EIS study records both frequency-dependent and frequency-independent resistive properties of a system. The electrode material impedance may be calculated using the input signals of a sinusoidal voltage V (ω) = V_0 sin ωt and the output response I (ω) = I_0 sin (ωt + ϕ),

$$Z\ (\omega) = \frac{V\ (\omega)}{I\ (\omega)} = \frac{V_0 \sin (\omega t)}{I_0 \sin (\omega t + \phi)} = Z_0 \frac{\sin \omega t}{\sin (\omega t + \phi)} \qquad (2.14)$$

Magnitude 'Z_0' is used to express the impedance and phase shift 'ϕ'. The Nyquist plot in **Fig. 2.15** illustrates the imaginary and real components of impedance. The Nyquist plot basic equivalent circuit (Randles cell) is depicted in the inset of **Fig. 2.15**. The Nyquist plot is useful for studying electrochemical devices equivalent series resistance (R_s), charge transfer resistance (R_{ct}), and diffusion impedance (W). In compared to CV, EIS use a sinusoidal voltage signal to measure current at different frequencies, whereas CV use a linear voltage.

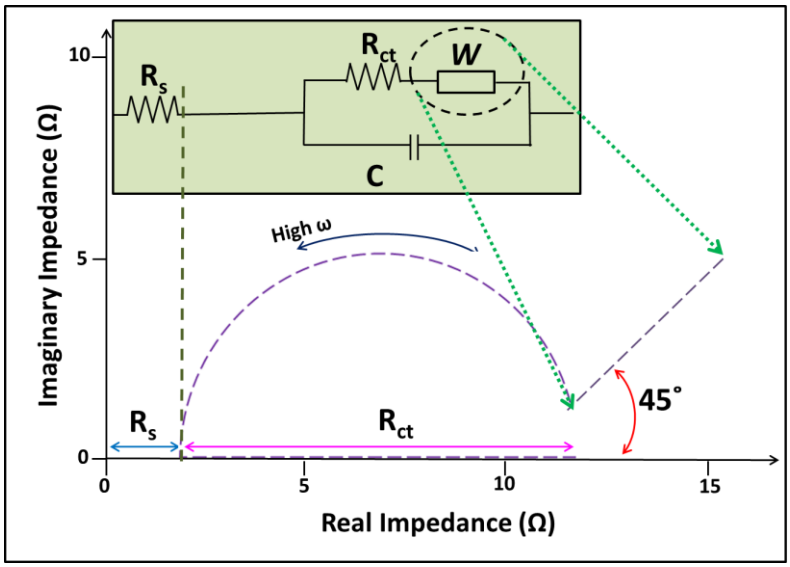

Fig. 2.15: A Nyquist plot with electrical equivalent circuit.

Some electrochemical terms in impedance spectroscopy are listed below,

a) Equivalent series resistance (R_s):

It contributes significantly to the impedance of electrochemical supercapacitor cell. The solution resistance between the RE and CE is compensated

for using a three-electrode cell. It is necessary to take into consideration the solution resistance that exists between the RE and WE while modeling an electrochemical supercapacitor cell. The resistance of an ionic solution varies based on concentration of ions, types of ions, temperature, and the area of the current flow. The comparable resistance is determined as follows: Given a constant current flowing through the limited area as (A) and length (l),

$$R = \rho \frac{l}{A} \tag{2.15}$$

where, 'ρ' denotes solution resistivity, the relation between solution conductivity (K) and solution resistance is as follows,

$$R = \frac{1}{\mathrm{K}} . \frac{l}{A} \ , \ \mathrm{K} = \frac{l}{RA} \tag{2.16}$$

The electrochemical supercapacitor devices lack a constant current distribution across the specified electrolyte area. As a result, it will be inaccurate to estimate solution resistance using solution conductivity. It is ascertainable from the EIS curve **[70]**.

b) Double layer capacitance (C):

It resides across the surrounding electrolyte solution and the electrode interface. As solution ions adsorb on the electrode surface, they form an interface. An insulating space, measured in angstroms (Å), is used to separate a charged electrode from the charged ions. A capacitor is formed when charges are separated by an insulator. A bare metal immersed in an electrolyte solution exhibits capacitor-like behaviour. Double layer capacitance can range from 20 to 60 μF per 1 × 1 cm^2 of electrode area, depending on factors such as electrode potential, concentration of ions, type of ions, oxide layers, temperature, roughness, and impurity adsorption.

c) Charge transfer resistance (R_{ct}):

In this case, the resistance is produced using a kinetically controlled electrochemical process. There is only one reaction that is in equilibrium. Consider the reversible reaction below,

$$\mathrm{Red} \leftrightarrow \mathrm{Ox} + \mathrm{ne}^- \tag{2.17}$$

A number of variables, including temperature, reaction type, reaction voltage, and reaction product concentration, affect the rate of charge transfer reaction occurs.

d) Diffusion impedance (*W*):

It is determined by the potential disturbance frequency. The producing impedance is referred to as Warburg impedance. At higher frequencies, electrolyte ions in solution have a shorter distance to travel, resulting in a minimal Warburg impedance. At lower frequencies, ions diffuse more, increasing the Warburg impedance **[71]**.

References:

[1] H. Choi, J. Kim, H. Kim, S. Lee, Y. Lee, Electrochim. Acta., 208, (2016), 202-210.

[2] Y. Ishida, R. Corpuz, T. Yonezawa, Acc. Chem. Res., 50, (2017), 2986-2995.

[3] R. Kumar, M. Raja Sekhar, Raghvendra, R. Laha, S. Pandey, Appl. Phys. A, 126, (2020), 859-869.

[4] C. Popescu, G. Dorcioman, A. Popescu, Laser ablation applied for synthesis of thin films: insights into laser deposition methods, in: Dongfang Yang (Ed.), Applications of Laser Ablation - Thin Film Deposition, Nanomaterial Synthesis and Surface Modification, InTech, (2016), 3-32.

[5] S. Lobe, C. Dellen, M. Finsterbusch, H. Gehrke, D. Sebold, C. Tsai, S. Uhlenbruck, O. Guillon, J. Power Sources, 307, (2016), 684-693.

[6] F. Shi, Introductory chapter: basic theory of magnetron sputtering, IntechOpen: London, UK, (2018).

[7] M. Chaudhari, R. Ahirrao, S. Bagul, Int. J. Res. Appl. Sci. Eng. Technol., 9, (2021), 5215-5232.

[8] T. Nimalan and M. Begam, Int. J. Thin. Fil. Sci. Tec., 13, (2024), 59-66.

[9] I. Stassen, M. Styles, G. Grenci, H. Gorp, W. Vanderlinden, S. Feyter, P. Falcaro, D. Vos, P. Vereecken, R. Ameloot, Nat. Mater., 15, (2016), 304-314.

[10] M. Choe, J. Koo, I. Park, H. Ohtsu, J. Shim, H. Choi, S. Park, J. Am. Chem. Soc., 144, (2022), 16726-16731.

[11] J. Ruiz, P. Girard-Lauriault, M. Wertheimer, Plasma Process. Polym., 12, (2015), 225-236.

[12] J. Schafer, K. Fricke, F. Mika, Z. Pokorna, L. Zajickova, R. Foest, Thin Solid Films, 630, (2017), 71-79.

[13] D. Pakula, M. Staszuk, M. Dziekonska, P. Kozmin, A. Cermak, Vacuum, 153, (2018), 184-190.

[14] R. Fadhil, E. Salim, W. Khalef, J. Mater. Sci.: Mater. Electron., 33, (2022), 21688-21701.

[15] B. Sankapal, E. Goncalves, A. Ennaoui, M. Lux-Steiner, Thin Solid Films, 451, (2004), 128-132.

[16] H. Ahn and Y. Um, J. Korean Phys. Soc., 67, (2015), 1045-1050.

[17] M. Kale, R. Borse, A. Gomaa Abdelkader Mohamed, Y. Wang, Adv. Funct. Mater., 31, (2021), 2101313-2101324.

[18] A. Hassanien and A. Akl, Appl. Phys. A, 124, (2018), 752-767.

[19] T. Kuech, Handbook of Crystal Growth: Thin Films and Epitaxy, Elsevier, Amsterdam, Second Edition, Volume III, (2014).

[20] S. Chaki, K. Mahato, T. Malek, M. Deshpande, J. Sci.: Adv. Mater. Devices, 2, (2017), 215-224.

[21] P. Katkar, S. Marje, V. Parale, C. Lokhande, J. Gunjakar, H. Park, U. Patil, Langmuir, 37, (2021), 5260-5274.

[22] M. Dhaouadi, M. Jlassi, I. Sta, I. Miled, G. Mousdis, M. Kompitsas, W. Dimassi, Am. J. Phys. Appl., 6, (2018), 43-50.

[23] D. Malavekar, S. Kale, V. Lokhande, U. Patil, J. Kim, C. Lokhande, J. Phys. Chem. C, 124, (2020), 28395-28406.

[24] R. Mane and C. Lokhande, Mater. Chem. Phys., 65, (2000), 1-31.

[25] V. Mane, D. Malavekar, S. Ubale, V. Lokhande, C. Lokhande, Inorg. Chem. Commun., 115, (2020), 107853-107904.

[26] B. Ezekoye, P. Offor, V. Ezekoye, F. Ezema, Int. J. Sci. Res., 2, (2013), 452-458.

[27] H. Pathan, and C. Lokhande, Bull. Mater. Sci., 27, (2004), 85-111.

[28] M. Ristov, G. Sinadinovski, I. Grozdanov, M. Mitreski, Thin Solid Films, 149, (1987), 65-71.

[29] Y. Nicolau and J. Menard, J. Cryst. Growth, 92, (1988), 128-142.

[30] A. Balu, V. Nagarethinam, M. Suganya, N. Arunkumar, G. Selvan, J. Electron Devices, 12, (2012), 739-749.

[31] C. Hu, X. Dang, S. Hu, J. Electroanal. Chem., 572, (2004), 161-171.

[32] V. Petkov, Mater. Today, 11, (2008), 28-38.

[33] http://xrd.co/component-parts-x-ray-diffractometer.

[34] https://www.rigaku.com/products/xrd/miniflex.

[35] M. Miranda and J. Sasaki, Acta Crystallogr A Found Adv., 74, (2018), 54-65.

[36] https://en.wikipedia.org/wiki/Raman_spectroscopy.

[37] I. Ebenezar, S. Ramalingam, C. Raja, P. Prabakar, J. Nano. Adv. Mat., 2, (2014), 11-25.

[38] J. Breier, S. White, C. German, Phil. Trans. R. Soc. A, 368, (2010), 3067-3086.

[39] A. Downes and A. Elfick, Sensors, 10, (2010), 1871-1889.

[40] https://bwtek.com/raman-components-of-a-raman-spectrometer/.

[41] https://www.mt.com/in/en/home/applications/L1_AutoChem_Applications/Ram a n-Spectroscopy.html.

[42] https://www.thermofisher.com/blog/microscopy/sputter-coating-for-sem how this sample-preparation-technique-assists-your-imaging/.

[43] http://mcff.mtu.edu/acmal/electronmicroscopy/FE_Form_Function.html.

[44] https://www.mtu.edu/acmal/shared-facilities/electron-optics/instrumentation/hitachi-s-4700-fe-sem/basic-science/form-function-1/.

[45] A. Mayeen, L. Shaji, A. Nair, N. Kalarikkal, Morphological characterization of nanomaterials, In Characterization of nanomaterials, Woodhead Publishing, (2018), 335-364.

[46] P. Sinha, A. Datar, C. Jeong, X. Deng, Y. Chung, L. Lin, J. Phys. Chem. C, 123, (2019), 20195- 20209.

[47] Z. ALOthman, Materials, 5, (2012), 2874-2902.

[48] http://www.pharmacopeia.cn/v29240/usp29nf24s0_c846.html.

[49] D. Lapham and J. Lapham, Int. J. Pharm., 568, (2019), 118522-118566.

[50] M. Siddiqui, S. Ali, H. Fei, H. Roshan, Earth Sci Rev., 181, (2018), 1-11.

[51] J. Rao, S. Anjum, M. Craig, J. Nicholls, J. Coat, Technol. Res., 15, (2018), 87-94.

[52] T. Chau, W. Bruckard, P. Koh, A. Nguyen, Adv. Colloid Interface Sci., 150, (2009), 106-115.

[53] http://www.ramehart.com/200.htm.

[54] T. Brousse, D. Belanger, J. Long, J. Electrochem. Soc., 162, (2015), 5185-5189.

[55] N. Chodankar, D. Dubal, G. Gund, C. Lokhande, J. Energy Chem., 25, (2016), 463-471.

[56] F. Chen, H. Wang, S. Ji, V. Linkov, R. Wang, Mater. Today Energy, 11, (2019), 211-217.

[57] K. Sun, H. Peng, J. Mu, G. Ma, G. Zhao, Z. Lei, Ionics, 21, (2015), 2309-2317.

[58] Y. Wang, Y. Song, Y. Xia, Chem. Soc. Rev., 45, (2016), 5925- 5950.

[59] M. Huang, F. Li, F. Dong, Y. Zhang, L. Zhang, J. Mater. Chem. A, 3, (2015), 21380-21423.

[60] M. Lukatskaya, B. Dunn, Y. Gogotsi, Nat. Commun., 7, (2016), 12647-12660.

[61] L. Shi, C. Pang, S. Chen, M. Wang, K. Wang, Z. Tan, P. Gao, J. Ren, Y. Huang, H. Peng, Z. Liu, Nano Lett., 17, (2017), 3681-3687.

[62] J. Wang, Y. Cui, D. Wang, Adv. Mater., 31, (2019), 1801993-1802017.

[63] N. Elgrishi, K. Rountree, B. McCarthy, E. Rountree, T. Eisenhart, J. Dempsey, J. Chem. Educ., 95, (2018), 197-206.

[64] C. Zoski, Handbook of electrochemistry, 1st ed.; Cynthia, Z., Ed., Elsevier Science: Amsterdam, The Netherlands, (2006).

[65] P. Veerakumar, A. Sangili, S. Manavalan, P. Thanasekaran, K. Lin, Ind. Eng. Chem. Res., 59, (2020), 6347- 6374.

[66] K. Kumar, N. Choudhary, Y. Jung, J. Thomas, ACS Energy Lett., 3, (2018), 482-495.

[67] K. Breitsprecher, C. Holm, S. Kondrat, ACS Nano, 12, (2018), 9733-9741.

[68] B. Mei, O. Munteshari, J. Lau, B. Dunn, L. Pilon, J. Phys. Chem. C, 122, (2018), 194- 206.

[69] D. Kampouris, X. Ji, E. Randviira, C. Banks, RSC Adv., 5, (2015), 12782-12791.

[70] http://www.gamry.com/application-notes/EIS/basics-of electrochemicalimpedance-spectroscopy.

[71] http://www.ecochemie.nl/download/Applicationnotes/Autolab-Application-NoteEIS06.pdf.

CHAPTER – III

Polyaniline and reduced graphene oxide/polyaniline (rGO/PANI) thin films by chemical bath deposition (CBD) method: Characterization and electrochemical performance

CHAPTER – III

Polyaniline and reduced graphene oxide/polyaniline (rGO/PANI) thin films by chemical bath deposition (CBD) method: Characterization and electrochemical performance

3.1 Introduction:

In response to the fast growth of the global economy, the depletion of fossil fuels, and the degradation of ecosystems, there is a critical need to improve extremely effective, inexhaustible, and environment friendly methods for the conversion and storage of energy. This has animated advances in converting renewable energy through greenways and innovations related to electrochemical energy storage, i.e. supercapacitors and batteries **[1, 2]**. Because of their inherent electrochemical properties, such as fast charge-discharge, long cycle stability, greater S_E compared to capacitors, and larger S_P than ordinary batteries, supercapacitors have been explored as key enabler for the next generation energy storage device.

Based on the methods used for charge storage, supercapacitor materials are divided into EDLC, and pseudocapacitor materials. The charge is stored in EDLC by electrolyte ions adhering to the electrode material surfaces. The pseudocapacitor charge storage device primarily relies on transferring charge through redox reactions on the electrode surface and in the electrolyte. Hence, the term pseudocapacitance has been used to characterize the properties of an electrode that exhibits capacitor-like behaviour in its electrochemical properties **[3]**. Only carbon-based materials consisting have demonstrated desirable flexibility; as a result, they have been extensively explored for flexible supercapacitors **[4, 5]**. CPs and transition metal compounds have also been largely composited and studied for supercapacitor applications due to their prominent energy storage properties **[6, 7]**.

In emerging materials, the two-dimensional and sp^2 hybridized carbon material known as graphene has emerged as a promising choice for next generation flexible electrode materials. This is because graphene sheets have a huge accessible surface area (2630 $m^2\ g^{-1}$), facilitating large double-layer capacitance. In addition, covalent sp^2 bonds between carbon atoms have a unique physical structure that promotes high electrical conductivity, which significantly lowers resistance of material **[8, 9]**. By adding rGO sheets in CPs matrix to improve their surface area, electrochemical processes, diffusion route, and increasing S_E and S_P. The non covalent bonding of rGO sheets and CPs is responsible for the efficient features of supercapacitors. The CP serves as separators to prevent the aggregation of rGO sheets, while rGO enhances the efficient polymerization of CP **[10]**. Hence, the combination of CP with rGO offers an efficient way of enhancing the stability of electrochemical cycles.

Among the CPs, the nanostructure of PANI is particularly interesting since it has a substantial influence on supercapacitor performance. It influences PANI matrix specific surface area and ion diffusivity during redox reactions, resulting in high C_s **[11]**. Nanostructured PANI materials have been synthesized in recent years using a variety of methods, including electrodeposition, SILAR method, etc. Patil et al. **[12]** reported an electrodeposition method to prepare PANI with a C_s of 581 F g^{-1}. Deshmukh et al. **[13]** reported that PANI-titanium oxide electrode prepared by CBD method and exhibited C_s of 783 F g^{-1}. Patil et al. **[14]** reported that deposition of silver nano sticks-PANI by dip coating method, which showed a highest C_s of 628 F g^{-1}. Microwave-assisted chemical oxidative polymerization method for developing PANI nanosheets on carbon cloth was reported by Zhou et al. **[15]**, with a C_s of 1034 F g^{-1}. Liu and coworkers **[16]** prepared graphene/PANI composite hydrogel film by electropolymerization method and achieved C_s of 853.7 F g^{-1}. Wang et al. **[6]** synthesized PANI-rGO/MWCNT nanocomposite by chemical oxidative polymerization of aniline on rGO sheets with C_s of 645 F g^{-1}.

This chapter covers the synthesis and characterisation of PANI and rGO/PANI thin films using CBD method.

3.2 Synthesis of PANI and rGO/PANI thin films:

3.2.1 Introduction:

The electrode material preparation method should be cost-effective and scalable, making it suitable for large scale commercialization of supercapacitors. From this point of view, the low temperature, binder-free CBD method is used to synthesis PANI and rGO/PANI electrodes. The main advantage of CBD method is that it significantly increases the electrical conductivity of the electrodes that are produced precisely on the conductive substrate. More electrolyte active sites are provided by direct material growth **[17]**. By combining rGO sheets with PANI nanoparticles produced using CBD method, a porous electrode structure can be formed. Following this, PANI and rGO/PANI films were characterized through various techniques such as structural analysis using XRD, chemical bonding study using Raman, chemical state determination using XPS, surface microstructural studies using FE-SEM, and BET is used to quantify the thin film material specific surface area. Additionally, wettability measurements were performed to investigate the interaction between PANI and rGO/PANI thin film electrodes with an electrolyte.

3.2.2 Experimental details:

3.2.2.1 Cleaning of substrate:

The uncontrolled development of material and the resulting non-uniform thin film deposition are caused by an impurity in the substrate. Thus, proper substrate cleaning is crucial for consistent film deposition. This study uses stainless steel (SS) as a substrate.

The following is the process used to clean the SS substrate:

Step 1: The impurities was removed from the SS substrate by cleaning it with acetone.

Step 2: Zero grade sand paper was used to mirror polish the SS substrate.

Step 3: Using DDW, the substrate was washed after polishing; and

Step 4: Then substrate was ultrasonically cleaned with DDW for 15 min then dried at ambient temperature.

3.2.2.2 Chemicals:

All chemicals of analytical reagent grade, like aniline monomer, sulphuric acid (H_2SO_4), ammonium persulfate (APS) ($(NH_4)_2S_2O_8$), were purchased from Thomas Baker Ltd. As a solvent, DDW was used and a SS 304 grade measuring 5×1 cm^2 was used as the substrate.

3.2.2.3 Synthesis of rGO:

The GO suspension was formed by exfoliating graphite, and then a chemical reduction method was used to produce rGO. The previously described process was used in the preparation of GO suspension. In a 500 mL conical flask, 2 g of graphite flakes with an average diameter of 100 μm and 100 mL of concentrated H_2SO_4 were added. The mixture was then held in an ice bath with constant stirring until 1 g of sodium nitrate ($NaNO_3$) was added. To keep the reaction temperature below 293 K, 8 g of potassium permanganate ($KMnO_4$) was gradually added to this mixture. Afterwards the completion of the addition, for 12 h the reaction mixture was constantly stirred at the ambient temperature. 100 mL of DDW was added after 1.5 h, and then 300 mL of DDW and 8 mL of 30% hydrogen peroxide (H_2O_2). As a result, the solution becomes yellowish. Subsequently, the mixture was repeatedly washed with 5% HCl and DDW until the pH reached 6.5. The GO slurry concentration was measured by use of the gravimetric weight difference method. For GO reduction,

hydrazine hydrate (N_2H_4) (reducing agent) was employed. 500 mL of GO solution with a density of 1 mg mL^{-1} was heated for 2 h at 363 K with 2.5 mL of N_2H_4 added. The residue was repeatedly cleaned with DDW after the reaction was finished, and it was then vacuum dried at 323 K. The rGO powder was utilized to deposit and characterize thin films. A schematic representation of rGO production process is depicted in **Fig. 3.1**.

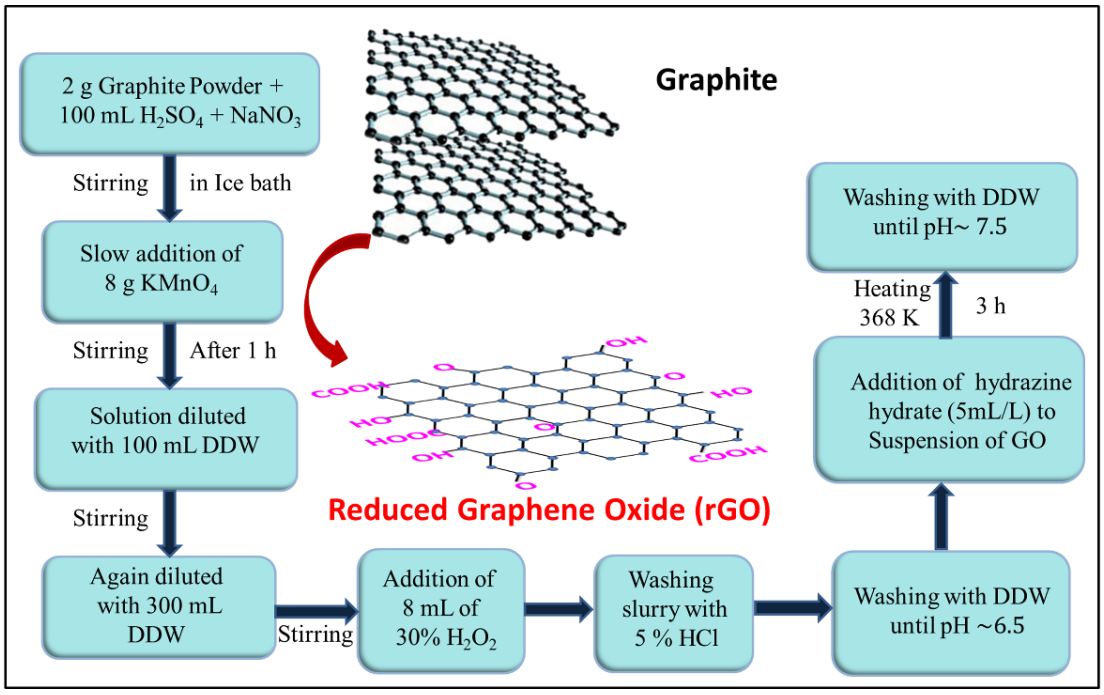

Fig. 3.1: A schematic representation of rGO production process.

3.2.2.4 Synthesis of PANI thin films:

A convenient method for significant deposition on many substrates is CBD method. It is quite an easy and cheap method compared to other methods. The development of nucleation is essential for the formation of precipitates. The result of nucleation in solution is that the molecular clusters produced quickly decompose, and particles combine to grow the film to a particular thickness. The controlled precipitation of the desired compound from a solution of its constituents is the fundamental principle of CBD method **[18, 19]**.

In thin film deposition, the reaction temperature is particularly significant because it affects the ion transport kinetics, that is affected by the reaction rate, morphology, thickness, surface wettability, and pore size **[20]**. However, a complete understanding of its impact on electrode electrochemical activity is still lacking. The electrode material specific surface area, which determines the electrode electroactive

area, is related to the pore size. As a result, understanding the influence of changes in the fundamental characteristics of a thin film material produced by reaction bath temperature on electrochemical characteristics is essential and practically significant. Such research will assist in the optimization of preparative parameters of the active electrode material for energy storage applications **[17]**. Hence, we have considered the possible effect of reaction temperature on the structural and supercapacitive performance of PANI electrode, particularly with chemical synthesis methods. Herein, PANI electrodes were prepared at different bath temperatures using CBD method. Moreover, the reaction bath temperature affected on some physical properties of electrodes such as the thickness of the films, specific surface area, and wettability of the electrode.

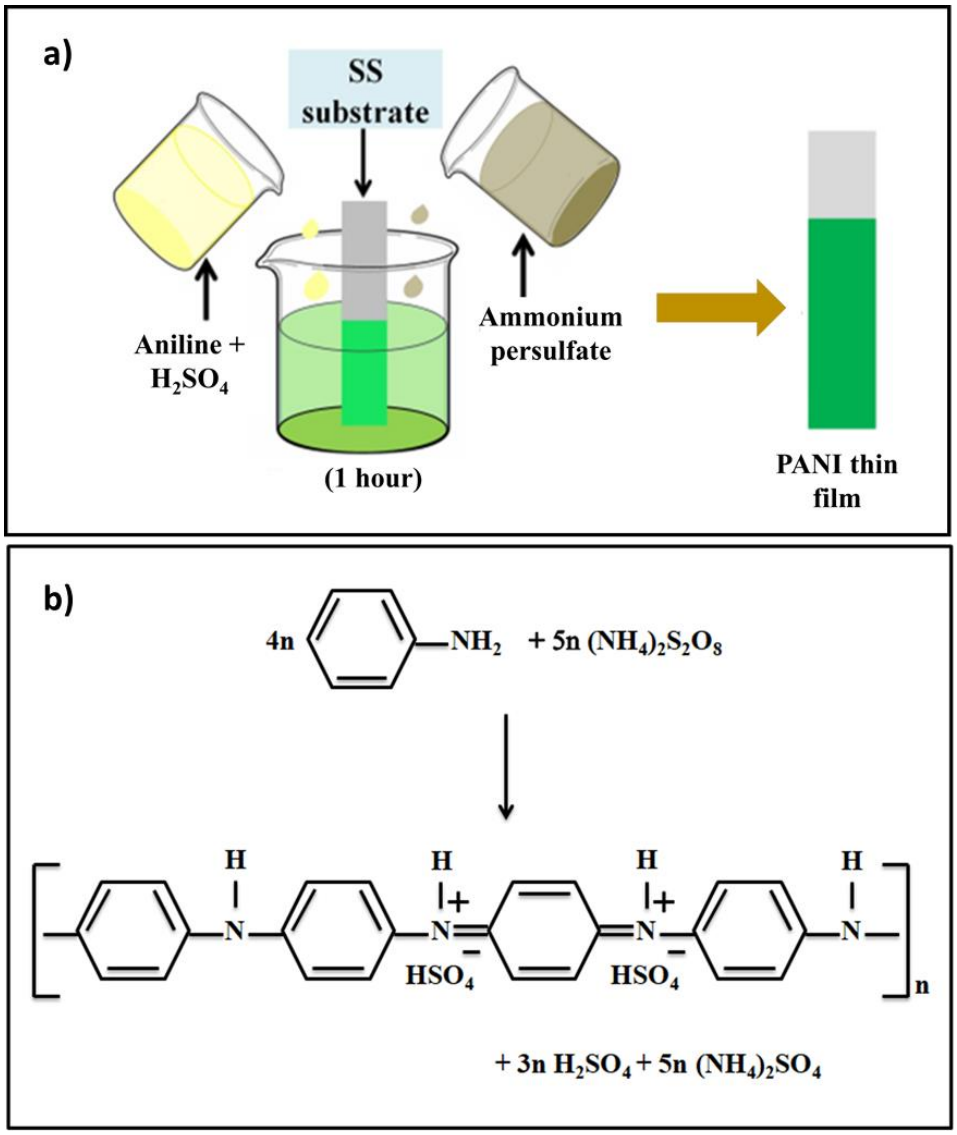

Fig. 3.2: a) Schematic presentation of PANI electrode preparation by CBD method at different temperatures (P1 to P4), and b) reaction mechanism of PANI. (Aniline is

oxidized by APS to form PANI. Sulfuric acid and ammonium sulphate are by-products).

The mechanism of PANI deposition is the chemical polymerization of aniline monomer in an acidic medium. For the deposition, 0.4 M aniline monomer was dissolved in 50 mL, 1 M H_2SO_4 solution, and to this solution, 50 mL of 0.1 M APS solution was added dropwise at speed of 2 mL s^{-1}. The solution was stirred vigorously at 400 rpm speed and kept to polymerize for an hour at different temperatures between 263 and 323 K with a pre-cleaned SS substrate (1 × 5 cm^2) immersed. **Fig. 3.2a** shows the schematic representation of PANI electrode preparation using CBD method.

In CBD method, film deposition involves ion-by-ion deposition at available nucleation sites on a submerged SS substrate surface. **Fig. 3.2b** illustrates the reaction mechanism of PANI. To initiate chemical polymerization, a proton from an aniline molecule is removed by APS, and the dimer gives chain propagation through oxidation and coupling. Due to protonic acid, doping of protons takes place on completion of polymerization **[21]**. As the reaction proceeds, due to the polymerization of aniline, the reaction solution turns green from its original bluish colour. After an hour, the SS substrate was removed from the reaction bath and rinsed 1-2 times with DDW. A green layer was observed on SS substrate, indicating that the conducting emeraldine salt phase of PANI has been obtained **[22]**. The PANI films deposited at temperatures of 263, 273, 303, and 323 K are denoted as P1, P2, P3, and P4, respectively.

Thickness study:

The weight difference method was applied to determine thin film thicknesses using a sensitive microbalance. The variation of thickness of PANI electrodes with reaction bath temperature is shown in **Fig. 3.3a**. Thickness (T) was determined by using the equation,

$$T = \frac{M}{A \times \rho} \qquad (3.1)$$

where 'M/A' is the mass per unit area deposited on SS substrate in g cm^{-2}, and 'ρ' is PANI density (1.329 g cm^{-3}). PANI film thickness increases with temperature, achieving a maximum of 1.0 μm at 303 K. The film thickness in CBD method is influenced by the nucleation growth process and the rate of nucleus production.

During the development phase, more nucleation sites improve coagulation even more to achieve maximal thickness **[23]**. At high temperatures, PANI conjugated structure breaks due to the delocalization of π-electron, and the ion doping level of PANI chains decreases. Because of decreased polymerization rate, film thickness decreases above 303 K **[24]**. Photograph of P1, P2, P3, and P4 films is displayed in **Fig. 3.3b**. The rate of polymerization increases with temperature, indicating that the colour of PANI films also changed with temperature from light green to dark green. An increase in the temperature above 303 K stimulates a decrease in the polymer chains propagation step, which results in changed colour of thin film.

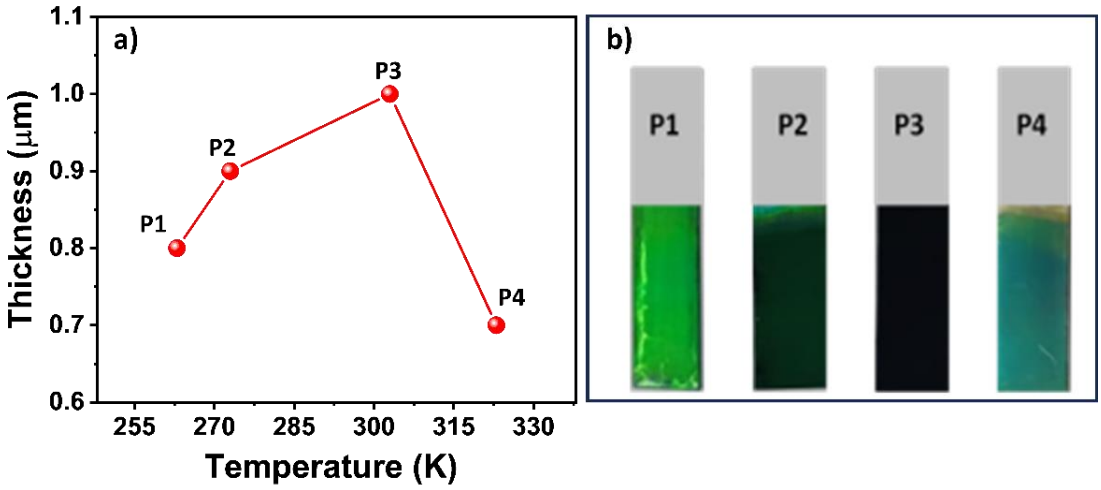

Fig. 3.3: a) The variation of thickness of PANI electrodes with reaction bath temperature, and b) photograph of PANI electrodes.

3.2.2.5 Synthesis of rGO/PANI thin films:

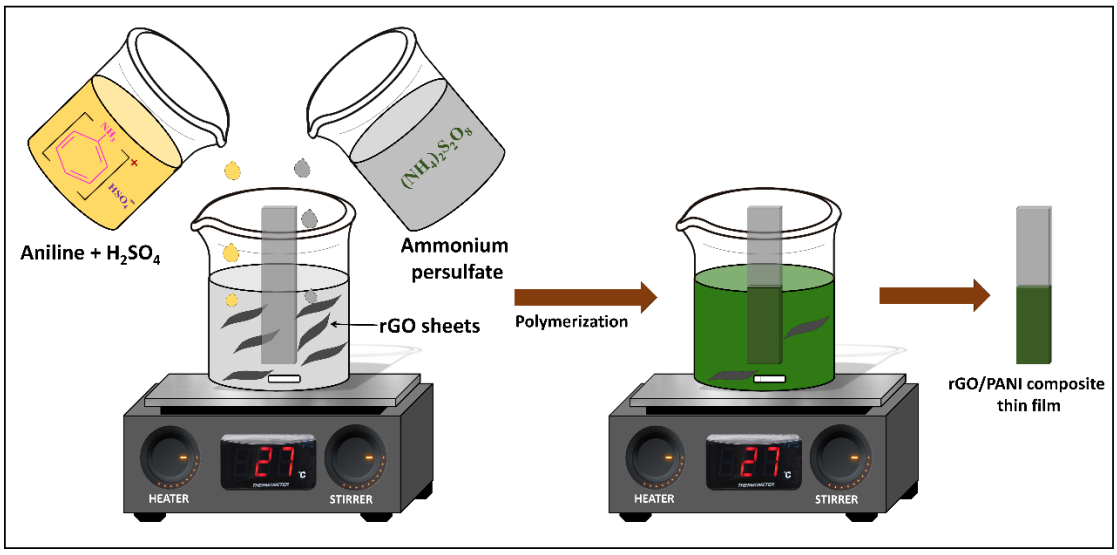

Fig. 3.4: Schematic presentation of rGO/PANI electrode preparation by CBD method.

For the synthesis of rGO/PANI films, 1 mg mL^{-1} rGO was added in 20 mL of DDW and sonicated for 4 h to evenly distribute rGO sheets. In a separate beaker, 0.1 M of aniline was added to 20 mL of 1 M of H_2SO_4 solution. In another beaker 0.1 M APS was dissolved in 20 mL of DDW. Both the solutions were added dropwise into rGO suspension at room temperature (303 K). A pre-cleaned SS substrate was immersed in the resultant mixture while the mixture aggressively stirred 400 rpm and allowed to polymerize for an hour. **Fig. 3.4** depicts the schematic presentation of rGO/PANI electrode preparation using CBD method.

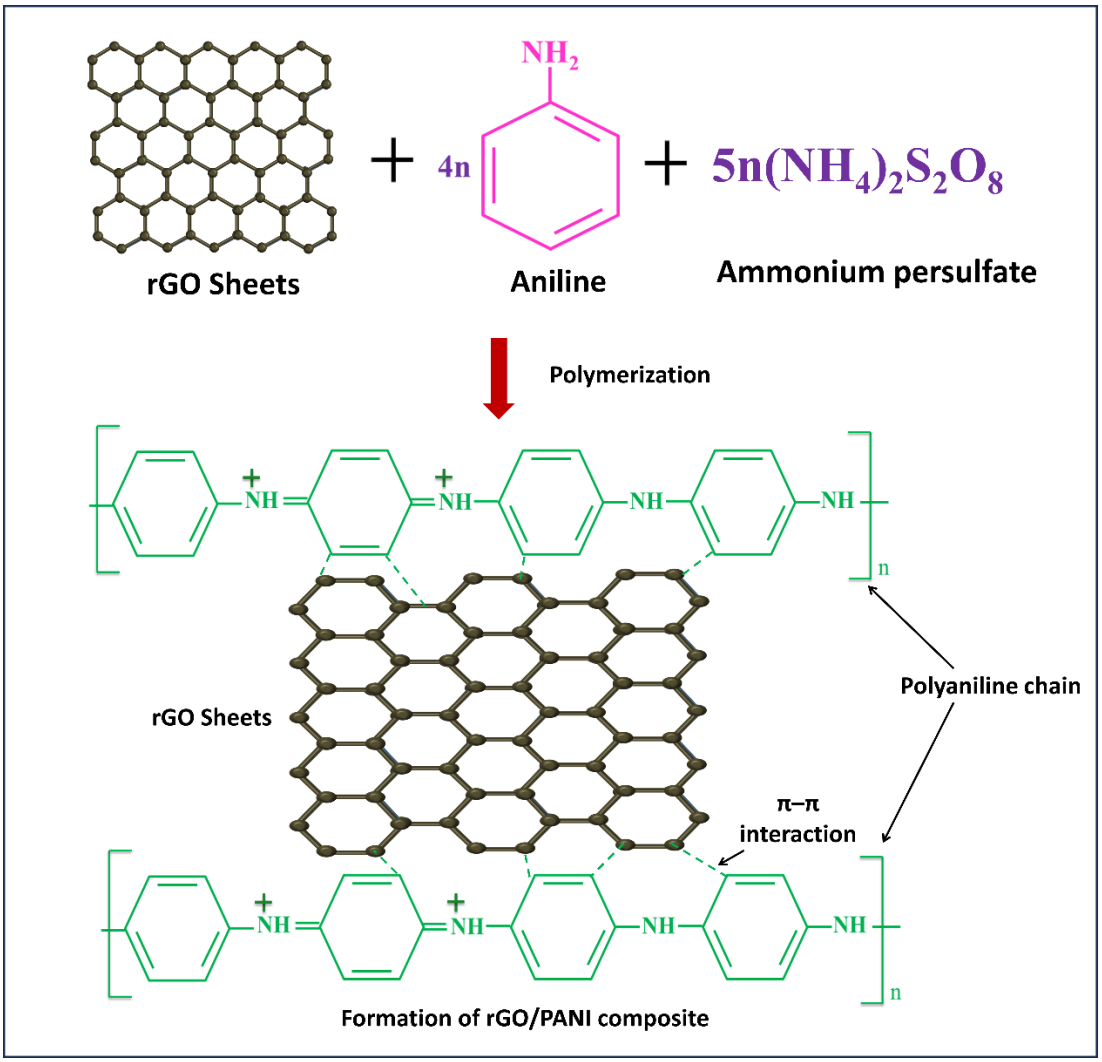

Fig. 3.5: Reaction mechanism of rGO/PANI composite electrode.

In the chemical deposition of rGO/PANI composite, π-π stacking interactions between PANI backbone and rGO surface encouraged positively charged monomers (anilinium cations) to adsorb on the negatively charged rGO surface **[25]**. As a result, essential polymerization occurred on an increasing number of nucleation sites, assisted by the immense specific surface area of rGO network, providing continuous

deposition of PANI with high surface coverage. **Fig. 3.5** shows the reaction and growth mechanism of PANI on rGO surface. In acidic environment, the aniline monomers change into anilinium cations ($C_6H_5NH_3^+$), which then quickly react with oxidant to generate spikes of aniline cations. Nucleation takes place on sites provided by rGO sheets by a chemical oxidative polymerization mechanism, and it can serve as a 'seed' to speed up the kinetics of spikes creation within a limited period and prevent additional overgrowth **[26]**. For rGO, PANI, and rGO/PANI, the corresponding thicknesses are 0.65, 1.0, and 1.52 μm, respectively. The thickness increased with rGO composite because rGO sheets electrostatically attract more aniline ions, leading to increased mass loading.

3.3 Material characterizations:

3.3.1 Physico-chemical characterizations:

The material crystal structure was examined with a Rigaku miniflex-600 X-ray diffractometer utilizing Cu K-α radiation (λ = 1.54 Å). Using FT-IR instrument Bruker Tensor 27, chemical bonding between constituent elements was analyzed. Raman spectroscopy of the samples was carried out using Raman spectrometer of Tokyo Instruments (Model: FLEX G) with a laser wavelength of 514.4 nm. The XPS was used to analyze the surface chemical composition of a thin film using a monochromatic Mg Kα radiation source (1253.6 eV) (VG Multilab 2000, Thermo VG Scientific, U.K.). A FE-SEM was used to investigate the morphology of the materials. N_2 sorption experiments were conducted utilizing the Quantachrome Instrument v11.02 to obtain specific surface area and pore size distribution information using BET and BJH studies. To capture photos of contact angle, the Rame Hart goniometer was used.

3.3.2 Electrochemical characterizations:

To examine the electrochemical characteristics of PANI and rGO/PANI electrodes, a Zive MP1 electrochemical workstation was utilized. The electrochemical properties were evaluated in an aqueous 1 M H_2SO_4 electrolyte. A three-electrode setup typically consists of a PANI or rGO/PANI thin films as the WE, a saturated calomel electrode (SCE) serving as the RE, and a platinum plate (Pt) as the CE. In this system, Pt offers very high electrical conductivity and hence, the performance of PANI or rGO/PANI can be evaluated correctly. **Fig. 3.6** depicts the electrochemical

workstation **(Fig. 3.6a)**, experimental setup **(Fig. 3.6b)**, and schematic for the three-electrode cell **(Fig. 3.6c)**. The supercapacitive performance of electrodes was assessed using C_s, R_s, R_{ct}, and cyclic stability. An electrochemical workstation was used to perform the CV, GCD, and EIS analyses (Zive MP1).

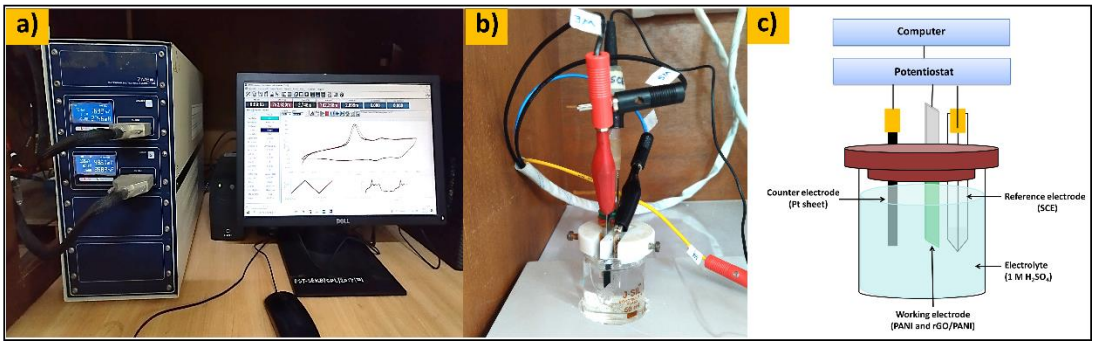

Fig. 3.6: a) The electrochemical workstation, b) experimental setup, and c) schematic representation of three-electrode cell.

3.3.2.1 Cyclic voltammetry (CV):

The CV is a crucial method for determining redox potentials and redox transfer processes. The C_s of electrode materials can be determined using CV curve. The CV study for PANI or rGO/PANI thin film electrodes was conducted within the potential window of -0.2 to +0.8 V/SCE. The C_s of the electrode material were calculated using **Equation 2.12**. The power law analysis was used to study the charge storage mechanism.

3.3.2.2 Galvanostatic charge discharge (GCD):

For PANI or rGO/PANI thin film electrodes, the GCD analysis was carried out within a similar potential window as the CV analysis. The shape of GCD curves indicates the type of charge storage properties. **Equation 2.13** was utilized to get the C_s values of thin film electrodes.

3.3.2.3 Electrochemical impedance spectroscopy (EIS):

The EIS study helps to investigate resistance and charge transfer processes. The electrochemical workstation (Zive MP1) utilized the EIS measurement to evaluate the quality of the interaction between the electrode/electrolyte. The EIS experiment was conducted at frequencies between 0.01 Hz and 100 kHz with potential amplitude of 10 mV.

3.4 Results and discussion:

3.4A Physico-chemical characterizations:

3.4A.1 Physico-chemical characterizations of PANI thin films:

3.4A.1.1 XRD study:

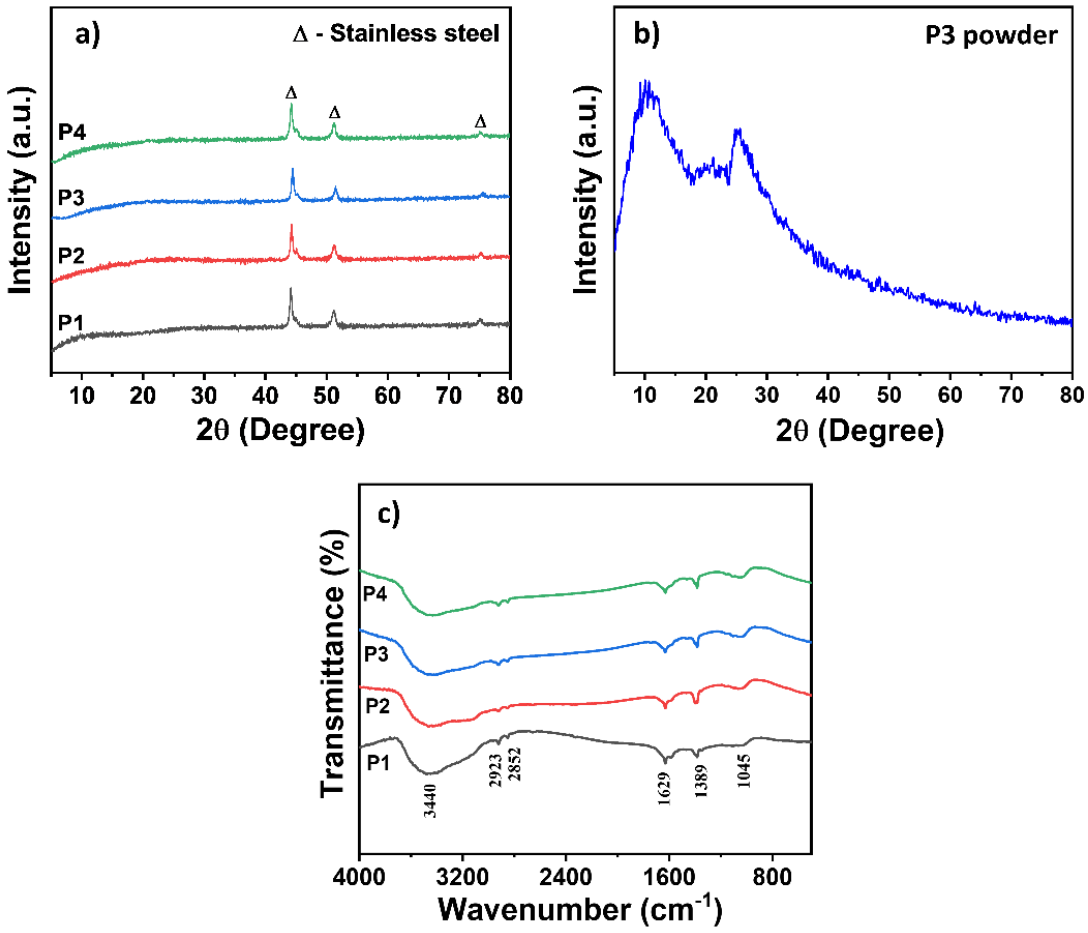

Fig. 3.7: a) The XRD patterns of PANI electrodes deposited at different temperatures, b) XRD pattern of P3 powder, and c) FT-IR spectra of PANI electrodes.

The XRD patterns presented in **Fig. 3.7a** are of PANI films deposited at different temperatures (P1 to P4). The patterns do not show any peak of PANI material instead, the presence of SS peaks with the notation 'Δ' indicates that all PANI samples are amorphous. It has been reported that PANI exhibits an amorphous nature at low temperatures (below 373 K) **[27]**. The XRD pattern of P3 powder is depicted in **Fig. 3.7b**. The diffraction patterns composed of two broad peaks at 10.19° and 25.10°, which might be attributed to scattering along a direction parallel to the polymer chain and given to the uniformity which is perpendicular to the polymers chain direction, indicating that PANI chain contains a mainly amorphous structure

[28]. The PANI achieved amorphous nature is more practical than crystalline because the deposition was performed at room temperature, only the lowest energy is available, which is required for particle arrangements in a particular direction. An amorphous material is not arranged in a regular or periodic pattern. So, the apparent volume void fractions of amorphous materials with highly porous structures can range upto 50% or more. Due to this, ions may easily intercalate and deintercalate inside the bulk of the amorphous electrode and the electrode capacity to store electrochemical charge is increased **[29, 30]**.

3.4A.1.2 FT-IR study:

To determine functional or bonding group presence in synthesized PANI thin films, FT-IR spectroscopy was conducted and the obtained spectra are depicted in **Fig. 3.7c**. In all four spectra, the intense peak at 3440 cm^{-1} represents stretching vibrations of the –OH group on the thin film surface **[31]**. The N–H characteristics bond in an aromatic ring attached to amines gives the absorption peak at 2923 cm^{-1} and 2852 cm^{-1}. The bands that appeared at 1629 cm^{-1} correspond to the aromatic quinoid ring deformation **[32]**. An absorption band at 1389 cm^{-1} is associated with C-N stretching vibrations in the polaronic structure **[33]**. The absorption band observed at 1045 cm^{-1} is caused by the out of plane bending vibration of the benzene ring C–H **[34]**. These distinct peaks confirmed that PANI contained the conducting emeraldine salt phase.

3.4A.1.3 FE-SEM study:

A significant and useful technique for examining the surface textural characteristics of thin film material is the FE-SEM. The FE-SEM images of PANI samples demonstrate the effect of polymerization temperature on the morphology of the samples. The surface morphologies of all PANI electrodes at magnifications of 25 KX and 75 KX are shown in **Fig. 3.8**. Sample P1 **(Fig. 3.8a and b)** shows the morphology of a quite hierarchically interrelated structure composed of a highly porous network of spikes. Sample P2 **(Fig. 3.8c and d)** shows similar morphology with a reduction in spike height. PANI sample prepared at higher temperatures **(Fig. 3.8e-h)** shows a further reduction in spike height. Increased reaction rate causes self-aggregation among nanoparticles at higher polymerization temperatures **[35]**. This study concludes that the polymerization temperature influences the texture of PANI. Such nanostructured P3 electrode would be a better electrode for supercapacitors

since it would possess built in pores with a higher surface area due to spikes on the surface.

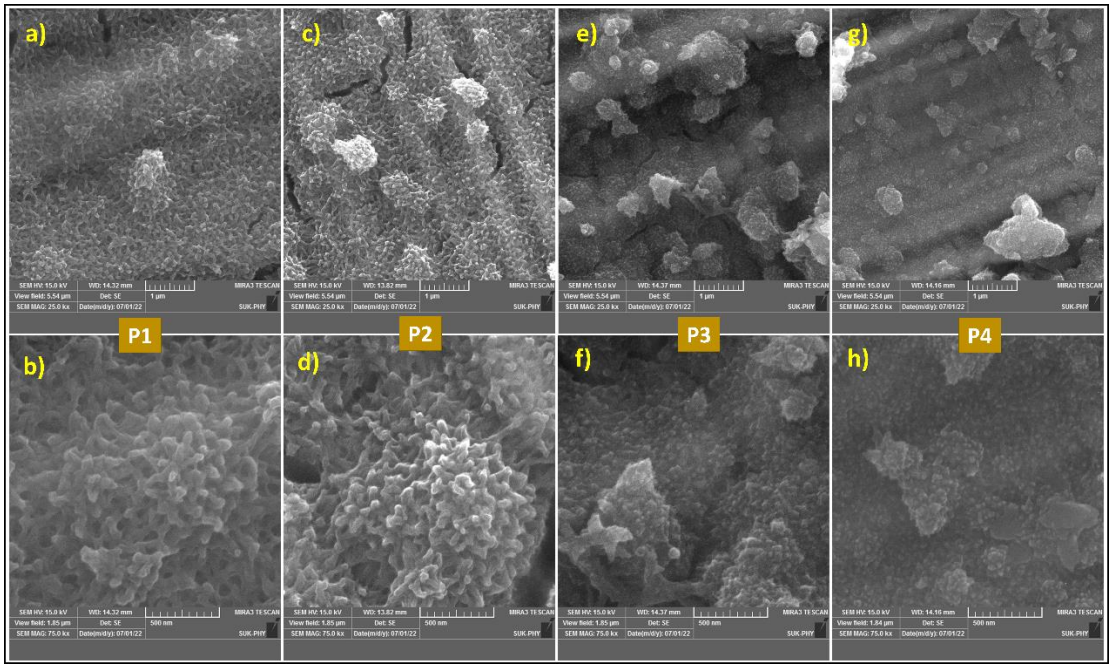

Fig. 3.8: FE-SEM images (a, b) P1, (c, d) P2, (e, f) P3, and (g, h) P4 electrodes at magnifications (25 KX and 75 KX).

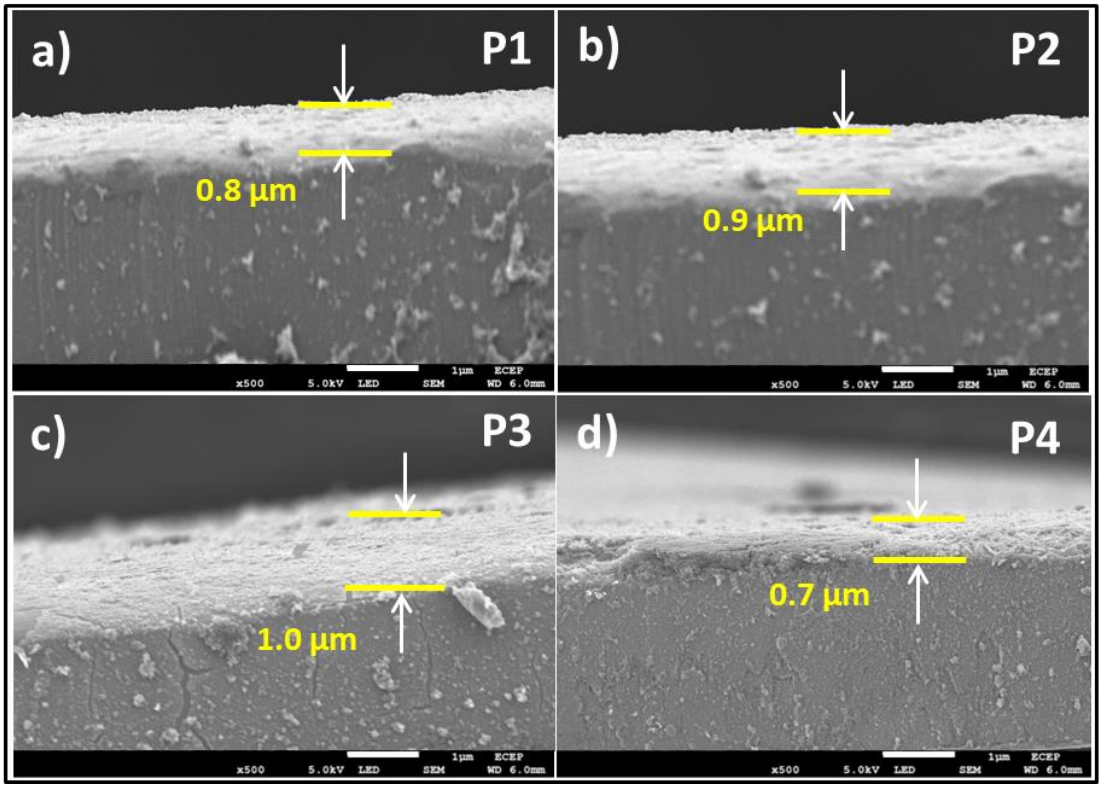

Fig. 3.9: Cross-sectional SEM images of a) P1, b) P2, c) P3, and d) P4 electrodes at 500X magnification.

The cross-sectional SEM images of all PANI electrodes are shown in **Fig. 3.9**. The rate of polymerization increases with temperature, indicating that the thickness of PANI film also increases with temperature. The measured film thickness as for P1, P2, P3, and P4 electrodes are about 0.8, 0.9, 1.0, and 0.7 μm, respectively. An increase in the temperature above 303 K stimulates a decrease in the polymer chains propagation step, which results in decreased film thickness **[24]**.

3.4A.1.4 BET and BJH studies:

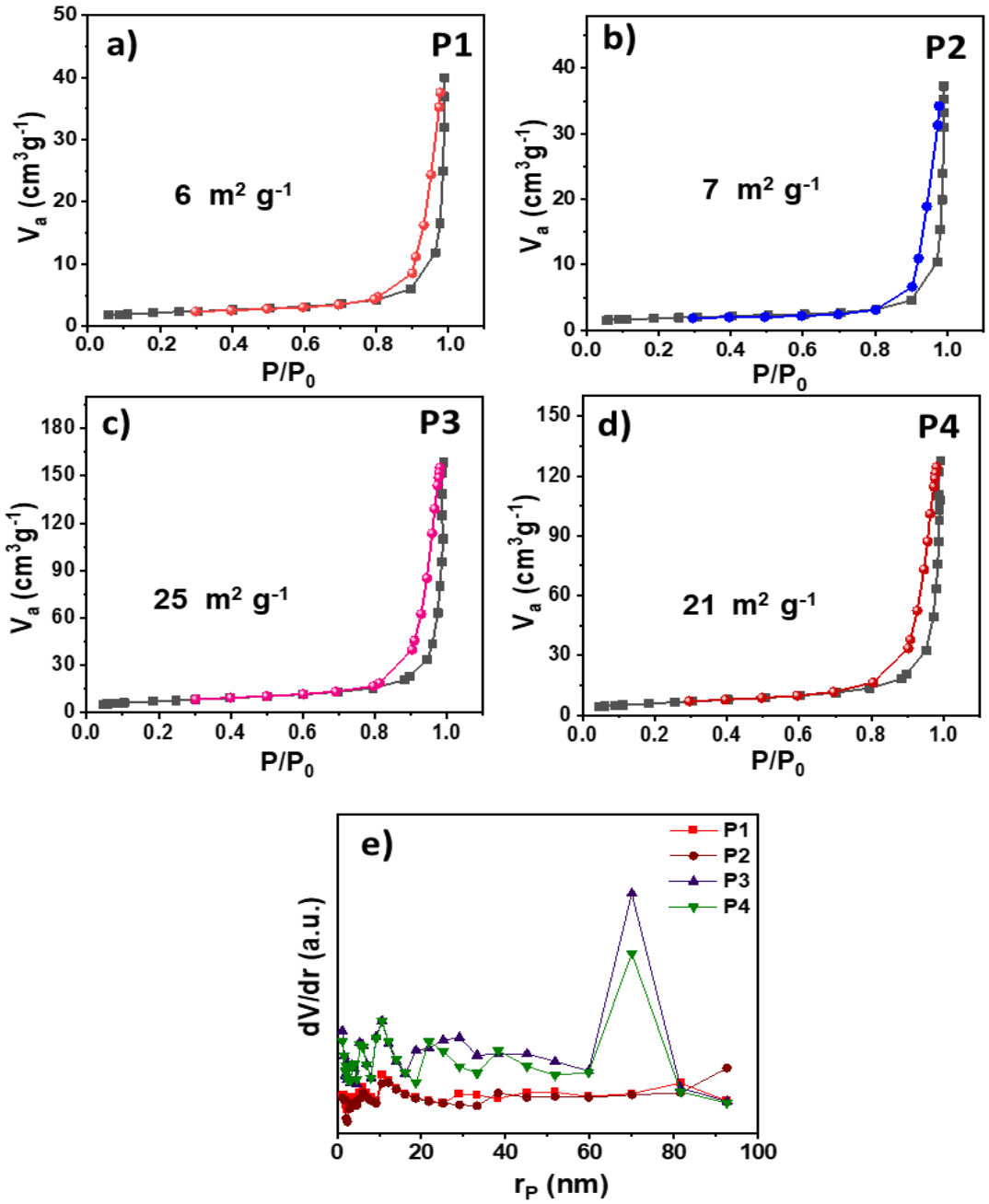

Fig. 3.10: The BET isotherms of a) P1, b) P2, c) P3, and d) P4 samples, and e) pore size distribution curves of P1 to P4 samples.

To assess the samples specific surface area and pore size distribution, a BET study was carried out. The BET isotherms of PANI samples are shown in **Fig. 3.10**. The type-IV isotherms for all PANI samples reveal the presence of mesopores with a diameter ranging from 2 to 50 nm. The samples P1, P2, P3, and P4 show specific surface areas of 6, 7, 25, and 21 $m^2\ g^{-1}$, respectively **(Fig. 3.10a-d)**, indicating P3 electrode has the highest surface area compared to others. The pore size distribution curves for P1 to P4 samples **(Fig. 3.10e)** indicate that the average pore size and pore volume of the samples P1, P2, P3, and P4 are 32.5, 37.1, 38, and 35.7 nm and 0.058, 0.0562, 0.238, and 0.19 $cm^3\ g^{-1}$, respectively. The mesoporous structure of all electrodes may facilitate electrolyte ion penetration and provide effective ion transfer inside the electrode, resulting in enhanced electrochemical performance even at high rates **[36]**. Significantly, P3 electrode have the largest surface area 25 $m^2\ g^{-1}$ than P1, P2, and P4 electrodes.

In **Fig. 3.10e** strong peak appeared in the BJH pore size distribution of P3 electrode at 70 nm, indicate that the sample formed a more concentrated pore size distribution at 70 nm **[37]**. The surface morphology is important in the charge storage process of a supercapacitor electrode. Such a higher specific surface area and mesoporous structure of P3 electrode, which attributed to the shortened diffusion path distance due to pore size enlargement. Due to its higher surface area, P3 electrode shows higher C_s than other electrodes. From this, it was concluded that the reaction temperature influences the structure and properties of PANI **[38]**.

3.4A.1.5 Contact angle study:

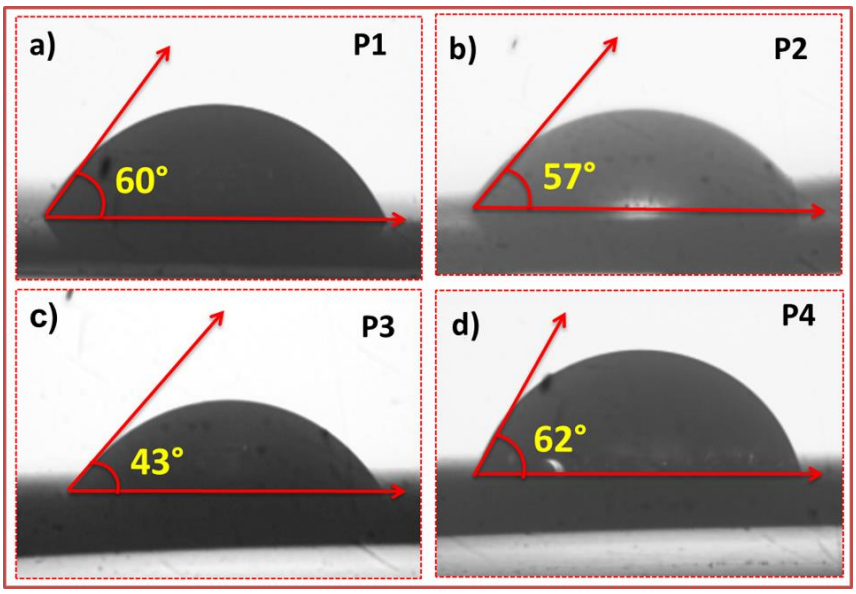

Fig. 3.11: The contact angle images of a) P1, b) P2, c) P3, and d) P4 electrodes.

The measurement of the contact angle is useful to find out the characteristics of the interface between electrolyte and electrode. The wettability of a solid surface has been considered an important factor to enhance the electrode capacity for reliable charge storage and improve C_s **[39]**. The electrode surface is hydrophilic if the contact angle is less ($\theta < 90°$) and hydrophobic if it is larger ($\theta > 90°$). **Fig. 3.11a-d** shows contact angle images of P1, P2, P3, and P4 with values of 60°, 57°, 43°, and 62°, respectively. Physical and chemical factors affect contact angle, such as the size and shape of the particle, purity, and surface roughness, which change the values of contact angle. As bath temperature rises, the topography of the electrode surface changes, affecting wettability **[17]**. P3 has a higher hydrophilicity (43°) in all prepared PANI samples, which increases the electrolyte interaction with the electrode.

3.4A.2 Physico-chemical characterizations of rGO/PANI thin films:

3.4A.2.1 XRD study:

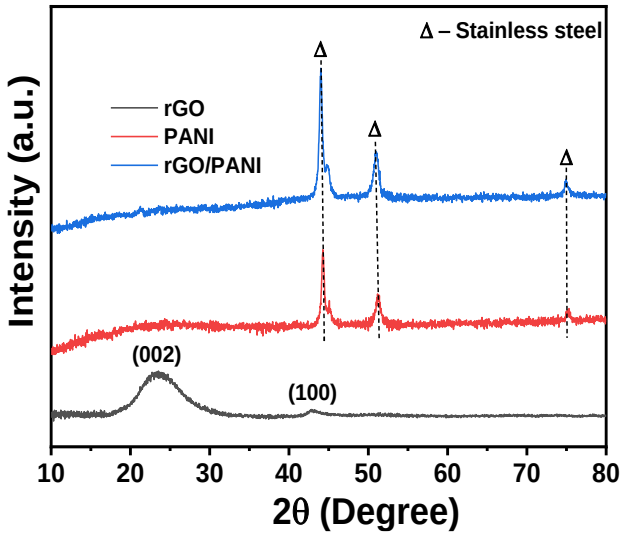

Fig. 3.12: The XRD patterns of rGO powder, PANI and rGO/PANI electrodes.

The XRD patterns of rGO, PANI and rGO/PANI composite thin films are shown in **Fig. 3.12**. Peaks from SS substrate are present and denoted by the symbol 'Δ'. It does not display any desired peaks of material, showing that PANI and rGO/PANI samples are amorphous **[40]**. The low concentration of rGO in rGO/PANI composite electrodes is probably reason of the lack of a rGO peak in the XRD analysis. Another possible reason for the absence of rGO peak might be in rGO/PANI composite is due to minimum number of rGO sheets layered with PANI **[41]**. The XRD pattern of rGO powder confirm rGO formation. According to JCPDS-Card No.

41-1487, the (002) and (100) planes of graphite are represented by the primary diffraction peak at 23.3° and the secondary peak at 43.1°, respectively **[42]**. The distinct XRD pattern indicates the formation of rGO. However, Raman study confirmed the existence of rGO in rGO/PANI composite. The PANI achieved amorphous nature is more practical than crystalline because the deposition was performed at room temperature, only the lowest energy is available, which is required for particle arrangements in a particular direction. Due to this, ions may easily intercalate and deintercalate inside the bulk of the amorphous electrode and the electrode capacity to store electrochemical charge is increased **[29]**.

3.4A.2.2 FT-IR study:

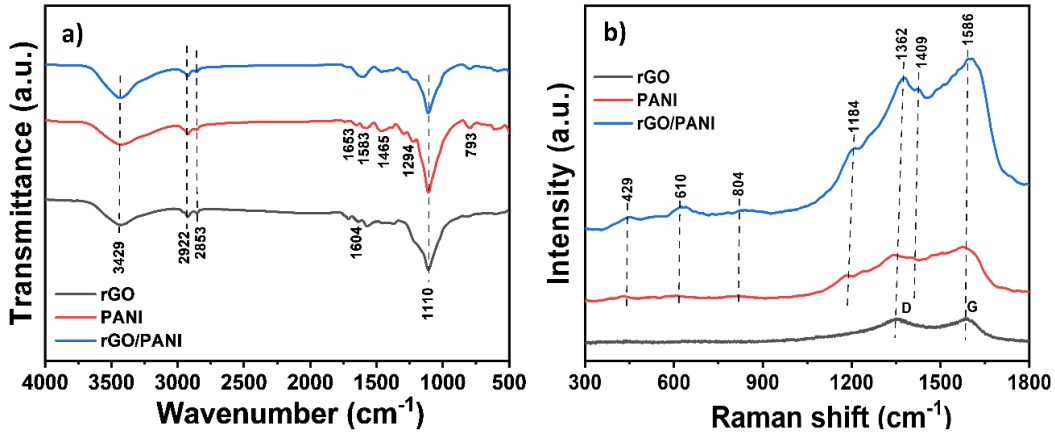

Fig. 3.13: a) The FT-IR spectra, and b) Raman spectra of rGO, PANI and rGO/PANI electrodes.

The FT-IR spectroscopy was used to determine the presence of bonding or functional groups in rGO, PANI and rGO/PANI thin films, and the resulting spectra are shown in **Fig. 3.13a**. The bands at 3429 cm^{-1} are related to water -OH bending vibrations **[43]**. In rGO spectrum, the stretching vibrations of CH_2 are responsible for the two minor peaks at 2922 and 2853 cm^{-1} **[44]**. The bands around 1604 and 1110 cm^{-1} are attributed to sp^2 vibration plane of C=C bond and stretching vibrations of rGO phenolic (C-O) group, respectively **[45]**. In PANI spectrum, the peaks of absorption at 2922 and 2853 cm^{-1} are produced by the N-H characteristics bond in an aromatic ring connected to amines of PANI. A series characteristic peaks of deformation of the aromatic quinoid ring at 1653 cm^{-1} **[32]**, stretching of a quinoid ring at 1583 cm^{-1}, while a benzenoid ring is stretched at 1465 cm^{-1} and stretching vibration of C-N at 1294 cm^{-1} **[46]**. The absorbance peaks of PANI at 1110 and 793

cm^{-1} correspond to C-H and N=Q=N stretching vibration mode, respectively **[47]**. The distinctive peaks of bare PANI as well as rGO peaks appear in the spectrum of rGO/PANI composite. The synthesis of PANI and a composite film of rGO/PANI is confirmed by FT-IR study.

3.4A.2.3 Raman study:

Raman spectroscopy was utilized to explore the chemical bonding properties of the bare and composite thin films. The Raman spectra of rGO, PANI and rGO/PANI, as seen in **Fig. 3.13b**, exhibit distinctive Raman peaks. The rGO Raman spectrum shows two large peaks at 1362 and 1586 cm^{-1} which correspond to D and G band of rGO, respectively. The G band indicates the in-plane mobility of carbon atoms, which is highly susceptible to strain and doping effects. The D-band depicts defects and flaws in carbon plane caused by the development of grain boundaries **[48]**. For bare PANI, the peak at 429 cm^{-1} is ascribed to the out-of-plane C-N-C deformation mode. A prominent peaks at 610 and 804 cm^{-1} indicate quinonoid ring C-H deformation and quinonoid ring C-H bending, respectively **[49]**. The peaks at 1184, 1362, 1409, and 1586 cm^{-1} are attributed to the C-H bending deformation, protonated C-N, C-C and C=C stretching, respectively **[50]**. The spectrum of rGO/PANI composites exhibit the typical peaks of bare PANI and two rGO peaks, which shows the existence of rGO and the formation of a composite thin film. The I_D/I_G ratio, determines the proportional number of disordered regions in the graphene structure, which is 0.92 for rGO/PANI thin film. This indicates the formation of certain rGO layers between PANI layers.

3.4A.2.4 XPS study:

Furthermore, XPS was utilized to study the material oxidation states and surface elemental composition. For rGO/PANI film, the survey spectrum in **Fig. 3.14a** shows that C1s and O1s could be distinguished with clarity, confirming the existence of rGO, while the existence of PANI is indicated by a prominent N1s signal in the latter sample. According to **Fig. 3.14b**, XPS spectrum of C1s from rGO shows four components that are ascribed to C-C (284.7 eV), C-N (285.6 eV), C-OH (286 eV), and C-O-C (288.8 eV) bonds **[51]**. The high resolution N1s spectrum of the composite can be divided into three distinct components **(Fig. 3.14c)**. Peaks are with binding energies of 398.9 eV for the imine (-N=) and 399.4 eV for the amine (-NH-) groups;

however, the peak at 400.2 eV is due to the positively charged nitrogen groups (N^+) of oxidized amine group **[52]**. As shown in **Fig. 3.14d**, the sample surface contains a very high atomic percentage of oxygen, which is ascribed to different oxidation states based on variations in the shape and position of the O1s peak. Three Gaussian peaks are observed in de-convoluted O1s signal. The creation of an O-C bond is indicated by the lattice oxygen peak with a 531 eV binding energy, while two further peaks with binding energies of 530 and 532.9 eVs are ascribed to non-lattice oxygen from the carboxyl and hydroxyl groups, respectively **[53]**.

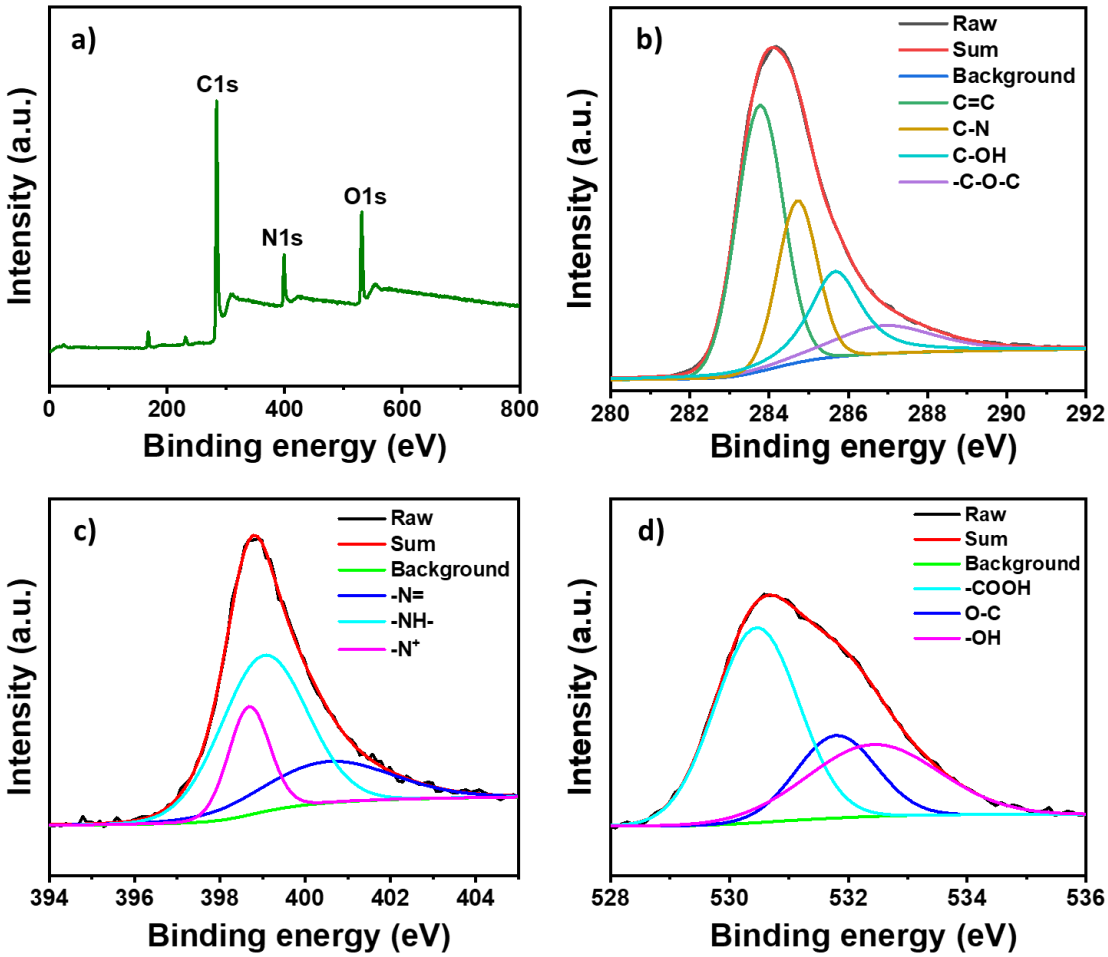

Fig. 3.14: a) Full XPS survey, and fitted spectra of b) C1s, c) N1s, and d) O1s for rGO/PANI electrode.

3.4A.2.5 FE-SEM study:

The surface morphologies of rGO, PANI and rGO/PANI thin films were studied using a FE-SEM at two magnifications (5 KX and 10 KX) **(Fig. 3.15)**. The sheet-like structure of rGO **(Fig. 3.15a and b)** shows a few sheets of graphene stacked

on over one another. Sheets can be observed as overlapping, wrinkled, crumpled, and shrinking at the edges, which might be due to the oxygen groups being lost in the process of reduction **[48]**. The PANI structure, which is composed of up of a hierarchically interwoven structure consisting a network of spikes, is seen in **Fig. 3.15c and d**. Because of its spikes-like shape, a sizable specific surface area offers high C_s and lower the electrolyte diffusion resistance of electrode materials, which makes it suitable for supercapacitor applications **[35]**. Additionally, in rGO/PANI composite, the presence of acidic aqueous media promotes the development of a uniform, homogeneous composite that intercalates rGO sheets with PANI spikes **(Fig. 3.15e and f)**. Due to the presence of functional groups such as -COOH, -OH, and -CHO, rGO in turn provides the nucleation sites that allows formation of polymeric chains of PANI. Here, PANI spikes might act as spacers to prevent rGO sheets from restacking, producing a porous electrode with uniformly distributed material **[54]**.

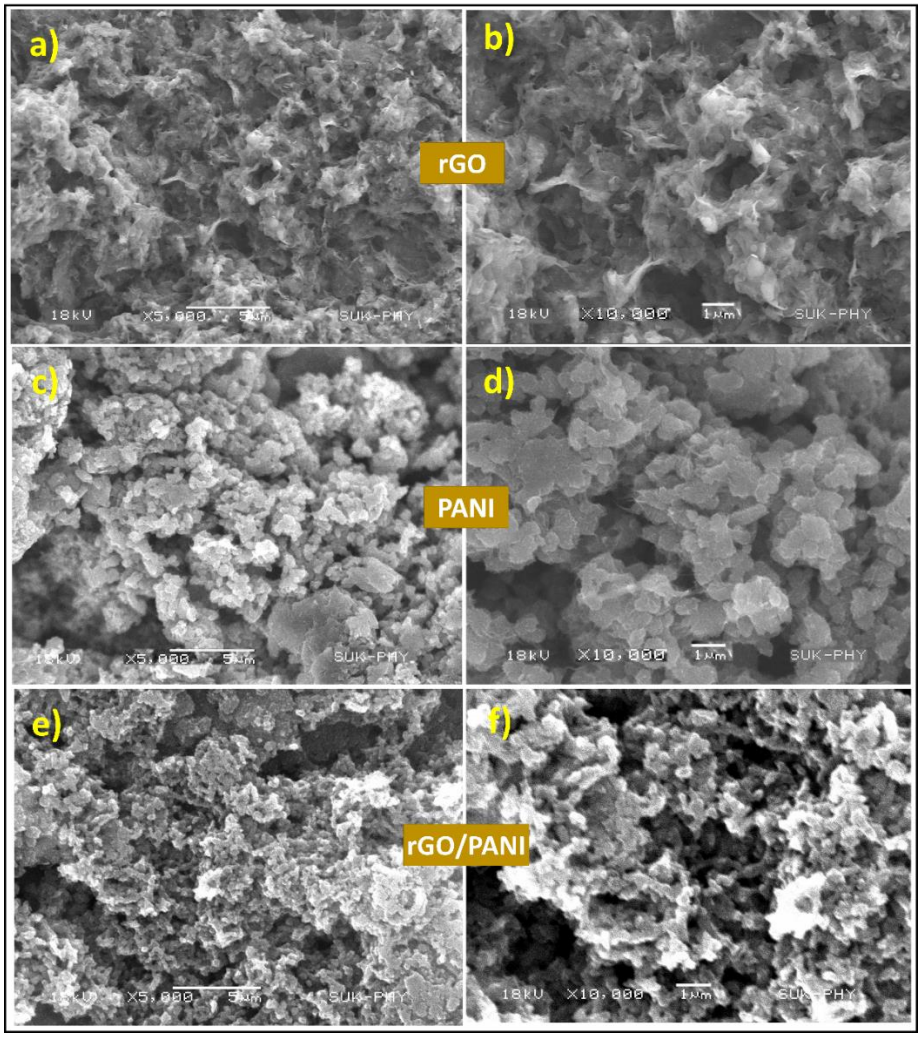

Fig. 3.15: The FE-SEM images of a, b) rGO, c, d) PANI and e, f) rGO/PANI electrodes at magnifications of 5 KX and 10 KX.

3.4A.2.6 BET and BJH studies:

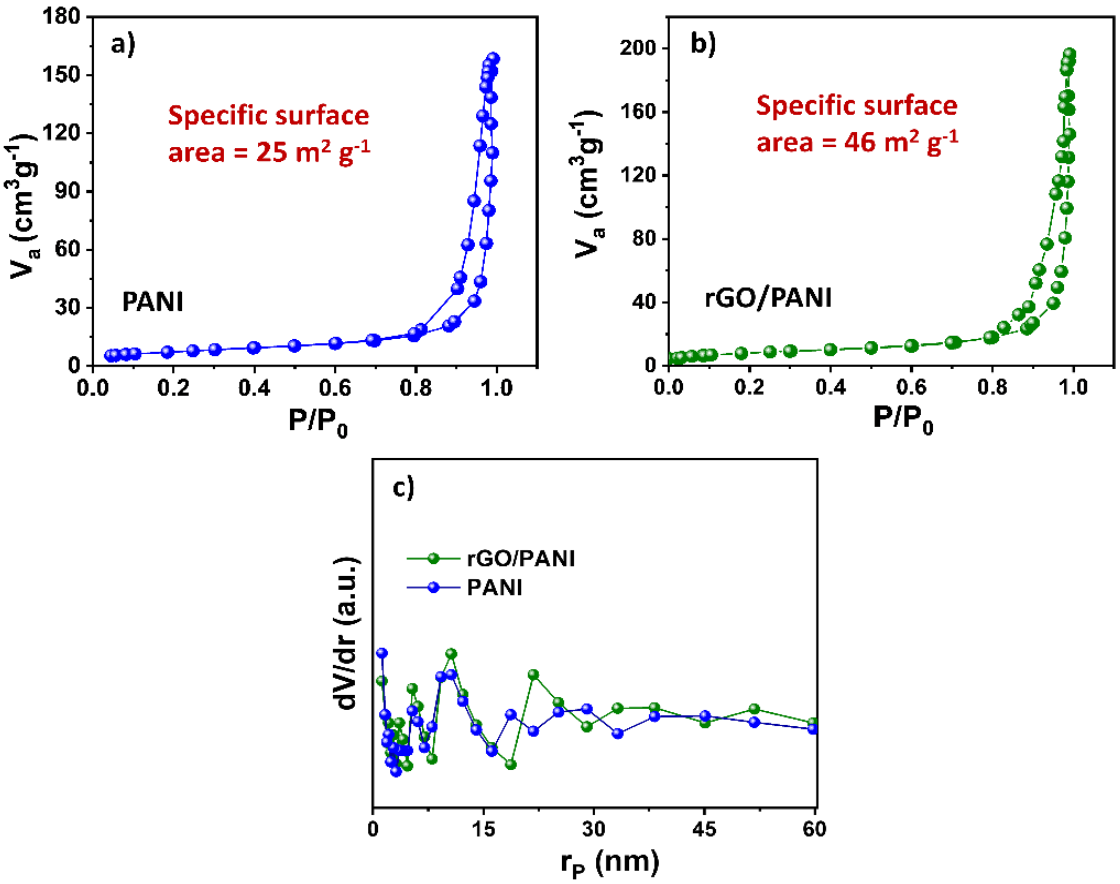

Fig. 3.16: The N_2 adsorption-desorption isotherms of a) PANI, b) rGO/PANI, and c) pore size distribution curves of PANI and rGO/PANI samples.

Measurements of the N_2 adsorption-desorption isotherms are utilized to analyse the porosity and specific surface area of PANI and rGO/PANI composite materials. As seen in **Fig. 3.16a and b**, it displays a type- IV isotherms, according to the IUPAC classification, which provides details regarding the mesoporous structure (2-50 nm). The specific surface areas of PANI and rGO/PANI are 25 and 46 $m^2\ g^{-1}$, respectively. These results indicate that adding rGO nanosheets into PANI material efficiently enhances surface area **[41]**. The distribution of pore sizes of PANI and rGO/PANI composite is determined using the BJH technique. As shown in **Fig. 3.16c** the average radius of the pores are 19 nm (PANI) and 20.9 nm (rGO/PANI) indicating the formation of mesoporous materials. The increased surface area with mesoporous structure can provide hierarchical pathways for the electrolyte to penetrate and allow for facile ion transport in the deep pore of particles **[55]**.

3.4A.2.7 Contact angle study:

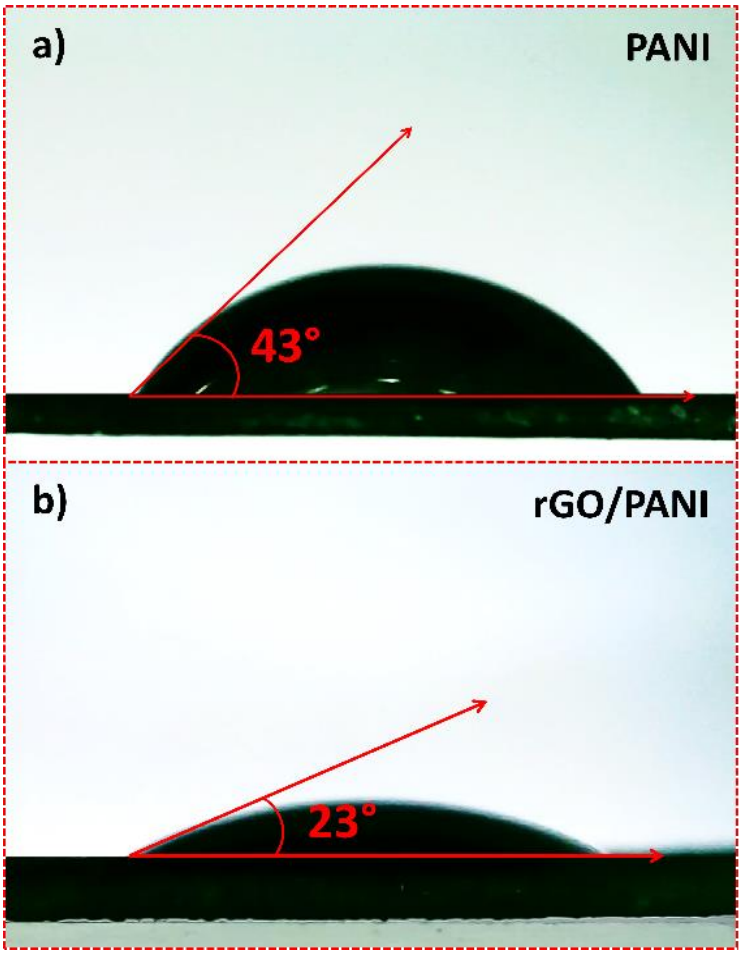

Fig. 3.17: The contact angle images of a) PANI, and b) rGO/PANI electrodes.

Wettability is one of the most vital aspects of an electrode surface in supercapacitor application which determines its supercapacitive behaviour. Surface wetness is determined by the morphology and chemical composition of the electrode surface. **Fig. 3.17a and b** show pictures of the contact angles between the surface of PANI and rGO/PANI films and 1 M H_2SO_4 electrolyte. The contact angles are measured to be 43° for PANI and 23° for rGO/PANI films. The porous nature of rGO/PANI electrode increases its ability to interact with the electrolyte by providing a huge number of active redox sites. This indicates that liquid enters a dispersed PANI spikes network on rGO sheets that is porous, reducing the contact angle resulting in a hydrophilic surface.

3.4B. Electrochemical characterizations:

3.4B.1 Electrochemical characterizations of PANI thin films:

3.4B.1.1 The CV study:

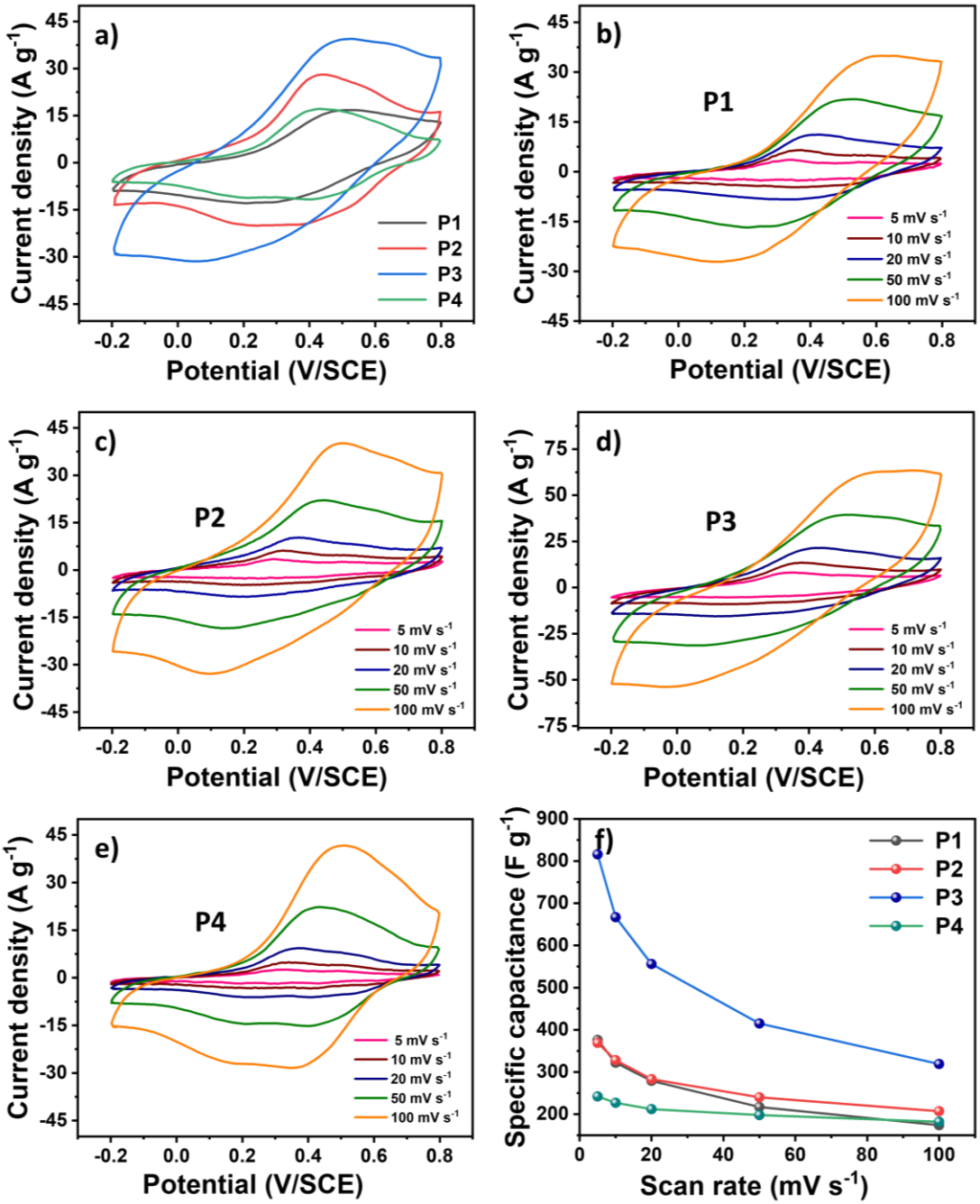

Fig. 3.18: a) Comparative CV curves of PANI electrodes at a scan rate of 50 mV s^{-1}, the CV curves at different scan rates of b) P1, c) P2, d) P3, and e) P4 electrodes, and f) the variation of the specific capacitance with various scan rate of all PANI electrodes.

The electrochemical measurement of P1 to P4 electrodes was studied in a standard three-electrode cell system in 1 M H_2SO_4 electrolyte. The CV curves for all samples in the potential range of -0.2 to + 0.8 V/SCE are shown in **Fig. 3.18a**.

Compared to others, P3 electrode has a greater current response and encloses maximum area by the CV curve than P1, P2, and P4 electrodes, indicating that P3 film expedites electronic and ionic transports. **Fig. 3.18b-e** provides the CV curves for P1, P2, P3, and P4 electrodes. It is seen that peak current and area under CV curves quickly increase with increased scan rates from 5 to 100 mV s^{-1}. The lower scan rate resulted in more charge storage than the higher one because the SO_2^{-4} ions from H_2SO_4 solution have more time to interact with the electrode material. The PANI is a pseudocapacitive material; hence, the all CV curves are nonrectangular in shape, indicating a faradic charge storage process. The C_s values for P1 to P4 electrodes calculated using **Equation 2.12** are 369, 376, 816, and 242 F g^{-1}, respectively at a scan rate of 5 mV s^{-1}. With 25 m^2 g^{-1} specific surface area and 38 nm average pore size, P3 electrode shows the highest specific surface area, and average pore size than those of P1, P2, and P4 electrodes. Increased temperature causes an increase in the reaction kinetics, which allows more particles to aggregate on the film surface, this causes barriers in particular regions of the porous structure of PANI thin film. This results in a reduction in the specific surface area and average pore size of P4 as compared to P3. Therefore, P3 increased C_s may be due to its increased surface area. Moreover, the increased effective surface area and improved C_s have been attributed to the wettability of the electrolyte on the electrode surface. Despite having similar morphologies, PANI films exhibit different mesoporous structures.

As a result, even if the morphologies remain similar, the contact angles vary. According to the FE-SEM images, surface roughness rises continuously from P1 to P3 and hence the contact angle reduces, but it increases again in P4 because of overoxidation of PANI. The aqueous electrolyte can effectively make contact with hydrophilic materials, resulting in lower charge transfer resistance and higher C_s of supercapacitors. The C_s typically increase as the electrode thickness increases up to a certain point due to the increase in ion accessible surface area and the rise in ion transport route and thereafter fall down. The C_s variation with scan rate for all electrodes are displayed in **Fig. 3.18f**. The decreasing C_s trend with rising scan rate suggests that there is not enough time to perform reversible redox reactions on all electrolyte ions at larger scan rate, and the inner surface of the electrode material is inaccessible.

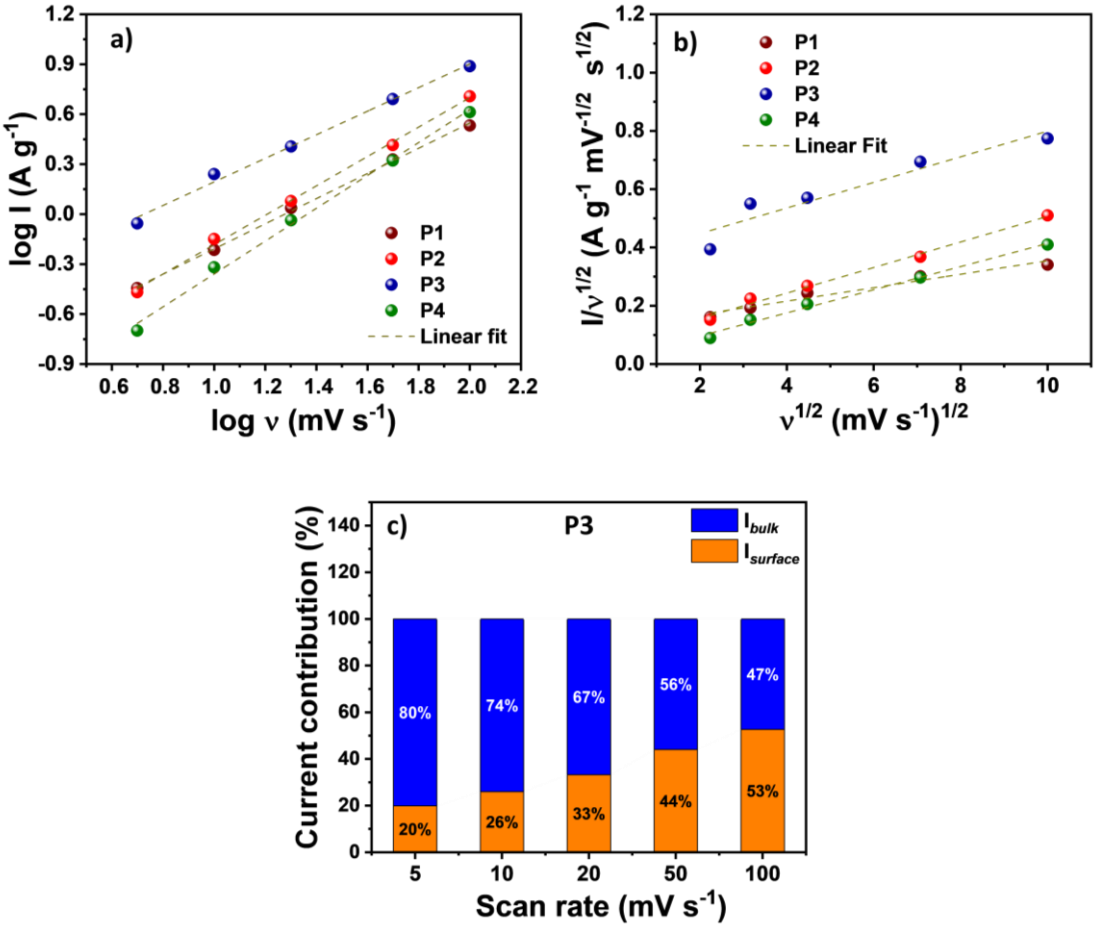

Fig. 3.19: a) Plots of log I vs. log υ, b) plots of $I/\nu^{1/2}$ vs. $\nu^{1/2}$ for PANI electrodes, and c) contribution of capacitive and diffusion-controlled currents with scan rates for P3 electrode.

Analysis of the charge storage mechanism for P3 electrode is carried out using the power law **[56]**,

$$I_p = a\nu^b \qquad (3.2)$$

where 'Ip' represents the peak current in ampere (A), 'ν' stands for scan rate in V s^{-1}, and 'a' and 'b' are variable parameters. In **Fig. 3.19a**, slope of log I vs log ν graph is used to calculate 'b'. There are two types of charge storage kinetics; one is diffusion-controlled, while the other is capacitive **[57]**. If the electrode material shows diffusion-controlled charge storage kinetics, the value of b ≅ 0.5, and for capacitive type charge storage kinetics, b ≅ 1. The b value for P3 electrode is 0.70, indicating that the charge storage kinetics involves both diffusion and capacitive processes. In addition, the exact contribution of charge storage kinetics is carried out using the following equation **[58]**,

$$I(\nu) = k_1\nu + k_2\nu^{0.5} = I_{surface} + I_{bulk} \quad (3.3)$$

where, $I_{surface}$ and I_{bulk} are capacitive and diffusion-controlled mechanism parameters, respectively. The estimated slopes and linear fit intercepts from **Fig. 3.19b** used for calculation of values of $I_{surface}$ and I_{bulk}, respectively. The percentage of P3 electrode charge that derives from both processes is shown in **Fig. 3.19c**. The current from the diffusion-controlled mechanism rises as the scan rate decreases, and the resulting C_s value increases. The capacitive process retains over 53% of the charge in P3 electrode at a scan rate of 100 mV s^{-1}, whereas this proportion declines to around 20% at a scan rate of 5 mV s^{-1}. The layered structure facilitates easy penetration of the electrolyte, which significantly contributes to the diffusion-controlled process **[59]**.

3.4B.1.2 The GCD study:

The comparative GCD plots of P1 to P4 electrodes at a 1 A g^{-1} applied current density are shown in **Fig. 3.20a**. In comparison to the other electrodes, P3 electrode has the greatest discharge time, indicating good electrochemical performance due to the largest specific surface area (25 m^2 g^{-1}) than other electrodes. The specific surface area of P4 is a little smaller (21 m^2 g^{-1}) than that of P3 due to the greater ratio of the mesopores in P4. At higher bath temperature increases over oxidation of PANI which reduces its electrochemical activity in sulfuric acid solution affecting its reversibility during charge and discharge cycles, and damaging its conjugated structure **[60]**. Due to this, P4 electrode has low C_s.

The GCD plots for all PANI electrodes at different current densities from 1 to 3 A g^{-1} in the potential range from -0.2 to + 0.8 V/SCE are depicted in **Fig. 3.20b-e**. The quasi-triangular charge-discharge curves indicate a faradic transformation, confirming the pseudocapacitive nature of PANI material. The C_s values of electrodes P1, P2, P3, and P4 are 247, 269, 723, and 211 F g^{-1}, respectively at 1 A g^{-1} current density. **Fig. 3.20f** displays the curve of C_s vs current density for PANI electrodes. The C_s decreased as the current density increased due to ion diffusion limitations during fast charging-discharging.

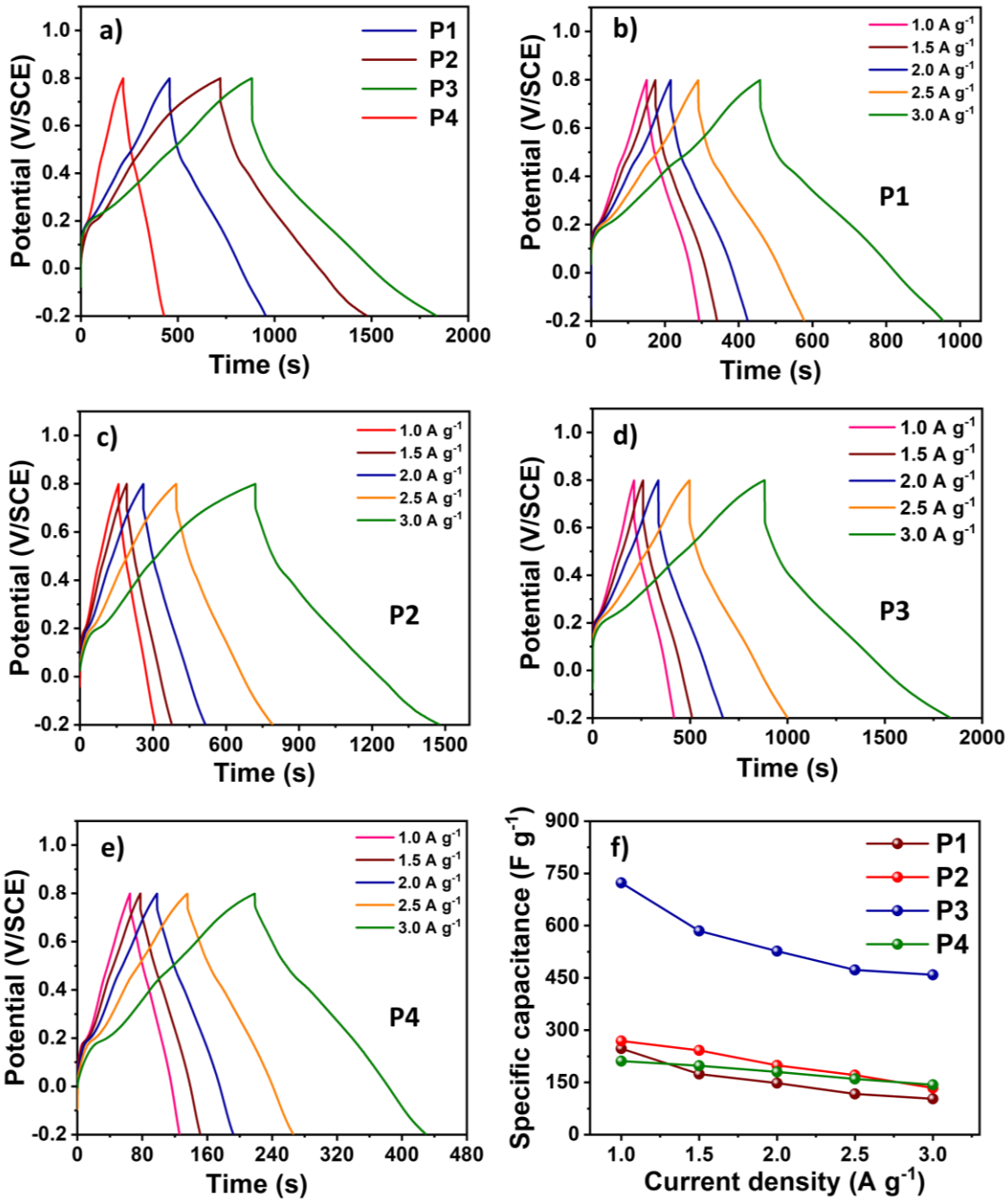

Fig. 3.20: a) The GCD plots of different PANI electrodes at a current density of 1 A g^{-1}, the GCD plots at different current densities of b) P1, c) P2, d) P3, and e) P4 electrodes, and f) the variation of the specific capacitance with different current density of all PANI electrodes.

3.4B.1.3 The EIS study:

The electrochemical impedance characteristic was evaluated using the EIS study of PANI electrodes and Nyquist plots are displayed in **Fig. 3.21a**. The role of charge transfer in energy storage is evaluated using EIS measurements. The equivalent circuit

utilized to match the EIS data by an electrolyte resistance (R_s), charge transfer resistance (R_{ct}), Warburg impedance (W), and constant phase element (Q) is illustrated in the inset of **Fig. 3.21a.** The enlarged view of the plots is provided in **Fig. 3.21b**. At the electrode/electrolyte interface, double-layer capacitance and the faradic reaction create R_{ct}, represented in EIS plots with a half circle on the Z' axis in the high frequency zone. The Q is produced due to electrode/electrolyte interface inhomogeneity caused by surface texture, porosity, and disorder with diffusion **[61]**. **Table 3.1** summarises the electrochemical impedance properties of PANI thin film electrodes.

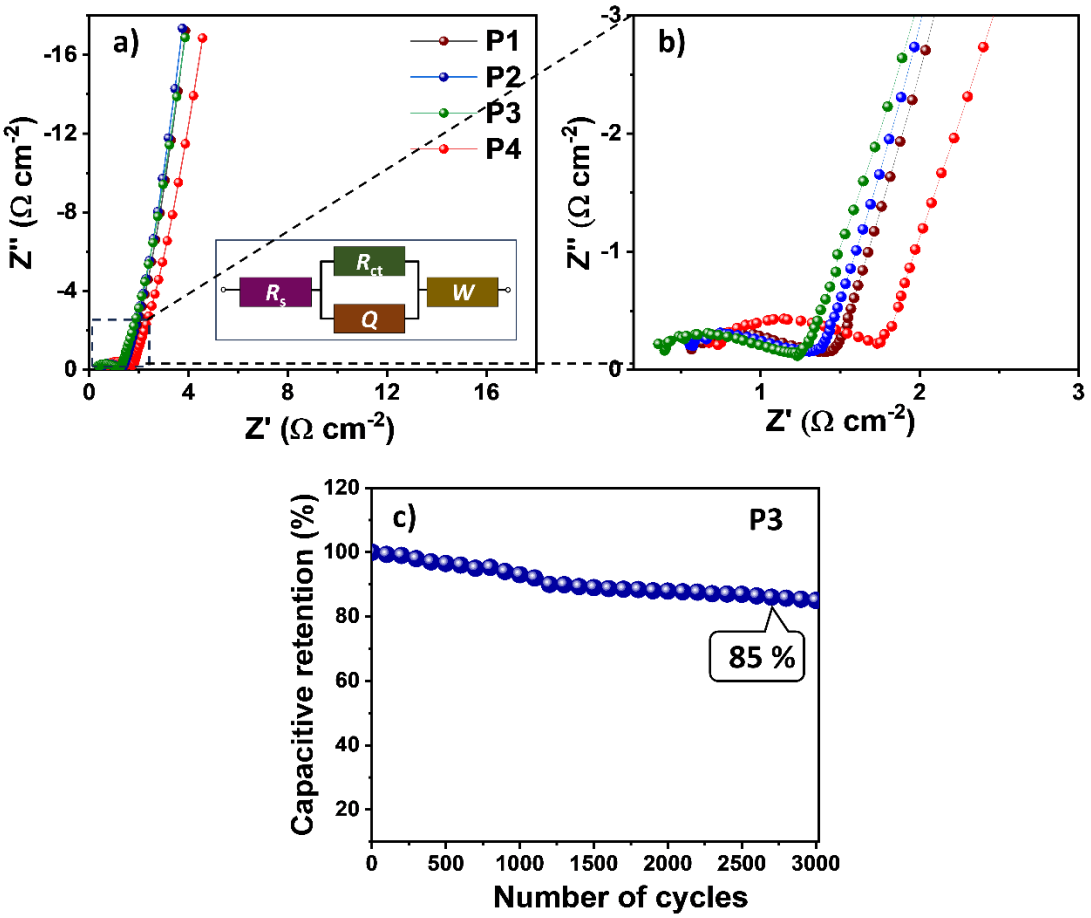

Fig. 3.21: a) The Nyquist plots of different PANI electrodes (the inset shows equivalent circuit), b) enlarged view of Nyquist plots, and c) the stability of P3 electrode over 3,000 cycles.

The P1, P2, P3, and P4 electrodes exhibit values of R_s = 0.5, 0.5, 0.2, and 0.6 Ω cm^{-2}, respectively. It is noticed that when specific surface area improves, R_s falls due to a boost in the mean free path of the electron, but R_s rises for P4 electrodes due to larger average pore size and lower specific surface area. The R_{ct} for P1, P2, P3, and

P4 electrodes is found to be 0.89, 0.88, 0.80, and 1.3 Ω cm^{-2}, respectively. The variance in the R_{ct} is significantly influenced by the electrode surface average pore size, indicating that P3 electrode pores, which have an average size of 38 nm, make it easier to make excellent contact with the electrolyte. So, the R_{ct} decreases **[62]**.

Table 3.1: The values of equivalent circuit components for PANI electrodes.

Electrodes	R_s (Ω cm^{-2})	R_{ct} (Ω cm^{-2})	Q (F)	W (mΩ cm^{-2})
P1	0.5	0.89	0.74	0.250
P2	0.5	0.88	0.71	0.122
P3	0.2	0.80	0.9	0.11
P4	0.6	1.3	0.68	0.12

3.4B.1.4 The stability study:

One of the most significant aspects of supercapacitor application is the cyclic stability of the electrode material. Using the GCD technique, the electrochemical cycling stability of P3 electrode was assessed. The cycling stability of P3 electrode is shown in **Fig. 3.21c**. The electrode shows 85% capacitance retention after 3,000 GCD cycles performed at current density of 3 A g^{-1}. The synthesis method is suitable for binder-free material deposition, as evidenced by the maximum electrochemical properties and moderate stability observed for P3 electrode.

3.4B.2 Electrochemical characterizations of rGO thin films:

The electrochemical analysis of rGO thin film was performed in 1 M H_2SO_4 electrolyte at potential ranging from -0.2 to +0.8 V/SCE. The CV curves at scan rates of 5-100 mV s^{-1} displayed in **Fig. 3.22a**, illustrates the double-layer capacitance characteristic of rGO. The GCD measurement at current densities ranging from 1 to 5 A g^{-1} is shown in **Fig. 3.22b**. This behaviour of rGO is indicated by the symmetrical shape of the GCD plots. The rGO electrode shows C_s of 277 F g^{-1} a scan rate of 5 mV s^{-1} and 254 F g^{-1} a current density of 1 A g^{-1}. The Nyquist plot of rGO electrode in the frequency range between 0.01 Hz and 100 kHz is shown in **Fig. 3.22c**, and the simulated equivalent electrical circuit is provided in the inset. The high frequency intercept with the X-axis of the Nyquist plot the R_s (0.21 Ω cm^{-2}). The R_{ct} for rGO was 15.2 Ω cm^{-2}. The straight line behaviour in the lower frequency range is attributed to ion diffusion in the electrolyte as the W. The electrochemical cycling

stability of rGO electrode is further studied for 5,000 GCD cycles and corresponding capacitive retention is plotted in **Fig. 3.22d**. After 5,000 cycles, rGO exhibited good capacitive retention of 96%.

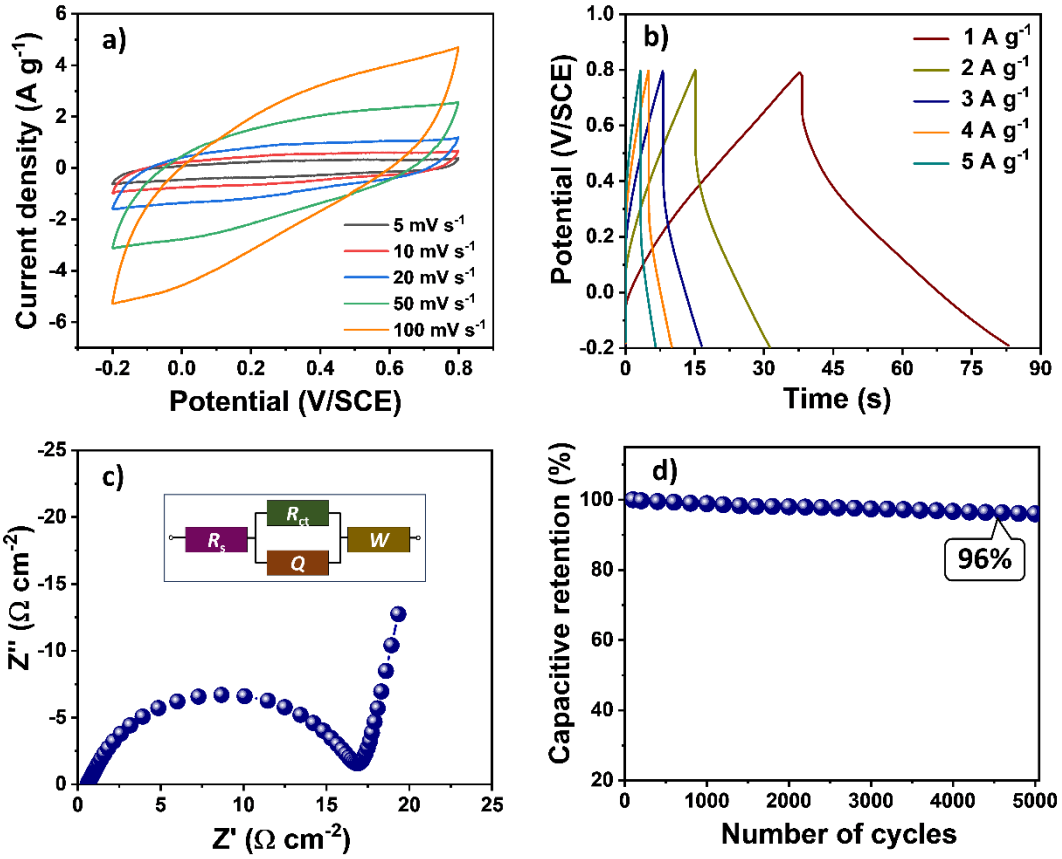

Fig. 3.22: a) The CV curves at different scan rates, b) GCD plots at different current densities, c) Nyquist plot (inset shows an equivalent circuit), and d) the stability over 5,000 cycles of rGO electrode.

3.4B.3 Electrochemical characterizations of rGO/PANI thin films:

3.4B.3.1 CV study:

The supercapacitive analysis of a rGO/PANI films was conducted in 1M H_2SO_4 electrolyte. The CV curves of PANI and rGO/PANI for various scan rates in the operating potential between -0.2 to +0.8 V/SCE are displayed in **Fig. 3.23a and b**. According to the CV curves, at low scan rates, the larger integral area promotes the interaction between electrolytic ions and active species since it gives them more time to interact and increase the number of redox reactions. However, when scan rate rises, there is a low interaction or accumulation of $(SO_4)^{2-}$, H^+, and $(HSO_4)^-$ ions with electrode because of their relatively short residence times, which limits the variety of

interactions between active species and ions at the electrode/electrolyte contact. Adding rGO to PANI matrix improves current responses and enhances redox peaks, resulting in raised area under the CV curves, indicating that rGO/PANI composite offer greater charge storage capabilities **[63]**. **Equation 2.12** is used to compute the electrode C_s values from the CV at various scan rate. For bare PANI and rGO/PANI electrodes, the maximum C_s values are 816 and 1130 F g^{-1} at 5 mV s^{-1}, respectively.

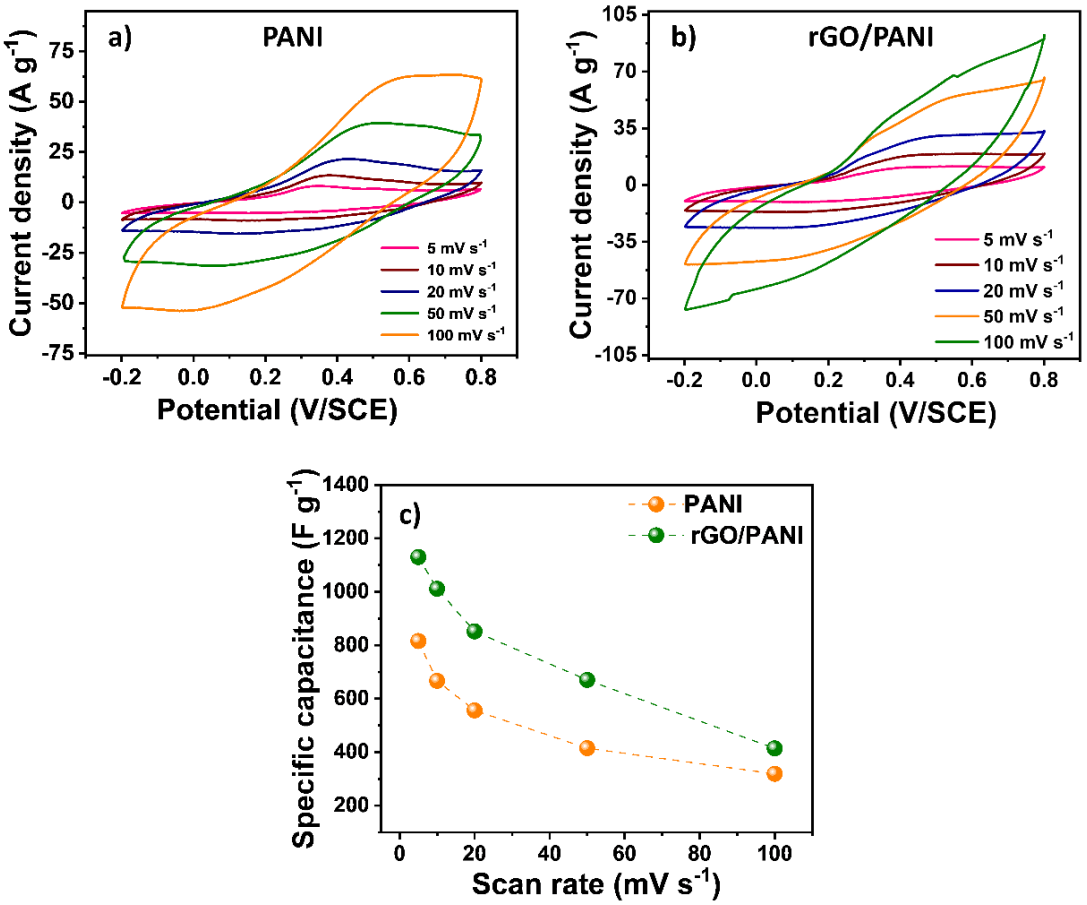

Fig. 3.23: a) The CV curves of a) PANI, b) rGO/PANI, and c) the variation of the specific capacitance with various scan rate of PANI and rGO/PANI electrodes.

The C_s variations for PANI and rGO/PANI electrodes materials with respect to scan rate was displayed together in **Fig. 3.23c**. Because of π-π interactions between sheets of rGO and PANI chain, high C_s was achieved in the composites, indicating bonding between PANI spikes and rGO layers enhances supercapacitive performance.

The properties of the electrode material are also evaluated using the current value that is obtained from the CV curves. The response of the log I vs log ν is seen in **Fig. 3.24a**. The CV responses are analysed using a power law **(Equation 3.2)** and

provide information about the kinetics of reaction at the electrode surface. According to the slope of log I vs log ν derived from the fitted linear curve, the 'b' value is calculated. For PANI and rGO/PANI calculated 'b' values are 0.70 and 0.61, respectively. Total charge storage is facilitated by diffusion-controlled and capacitive charge storage mechanisms. These two charge storage mechanisms are differentiated using the **Equation 3.3**.

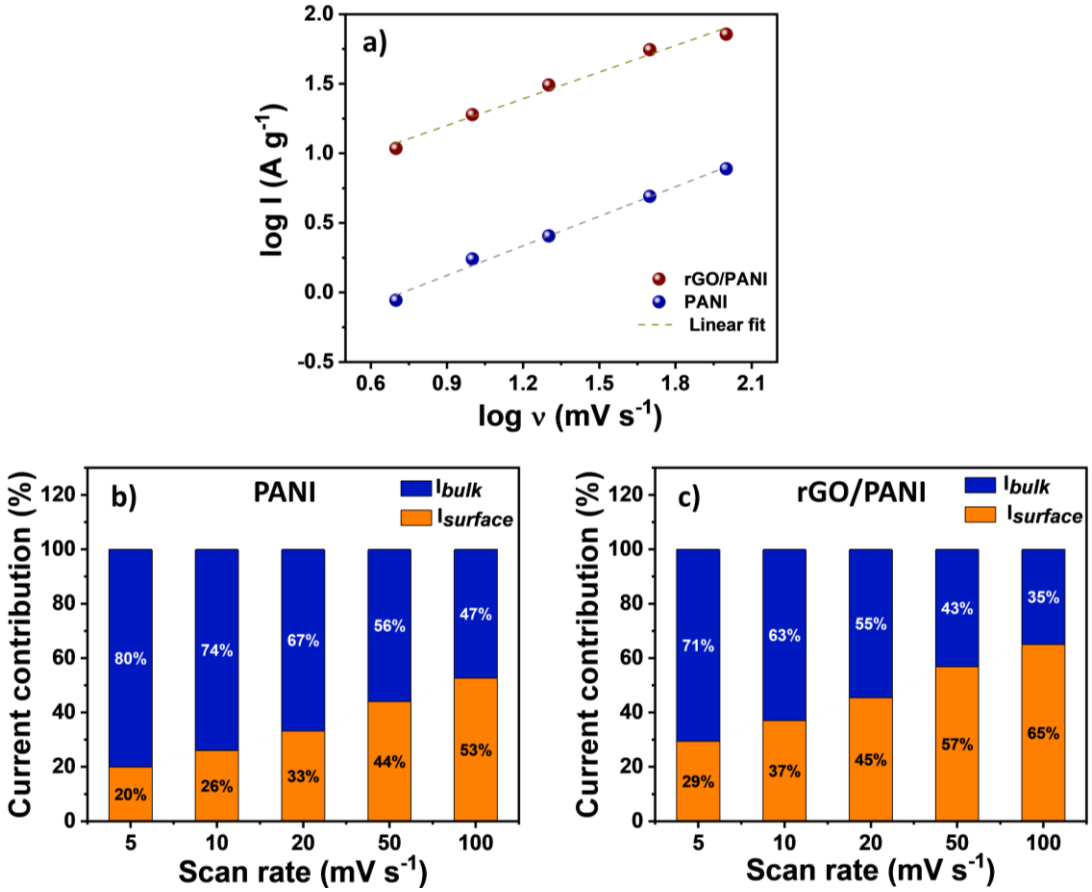

Fig. 3.24: a) Plots of log I vs log ν, percentage current contribution of capacitive and diffusion mechanisms for b) PANI, and c) rGO/PANI electrodes.

Fig. 3.24b and c show charge contribution graphs of PANI and rGO/PANI at various scan rate. As the scan rate drops, the current from the diffusion-controlled mechanism rises, leading to an increase in the C_s value. At a scan rate of 5 mV s^{-1}, PANI electrode exhibits a greater charge storage through diffusion process, accounting for approximately 80% of the total current. In contrast, for rGO/PANI composite electrode, the current resulting from the diffusion process is about 71% at a scan rate of 5 mV s^{-1}. The drop in diffusion-controlled charge storage with composition is due to the EDLC characteristic of rGO **[59]**.

3.4B.3.2 GCD study:

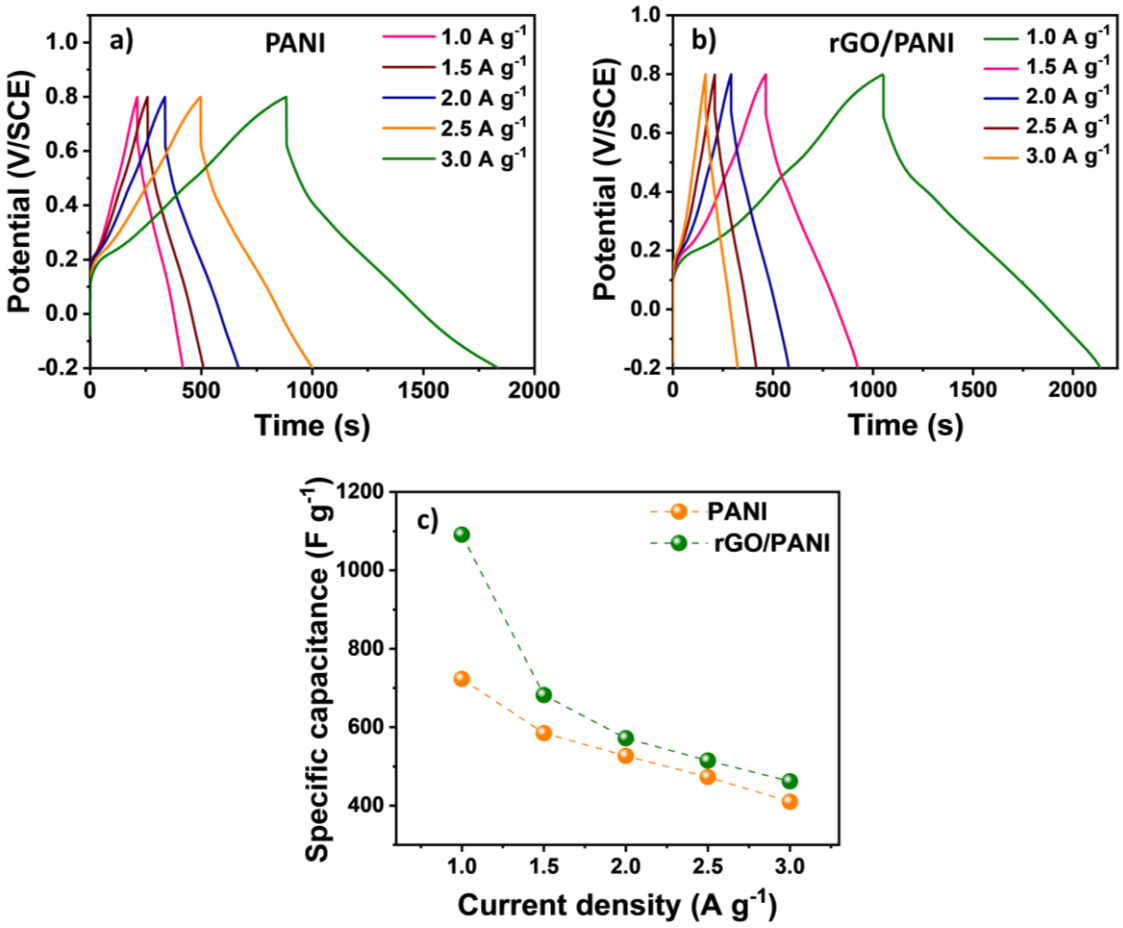

Fig. 3.25: The GCD plots of a) PANI, b) rGO/ PANI electrodes at different current densities, and c) the variation of the specific capacitance with different current densities of PANI and rGO/PANI electrodes.

The GCD plots of PANI and rGO/PANI composite are displayed in **Fig. 3.25a and b** at a current density ranging from 1 to 3 A g^{-1}. The rGO/PANI composite exhibits the charge-discharge characteristics of both PANI and rGO, as well as a longer discharge time, which suggests that the composite has a higher C_s. The calculated C_s using **Equation 2.13** are 723 and 1091 F g^{-1} at 1 A g^{-1} current density for PANI and rGO/PANI composite electrodes, respectively. The C_s variation with different current density of PANI and rGO/PANI electrodes is depicted in **Fig.3.25c**. The spikes of PANI cross link with one other to produce a framework equally dispersed on rGO surface, allowing electrolyte to penetrate the interior surface and fully utilize the active material **[64]**.

3.4B.3.3 EIS study:

At the interface, the charge transport characteristics of the electrode materials are evaluated utilizing the EIS method. The high frequency portion of the Nyquist plots in **Fig.3.26a** formed a semicircle, and virtually straight line at low frequency portion. The inset of **Fig.3.26a** show the enlarged view of plots at high frequency regions and electrical equivalent circuit made up of R_s, R_{ct}, W and Q. It revealed that in comparison to PANI electrode (0.2 and 0.80 Ω cm^{-2}), rGO/PANI composite electrode showed lower R_s and R_{ct} values of 0.13 and 0.41 Ω cm^{-2}, respectively. These low R_s and R_{ct} values demonstrate the better electrical conductivity and ion diffusion of rGO/PANI composite, which results in excellent results as an electrode material for supercapacitors.

3.4B.3.4 Stability study:

The cyclic stability of PANI and rGO/PANI electrodes was studied at current density of 3 A g^{-1} for 3,000 GCD cycles **(Fig. 3.26b)**. The capacitive retention is 85 and 92% for PANI and rGO/PANI, respectively. More retention is seen in rGO/PANI composite electrode as compared to PANI. The rGO/PANI thin film electrode exhibited better cycling stability than PANI thin film electrode due to rGO incorporation, which helped in fast electron transfer in rGO/PANI composite **[65]**.

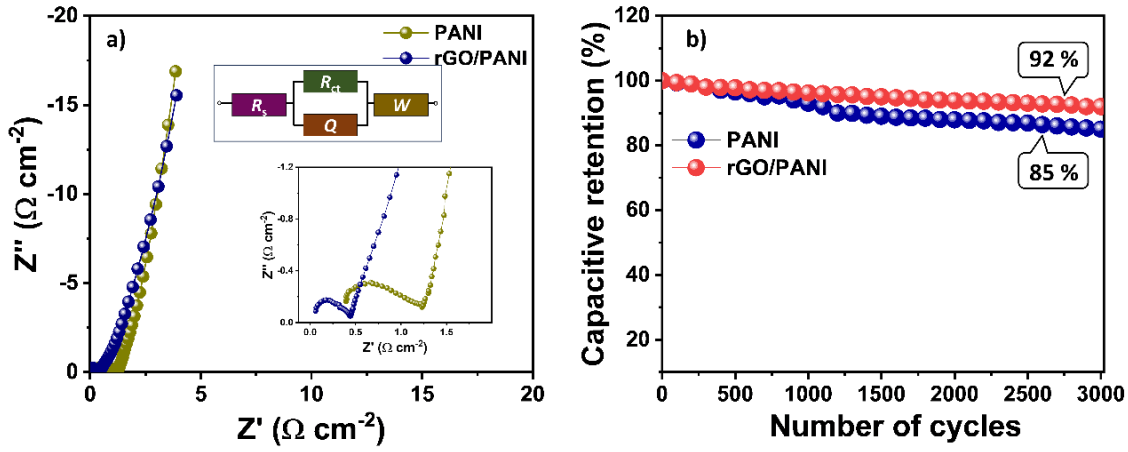

Fig. 3.26: a) Nyquist plots (inset show an enlarged view of plots and equivalent circuit), and b) specific capacitance retention over 3,000 GCD cycles of PANI and rGO/PANI electrodes.

3.5 Conclusions:

In conclusion, PANI and rGO/PANI composite electrodes were deposited on SS substrate using CBD method. The composite film shows PANI spikes anchoring on rGO sheets. The specific surface area of PANI increased from 25 to 46 $m^2\ g^{-1}$ after the addition of rGO. In comparison to PANI thin film, rGO/PANI composite electrode enhanced electrochemical performance, achieving a highest C_s of 1130 F g^{-1} at a 5 mV s^{-1} scan rate in 1 M H_2SO_4 electrolyte. With the addition of rGO, the value of R_s decreased for rGO/PANI electrode (0.13 Ω cm^{-2}) as compared to pure PANI (0.2 Ω cm^{-2}). The rGO/PANI film electrode exhibited higher electrochemical cycling stability (92%) in comparison to PANI film electrode (85%). As a result, rGO/PANI composite electrode is an intriguing material for supercapacitor applications.

References:

[1] P. Deshmukh, R. Bulakhe, S. Pusawale, S. Sartale, C. Lokhande, RSC Advances, 5, (2015), 28687-28695.

[2] B. Yan, L. Feng, J. Zheng, Q. Zhang, S. Jiang, C. Zhang, Y. Ding, J. Han, W. Chen, S. He, Inorg. Chem. Front., 9, (2022), 6108-6123.

[3] T. Brousse, D. Belanger, J. Long, J. Electrochem. Soc., 162, (2015), A5185-A5189.

[4] S. Palsaniya, H. Nemade, A. Dasmahapatra, Carbon, 150, (2019), 179-190.

[5] W. Gan, J. Sun, Z. Wu, C. Ma, W. Li, S. Liu, Energy Fuel, 35, (2021), 8295-8302.

[6] C. Wang, Y. Yang, R. Li, D. Wu, Y. Qin, Y. Kong, Chem. Commun., 56, (2020), 4003-4009.

[7] P. Bagwade, D. Malavekar, S. Ubale, R. Bulakhe, I. In, U. Patil, C. Lokhande, Electrochim. Acta, 408, (2022), 139933-139948.

[8] Z. Yang, J. Tian, Z. Yin, C. Cui, W. Qian, F. Wei, Carbon, 141, (2019), 467-480.

[9] H. Fan, N. Zhao, H. Wang, J. Xu, F. Pan, Mater. Chem. A, 2, (2014), 12340-12348.

[10] L. Ding, Z. Qin, Z. Dou, Y. Shen, Y. Cai, Y. Zhang, Y. Zhou, J. Mater. Sci., 53, (2018), 7595-7608.

[11] X. Wang, M. Xu, Y. Fu, S. Wang, T. Yang, K. Jiao, Electrochim. Acta, 222, (2016), 701-708.

[12] D. Patil, S. Pawar, S. Patil, P. Salavi, S. Kolekar, R. Devan, Y. Ma, J. Kim, J. Shin, P. Patil, J. Alloys Compd., 646, (2015), 1089-1095.

[13] P. Deshmukh, S. Patil, R. Bulakhe, S. Pusawale, J. Shim, C. Lokhande, RSC Advances, 5, (2015), 68939-68946.

[14] D. Patil, S. Pawar, S. Mali, C. Hong, J. Kim, P. Patil, J. Shin, J. Nanosci. Nanotechnol., 17, (2017), 4194-4199.

[15] C. Zhou, S. He, H. Yang, J. An, L. Yang, P. Yan, H. Zhang, Electrochim. Acta, 390, (2021), 138818-138829.

[16] Z. Liu, Z. Zhao, A. Xu, W. Li, Y. Qin, J. Alloys Compd., 875, (2021), 159931-159941.

[17] D. Malavekar, S. Kale, V. Lokhande, U. Patil, J. Kim, C. Lokhande, J. Phys. Chem. C, 124, (2020), 28395-28406.

[18] S. Kale, A. Lokhande, R. Pujari, C. Lokhande, J. Colloid Interface Sci., 532, (2018), 491-499.

[19] H. Shelke, A. Lokhande, A. Patil, J. Kim, C. Lokhande, Surf. Interfaces, 9, (2017), 238-244.

[20] O. Reyes, D. Maldonado, J. Escorcia-Garcia, P. Sebastian, J. Mater. Sci. Mater. Electron., 29, (2018), 15535-15545.

[21] D. Dhawale, A. Vinu, C. Lokhande, Electrochem. Acta, 56, (2011), 9482-9487.

[22] T. Lee, I. Kim, S. Roh, H. Jung, S. Lee, H. Kim, D. Yoon, Y. Hong, G. Lee, Anal. Chim. Acta, 1158, (2021), 338387-338396.

[23] B. Patil, S. Patil, C. Lokhande, Electroanalysis, 26, (2014), 2023-2032.

[24] T. Hongling, D. Yamei, Z. Congyun, G. Jingyu, S. Qian, K. Jinqing, Int. J. Electrochem. Sci., 9, (2014), 7239-7252.

[25] S. Kulkarni, U. Patil, I. Shackery, J. Sohn, S. Lee, B. Park, S. Jun, J. Mater. Chem. A, 2, (2014), 4989-4998.

[26] S. Kulkarni, S. Joshi, C. Lokhande, Chem. Eng. J., 166, (2011), 1179-1185.

[27] B. Singha and B. Dasa, J. Pure Appl. Phys., 58, (2020), 735-739.

[28] M. Fuseini, A. El Shazly, M. El-Kady, Mater. Sci. Forum, 108, (2020), 114-120.

[29] J. Pan, W. Zhong, Z. Gao, X. Yang, Y. Zhang, Y. Guan, X. Yan, N, Ceram. Int., 47, (2021), 27833-27842.

[30] Q. Li, Y. Xu, S. Zheng, X. Guo, H. Xue, H. Pang, Small, 14, (2018), 1800426-1800445.

[31] V. Mane, S. Kale, S. Ubale, V. Lokhande, C. Lokhande, Mater. Today Chem., 20, (2021), 100473-100488.

[32] S. Sawant, M. Waikar, A. Rasal, G. Chodankar, S. Dhas, A. Moholkar, M. Shirsat, S. Chakarvarti, R. Sonkawade, J. Mater. Sci. Mater. Electron, 32, (2021), 11865-11876.

[33] S. Yeasmin, S. Talukdar, D. Mahanta, Electrochim. Acta, 389, (2021), 138660-138669.

[34] X. Ni, Y. Jiang, H. Chen, K. Li, H. Chen, Q. Wu, A. Ju, Chin Chem Lett., 32, (2021), 2448-2452.

[35] K. Lin, L. Hu, K. Chen, M. Siao, W. Ji, C. Yang, J. Yeh, K. Chiu, Eur. Polym. J., 88, (2017), 311-319.

[36] T. Li, B. Ding, J. Wang, Z. Qin, J. Fernando, Y. Bando, A. Nanjundan, Y. Kaneti, D. Golberg, Y. Yamauchi, ACS Appl. Mater. Interfaces, 12, (2020), 14993-15001.

[37] A. Valipour, N. Hamnabard, S. Meshkati, M. Pakan, Y. Ahn, Dalton Trans., 48, (2019), 5429-5443.

[38] Y. Yuan, W. Zhu, G. Du, D. Wang, J. Zhu, X. Zhu, G. Pezzotti, Electrochim. Acta, 282, (2018), 286-294.

[39] D. Patil, D. Malavekar, V. Lokhande, P. Bagwade, S. Khot, T. Ji, C. Lokhande, Energy Technol., 10, (2022), 2200295-2200310.

[40] Z. Neisi, Z. Ansari-Asl, A. Dezfuli, J. Inorg. Organomet. Polym. Mater., 29, (2019), 1838-1847.

[41] A. Bagde, D. Malavekar, A. Lokhande, S. Khot, C. Lokhande, J. Alloys Compd., 980, (2024), 173591-173603.

[42] S. Mehta, D. Nadargi, M. Tamboli, T. Alshahrani, V. Minnam Reddy, E. Kim, I. Mulla, C. Park, S. Suryavanshi, Sci. Rep., 11, (2021), 5023-5040.

[43] X. Liu, J. Wang, G. Yang, ACS Appl. Mater. Interfaces, 10, (2018), 20688-20695.

[44] M. Ruidiaz-Martinez, M. Alvarez, M. Lopez-Ramon, G. Cruz-Quesada, J. Rivera-Utrilla, M. Sanchez-Polo, Catalysts, 10, (2020), 520-545.

[45] M. Mitra, C. Kulsi, K. Chatterjee, K. Kargupta, S. Ganguly, D. Banerjee, S. Goswami, RSC Adv., 5, (2015), 31039-31048.

[46] W. Tang, L. Peng, C. Yuan, J. Wang, S. Mo, C. Zhao, Y. Yu, Y. Min, A. Epstein, Synth. Met., 202, (2015), 140-146.

[47] J. Liu, P. Du, Q. Wang, D. Liu, P. Liu, Electrochim. Acta, 305, (2019), 175-186.

[48] H. Habib, I. Wani, S. Husain, J. Energy Storage, 55, (2022), 105732-105748.

[49] D. Ahirrao, K. Mohanapriya, H. Wilson, N. Jha, Appl. Surf. Sci., 510, (2020), 145485-145537.

[50] T. Wang, H. Sun, T. Peng, B. Liu, Y. Hou, B. Lei, J. Mol. Struct., 1221, (2020), 128835-128853.

[51] X. Liu, S. Zou, K. Liu, C. Lv, Z. Wu, Y. Yin, T. Liang, Z. Xie, J. Power Sources, 384, (2018), 214-222.

[52] A. Moyseowicz and G. Gryglewicz, Compos. B. Eng., 159, (2019), 4-12.

[53] J. Han, W. Liu, T. Zhang, K. Xue, W. Li, F. Jiao, W. Qin, Sci. Rep., 7, (2017), 42536-42548.

[54] M. Kumar, K. Yasoda, S. Batabyal, N. Kothurkar, Mater. Res. Express, 5, (2018), 045505-045512.

[55] J. Zhao, H. Pang, J. Deng, Y. Ma, B. Yan, X. Li, S. Li, J. Chen, W. Wang, CrystEngComm, 15, (2013), 5950-5955.

[56] T. Islam, M. Hasan, S. Shah, M. Karim, F. Al-Mubaddele, M. Zahir, M. Dar, M. Hossain, M. Aziz, A. Ahammad, J. Energy Storage, 32, (2020), 101908-101920.

[57] D. Malavekar, V. Lokhande, V. Mane, S. Ubale, U. Patil, C. Lokhande, J. Phys Chem Solids, 141, (2020), 109425-109479.

[58] X. Zhao, Y. Hou, Y. Wang, L. Yang, L. Zhu, R. Cao, Z. Sha, RSC Adv., 7, (2017), 40286-40294.

[59] N. Chodankar, D. Dubal, G. Gund, C. Lokhande, J Energy Chem., 25, (2016), 463-471.

[60] C. Hu and C. Chu, J. Electroanal. Chem., 503, (2001), 105-116.

[61] S. Marje, V. Patil, V. Parale, H. Park, P. Shinde, J. Gunjakar, C. Lokhande, U. Patil, Chem. Eng. J., 429, (2022), 132184-132199.

[62] V. Mane, D. Malavekar, S. Ubale, V. Lokhande, C. Lokhande, Inorg. Chem. Commun., 115, (2020), 107853-107904.

[63] G. Singh, Y. Kumar, S. Husain, Polym. Adv. Technol., 32, (2021), 4490-4501.

[64] O. Sadak, M. Prathap, S. Gunasekaran, Carbon, 144, (2019), 756-763.

[65] H. Cong, X. Ren, P. Wang, S. Yu, Energy Environ. Sci., 6, (2013), 1185-1191.

CHAPTER – IV

Polypyrrole and reduced graphene oxide/polypyrrole (rGO/Ppy) thin films by successive ionic layer adsorption and reaction (SILAR) method: Characterization and electrochemical performance

CHAPTER – IV

Polypyrrole and reduced graphene oxide/polypyrrole (rGO/Ppy) thin films by successive ionic layer adsorption and reaction (SILAR) method: Characterization and electrochemical performance

4.1 Introduction:

Among the different pseudocapacitive materials used in supercapacitors, Ppy have attracted much attention, either individually or as a composite. In charge/discharge, Ppy experience irreversible volumetric expansion and contraction, which limits their rate capacity **[1]**. As a result, improvement in the electrochemical properties of Ppy can be achieved by incorporating graphene, specifically rGO nanosheets, into an efficient composite structure. The EDLC materials show higher S_P, good cyclic stability, but low C_s. However, with a quick and reversible faradaic charge transfer process through the surface, pseudocapacitive materials can improve capacitances for greater S_E. Due to these factors, it is advantageous to combine different materials with high conductivity and capacity, which may result in significant benefits by incorporating their superior characteristics **[2]**. Additionally, functional groups like -OH, -COOH, and -CHO of rGO offer superior defect sites for the development of Ppy over rGO sheets. However, there is still a problem with the synthesis of the composite electrode without using a binder on the conductive substrate **[3]**.

Considering above points, this chapter presents an analysis of the structural and electrochemical characteristics of SILAR deposited Ppy and rGO/Ppy electrodes. Layer structured rGO sheets with interconnected Ppy nanoparticles and an evenly distributed porous shape were produced. The charge storing mechanism of composite and bare electrodes was investigated using electrochemical techniques in 1 M H_2SO_4 electrolyte.

4.2. Synthesis and characterization of Ppy and rGO/Ppy thin films:

4.2.1 Introduction:

The electrode materials must be synthesized using a simple and affordable method. According to these perspectives, SILAR method is used for producing Ppy and rGO/Ppy thin films at ambient temperature on SS substrates. The present section deals with the porous electrode structure is created by layer-by-layer (LBL) deposition of rGO sheets followed by a SILAR method for Ppy deposition.

4.2.2 Experimental details:

4.2.2.1 Chemicals:

All chemicals of analytical grade (AR) were purchased from Thomas Baker Ltd., such as pyrrole monomers, APS, and H_2SO_4 were used no additional purification. As a solvent, DDW was used. The SS 304-grade sheet of thickness 0.05 mm was used to deposit Ppy and rGO/Ppy.

4.2.2.2 Synthesis of Ppy thin films:

A two beaker SILAR method was used to deposit Ppy thin films onto SS substrates. The pyrrole monomers were polymerized using a chemical oxidative polymerization process. The first beaker, 0.1 M pyrrole solution in 1 M H_2SO_4 serves as a cationic precursor and in the second beaker, 0.05 M APS solution in 1 M H_2SO_4 was used as an oxidizing agent at room temperature. In a beaker containing pyrrole monomer solution, the SS substrate was immersed for 10 s, allowing the adsorption of pyrrole monomer on surface of SS substrate. This substrate was then immersed for 10 s in a beaker containing APS solution. Pyrrole was oxidized in this reaction step, resulting in the formation of a black colored layer of Ppy on SS surface. In SILAR method, film thickness is influenced by the rate of nucleus production and growth. The film thickness increased as the number of deposition cycles increased. Hence, to optimize film thickness Ppy thin films deposited at 30, 40, 50, and 60 SILAR cycles are denoted as Ppy30, Ppy40, Ppy50 and Ppy60, respectively. After a certain deposition cycles, a reduction in film thickness is observed due to the development of an outer porous layer of the film, which may experience stress and eventually delaminate, causing the film material to peel off.

Using the gravimetric weight difference method, the thickness of synthesized films was determined using density of Ppy as 1.60 g cm^{-3} **(Equation 3.1)**. The thickness of Ppy30, Ppy40, Ppy50 and Ppy60 are 0.25, 0.37, 0.50, and 0.42 μm, respectively as shown in **Fig. 4.1**. The thickness rose from 30 to 50 cycles and then dropped after 50 cycles because of overgrowth of Ppy, which caused the film to collapse. As the film thickness increases, it also increases the amount of mass deposited on substrate, which reduces tension on the substrate and induces peeling of the overgrowth mass **[4]**.

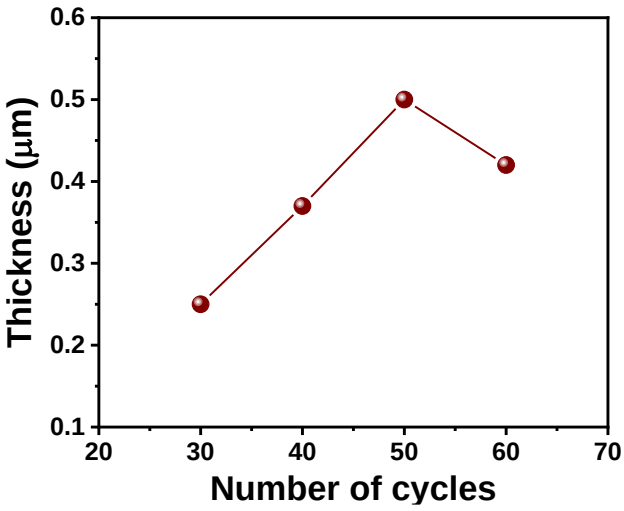

Fig. 4.1: The variation of thickness of Ppy electrodes with different SILAR cycles.

4.2.2.3 Synthesis of rGO/Ppy thin films:

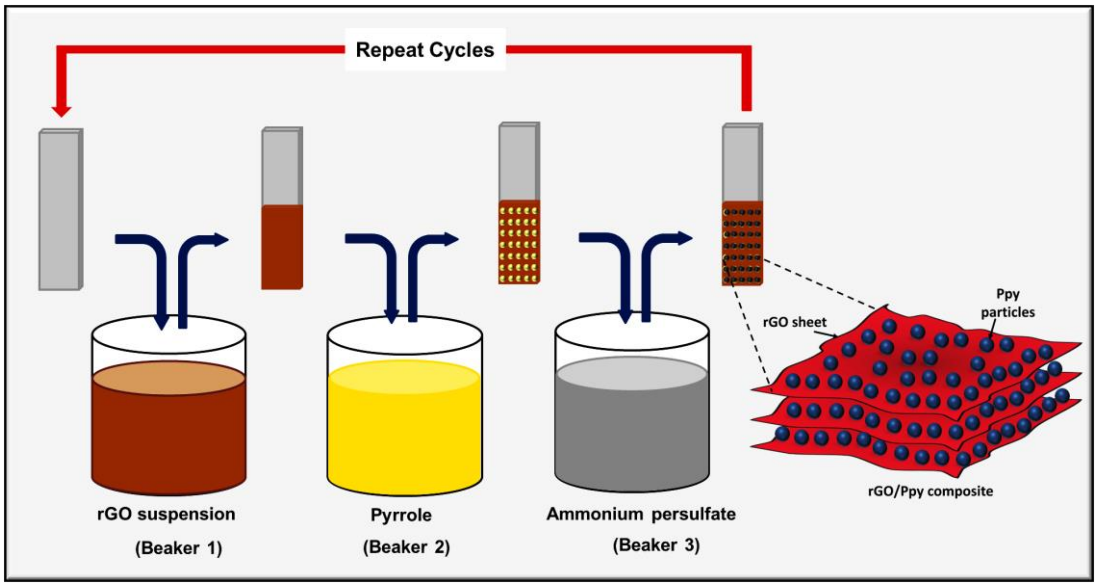

Fig. 4.2: Schematic illustration of rGO/Ppy thin film preparation by SILAR method.

In composite materials, the ratio between the constituting materials significantly influences charge storage properties, especially when the materials exhibit different charge storage mechanisms. For instance, in the current work, rGO primarily stores charge via an EDLC mechanism, while Ppy contributes through a pseudocapacitive mechanism. This contrast in behaviour has a profound impact on the overall charge storage performance **[5]**. Additionally, increasing rGO concentration enhances the adsorption of Ppy monomers on rGO sheets, a factor that requires further study to achieve optimal supercapacitive performance. Considering

these factors, we have studied optimized data of effect of different rGO concentrations on the performances of rGO/Ppy composites for supercapacitors.

Thin films of rGO/Ppy composite were deposited using the three beaker SILAR method, which included following steps: the SS substrate was dipped in the first beaker for 40 s, containing rGO suspension of with varying concentrations from 0.5 to 1.5 mg mL^{-1}, and dried for 20 s at ambient temperature. Further deposition was followed by the process mentioned in the above **section 4.2.2.2** for Ppy deposition on rGO sheets. This completes one cycle of rGO/Ppy deposition, and 50 cycles of this were performed. For rGO/Ppy deposition, a SILAR coating system (HOLMARC-HOTH03A) was used. **Fig. 4.2** depicts schematic illustration of rGO/Ppy thin film preparation by SILAR method. During the composite material deposition, positively charged pyrrole monomer is adsorbable to the negatively charged rGO surface due to interfacial factors such as electrostatic forces, hydrogen bonds, and π-π stacking. Thin films produced with rGO dispersion 0.5, 1.0, and 1.5 mg mL^{-1} concentrations are labeled as RP0.5, RP1.0, and RP1.5, respectively.

4.2.2.4 Material characterizations:

4.2.2.4A Physico-chemical characterizations:

All physico-chemical analysis of Ppy and rGO/Ppy thin films were carried out in according to **section 3.3.1.**

4.2.2.4B Electrochemical characterizations:

A standard three-electrode configuration was utilized to carry out the electrochemical measurement. The Ppy and rGO/Ppy electrodes served as the working electrode (area 1 × 1 cm^2), a SCE as a reference electrode and a platinum plate as a counter electrode in 1 M H_2SO_4 electrolyte.

4.3 Results and discussion:

4.3.1 Growth mechanism of Ppy and rGO/Ppy thin films:

The process of chemical polymerization of pyrrole maintains electroneutrality by incorporating anions from the reaction solution. Usually, these counterions are the anions of the oxidant or its reduced product. Usually, the anions of the chemical

oxidant or its reduced product are these counterions. In this study, APS is utilized as a chemical oxidant during polymerization. The chemical reaction mechanism of Ppy can involve the following reaction process **(Fig.4.3) [6]**.

As the substrate gets dipped in the cationic beaker, the monomeric pyrrole changes into pyrrolic cations in an acidic solution and adsorbs on surface of the SS substrate. Afterward substrate is immersed in the anionic beaker then reacts with an oxidant (APS) with one of the pyrrole electron by breaking the π bond in pyrrole. In order to form a pair, the free electron in one pyrrole attacks another pyrrole π bond. This releases another free electron, which leads to the formation of polypyrrole chain.

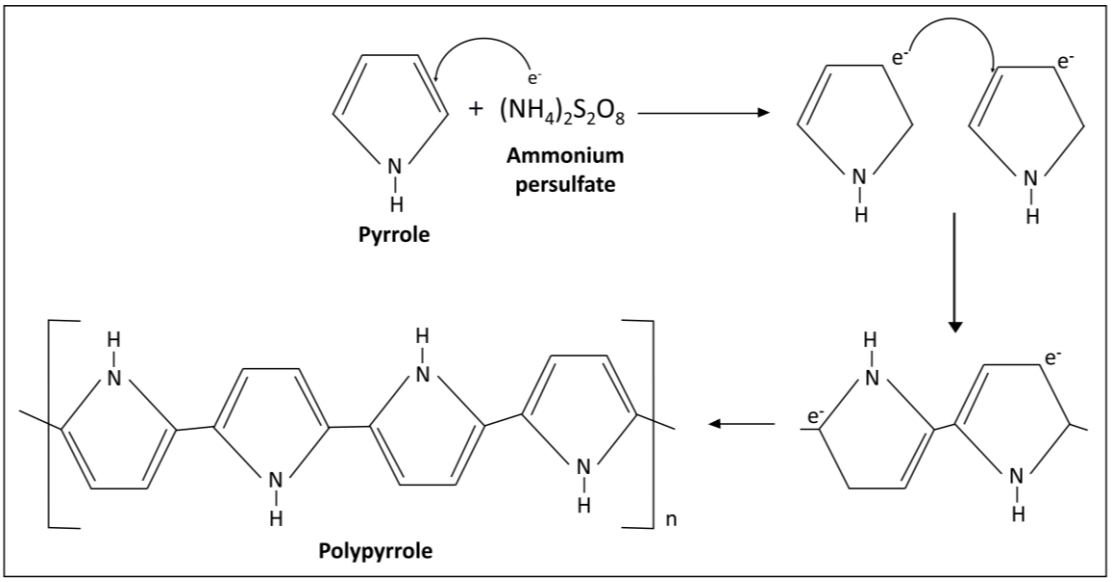

Fig. 4.3: The chemical reaction mechanism of Ppy formation.

The rGO and Ppy interact by non-covalent functionalization to generate a nanocomposite material in which Ppy and rGO serve as electron donor and acceptor properties, respectively. The charge transfer mechanism and structural relationship between rGO sheets and Ppy are affected by a number of factors, such as APS to pyrrole molar ratio, the number of SILAR cycles, the degree of protonation produced by H_2SO_4, and the different van der Waals interactions that occur. Dimer, semi-dine, and trimer of pyrrole are produced by chemically oxidizing pyrrole monomer with H_2SO_4, which acts as a dopant. The nucleation mechanism that proceeds to pyrrole monomer polymerization uses the trimer as a growth initiator. The negatively charged rGO surface adsorbs this positively charged pyrrole monomer via interfacial forces like electrostatic forces, hydrogen bonding, and stacking. The existence of functional groups in rGO like carboxyl, hydroxyl, and epoxy groups induce the consistent

distribution of Ppy matrix on rGO sheets, which are further maintained via interfacial interactions. The layers of rGO nanosheet and Ppy are attached to each other by H-bonds that form between rGO hydroxyl group and Ppy radical **[7]**. Stronger H-bonds are produced as a response to the electrostatic forces of attraction generated by protonated N, which is created from H_2SO_4, and single pairs on -OH saturated rings. This enables the two molecules to bond properly. The composite is additionally stabilized due to the existence of π bonds in the basal planes of rGO, and π-π stacking that takes place between the aromatic rings and quinoid rings of Ppy. **Fig. 4.4** depicts the reaction mechanism of rGO/Ppy composite electrode.

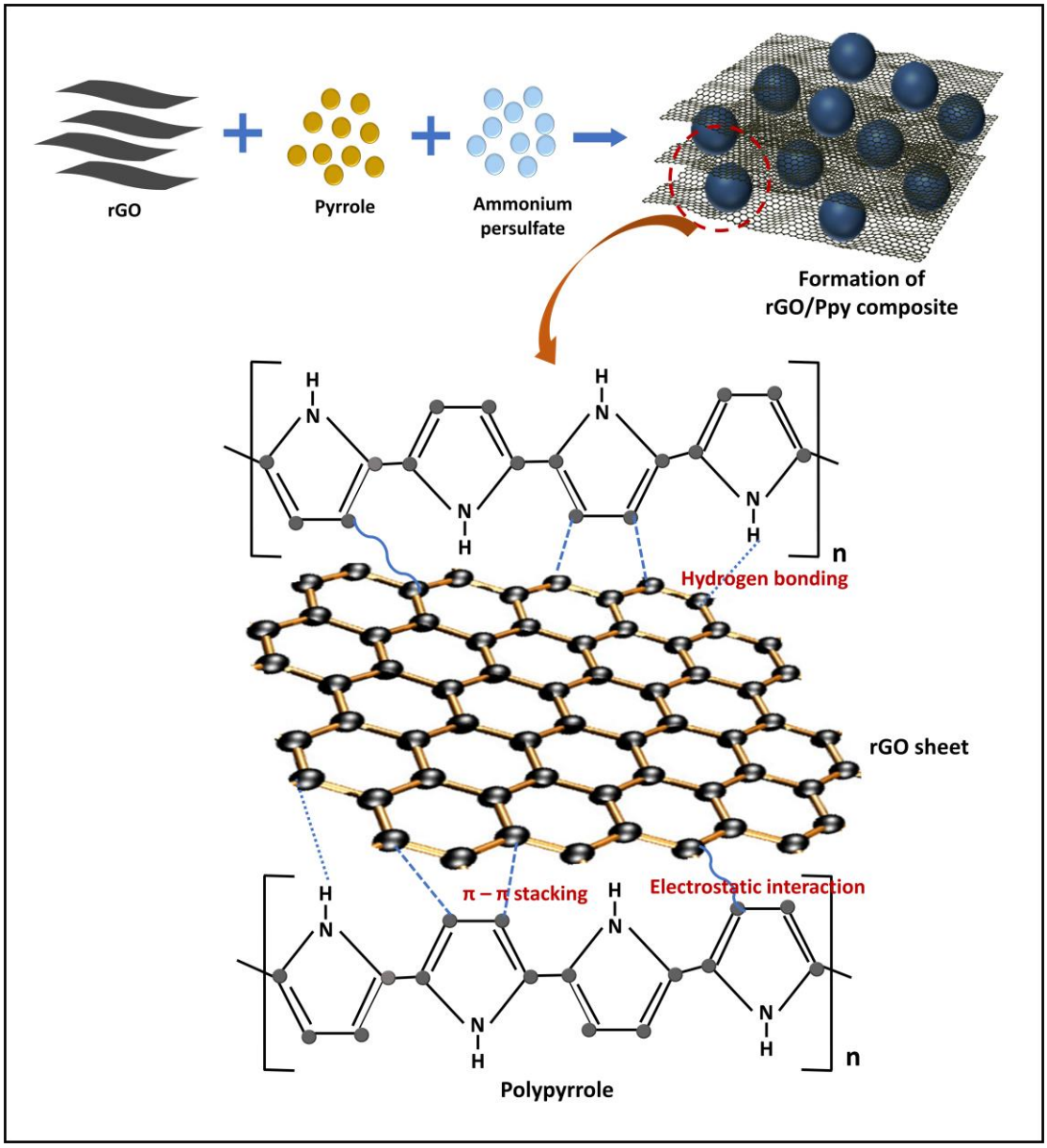

Fig. 4.4: The chemical reaction mechanism of rGO/Ppy composite electrode.

4.3.2 Physico-chemical characterizations of Ppy and rGO/Ppy thin films:

4.3.2.1 XRD studies:

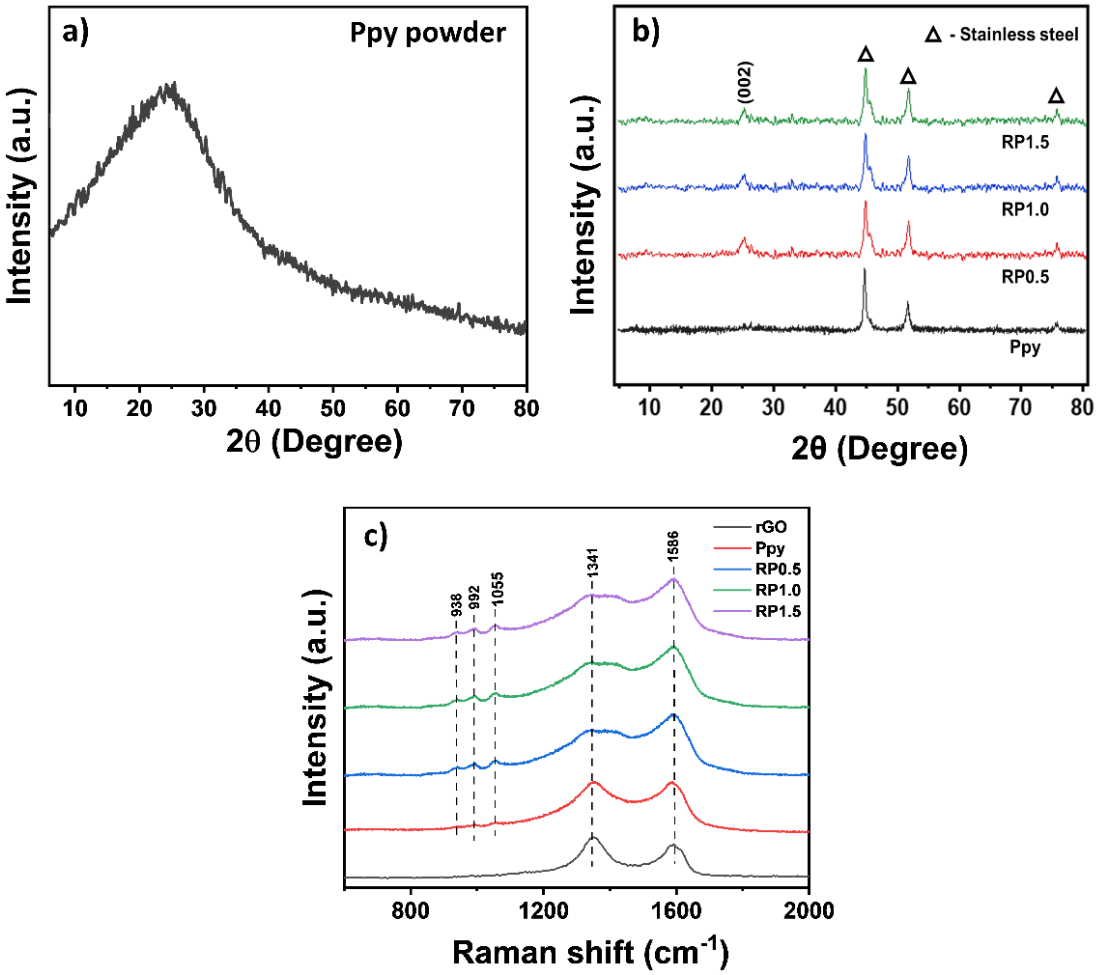

Fig. 4.5: a) The XRD pattern of Ppy powder, b) the XRD patterns, and c) Raman spectra of Ppy and rGO/Ppy electrodes.

The XRD pattern of Ppy powder is shown in **Fig. 4.5a**. The wide diffraction peak at 2θ = 24.6° in XRD pattern demonstrates the amorphous nature of Ppy **[8]**. The XRD patterns of Ppy and rGO/Ppy thin film samples in **Fig. 4.5b** does not display any peak of the required materials other than SS peaks indicated by the symbol 'Δ'; confirming the all samples are amorphous. The absence of periodic structure of atoms in Ppy sample was caused by the atomic shielding that exists between nucleated entity and material layers that have been adsorbed **[9]**. Additionally, the structure of amorphous material considerably improves the electrochemical properties by enhancing the specific surface area and material structural flexibility, which permits ions from electrolytes to diffuse more deeply into the active material **[10]**. The peak at 25.07° observed in XRD patterns of all RP series thin films is ascribed to (002)

crystallographic plane of graphite (PDF No. 41-1487). The characteristic rGO peak ensures formation of stacked rGO in Ppy material **[11]**.

4.3.2.2 Raman studies:

The chemical bonding properties of rGO, Ppy, and RP series composite were examined using Raman spectroscopy **(Fig. 4.5c)**. The peaks in rGO spectrum at 1341 and 1586 cm^{-1} associate with D and G bands, respectively. The D bands are ascribed to the aromatic ring vibrations that occurred in the K-point phonons of the A_{1g} symmetry, which relate to the edges and structural defects. The G bands show first order dispersion of the E_{2g} vibration mode, which is linked to vibrations of carbon bonding having sp^2 hybridization. Furthermore, the degree of disorder is reflected the D and G bands intensity ratio **[12]**. In Ppy spectrum, the peaks at 1586 cm^{-1}, is caused by polymer backbones π conjugated structure. At 1341 cm^{-1}, the peak related to the ring stretching mode of polymer **[13]**. The Ppy C-H in-plane bending modes are shown by the peak at 1055 cm^{-1}. The two modest peaks at 992 and 938 cm^{-1} indicate ring deformation in the quinoid polaronic and bipolaronic structures, respectively **[14]**. The RP series spectra show the characteristic peaks of rGO and Ppy. The ratio (I_D/I_G) is one of the most important parameters in estimating the relative number of disordered regions in graphene matrix. A larger ratio denotes fewer sp^2 domains and larger defects **[15]**. Considerable disorder and the growth of stacked rGO in the composite material are revealed by I_D/I_G ratio for RP series composites equal to 0.94.

4.3.2.3 FE-SEM studies:

The Ppy and RP series thin film surface morphologies were captured at two magnifications (5 KX and 20 KX) as displayed in **Fig. 4.6**. The FE-SEM images of Ppy **(Fig. 4.6a and b)**, display a spherical shape and form agglomerates. In RP series composite **(Fig. 4.6c-h)** exhibits graphene nanosheets evenly covered with Ppy spherical particles, suggesting that the π-π interactions between the precursors strongly restrict the restacking of rGO sheets. To prevent graphene sheets from restacking, spherical particles can act as spacers, resulting in equally dispersed Ppy material and formation of porous electrode. With increased rGO concentration from 0.5 to 1.0 mg mL^{-1}, the sizes of spherical particles are variable and more rGO nanosheets are covered with spherical particles. A large number of spherical particles are seen for RP1.0 electrode. In addition, there are large voids and gaps created by the

randomly interlinked particles over rGO sheets. Surface irregularity with gaps and cavities improves ion movement by reducing diffusion lengths **[16]**. Changes in rGO concentration influence the growth rate, which in turn affects the particle size of Ppy. On the other hand, high rGO concentration (1.5 mg mL^{-1}) can result in a more condensed structure because of graphene sheets collapse or restacking **[5]**. It is evident that after adding the proper rGO concentration in Ppy material, additional Ppy coated graphene sheets are accessible in the porous structure. The overlap of separate sheets allows electrolyte ions to travel quickly and form a layered structure that facilitates diffusion of electrolyte and accelerates redox processes.

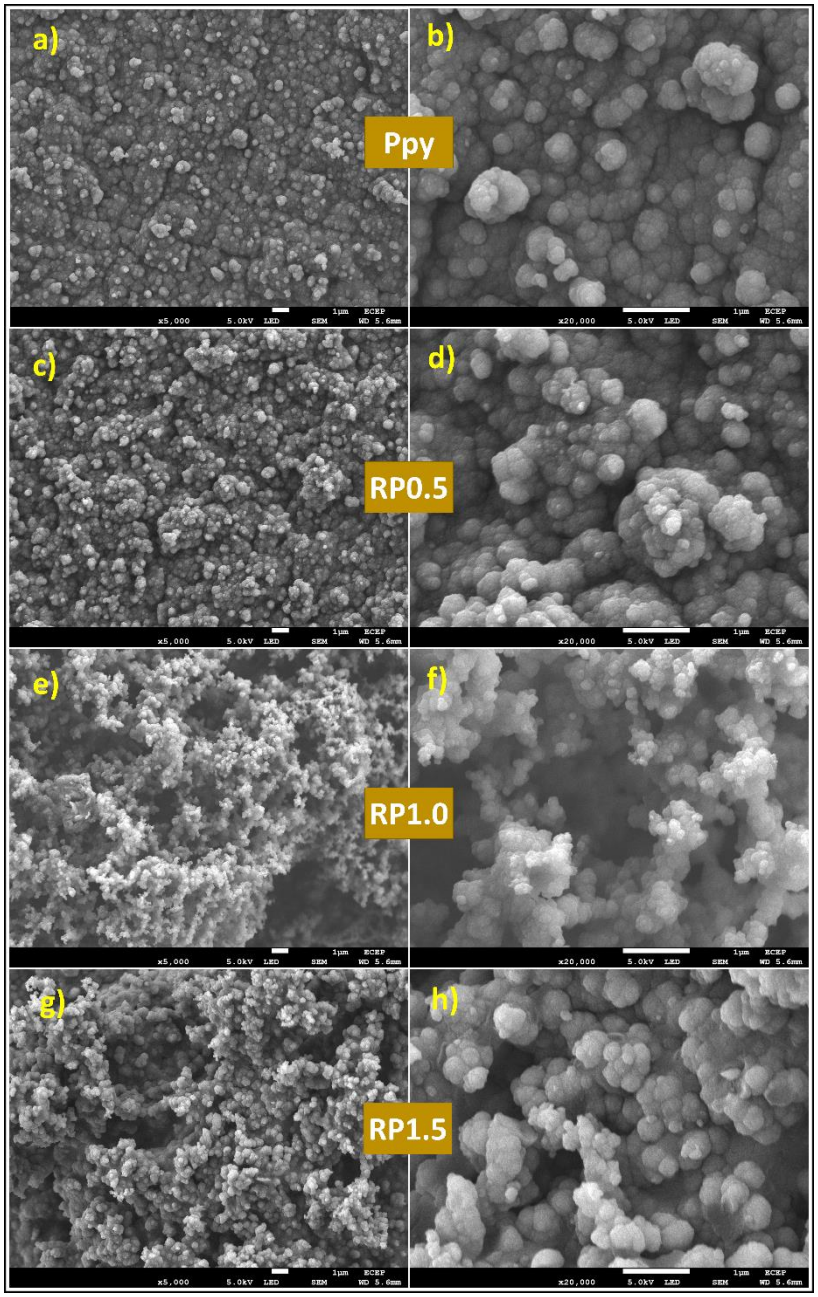

Fig. 4.6: The FE-SEM images of samples a, b) Ppy, c, d) RP0.5, e, f) RP1.0, and g, h) RP1.5 at magnifications of 5 KX and 20 KX.

4.3.2.4 XPS studies:

The existence of the elements C1s, N1s, and O1s is shown by the common spectral properties at binding energies of these elements in the XPS survey spectrum **(Fig. 4.7a)** for RP1.0 sample. As seen in **Fig. 4.7b**, the deconvoluted C1s spectrum of rGO shows five leading spectral peaks ascribed to C=C (284.4 eV), C-N (285.6 eV), C-O (286.3 eV), C=O (287.9 eV), and O-C=O (290.6 eV) **[17]**. The high resolution N1s spectrum is composed of three separate components **(Fig. 4.7c)**. For the imine nitrogen (-N=) and amine nitrogen (-NH-) groups, the peaks possessed binding energies of 398 and 399 eV, respectively. The nitrogen groups with a positive charge (-NH^+-) of the oxidized amine group are responsible for the peak at 400.3 eV **[18]**. The deconvoluted O1s signal shows three Gaussian peaks as seen in **Fig. 4.7d**. The peaks located at binding energies of 531.03, 532.3, and 533.4 eV, which might be attributed the existence of several oxygen functions such as C=O, O-C=O, and COOH groups, respectively **[19]**.

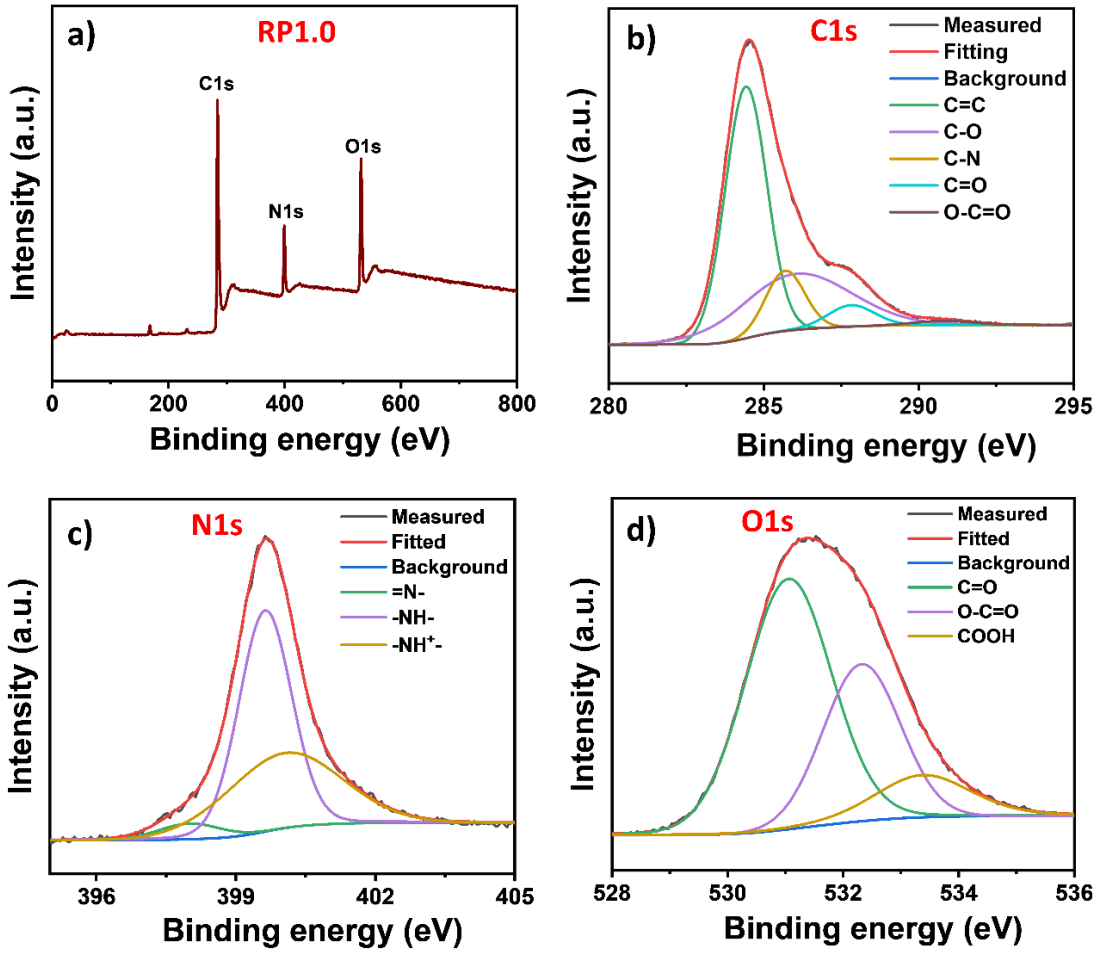

Fig. 4.7: a) Full XPS survey and fitted spectra of b) C1s, c) N1s, and d) O1s for RP1.0 electrode.

4.3.2.5 BET and BJH studies:

The N_2 adsorption-desorption isotherms for Ppy and RP1.0 along with their pore size distributions are depicted in **Fig. 4.8**. Based on the IUPAC standard, these isotherms demonstrated a type-III isotherm with a minor hysteresis loop suggesting poorly developed porosity or presence of macropores structure **[20]**. For Ppy and RP1.0 samples, the specific surface area is determined to be 18 and 41 m^2 g^{-1}, respectively (**Fig. 4.8a)**. The RP1.0 has a larger surface area and slightly increase in porosity than Ppy (non-porous), demonstrating that the development of composite material with rGO enhances the overall surface area and porosity of the material. Large surface area of RP1.0 material can offer more active sites for ion adsorption/exchange to boost C_s. Due to this, ions from the electrolyte can quickly penetrate both the interior and exterior of the composite materials. Additionally, the average pore size for Ppy and RP1.0 samples is 15.7 and 21.3 nm, respectively **(Fig. 4.8b)** which is adequate for ion electrosorption. Consequently, the composites inner and outer surfaces are freely accessible to the ions from the electrolyte. Moreover, RP1.0 has a higher pore volume (1.040 cm^3 g^{-1}) than Ppy (0.075 cm^3 g^{-1}). Therefore, the electrode/electrolyte interaction will be enhanced by the composite material having a greater surface area and more pore volume resulting in improved redox capabilities **[15]**.

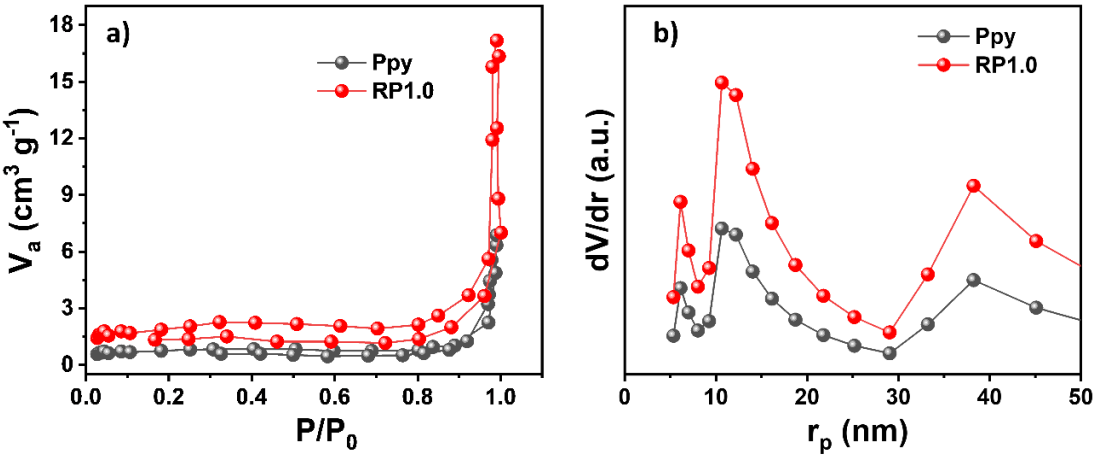

Fig. 4.8: a) The N_2 adsorption-desorption isotherms, and b) pore size distribution curves of Ppy and RP1.0 samples.

4.3.2.6 Contact angle studies:

The measurement of the contact angle is useful to find out the characteristics of the interface between the electrolyte and the electrode. **Fig. 4.9a-c**, exhibits rGO,

Ppy, and RP1.0 thin films electrolyte contact angle photographs with values of 64°, 53°, and 41°, respectively. Hydrophilic surfaces can effectively make direct contact with an electrolyte in supercapacitive applications. It is known that an electrode surface with a hydrophilic nature is necessary for optimal performance in an electrochemical supercapacitor **[21]**.

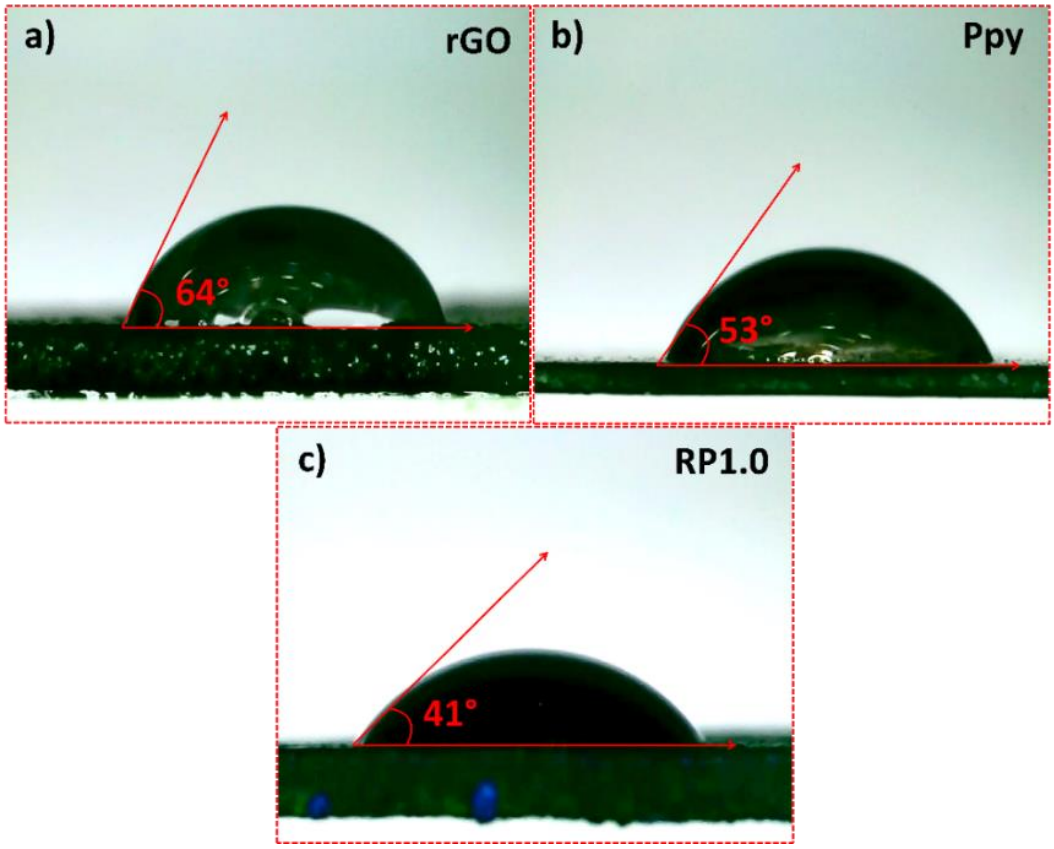

Fig. 4.9: a) The contact angle photographs of a) rGO, b) Ppy, and c) RP1.0 electrodes.

4.3.3 Electrochemical characterizations of Ppy and rGO/Ppy thin films:

4.3.3.1 The CV studies:

The effect of rGO concentration in Ppy composition on structure and morphology, as well as its subsequent impact is studied further for electrochemical analyses. A three-electrode electrochemical cell setup is used for studying the electrochemical characteristics of rGO, Ppy, and RP series thin film electrodes. The comparative CV curves for rGO, Ppy, and RP series electrodes at a 50 mV s^{-1} are displayed in **Fig. 4.10a** within an optimal potential range of -0.4 to +0.6 V/SCE. The raised CV curve area for RP1.0 electrode indicates a strong connection between the specific surface area and CV curve, which results in a larger capacity to store charges than the other electrodes.

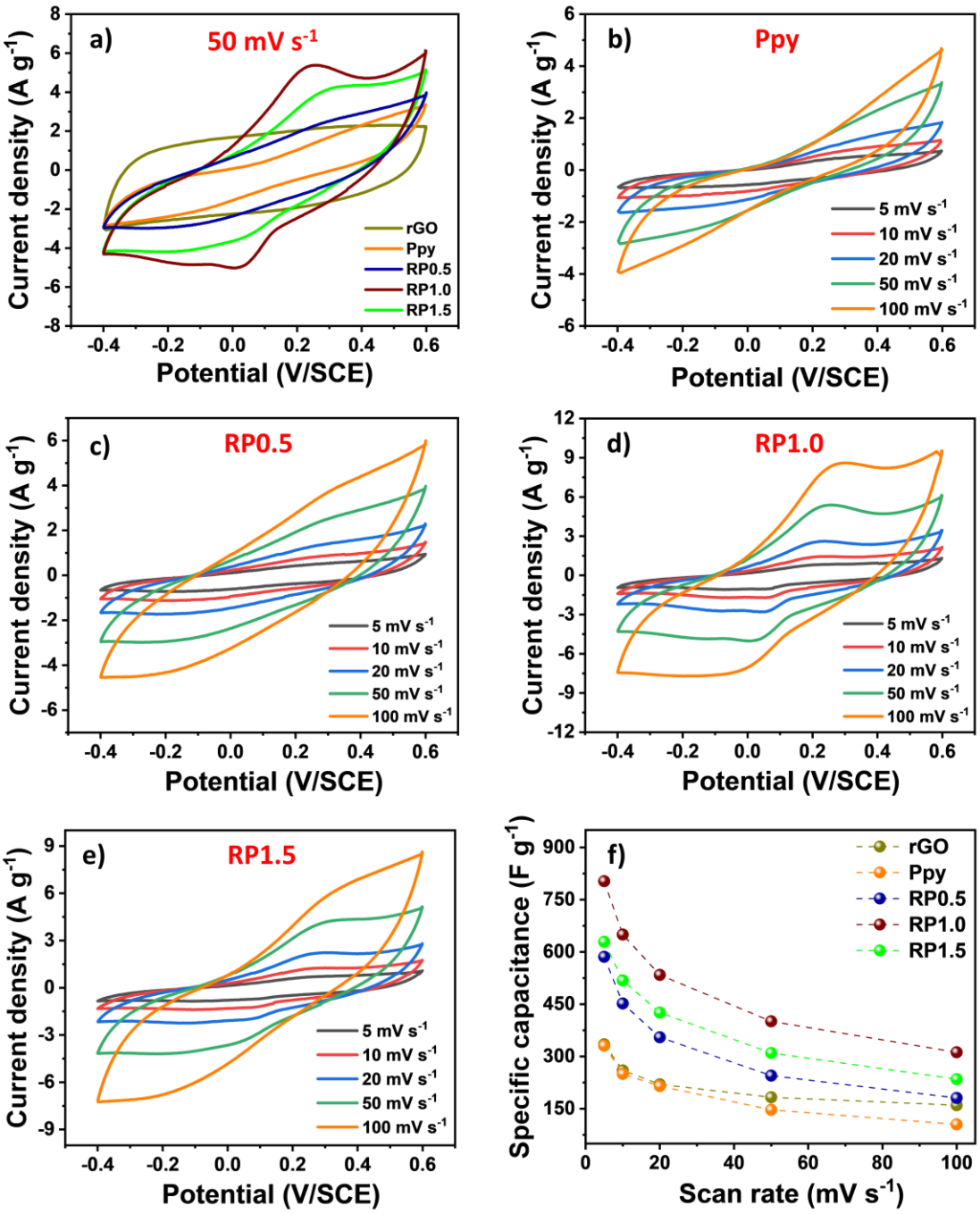

Fig. 4.10: a) Comparative CV curves at 50 mV s^{-1} scan rate of rGO, Ppy, and rGO/Ppy electrodes, the CV curves at different scan rates of b) Ppy, c) RP0.5, d) RP1.0, and e) RP1.5 electrodes, and f) the variation of the specific capacitance with various scan rate of all electrodes.

Furthermore, as depicted in **Fig. 4.10b-e**, the CV curves from 5 to 100 mV s^{-1} scan rates for electrodes of rGO, Ppy, RP0.5, RP1.0 and RP1.5. The rising area under CV curves and shift in peak position with scan rate suggests pseudocapacitive behavior of RP1.0 electrode. A faster scan rate in the redox reaction generates ion

saturation or depletion in the electrolyte within the electrode, which mostly increases the resistance of ions **[22]**. At the time of charging, electrolyte ions are intercalated into the majority of the active electrode material and they are deintercalated at the time of discharging. The C_s values of the electrodes are determined from the CV curves at various scan rate using **Equation 2.12**. The largest C_s is determined to be 803 F g^{-1} at a 5 mV s^{-1} scan rate for RP1.0 electrode. Furthermore, as illustrated graphically in **Fig. 4.10f**, the estimated values of C_s for rGO, Ppy, RP0.5, and RP1.5 are 330, 331, 586, and 629 F g^{-1}, respectively. The rGO provides electron transfer channels as well as functions as a spacer, resulting in the creation of smaller Ppy particles sandwiched between rGO sheets, which conduct fast redox processes.

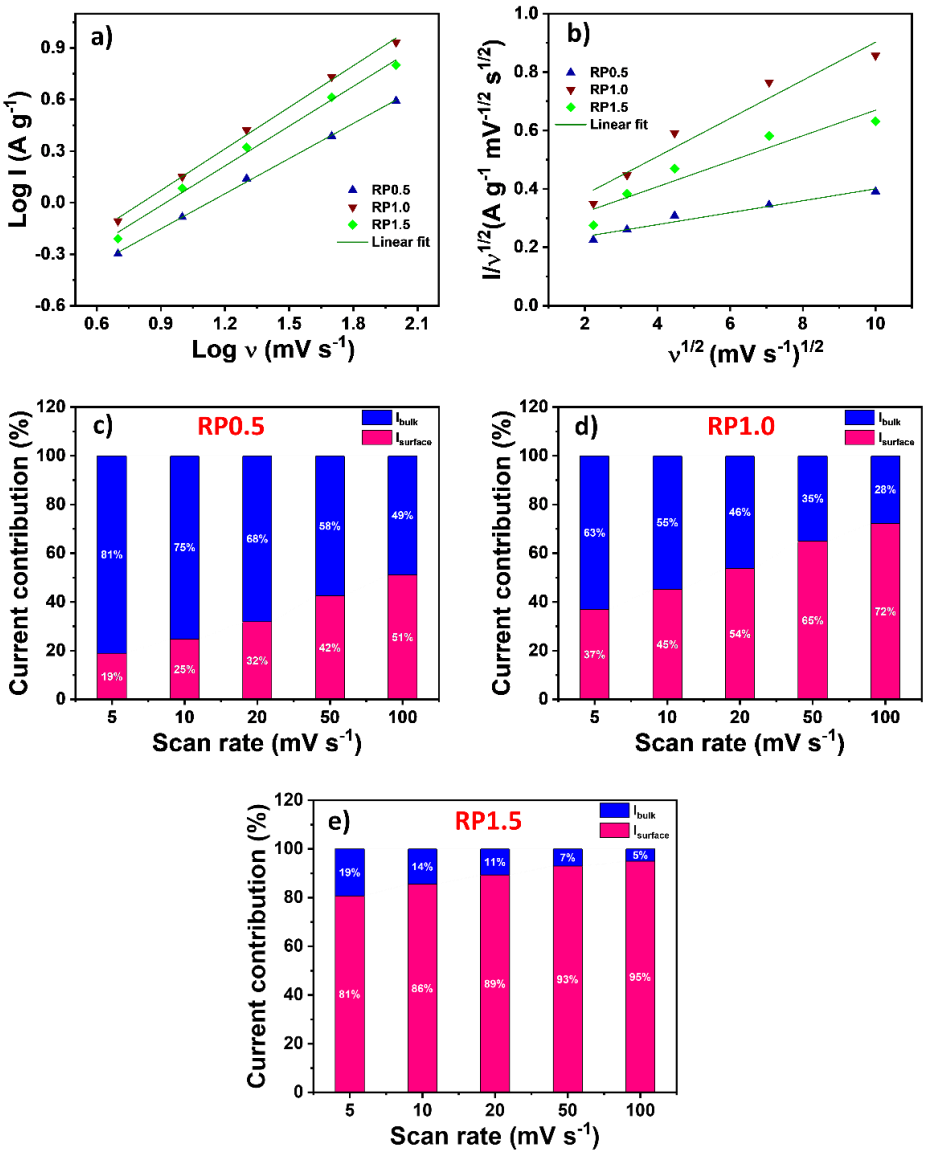

Fig. 4.11: a) Plots of log I vs. log υ, b) plots of $I/\upsilon^{1/2}$ vs. $\upsilon^{1/2}$ of RP series electrodes, contribution of capacitive and diffusion-controlled currents with scan rates of c) RP0.5, d) RP1.0, and e) RP1.5 electrodes.

The CV curve gives further quantitative information into the charge storage process. The RP series composite electrodes charge storage kinetics were examined using the power law **(Equation 3.2)**.

The 'b' values, determined using the slope of **Fig. 4.11a**, are 0.68, 0.80, and 0.77 for RP0.5, RP1.0, and RP1.5, respectively. These values indicate that a combination of surface and diffusion-controlled process is responsible for the charge kinetics. **Fig. 4.11b**. displays the k_1 and k_2 values, which are obtained from the slopes and intercepts of the linear fit of the $I/\nu^{1/2}$ and $\nu^{1/2}$ plot. The scan rate dependent current response of RP0.5, RP1.0, and RP1.5 electrodes calculated from **Equation 3.3** are depicted graphically in **Fig. 4.11c-e**. The total contribution at lower scan rate indicates a more diffusion-controlled charge storage; conversely, raising the scan rate results in enhancement in surface-controlled charge storage. Therefore, for RP1.0 electrode, the charge storage contribution from bulk of electrode is 63% at a 5 mV s^{-1} and 28% at a 100 mV s^{-1} scan rate. The layered structure, which permits facile electrolyte penetration, is largely responsible for the diffusion-controlled process contribution.

4.3.3.2 The GCD studies:

To acquire a better understanding of the capacitive performance of rGO, Ppy, and RP series thin film electrodes, the comparison of GCD measurement was performed within -0.4 to +0.6 V/SCE at a current density of 1 A g^{-1}, as shown in **Fig. 4.12a**. The obtained results correlate with CV, showing that RP1.0 has the largest discharge time among all the prepared electrode in this study, because of the immense surface area and convenient pathway offered by the porous surface for electrochemical processes. The GCD plots for c at several current densities (1 to 5 A g^{-1}) are shown in **Fig. 4.12b-e**. Discharge curves exhibit nonlinear behaviour at various current density with a small initial IR drop, pointing to a faradic contribution is supported to the EDLC mechanism of charge storage in RP series electrodes **[23]**. The highest C_s calculated from **Equation 2.13** is 684 F g^{-1} at 1 A g^{-1} current density for RP1.0 electrode. At a 1 A g^{-1} current density, the values of C_s for rGO, Ppy, RP0.5, and RP1.5 are 330, 331, 586, and 629 F g^{-1}, respectively. The C_s variation with current density is depicted in **Fig. 4.12f**.

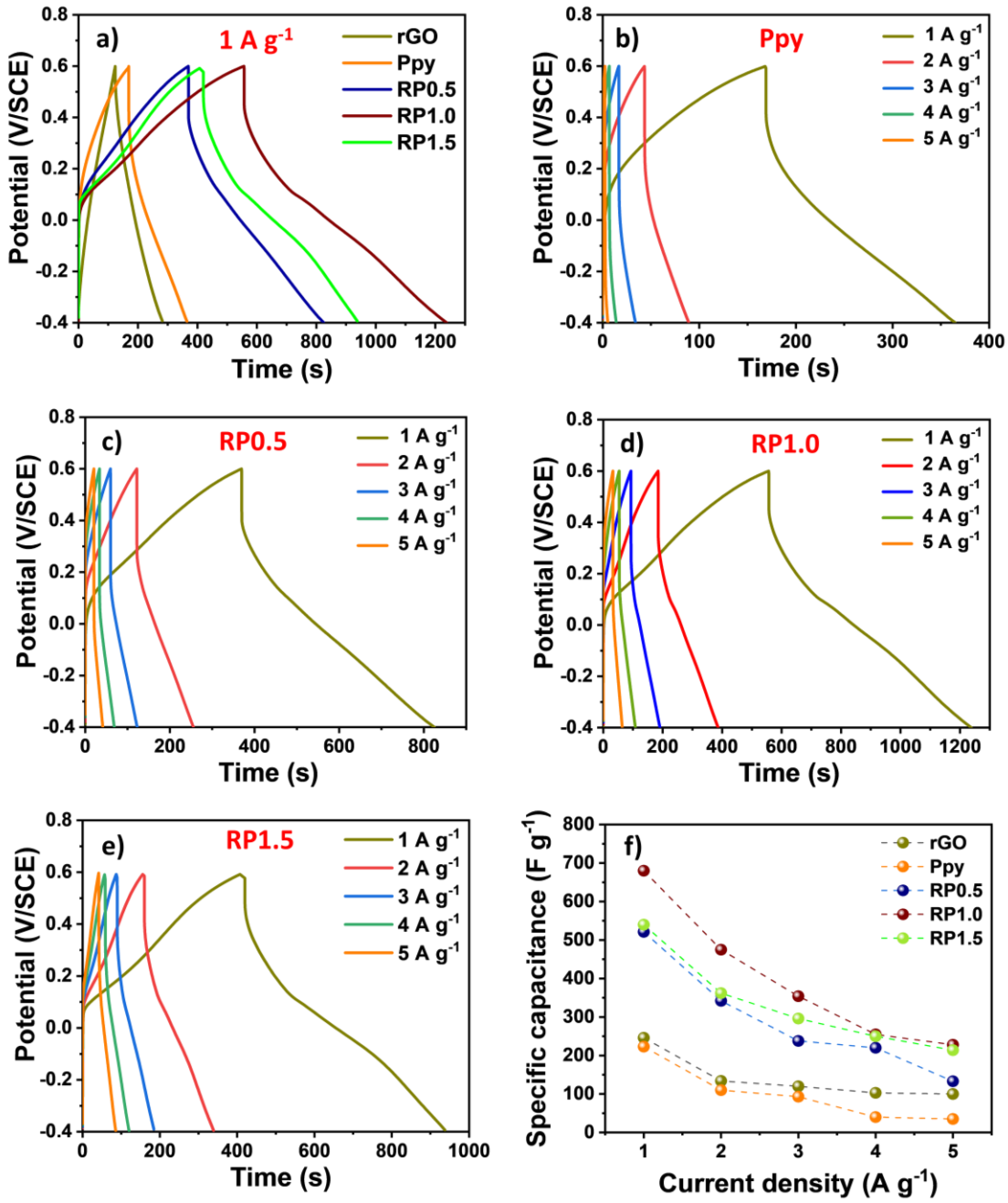

Fig. 4.12: a) Comparative GCD plots of rGO, Ppy, and rGO/Ppy electrodes at 1 A g^{-1} current density, the GCD plots at current densities from 1 to 5 A g^{-1} of b) Ppy, c) RP0.5, d) RP1.0, e) RP1.5 electrodes, and f) the variation of the specific capacitance with different current density of all electrodes.

4.3.3.3 The EIS studies:

In order to comprehend the different supercapacitive properties, to perform the EIS studies with a 10 mV amplitude and an operating frequency of 100 kHz to 0.1 Hz. **Fig. 4.13a** displays the Nyquist plots for rGO, Ppy and RP series electrodes. A

equivalent circuit was used to match the experimental results of the Nyquist plots (inset of **Fig. 4.13a**), and **Table 4.1** provides several types of parameters, including R_s, R_{ct}, and W. Each Nyquist plot shows a nearly straight line for the lower frequency zone and a semicircle for the higher frequency zone.

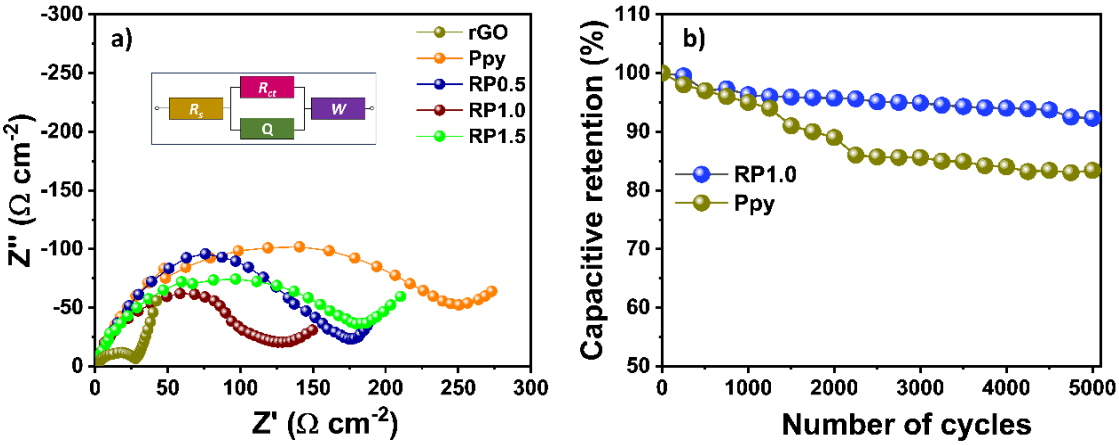

Fig. 4.13: a) Nyquist plots of rGO, Ppy and different rGO/Ppy electrodes (the inset shows fitted equivalent circuit), and b) plots of capacitive retention vs number of cycles of Ppy and RP1.0 electrodes.

According to the EIS data, RP1.0 thin film electrode exhibits excellent electrochemical performance and low resistance. The formation of a binder-free stoichiometric thin film requires an appropriate concentration of rGO in Ppy, allowing for improved conducting characteristics in electrochemical processes. The RP1.0 thin film exhibited this type of characteristics. Low rGO concentrations result in higher R_s and R_{ct} values, which might be due to a shortage of appropriate active sites, whereas increases in R_{ct} value are observed as the concentration of rGO rises further due to stacking of rGO sheets, disrupting the porous structure, which may restrict or slow down the mobility of ion through the electrode. The appropriate rGO concentration provides a quick pathway for flow of electron. Additionally, it contributes to the electrode exceptional electrochemical capabilities by producing a porous surface that enhances electrolyte transport and provides more electroactive sites for redox processes **[24]**.

Table 4.1. Electrochemical impedance spectroscopic data of rGO, Ppy and RP series electrodes.

Electrodes	R_s (Ω cm^{-2})	R_{ct} (Ω cm^{-2})	Q (F)	W (Ω cm^{-2})
rGO	0.59	19	0.871	0.026
Ppy	0.90	209	0.716	0.49
RP0.5	0.72	145	0.826	0.37
RP1.0	0.15	98	0.986	0.21
RP1.5	0.36	130	0.900	0.33

4.3.3.4 The Stability studies:

Another key parameter for assessing the performance of a good supercapacitor is the material cycling stability. The electrochemical cycling stability of Ppy and RP1.0 electrodes over 5,000 GCD cycles and the related capacitive retention are presented in **Fig. 4.13b**. Over 5,000 cycles, Ppy and RP1.0 electrodes showed an effective 83% and 90% capacitive retention, respectively. Faster transport of electrons in RP1.0 composite was achieved by the inclusion of rGO, which led to RP1.0 thin film electrode exhibiting superior cycle stability than Ppy thin film electrode.

4.5 Conclusions:

In summary, the facial SILAR method was used to synthesize rGO/Ppy composite thin films on SS substrates. Variations in rGO concentration change the growth kinetics of rGO/Ppy thin film electrodes, which influencing the materials physico-chemical properties. Therefore, the average particle size decreased to 21.3 nm by adding 1 mg mL^{-1} rGO to rGO/Ppy composite, which produced a porous structure with an impressive specific surface area of 41 m^2 g^{-1}. The innate redox properties of rGO and Ppy, as well as their synergy with the maximum surface area of RP1.0 electrode, give enhanced electrochemical properties with the highest C_s of 803 F g^{-1} at a 5 mV s^{-1} scan rate. The electrochemical cycling stability of RP1.0 film electrode (90%) is higher than that Ppy film electrode (83%). The findings demonstrated that employing the facile SILAR synthesis method produced a composite thin film of rGO and Ppy with tunable morphologies and specific surface areas. Furthermore, the optimized RP1.0 electrode proved to be a suitable cathode material for supercapacitor devices.

References:

[1] K. Kong, W. Xue, W. Zhu, W. Ye, Z. Zhang, R. Zhao, D. He, J. Power Sources, 470, (2020), 228452-228460.

[2] R. Hou, G. Gund, K. Qi, P. Nakhanivej, H. Liu, F. Li, B. Xia, H. Park, Energy Storage Mater., 19, (2019), 212-241.

[3] A. Fouda, A. Salem, F. El-Tantawy, H. Salem, E. Duraia, Superlattices Microstruct, 124, (2018), 240-247.

[4] N. Maile, S. Shinde, K. Patil, A. Fulari, A. Shahzad, D. Lee, V. Fulari, SN Appl. Sci., 1, (2019), 1333-1343.

[5] D. Patil, D. Malavekar, J. Kim, C. Lokhande, J. Energy Storage, 72, (2023), 108729-108743.

[6] D. Dubal, S. Patil, A. Jagadale, C. Lokhande, J. Alloys Compd., 509, (2011), 8183-8191.

[7] Q. Wang, H. Song, W. Li, S. Wang, L. Liu, T. Li, Y. Han, J. Power Sources, 517, (2022), 230737-230747.

[8] S. Ahmad, I. Khan, A. Husain, A. Khan, A. Asiri, Polym., 12, (2020), 3047-3060.

[9] F. Almuntaser, S. Majumder, P. Baviskar, J. Sali, B. Sankapal, Appl. Phys. A, 123, (2017), 555-563.

[10] D. Malavekar, V. Lokhande, V. Mane, S. Ubale, U. Patil, C. Lokhande, J. Phys. Chem. Solids, 141, (2020), 109425-109479.

[11] S. Mehta, D. Nadargi, M. Tamboli, T. Alshahrani, V. Minnam Reddy, E. Kim, I. Mulla, C. Park, S. Suryavanshi, Sci. Rep., 11, (2021), 5023-5040.

[12] X. Fan, Z. Yang, N. He, RSC Adv., 5, (2015), 15096-15102.

[13] S. Biswas and L. Drzal, Chem. Mater., 22, (2010), 5667-5671.

[14] S. Kulandaivalu, M. Hussein, A. Jaafar, M. Abdah, N. Azman, Y. Sulaiman, RSC Adv., 9, (2019), 40478-40486.

[15] S. Kulandaivalu and Y. Sulaiman, J. Power Sources, 419, (2019), 181-191.

[16] M. Kumar, K. Yasoda, S. Batabyal, N. Kothurkar, Mater. Res. Express, 5, (2018), 045505-045512.

[17] J. Chen, Y. Wang, J. Cao, L. Liao, Y. Liu, Y. Zhou, J. Ouyang, D. Jia, M. Wang, X. Li, Z. Li, Electrochim. Acta, 361, (2020), 137036-137048.

[18] A. Moyseowicz and G. Gryglewicz, Compos. B. Eng., 159, (2019), 4-12.

[19] J. Han, W. Liu, T. Zhang, K. Xue, W. Li, F. Jiao, W. Qin, Sci. Rep., 7, (2017), 42536-42548.

[20] A. Moyseowicz, Z. Gonzalez, R. Menéndez, G. Gryglewicz, Compos. Part B Eng., 145, (2018), 232-239.

[21] D. Dubal, D. Dhawale, R. Salunkhe, V. Fulari, C. Lokhande, J. Alloys Compd., 497, (2010), 166-170.

[22] V. Mane, S. Kale, S. Ubale, V. Lokhande, C. Lokhande, Mater. Today Chem., 20, (2021), 100473-100488.

[23] S. Kale, A. Lokhande, R. Pujari, C. Lokhande, J. Colloid Interface Sci., 532, (2018), 491-500.

[24] D. Malavekar, V. Lokhande, V. Mane, S. Kale, R. Bulakhe, U. Patil, I. In, C. Lokhande, J. Solid State Electrochem., 24, (2020), 2963-2974.

CHAPTER – V

Synthesis and characterization of tungsten oxide (WO_3) thin films by CBD method

CHAPTER – V

Synthesis and characterization of tungsten oxide (WO_3) thin films by CBD method

5.1 Introduction:

The supercapacitor involves of two electrodes (cathode and anode) surrounded by an electrolyte (organic or aqueous) and a separator that allows ion transport while maintaining electrical isolation between the electrodes **[1, 2]**. Supercapacitor may be classified into two kinds based on their configuration i.e SSCs and ASCs. SSCs are simple configurations with two same electrodes and ASCs are an additional configuration consisting of two distinct electrodes. If aqueous electrolytes are utilized, the thermodynamic breakdown potential of water molecules determines the operating voltage of supercapacitors. Due to ASCs and SSCs have distinct work functions and working windows for their electrode materials, ASCs have a higher operating potential while SSCs have a lower operating potential **[3, 4]**.

Recently, numerous electrode materials have been used in the development of ASCs. Carbon-based materials like graphene, CNTs, and AC are the most commonly used materials for ASCs device fabrication **[5, 6]**. These materials have advantages for this application because of their superior electrical conductivity, broad surface area, ease of surface texture modification, and availability. Some examples of ASCs device with carbon electrodes include $NiCo_2O_4$//AC **[7]**, $CoFe_2O_4$/CNTs//AC **[8]**, and MOF-CNT//AC **[9]**. However, the issues with using carbon-based materials as an electrode material include graphene sheets restacking and the aggregation of AC and CNTs. Another drawback that limits the practical usage of graphene-based electrodes is their low C_s. Recent work has addressed these problems by fabricating and testing ASCs with two pseudocapacitive electrodes for electrochemical properties. ASCs that utilize battery-type or pseudocapacitive materials as the two electrodes such as Dy_2Se_3//MnO_2 **[10]**, GO/Yb_2S_3//MnO_2 **[11]**, and NiCoLDH//Fe_2O_3 **[12]**.

A variety of metal oxides, such as tungsten, nickel, and ruthenium oxides, are utilized as thin film electrodes in supercapacitors **[13]**. Among the various metal oxides, tungsten oxide, an n-type transition metal oxide, has several uses. Tungsten trioxide (WO_3) is a highly versatile and interesting electrode material for a variety of applications among the numerous types of tungsten oxide. The WO_3 is commonly used in aqueous batteries, oxidation catalysts, supercapacitors, and other industries because of its less toxicity, abundant supplies, and simple production method **[14]**. Particularly in the supercapacitor field, WO_3 is a promising material for negative window electrodes. The WO_3 superior supercapacitive characteristics can be attributed to two aspects.

From an electrochemical perspective, WO_3 exhibits superior supercapacitive characteristics such as a large theoretical capacitance (1112 F g^{-1}), in aqueous electrolytes, a broad negative operating potential window (~0.8 V), excellent electrochemical supercapacitive performance, resulting in less chemical corrosion of current collectors. From an economic and environmental protection perspective, WO_3 is inexpensive, easily available, and environmentally harmless **[15]**. Due to its distinct physical and chemical characteristics, WO_3 is an excellent material for pseudocapacitor thin film electrodes.

Recently, researchers have focused on WO_3 as a negative electrode in ASCs devices. The WO_3 thin films are prepared using a variety of chemical methods, including as spray pyrolysis **[16]**, electrodeposition **[17]**, CBD **[18]**, and hydrothermal **[19, 20]**. Direct development of WO_3 nanostructures on a current collector, without the use of binders, can improve electrochemical performance significantly. This has several benefits, including increased accessibility to electrochemically active areas, enhanced cycle stability, increased contact with the current collector, and faster access to electrolyte ions. The CBD is a cost-effective and simple method for creating a binder-free WO_3 electrode. This method allows for adherent, consistent, and large-area deposition. Consequently, the huge scale deposition of various inorganic materials having a variety of structures and surface morphologies is prepared using CBD method **[21, 22]**.

This chapter describes the preparation of WO_3 thin films on SS substrates using CBD method. The WO_3 thin films were analyzed using XRD, BET, FE-SEM, and contact angle techniques. The electrochemical performance of WO_3 thin films were evaluated using CV, GCD, and EIS techniques in 1 M H_2SO_4 electrolyte.

5.2. Experimental details:

5.2.1. Chemicals:

Analytical grade sodium tungstate (Na_2WO_4), and hydrochloric acid (HCl), sulphuric acid (H_2SO_4) were utilized with no further purification. As a solvent, DDW was used and SS 304-grade measuring 5 × 1 cm^2 was used as the substrate.

5.2.2 Synthesis of WO_3 thin films:

The CBD method was utilized to deposit WO_3 thin film. The experiment details are as follows: 0.05 M Na_2WO_4 was dissolved in 50 mL of DDW, and dilute

HCl was added dropwise into Na_2WO_4 solution to maintain pH at 1.5±0.1. Due to acidification, milky white or yellowish tungstic particles (H_2WO_4) were formed. The final solution was kept at 353 K while the SS substrate was immersed for 8 h. As temperature increases, controlled nucleation formation takes place in the solution. On the SS substrate surface, WO_3 particles develop due to controlled heterogeneous nucleation and particle growth **[23]**. The following chemical mechanism can be used to describe the growth process of WO_3 **[24]**.

Na^+ and WO_4^{2-} (metal ions) are released when Na_2WO_4 dissociates into water.

$$Na_2WO_4 \rightarrow Na^+ + WO_4^{2-} \quad (5.1)$$

Slowly adding dilute HCl to Na_2WO_4 solution produces yellowish clear tungstic acid (H_2WO_4) at a pH of around 1.5±0.1.

$$Na_2^+ + WO_4^{2-} + 2HCl \rightarrow H_2WO_4 + 2NaCl \quad (5.2)$$

The decomposition of H_2WO_4 initiates nucleation in the solution, resulting in the formation of WO_3 nuclei.

$$H_2WO_4 \rightarrow WO_3 + H_2O \quad (5.3)$$

The weight difference method was applied to determine the thicknesses of thin films using a sensitive microbalance, considering that the developed material density is the same as WO_3 bulk density (7.16 g cm^{-3}). The WO_3 thin film thickness was determined to be 1.5 µm.

5.3 Material characterization:

5.3.1 Physico-chemical characterizations:

The physico-chemical characterisations of WO_3 thin films were similar to that of PANI thin films, discussed in **section 3.3.1**.

5.3.2 Electrochemical characterizations:

The electrochemical characteristics of WO_3 electrodes were measured using Zive MP1 electrochemical workstation. Electrochemical studies were conducted using a typical three-electrode setup consisting of a counter electrode (platinum plate), a reference electrode (SCE), and a working electrode (WO_3 electrode) with an active material area of 1 × 1 cm^2. An aqueous 1 M H_2SO_4 solution serves as the electrolyte. In the potential range of −0.6 to 0 V/SCE, the electrochemical experiments were

carried out using CV and GCD techniques. EIS experiment was conducted at frequencies between 0.01 Hz and 100 kHz with potential amplitude of 10 mV. The C_s value of WO_3 electrode from CV and GCD experiments was determined using **Equations. 2.12 and 2.13**.

5.4. Results and discussion:

5.4A Physico-chemical characterizations:

5.4A.1 XRD study:

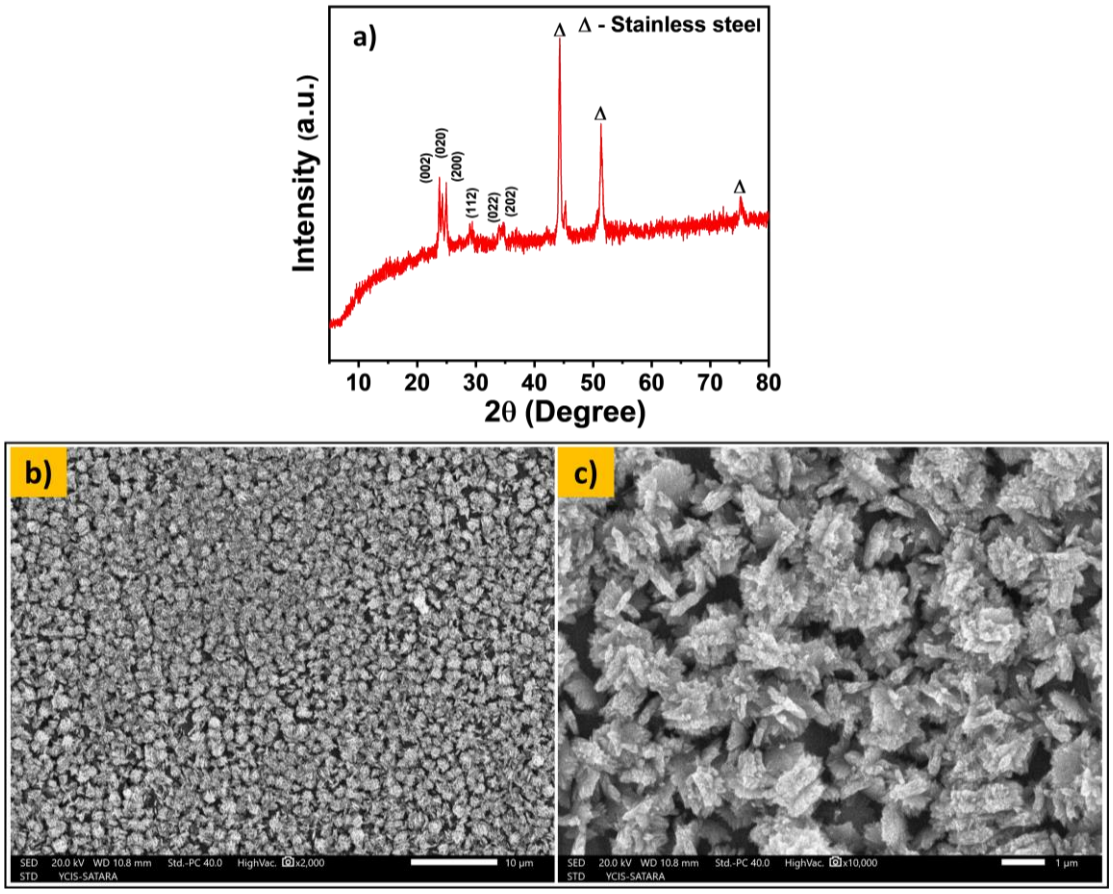

Fig. 5.1: a) The XRD pattern, and FE-SEM images at b) 2 KX, and c) 10 KX magnifications of WO_3 electrode.

The XRD pattern of WO_3 thin film is shown in **Fig. 5.1a**. The diffraction peaks are assigned to (002), (020), (200), (112), (022), and (202) crystallographic planes of monoclinic WO_3 (ICDD file no. 00-043-1035). The peaks identified by the sign 'Δ' are those of the SS substrate. The low intensity of the diffraction peaks indicates that WO_3 is nanocrystalline. The irregular arrangement of the particles in the thin film facilitates simple and quick intercalation/deintercalation of the electrolyte

ion inside the electrode material, which increases the number of accessible active sites and improves electrochemical activities **[25]**.

5.4A.2 FE-SEM study:

The surface morphology of WO_3 thin film is provided in **Fig. 5.1b and c** at a magnification of 2 KX and 10 KX, respectively. Uniform thin film formation is observed at a lower magnification whereas, at higher magnification, surface morphology shows interconnected nanoflakes with 1 μm length forming a flower-like pattern.

5.4A.3 BET study:

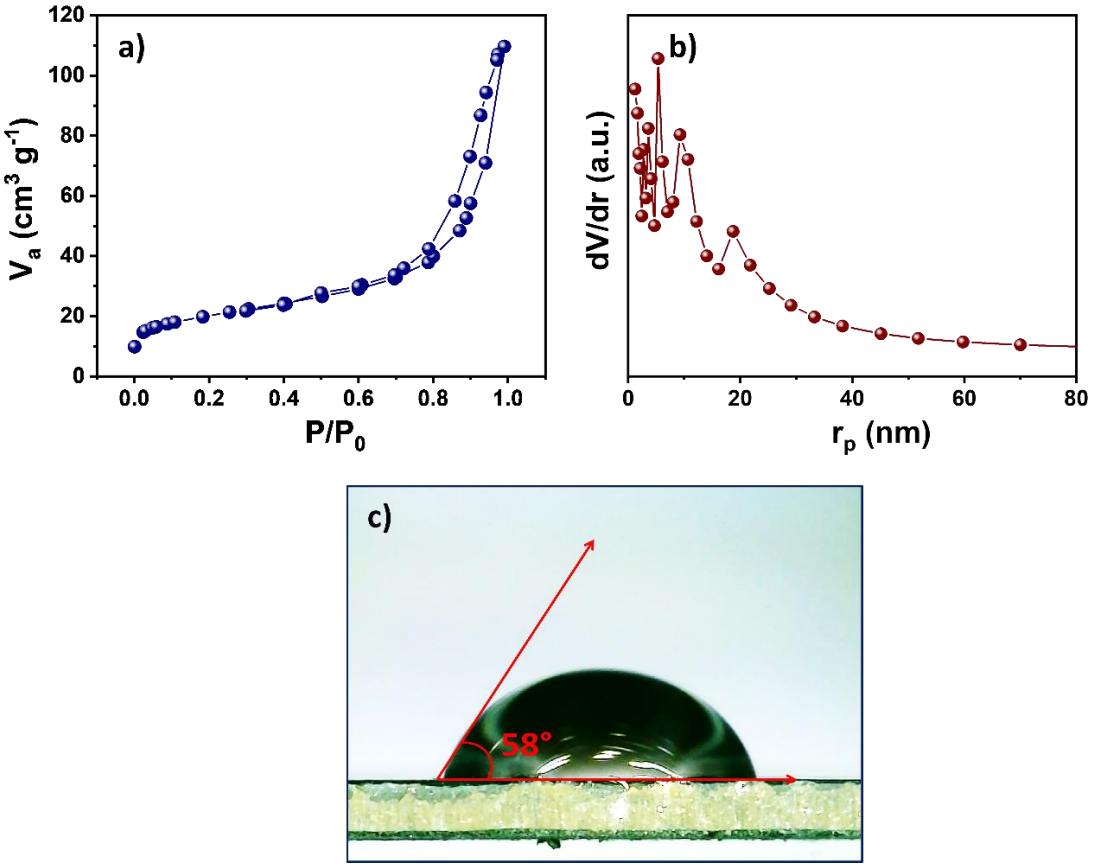

Fig. 5.2: a) The BET isotherm, b) pore size distribution curve, and c) contact angle image of WO_3 electrode.

It is widely known that the electrode charge storage capacity improves proportionately as the electrode material surface area rises. The N_2 adsorption and desorption isotherms are analyzed by the BET technique to determine the precise surface area of WO_3 film. **Fig. 5.2a** displays the BET isotherm for WO_3 sample. It shows the type-IV isotherm based on IUPAC standard, indicating a mesoporous

surface. According to the BJH technique, **Fig. 5.2b** shows the curves of pore size distribution. The WO_3 showed specific surface area of 54 m^2 g^{-1} with a mean pore diameter of 9.64 nm. The pore size enlargement provides easy access for ion conduction and decreases ion transport resistance, to enable a faster charge-discharge process and improved electrical conductivity as additional charges interacts with the surface **[26]**.

5.4A.4 Contact angle study:

The contact angle image of WO_3 thin film is displayed in **Fig. 5.2c**. The hydrophilic behaviour of WO_3 film is indicated by the contact angle value of 58°. This kind of surface facilitates lower resistance during electrochemical processes.

5.4B Electrochemical characterizations:

5.4B.1 The CV study:

The electrochemical characteristics of WO_3 thin film were measured in 1 M H_2SO_4. The charge storage mechanism of WO_3 was studied using CV techniques **(Fig. 5.3a)**. The CV curves at various scan rates, from 5 to 100 mV s^{-1}. In relation to the 5, 10, 20, 50, and 100 mV s^{-1} scan rates, the values of C_s are 620, 567, 506, 418, and 328 F g^{-1}, respectively. The C_s of WO_3 electrode is comparable with previously reported literature; for instance, Gupta et al. **[27]** prepared WO_3 using wet chemical method and achieved a C_s of 606 F g^{-1}. Liu and coworkers **[28]** prepared WO_3 by grafting hydrothermal method, which exhibited C_s of 2552 mF cm^{-2}. Zheng et al. **[29]** synthesized by hydrothermal method and achieved a C_s of 538 F g^{-1}. Kariper et al. **[23]** developed WO_3 nano-sized particles using CBD method and exhibited C_s of 588 F g^{-1}. This leads to the conclusion that WO_3 electrode synthesized using CBD method improved electrochemical characteristics than than earlier reported WO_3 electrodes. The C_s variation with scan rate for WO_3 electrode is displayed in **Fig. 5.3b**. The decreased C_s value is associated with a smaller interaction time that cannot enable maximum contribution from the electrode at higher scan rates.

5.4B.2 The GCD study:

The GCD plots of WO_3 electrode at various current densities from 2 to 6 A g^{-1} are shown in **Fig. 5.3c**. The quasi-triangular charge-discharge curves indicate a faradic transformation, confirming the pseudocapacitive nature of the material. There is a direct correlation between the applied voltage and the electrode charge **[30]**. As

the current density increased from 2 and 6 A g^{-1}, C_s of WO_3 thin film electrodes changed from 446 to 291 F g^{-1}. The nanoflakes-like structure allows for a rapid charge transfer and gives the highest C_s.

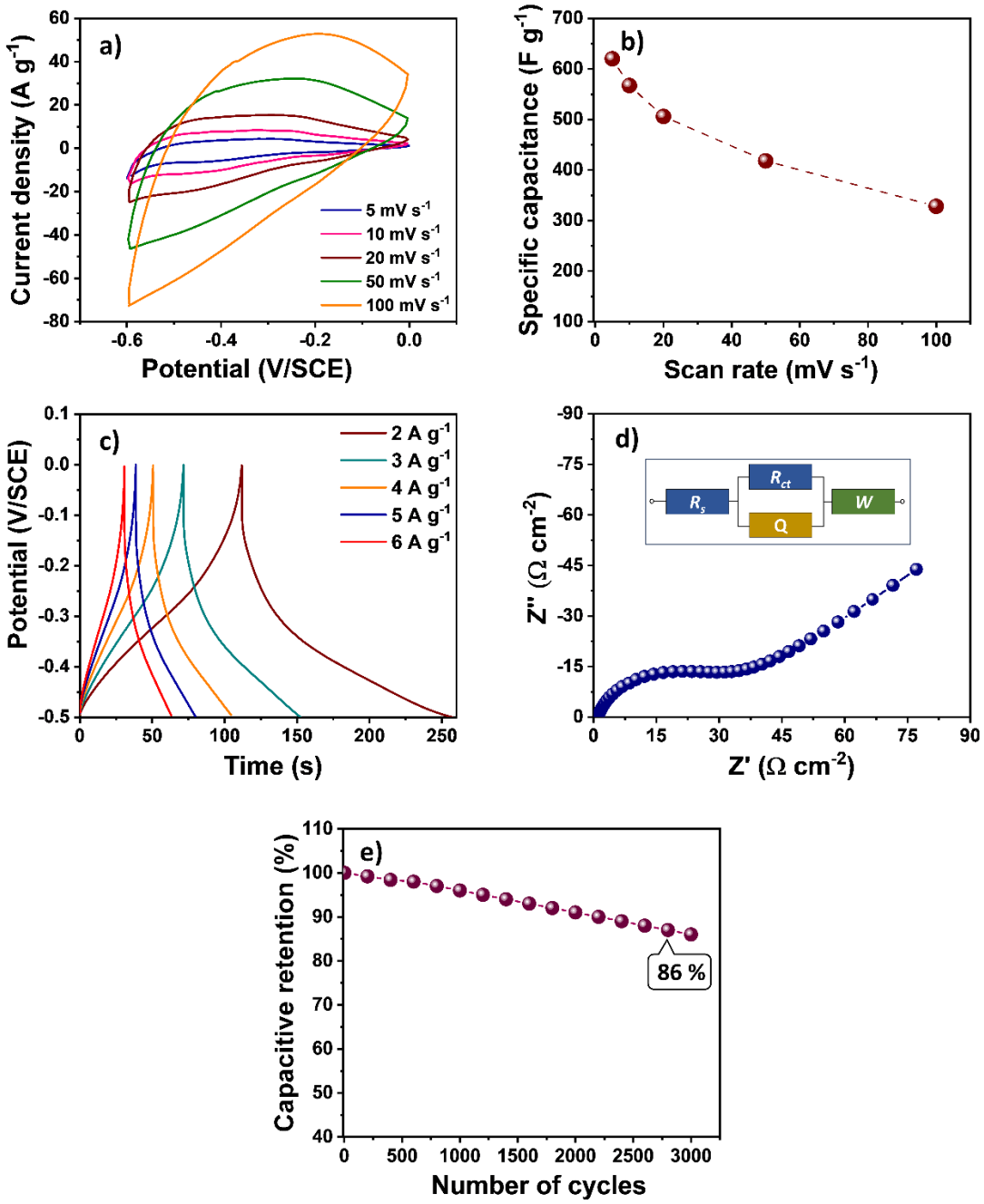

Fig. 5.3: a) The CV curves at different scan rates, b) the variation of the specific capacitance with various scan rate, c) the GCD plots at different current densities, d) the Nyquist plot (the inset shows fitted equivalent circuit), and e) the stability over 3,000 cycles of WO_3 electrode.

5.4B.3 The EIS study:

The electrochemical impedance characteristic was evaluated using the EIS study of WO_3 electrode and Nyquist plots are displayed in **Fig. 5.3d**. The role of charge transfer in energy storage is evaluated using EIS measurements. The equivalent circuit utilized to match the EIS data by an R_s, R_{ct}, W, and Q is illustrated in the inset of **Fig. 5.3d**. It revealed that WO_3 electrode exhibited lower R_s and R_{ct} values of 0.6 and 29 Ω cm^{-2}, respectively. Notably, WO_3 synthesized by CBD method showed lower R_s value as compared to the previous studies. Gupta et al. **[27]** prepared WO_3 electrode by wet chemical method and exhibited R_s of 1.45 Ω cm^{-2}. Shinde and coworkers **[31]** prepared WO_3 electrode using hydrothermal method and achieved 1.85 Ω cm^{-2} R_s value. Yao al. **[32]** synthesized WO_3 via hydrothermal method, which exhibited R_s of 2.61 Ω cm^{-2}. A WO_3 nanotube bundles as electrode materials developed via hydrothermal method was reported by Wu and coworkers **[33]** with exhibited R_s of 0.79 Ω cm^{-2}. These lower R_s value show that the excellent properties of WO_3 electrode for supercapacitors because of its higher diffusion of ions and electrical conductivity **[34]**. The electrolyte ions diffusion within the pores on the electrode surface is shown by the value of W (6.9 Ω cm^{-2}).

5.4B.4 The stability study:

For selecting an electrode material for a supercapacitor, one of the most essential factors is cyclic stability. The chemical stability of material is influenced by several factors, including composition of material, concentration, working potential window, electrolyte type, and current density during charging and discharging **[35]**. The stability of WO_3 electrode during electrochemical cycling is further studied for 3,000 GCD cycles, and corresponding capacitive retention is plotted in **Fig. 5.3e**. After 3,000 cycles, WO_3 electrode exhibited good capacitive retention of 86%.

5.5 Conclusions:

In summary, CBD method was used to synthesize WO_3 electrode on a SS substrate. The FE-SEM analysis showed interlinked nanoflakes-like surface morphology. With a contact angle of 58°, WO_3 thin film showed hydrophilic properties. Furthermore, WO_3 electrode demonstrated C_s of 620 F g^{-1} at a scan rate of 5 mV s^{-1}. The WO_3 electrode exhibited low resistance parameters, including R_s (0.6 Ω cm^{-2}) and R_{ct} (29 Ω cm^{-2}) and over 3,000 GCD cycles, 86% of the capacitance was

retained. This study indicates that, effective C_s and lower resistive parameters of WO_3 electrode make it the best candidate as an anode in the fabrication of ASC devices with CPs.

References:

[1] S. Bokhari, Y. Hao, A. Siddique, Y. Ma, M. Imtiaz, R. Butt, P. Hui, Y. Li, S. Zhu, Results Mater., 1, (2019), 100007-100012.

[2] Q. Wang, H. Song, W. Li, S. Wang, L. Liu, T. Li, Y. Han, J. Power Sources, 517, (2022), 230737-230747.

[3] A. Zardkhoshoui, S. Davarani, A. Asgharinezhad, Dalton Trans., 48, (2019), 4274-4282.

[4] P. Pazhamalai, K. Krishnamoorthy, S. Sahoo, S. Kim, Electrochim. Acta, 295, (2019), 591-598.

[5] S. Sadavar, N. Padalkar, R. Shinde, A. Patil, U. Patil, V. Magdum, Y. Chitare, S. Kulkarni, R. Bulakhe, V. Parale, J. Gunjakar, ACS Appl. Energy Mater., 5, (2022), 2083-2095.

[6] M. Iqbal, M. Faisal, S. Ali, S. Farid, A. Afzal, Electrochim. Acta, 346, (2020), 36039-36085.

[7] Z. Lu, D. Xuan, D. Wang, J. Liu, Z. Wang, Q. Liu, D. Wang, Y. Ye, Z. Zheng, S. Li, New J. Chem., 45, (2021), 9230-9242.

[8] L. Yue, S. Zhang, H. Zhao, Y. Feng, M. Wang, L. An, X. Zhang, J. Mi, Solid State Ion., 329, (2019), 15-24.

[9] A. Anwer, M. Ansari, F. Mashkoor, S. Zhu, M. Shoeb, C. Jeong, J. Alloys Compd., 955, (2023), 170038-170052.

[10] S. Khot, D. Malavekar, R. Nikam, S. Ubale, P. Bagwade, D. Patil, V. Lokhande, C. Lokhande, Synth. Met., 287, (2022), 117075-117088.

[11] S. Ubale, R. Bulakhe, V. Mane, D. Malavekar, I. In, C. Lokhande, J. Electroanal. Chem., 897, (2021), 115589-115607.

[12] H. Liang, H. Jia, T. Lin, Z. Wang, C. Li, S. Chen, J. Qi, J. Cao, W. Fei, J. Feng, J. Colloid Interface Sci., 554, (2019), 59-65.

[13] R. Chandrashekhar and A. Yadav, Ph. Transit., 96, (2023), 196-215.

[14] G. Mineo, E. Bruno, S. Mirabella, Nanomater., 13, (2023), 1418-1439.

[15] P. Shinde and S. Jun, ChemSusChem., 13, (2020), 11-38.

[16] C. Wu, Y. Zhang, L. Yang, B. Xiao, A. Jiao, K. Li, T. Chen, Z. Huang, H. Lin, Langmuir, 38, (2022), 15506-15521.

[17] V. Quy, I. Jo, S. Kang, K. Ahn, J. Ind. Eng. Chem., 94, (2021), 264-271.

[18] S. Patil, R. Nikam, C. Lokhande, R. Patil, J. Mater. Sci.: Mater. Electron., 34, (2023), 1956-1973.

[19] F. Tehrani, H. Ahmadian, M. Aliannezhadi, Mater. Res. Express., 7, (2020), 015911-015920.

[20] M. Jamali and F. Tehrani, Mater. Sci. Eng. B., 270, (2021), 115221-115229.

[21] D. Malavekar, S. Kale, V. Lokhande, U. Patil, J. Kim, C. Lokhande, J. Phys. Chem. C, 124, (2020), 28395-28406.

[22] Y. Kumar, S. Singh, D. Kulurumotlakatla, H. Kim, New J Chem., 44, (2020), 522-531.

[23] I. Kariper, F. Tezel, O. Gokkus, Phys. Lett. A, 388, (2021), 127059-127065.

[24] V. Lokhande, A. Lokhande, G. Namkoong, J. Kim, T. Ji, Results Phys., 12, (2019), 2012-2020.

[25] S. Ghosh, R. Santhosh, S. Jeniffer, V. Raghavan, G. Jacob, K. Nanaji, P. Kollu, S. Jeong, A. Grace, Sci. Rep., 9, (2019), 16315-16330.

[26] S. Bhosale, S. Kumbhar, S. Pujari, V. Patil, N. Kumar, R. Salunkhe, C. Lokhande, J. Gunjakar, U. Patil, J. Energy Storage, 72, (2023), 108417-108434.

[27] S. Gupta, H. Nishad, S. Chakane, S. Gosavi, D. Late, P. Walke, Nanoscale Adv., 2, (2020), 4689-4701.

[28] X. Liu, Q. Yang, L. Yuan, D. Qi, X. Wei, X. Zhou, S. Chen, L. Cao, Y. Zeng, J. Jia, C. Wang, J. Chem. Eng., 425, (2021), 131431-131444.

[29] F. Zheng, J. Wang, W. Liu, J. Zhou, H. Li, Y. Yu, P. Hu, W. Yan, Y. Liu, R. Li, Q. Zhen, Electrochim. Acta, 334, (2020), 135641-135682.

[30] P. Katkar, S. Marje, V. Parale, C. Lokhande, J. Gunjakar, H. Park, U. Patil, Langmuir, 37, (2021), 5260-5274.

[31] P. Shinde, A. Lokhande, A. Patil, C. Lokhande, J. Alloys Compd., 770, (2019), 1130-1137.

[32] S. Yao, X. Zheng, X. Zhang, H. Xiao, F. Qu, X. Wu, Mater. Lett., 186, (2017), 94-101.

[33] X. Wu and S. Yao, Nano Energy, 42, (2017), 143-150.

[34] F. Zheng, C. Xi, J. Xu, Y. Yu, W. Yang, P. Hu, Y. Li, Q. Zhen, S. Bashir, J. Liu, J. Alloys Compd., 772, (2019), 933-942.

[35] Q. Wu, T. He, Y. Zhang, J. Zhang, Z. Wang, Y. Liu, L. Zhao, Y. Wu, F. Ran, J. Mater. Chem., 43, (2021), 24094-24147.

CHAPTER – VI

Fabrication and performance evaluation of flexible solid-state ASC devices based on rGO/PANI and rGO/Ppy thin films

CHAPTER – VI

Fabrication and performance evaluation of flexible solid-state ASC devices based on rGO/PANI and rGO/Ppy thin films

6.1 Introduction:

Recent energy storage systems use the lightweight, portable supercapacitors for their fabrication **[1, 2]**. Supercapacitors offer applications in wearable, portable, and commercialized pocket electronic devices due to their mechanical flexibility, small size, low cost, and environmentally safe energy storage **[3, 4]**. Energy storage systems require improved S_E and S_P through the use of various electrode materials and electrolytes. Enhancing the device working voltage may be achieved effectively using the asymmetric configuration of the supercapacitor **[5]**. In order to improve the supercapacitor devices S_E, an asymmetric configuration of supercapacitors is more desirable over a symmetric one **[6-9]**. Different combinations of the cathode and anode, such as NiCoLDH//Fe_2O_3 **[10]**, MWCNTs/MnO_2 **[11]**, $NiWO_4$//Fe_2O_3 **[12]**, rGO//NiV_2O_6 **[13]**, NiO, and $NiCo_2O_4$ **[14]**, have been described in the literature. Polymer gel electrolytes based supercapacitors have many advantages like reduced size, leakage-free systems, effective ionic separators, exceptional electrochemical stability over a larger range, and flexible supercapacitor configurations **[15]**.

The CPs electrodes, including PANI and Ppy, can operate in a broad potential range. Thus, combining polymeric gel electrolytes with these electrode materials can significantly improve flexible supercapacitor performance. The WO_3 electrode is the best candidate as an anode electrode in the fabrication of flexible solid-state ASC device due to effective C_s and lower resistive parameters of WO_3 electrode as compared to carbon-based materials. Additionally, easy synthesis process, low price, and interesting redox properties of CPs based electrodes making them suitable for developing flexible solid-state ASC devices **[16, 17]**.

In this chapter, flexible solid-state ASC devices is built with rGO/PANI and rGO/Ppy composite electrodes as the cathode, a WO_3 as the anode, and PVA-H_2SO_4 gel as an electrolyte as well as a separator. This chapter covers the development and electrochemical performance analysis of flexible solid-state ASC devices in the configuration of rGO/PANI/PVA-H_2SO_4/WO_3 and rGO/Ppy/PVA-H_2SO_4/WO_3.

6.2 Experimental details:

6.2.1 Introduction:

This section explains the electrode synthesis (rGO/PANI, rGO/Ppy, and WO_3), polymer gel electrolyte (PVA-H_2SO_4) preparation and fabrication of rGO/PANI/PVA-H_2SO_4/WO_3 and rGO/Ppy/PVA-H_2SO_4/WO_3 flexible solid-state ASC devices.

6.2.2 Electrode preparation:

The rGO/PANI thin films were synthesized using CBD method, while rGO/Ppy thin films were prepared on flexible SS substrates using SILAR method. Chapters III and IV provide the optimized preparative parameters for rGO/PANI and rGO/Ppy thin film electrodes, respectively. The CBD method was used to produce WO_3 thin film electrode on a flexible SS substrate and optimized preparative parameters of WO_3 electrode was described in chapter V.

6.2.3 Preparation of polymer gel electrolyte:

For manufacturing the flexible solid-state ASC devices, a gel electrolyte with H_2SO_4 was prepared using water soluble PVA polymer. To make the gel electrolyte, 3 g of PVA in 30 mL of DDW was dissolved and stirred constantly for 4 h at 333 K. Following that, 20 mL of a 1 M H_2SO_4 solution was simply added and the resultant mixture was rapidly stirred for 6 h until a transparent viscous appearance was achieved **[18]**. The PVA-H_2SO_4 gel electrolyte was applied to the electrodes to fabricate rGO/PANI/PVA-H_2SO_4/WO_3 and rGO/Ppy/PVA-H_2SO_4/WO_3 devices. The evaporation rate of the electrolyte was reduced due to gel formation, which increased the device cycle life.

6.2.4 Fabrication of flexible solid-state ASC devices:

The flexible solid-state ASC device was built using flexible electrodes consisting of rGO/PANI (cathode) and WO_3 (anode). Electrodes measuring 5×5 cm^2 were utilized and plastic tape is used to seal edges to avoid short connections. The entire electrode was coated with the polymer gel electrolyte, and was then allowed to dry at ambient temperature. After drying, polymer gel electrolyte was applied to electrodes to ensure appropriate contact with the electrolyte. After that, translucent plastic strips were used to pack the electrodes tightly to prevent any leaks. Then for 3 h, the device was kept at 1 ton of pressure in a hydraulic press. For rGO/Ppy/PVA-H_2SO_4/WO_3 ASC device, the same procedure was used.

6.2.5 Electrochemical characterization of flexible solid-state ASC devices:

In order to find an appropriate operating potential window of flexible solid-state ASC devices, CV and GCD studies were carried out at varying scan rates and current densities, respectively. **Equations 1.2 and 1.3** were utilized to find out ASC

device S_E (Wh kg^{-1}) and S_P (W kg^{-1}), respectively. The CV curves were conducted at various bending angles in order to assess the flexibility of ASC devices. The ASC devices cycling stability was examined over 5,000 cycles of CV and GCD studies.

6.3. Results and discussion:

6.3A Electrochemical studies of flexible solid-state rGO/PANI/PVA-H_2SO_4/WO_3 ASC device:

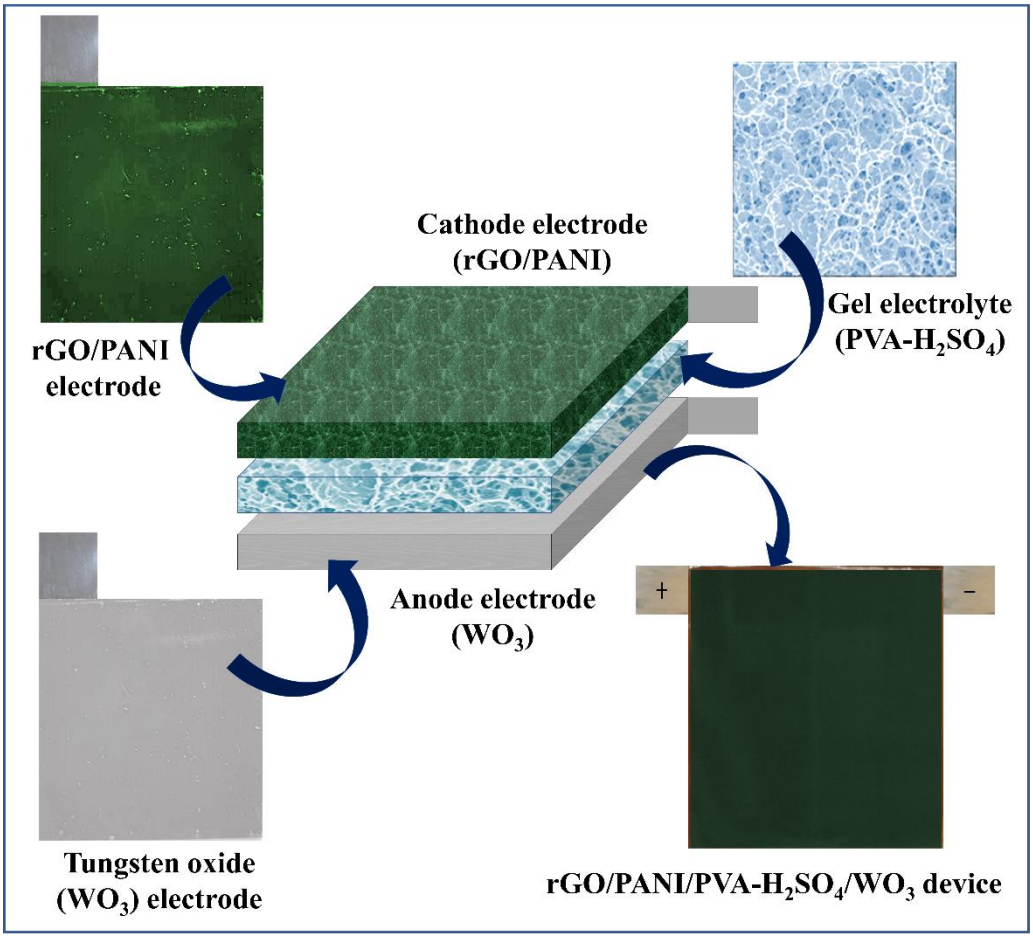

Fig. 6.1: Schematic of fabrication of flexible solid-state rGO/PANI/PVA-H_2SO_4/WO_3 ASC device.

The ASC was designed to explore the applicability of rGO/PANI electrode in supercapacitor device. This ASC device was built with rGO/PANI as a cathode, WO_3 as an anode, and a polymer based PVA-H_2SO_4 gel electrolyte. **Fig. 6.1** depicts the schematic of fabrication of ASC device. **Fig. 6.2a** depicts the CV curves for WO_3 and rGO/PANI electrodes at a scan rate of 50 mV s^{-1}. According to the three- electrode tests, the cathodic working potential window of rGO/PANI is from −0.2 to +0.8

V/SCE, whereas WO_3 electrode exhibits an anodic working potential window between −0.6 to 0.0 V/SCE. As a result, the designed ASC is able to perform within the 0.0 to +1.4 V working potential range. To accomplish high electrochemical performance of ASC device, charge balancing of two electrodes is essential. **Equation 2.11** was used to calculate the cathode to anode electrodes mass ratio. The mass ratio (m^+/m^-) of two electrodes was determined to be 0.32. Charge balancing is obvious when the combined charge value of two electrodes is the same, regardless of the quantity of deposited mass.

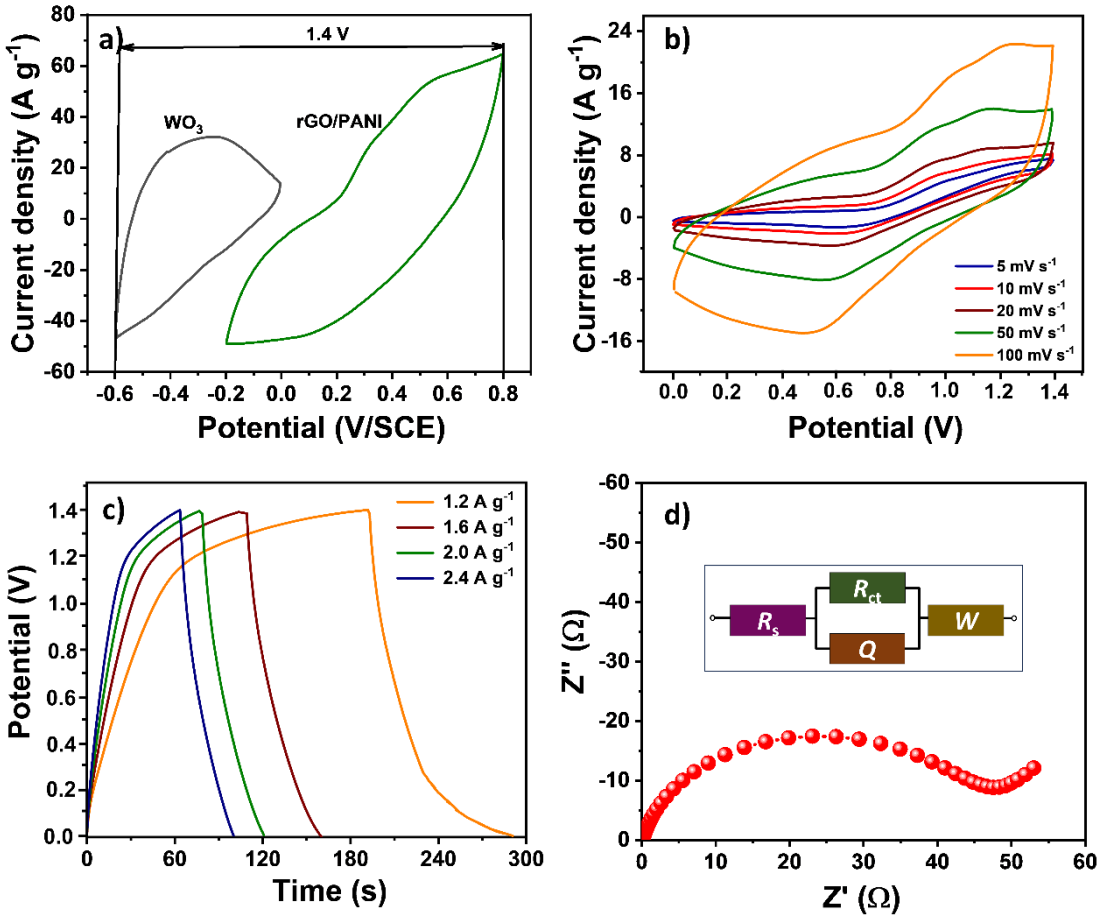

Fig. 6.2: a) Combined CV curves of WO_3 and rGO/PANI electrodes, and b) the CV curves at different scan rates, c) the GCD plots at different current densities, and d) the Nyquist plot (the inset shows an equivalent circuit) of rGO/PANI/PVA-H_2SO_4/WO_3 ASC device.

At a working voltage of +1.4 V, the device exhibits greater area enclosed by the CV curve, resulting in a probable increase in S_P and S_E. Therefore, CV curves of rGO/PANI/PVA-H_2SO_4/WO_3 within 0 to +1.4 V at scan rates of 5-100 mV s^{-1} are displayed in **Fig. 6.2b**. Even at measured scan rates, ASC gives typical

pseudorectangular CV shapes, implying pseudocapacitive behaviour with quick redox reaction kinetics of rGO/PANI and WO_3 electrodes. The C_s values for scan rates of 5, 10, 20, 50, and 100 mV s^{-1} are 117, 81, 62, 53, and 31 F g^{-1}, respectively. **Fig. 6.2c** displays the GCD curves of ASC device for current densities between 1.2 to 2.4 A g^{-1}. The greatest operating voltage for water based electrolytes varies with the electrode materials **[19]**. According to **Equation 2.12**, at a current density of 1.2 A g^{-1}, maximum C_s obtained from the GCD curve is 88 F g^{-1}. Bigdeli et al. **[20]** fabricated phosphor-doped graphene oxide (PGO)@PANI//AC ASC device and showed C_s of 27 F g^{-1}. Roy and coworkers **[21]** prepared V_2O_5-PANI//$NiMn_2O_4$ ASC device and achieved C_s of 71 F g^{-1}. The desired electrochemical performance is attributed to the complimentary impacts of the constituent electrode layered structures of pseudocapacitive PANI spikes and faradic rGO, which maintain their properties even at high current densities.

A Nyquist plot of rGO/PANI/PVA-H_2SO_4/WO_3 ASC device is depicted in **Fig. 6.2d**, and an inset displays a well fitted equivalent circuit. The high frequency portion of the Nyquist plot formed a semicircle, and virtually straight line at low frequency portion. The high frequency intercept with the X-axis reflected an R_s, it was computed as the sum of the intrinsic resistance of the active material, the electrode/electrolyte contact resistance, and the electrolyte solution resistance. The diameter of the semicircle in the high frequency zone was used to calculate the R_{ct}. However, at lower frequencies, the straight line displayed the ion diffusion behaviour in the electrode pores i.e. *W*. It revealed that ASC device showed a smaller R_s and R_{ct} values of 0.12 and 47 Ω, respectively. The small impedance value of ASC device indicates excellent contact between electrodes and PVA-H_2SO_4 gel electrolyte.
The electrochemical processes are improved by such minimal impedance without causing a significant ohmic loss at the interface of electrode and electrolyte **[22]**.

The corresponding C_s determined from CV curves for different scan rate are plotted in **Fig. 6.3a**. The C_s decreased with rising scan rate because of the fast operation of charge storage over the potential window **[23]**. **Fig. 6.3b** demonstrates the plots of C_s vs current density. The C_s decreased with current density because of the fast operation of charge storage over the potential window.

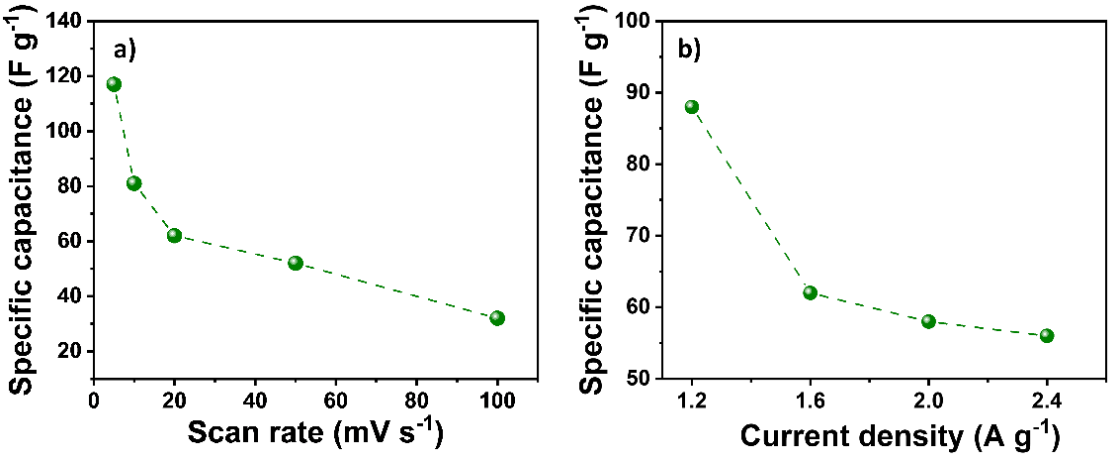

Fig. 6.3: Variation of specific capacitance with a) scan rate, and b) current density of rGO/PANI/PVA-H_2SO_4/WO_3 ASC device.

The life of the supercapacitor is one essential factor that lowers the cost of maintaining all portable electronic equipment and results in commercially viable appliances. The cycling stability of ASC studied by CV at 50 mV s^{-1} over 5,000 cycles is depicted in **Fig. 6.4a**. After 5,000 CV cycles the ASC provides 82% capacitive retention. The degradation in capacitive retention might be caused by a combination of the effect of active material delamination produced by ion insertion and insufficient device sealing. Rashti et al. **[24]** fabricated ASC device using $NiCo_2O_4$-PANI-rGO electrode and reported 78% stability retention over 3,500 cycles. Lee et al. **[25]** fabricated ASC device using PANI electrode and reported 80% cyclic retention after 3,000 cycles. Supercapacitors with liquid electrolytes have a relatively poor electrochemical stability because of electrolyte evaporation and chemical changes throughout cycling. Consequently, another option for liquid electrolyte has been developed such as quasi-solid polymer gel electrolyte. These electrolytes reduced rate of electrolyte evaporation results in long term stability.

To evaluate ASC device flexibility, the C_s were calculated at several bending angles from 0° to 160° **(Fig. 6.4b)**. The ASC device demonstrated 93% capacitive retention at a 160° bending angle. Inset of **Fig. 6.4b** shows CV curves at various bending angles. Additionally, the S_E and S_P values of ASC device are computed and displayed in **Fig. 6.4c**. The ASC device provided the largest S_E of 32 Wh kg^{-1} at 1152 W kg^{-1} of S_P. The estimated S_E and S_P values of ASC device are compared with earlier reported PAN supercapacitors such as, AC//PANI-M90 (14.7 Wh kg^{-1} at 378 W kg^{-1}) **[25]**, AC//MOF/PANI (23.11 Wh kg^{-1} at 1600 W kg^{-1}) **[26]**, PANI-$SrTiO_3$–

250//AC (13.2 Wh kg^{-1} at 299 W kg^{-1}) **[27]**, and PANI-$ZnCo_2O_4$//AC (13.25 Wh kg^{-1} at 375 W kg^{-1}) **[28]**. Among the ASC devices reported so far, the current rGO/PANI/PVA-H_2SO_4/WO_3 device achieved comparable S_E and S_P values.

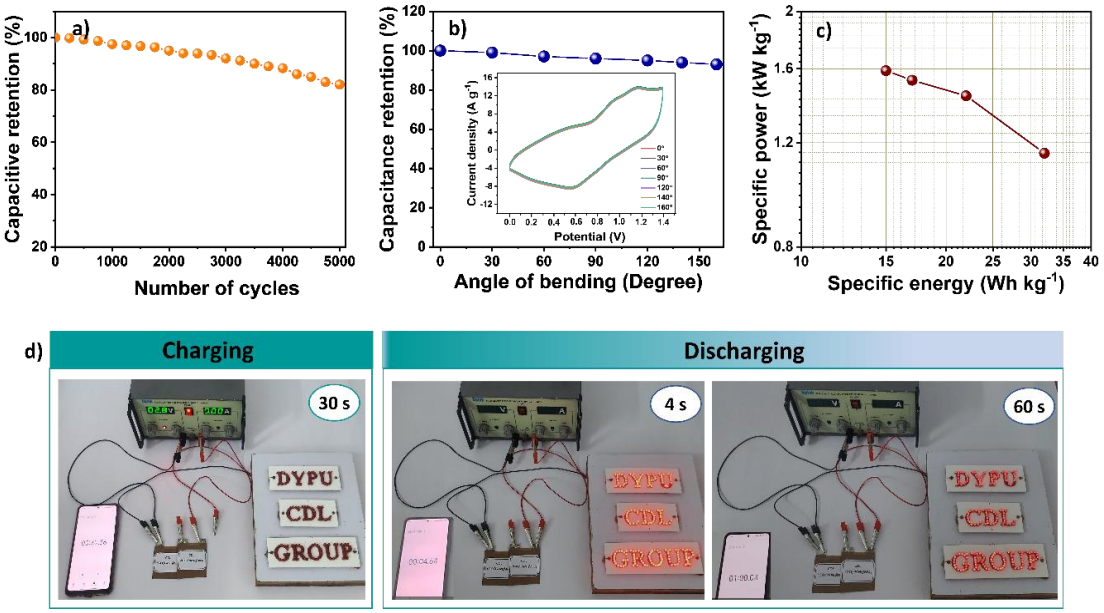

Fig. 6.4: a) The stability plot, b) capacitive retention after bending of the device at various bending angles (the inset shows the CV curves at various bending angles), c) the Ragone plot, and d) practical application to glow 201 red LEDs panel of rGO/PANI/PVA-H_2SO_4/WO_3 device.

To check the practical use of rGO/PANI/PVA-H_2SO_4/WO_3 device, two devices were connected in series, and charged at 2.8 V for 30 s. Two ASC devices in series easily light up 201 light emitting diodes (LEDs) for 60 s **(Fig. 6.4d)**. This study demonstrated the practical use of rGO/PANI/PVA-H_2SO_4/WO_3 device in various portable electronic devices. The exceptional charge storage capacity is shown by the reported initial output power of 25.2 mW cm^{-2}.

6.3B Electrochemical studies of flexible solid-state rGO/Ppy/PVA-H_2SO_4/WO_3 ASC device:

The ASC device was fabricated to evaluate the device level practical viability of prepared electrode utilizing two-electrode approach. The ASC device was assembled utilizing rGO/Ppy and WO_3 electrodes, which serve as a cathode and anode, respectively, and PVA-H_2SO_4 as a quasi-solid gel electrolyte. **Fig. 6.5** shows the schematic of fabrication of an ASC device with the configuration of

rGO/Ppy/PVA-H_2SO_4/WO_3. The mass balancing **Equation 2.11** is utilized for calculating the proper mass ratio to the pair of both electrodes in order to enhance ASC device capacity to store energy.

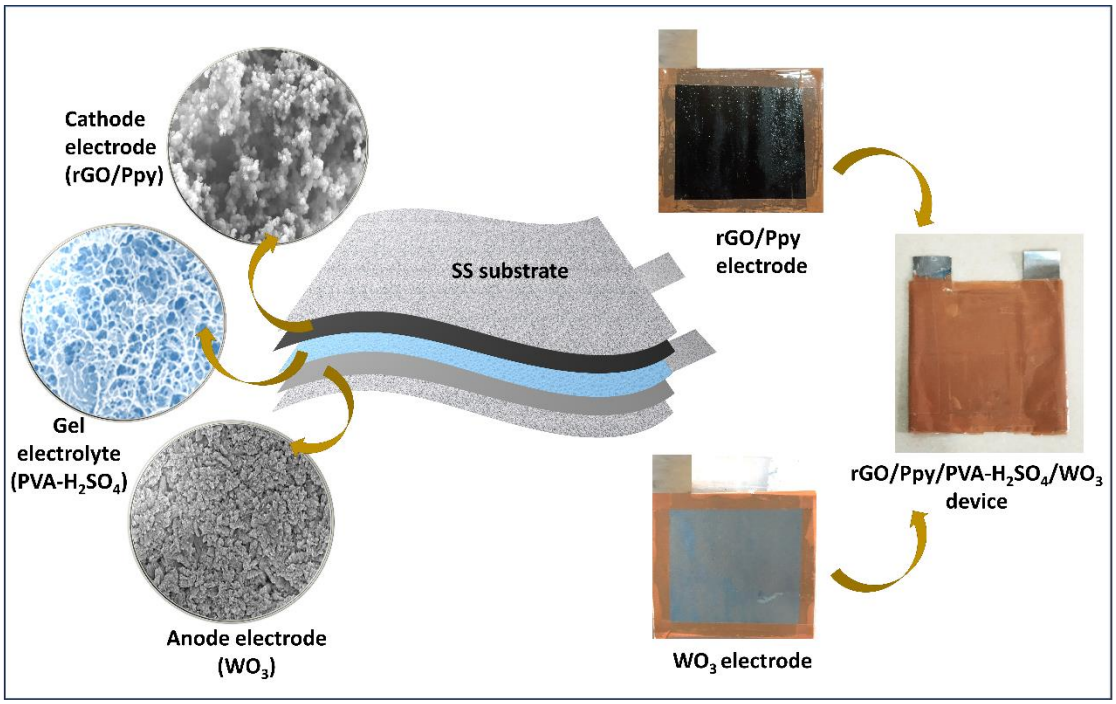

Fig. 6.5: Schematic of fabrication of rGO/Ppy/PVA-H_2SO_4/WO_3 ASC device.

The CV curves for multiple potentials (ranging between +0.8 to +1.3 V) are displayed in **Fig. 6.6a**, performed at a constant scan rate of 50 mV s^{-1} to optimize the electrochemical potential window of ASC. The working potential and the area covered by the CV curves are the most effects on the value of C_s. As illustrated in **Fig. 6.6b**, the CV profiles for the ASC device are acquired in a potential window of 0 to +1.3 V, at 5 to 100 mV s^{-1} scan rates. While charging or discharging occurs in the ASC device, $(SO_4)^{2-}$ ions from the electrolyte intercalate or de-intercalate at the interface of rGO/Ppy electrode, and at the same time, $(H)^+$ ions intercalate or de-intercalate at the interface of WO_3 electrode. According to CV profiles, the device C_s is 56 F g^{-1} at a 5 mV s^{-1} scan rate.

Similar to this, **Fig. 6.6c** shows the device relevant working potential (from +0.8 to +1.3 V) selection for GCD with a constant 2 A g^{-1} current density. Longer charge-discharge times signify more capacity for storing charge at +1.3 V in GCD plot, revealing that ASC device exhibits superior charge storing capability. **Fig. 6.6d** illustrates the device GCD curves for currents density between 1.2 and 2.0 A g^{-1},

across the working potential region of 0 to +1.3 V. According to calculations, the ASC maximum C_s is 49 F g^{-1} at a current density of 1.2 A g^{-1}.

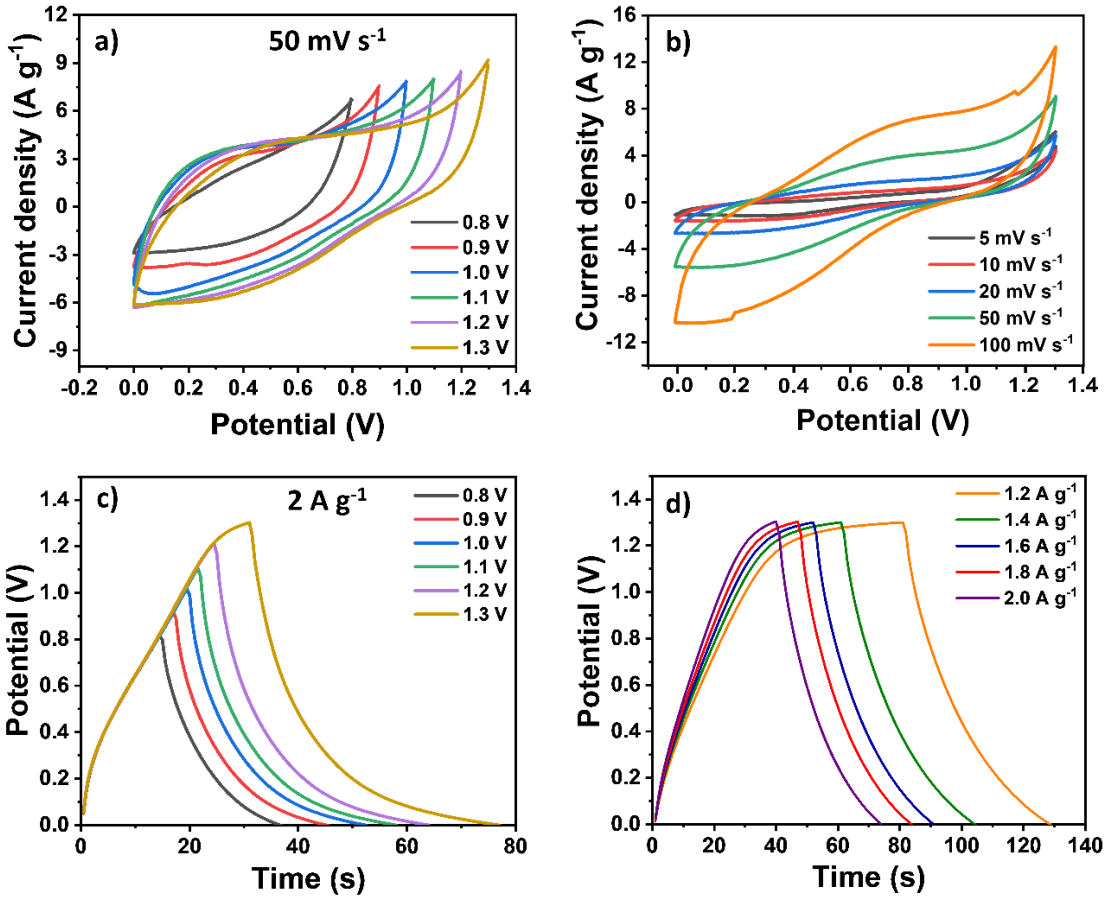

Fig. 6.6: a) The CV curves at different potential windows (+0.8 to +1.3 V), b) CV curves at scan rates from 5 to 100 mV s^{-1}, c) GCD plots at different potential windows (+0.8 to +1.3 V), and d) GCD plots at different current densities of rGO/Ppy/PVA-H_2SO_4/WO_3 ASC device.

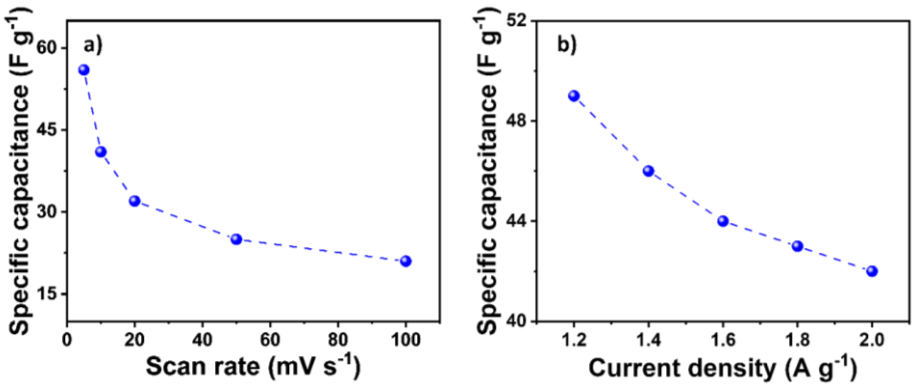

Fig. 6.7: Variation of specific capacitance with a) scan rate, and b) current density of rGO/Ppy/PVA-H_2SO_4/WO_3 ASC device.

Fig. 6.7a and b show the variation of C_s with scan rate and charging current density, respectively. The C_s decreased as the current density increased due to ion diffusion limitations during fast charging-discharging.

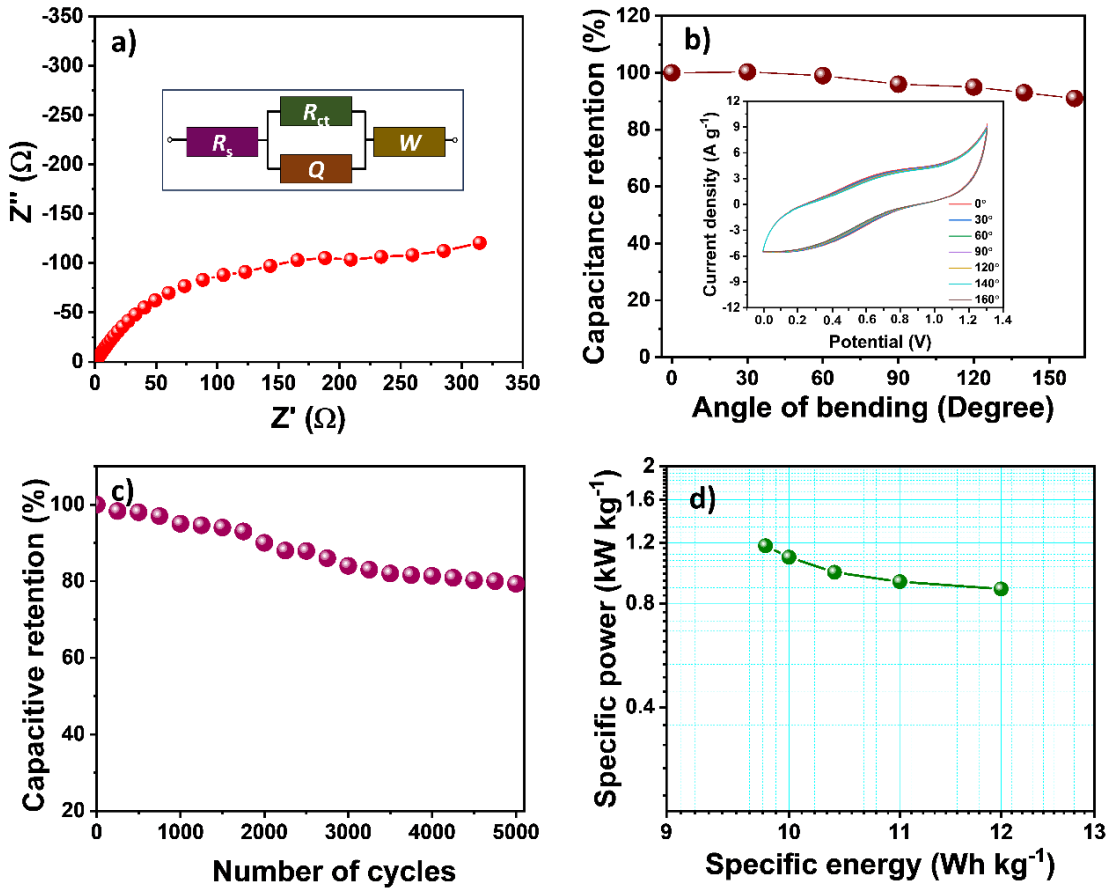

Fig. 6.8: a) Nyquist plot (inset shows fitted equivalent circuit), b) plot of capacitance retention after bending of the device at various bending angles (inset shows CV curves at various bending angles), c) plot of capacitive retention vs number of GCD cycles, and d) Ragone plot of rGO/Ppy/PVA-H_2SO_4/WO_3 ASC device.

Additionally, as seen in **Fig. 6.8a**, the EIS technique is utilized to compare the charge transfer mechanism of the ASC and the inset depicts the fitted equivalent circuit. The ASC displays minimum R_s (0.3 Ω) and R_{ct} (240 Ω) values. These lower R_s and R_{ct} values in ASC device reflect superior capacitive behaviour and good conductivity of rGO/Ppy and WO_3 electrodes. A higher R_{ct} value implies that the charge transfer to the electrode is more complicated. The layered electrode structure of rGO/Ppy provides increased electro-active sites for electrochemical processes and a vertical route for electron transfer and diffusion of ions; hence, it has good charge

transfer kinetics, indicated by a relatively low value of R_s and R_{ct}, resulting in an increase in surface conductivity **[29]**.

For supercapacitors to be used in a variety of portable electronic devices, their mechanical flexibility must be ensured without losing their electrochemical properties. To evaluate the effect of bending on the electrochemical characteristics and the charge storage of ASC device, CV at a 50 mV s^{-1} scan rate at different bending angles were measured. The device photographs at various bending angles are shown in **Fig. 6.9**. **Fig. 6.8b** illustrates the capacitance retention versus the bending angle, revealing that the device maintains 91% of its initial capacitance even when subjected to a twist at an angle of 160°. It was observed that the CV curves retain their form even when the device is bent at 160° angle (inset of **Fig. 6.8b**), indicating excellent contact between the active electrode material and the gel electrolyte as well as high adherence of the active electrode material to the current collector.

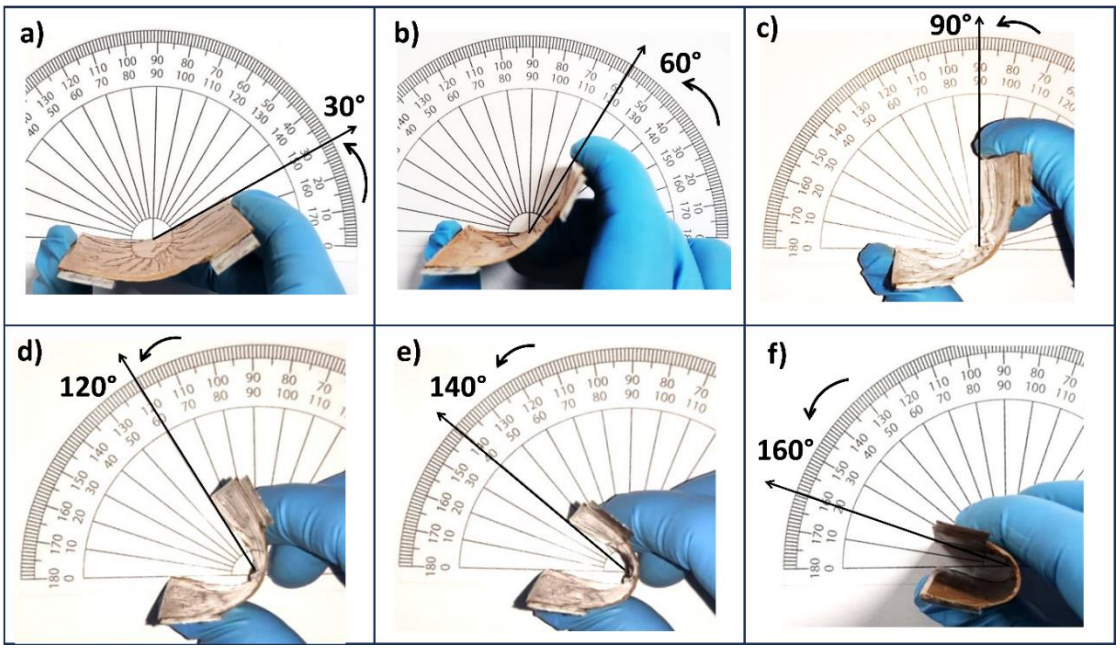

Fig. 6.9: Photographs of rGO/Ppy/PVA-H_2SO_4/WO_3 ASC device at various bending angles.

In addition to the mechanical flexibility, the ASC device has enhanced GCD cycling stability when tested at a 1.2 A g^{-1} current density over 5,000 cycles as shown in **Fig. 6.8c**. After 5,000 GCD cycles, the device capacitance maintained at 79% of its initial value, indicating a greater lifespan. Cycling can cause degradation of active components, resulting in a decrease in C_s value **[30]**. Khoh et al. **[31]** fabricated MnO_2/rGO/ITO//Ppy/rGO/ITO ASC device and reported 75% stability retention over

2,000 cycles. Yang et al. **[32]** fabricated Ppy-Ni//AC-Ni ASC device and achieved 82% capacitive retention after 2,000 cycles.

The crucial parameters for assessing the practical applications of supercapacitor devices are S_E and S_P. In this instance, estimated S_E and S_P using the formulas from **Equations 1.2 and 1.3**, respectively are represented in the Ragone plot **(Fig. 6.8d)**. The highest S_E is estimated to be 12 Wh kg^{-1} at 881 W kg^{-1} S_P. Additionally, the S_E remains substantial, reaching up to 9.8 Wh kg^{-1}, with an equivalent maximal S_P of 1176 W kg^{-1}. The estimated S_E and S_P values of ASC device are compared with earlier reported Ppy based supercapacitors. For example, Zhu et al. **[33]** fabricated device using Ppy/rGO electrode and reported S_E of 7 Wh kg^{-1} at 89 W kg^{-1}. Lim and coworkers **[34]** fabricated C-Ppy/graphene based device and obtained S_E of 8 Wh kg^{-1} at 115 W kg^{-1}. Chee et al. **[35]** assembled device using Ppy/GO/ZnO electrode and reported S_E of 10 Wh kg^{-1} at 258 W kg^{-1}. Majumder et al. **[36]** fabricated Ppy/CuO/Eu_2O_3-2 based device and showed S_E of 4 Wh kg^{-1} at 249 W kg^{-1}. Compared to other reported devices, the current ASC device obtained modest S_E with no substantial power consumption.

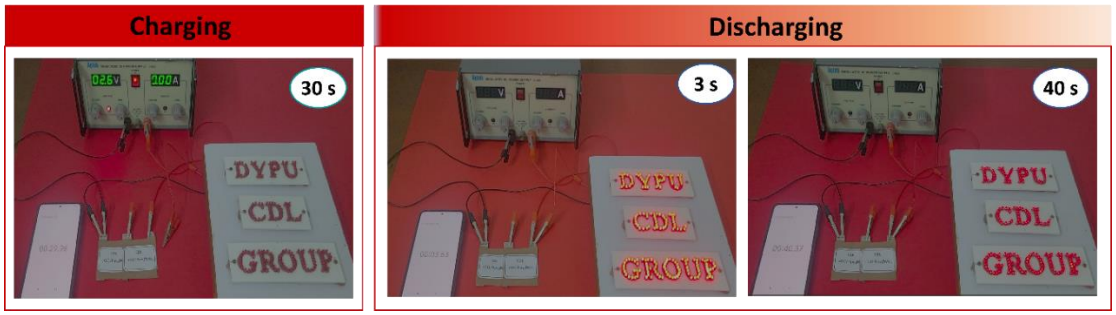

Fig. 6.10: Demonstration of glowing 201 LEDs panel using serially connected rGO/Ppy/PVA-H_2SO_4/WO_3 ASC device.

The ASC device practical application is exhibited using lightning LEDs from two series connected devices. The ASC devices glow up 201 red LEDs for 40 s after 30 s of charging. Photographs captured during the ASC device discharge are displayed in **Fig. 6.10**. At first, two series connected ASC devices were used to store 14.04 mW cm^{-2} of power.

6.4 Conclusions:

In conclusion, rGO/PANI/PVA-H_2SO_4/WO_3 flexible solid-state ASC device was built with rGO/PANI as a cathode, WO_3 as an anode, and a polymer based PVA-

H_2SO_4 gel electrolyte. In the same way, rGO/Ppy/PVA-H_2SO_4/WO_3 ASCs device was also assembled. The rGO/PANI/PVA-H_2SO_4/WO_3 ASC device demonstrated superior electrochemical characteristics, with a maximal C_s of 117 F g^{-1}, S_E of 32 Wh kg^{-1}, and S_P of 1152 W kg^{-1}. For rGO/Ppy/PVA-H_2SO_4/WO_3 ASC device, the C_s, S_E, and S_P were 56 F g^{-1}, 12 Wh kg^{-1} and 881 W kg^{-1}, respectively. Moreover, after 5,000 GCD cycles, rGO/PANI/PVA-H_2SO_4/WO_3 ASC device shown exceptional cycling stability of 82%, whereas rGO/Ppy/PVA-H_2SO_4/WO_3 ASC device demonstrated 79% cycling stability. These flexible solid-state ASC devices showed excellent high-rate capability and mechanical flexibility. In a practical demonstration, rGO/PANI/PVA-H_2SO_4/WO_3 and rGO/Ppy/PVA-H_2SO_4/WO_3 flexible solid-state ASC devices light up 201 red LEDs by connecting two devices in series (with an overall area of 5 × 5 cm^2). In the initial stage, 25.2 mW cm^{-2} of power was dissipated via rGO/PANI/PVA-H_2SO_4/WO_3 ASC device, and 14.04 mW cm^{-2} through rGO/Ppy/PVA-H_2SO_4/WO_3 ASC device. According to the results, rGO/PANI/PVA-H_2SO_4/WO_3 flexible solid-state ASC device shows better performance because of its large potential window. The present research shows that rGO/PANI and rGO/Ppy electrodes can be utilized as cathode materials to fabricate flexible solid-state ASC devices.

References:

[1] J. Goncalves, M. da Silva, M. Silva, P. Martins, E. Nossol, H. Toma, L. Angnes, Energy Adv., 1, (2022), 793-841.

[2] R. Choudhary, S. Ansari, B. Purty, J. Energy Storage, 29, (2020), 101302-101338.

[3] A. Beaucamp, M. Muddasar, T. Crawford, M. Collins, M. Culebras, Int. J. Biol. Macromol., 221, (2022), 1142-1149.

[4] W. Zhao, Y. Zheng, L. Cui, D. Jia, D. Wei, R. Zheng, C. Barrow, W. Yang, J. Liu, J. Chem. Eng., 371, (2019), 461-470.

[5] H. Heme, M. Alif, S. Rahat, S. Shuchi, J. Energy Storage, 42, (2021), 103018-103043.

[6] N. Chodankar, H. Pham, A. Nanjundan, J. Fernando, K. Jayaramulu, D. Golberg, Y. Han, D. Dubal, Small, 16, (2020), 2002806-2002841.

[7] D. Malavekar, S. Kale, V. Lokhande, U. Patil, J. Kim, C. Lokhande, J. Phys. Chem. C, 124, (2020), 28395-28406.

[8] J. Wang, Y. Cui, D. Wang, Adv. Mater., 31, (2019), 1801993-1802017.

[9] D. Dubal, N. Chodankar, D. Kim, P. Gomez-Romero, Chem. Soc. Rev., 47, (2018), 2065-2129.

[10] H. Liang, H. Jia, T. Lin, Z. Wang, C. Li, S. Chen, J. Qi, J. Cao, W. Fei, J. Feng, J. Colloid Interface Sci., 554, (2019), 59-65.

[11] N. Chodankar, S. Ji, D. Kim, J. Taiwan Inst. Chem. Eng., 80, (2017), 503-510.

[12] D. Patil, D. Malavekar, V. Lokhande, P. Bagwade, S. Khot, T. Ji, C. Lokhande, Energy Technol., 10, (2022), 2200295-2200310.

[13] Y. Li, H. Sun, Y. Yang, Y. Cao, W. Zhou, H. Chai, J. Colloid Interface Sci., 3, (2020), 298-307.

[14] L. Zhang, W. Zheng, H. Jiu, C. Ni, J. Chang, G. Qi, Electrochim. Acta, 215, (2016), 212-222.

[15] A. Lokhande, S. Teotia, A. Shelke, T. Hussain, I. Qattan, V. Lokhande, S. Patole, J. Kim, C. Lokhande, Chem. Eng., 1, (2020), 125711-125749.

[16] Y. Sui, Y. Ma, Y. Gao, J. Song, Y. Ye, H. Niu, W. Ma, P. Zhang, C. Qin, New J. Chem., 45, (2021), 10654-10663.

[17] J. Zhou, Q. Kang, S. Xu, X. Li, C. Liu, L. Ni, N. Chen, C. Lu, X. Wang, L. Peng, X. Guo, Nano Res., 15, (2022), 285-295.

[18] V. Mane, D. Malavekar, S. Ubale, R. Bulakhe, I. In, C. Lokhande, Electrochim. Acta, 335, (2020), 135613-135662.

[19] R. Tripathy, A. Samantara, J. Behera, Sustain. Energy Fuel, 5, (2021), 1184-1193.

[20] H. Bigdeli, M. Moradi, S. Borhani, E. Jafari, S. Hajati, M. Kiani, Physica E Low Dimens. Syst. Nanostruct., 100, (2018), 45-53.

[21] A. Roy, A. Ray, P. Sadhukhan, S. Saha, S. Das, Mater. Res. Bull., 107, (2018), 379-390.

[22] S. Sadavar, N. Padalkar, R. Shinde, A. Patil, U. Patil, V. Magdum, Y. Chitare, S. Kulkarni, R. Bulakhe, V. Parale, J. Gunjakar, ACS Appl. Energy Mater., 5, (2022), 2083-2095.

[23] B. Liang, Y. Chen, J. He, C. Chen, W. Liu, Y. He, X. Liu, N. Zhang, V. Roy, ACS Appl Mater Interfaces, 10, (2018), 3506-3514.

[24] A. Rashti, B. Wang, E. Hassani, F. Farshad., X. Zhang, T. Oh, Energy Fuel, 34, (2020), 6448-6461.

[25] C. Lee, F. Omar, A. Numan, N. Duraisamy, K. Ramesh, S. Ramesh, J. Solid State Electrochem., 21, (2017), 3205-3213.

[26] M. Iqbal, M. Faisal, S. Ali, S. Farid, A. Afzal, Co-MOF/polyaniline-based electrode material for high performance supercapattery devices, Electrochim. Acta, 346, (2020), 36039-36085.

[27] S. Shahabuddin, A. Numan, M. Shahid, R. Khanam, R. Saidur, A. Pandey, S. Ramesh, Ceram. Int., 45, (2019), 11428-11437.

[28] F. Omar, A. Numan, N. Duraisamy, S. Bashir, K. Ramesh, S. Ramesh, J. Alloys Compd., 716, (2017), 96-105.

[29] M. Parel, A. Gillado, M. Herrera, Surf. Interfaces, 10, (2018), 74-81.

[30] S. Marje, V. Patil, V. Parale, H. Park, P. Shinde, J. Gunjakar, C. Lokhande, U. Patil, J. Chem. Eng., 429, (2022), 132184-132199.

[31] W. Khoh and J. Hong, Colloids Surf. A: Physicochem. Eng. Asp., 456, (2014), 26-34.

[32] X. Yang, Z. Lin, J. Zheng, Y. Huang, B. Chen, Y. Mai, X. Feng, Nanoscale, 8, (2016), 8650-8657.

[33] J. Zhu, Y. Xu, J. Wang, J. Wang, Y. Bai, X. Du, Phys. Chem. Chem. Phys., 17, (2015), 19885-19894.

[34] Y. Lim, H. Lim, S. Lim, N. Huang, RSC Adv., 4, (2014), 56445-56454.

[35] K. Chee, H. Lim, I. Harrison, K. Chong, Z. Zainal, C. Ng, N. Huang, Electrochim. Acta, 157, (2015), 88-94.

[36] M. Majumder, R. Choudhary, A. Thakur I. Karbhal, RSC Adv., 7, (2017), 20037-20048.

CHAPTER – VII

Summary and conclusions

Summary and conclusions

In recent years, electrical energy storage devices are now more easily accessible, including batteries, capacitors, and supercapacitors. The supercapacitor can hold charge quickly and have a better S_P than batteries. The supercapacitors are commonly used in portable and wearable electronics, particularly medical and defence-related application. The batteries are not appropriate for use in portable electronic devices due to their short lifespan, minimal power, and safety concerns. In contrast, supercapacitors provide improved S_E, environmental storage of energy, greater S_P, and electrochemical cycle stability. Consequently, supercapacitor device is developing quickly as an alternative to capacitors and batteries. These days, supercapacitors are utilized in wide range of applications, including flash cameras, telecommunications, hybrid electric vehicles, and power backup supplies, etc. In hybrid electric vehicles, more power is needed to get started.

Hybrid electric vehicles rely on supercapacitors for their high starting power and energy. The supercapacitors have limits with aqueous electrolytes, such as smaller metal cations reduction potential and increased resistance to metal oxides. The novel energy storage supercapacitor device, the flexible solid-state ASC device, attracts attention because of its extended cycle life, high S_P, safety, and friendliness to the environment. Further research into electrode materials is needed to improve the performance of supercapacitors and address their limitations. The optimal active electrode materials combined with a supportable electrolyte effectively increases the flexible solid-state supercapacitor device power and energy capabilities quickly.

According to earlier studies, materials including metal oxides, CPs, and carbon-based materials improve the electrochemical properties of supercapacitor devices. CPs have special and significant characteristics, especially the capacity to change between redox states and strong electrical conductivity like metals. Thus, the fabrication of inexpensive and highly effective electrode materials of CPs family is necessary.

The present work describes, synthesis of CPs (PANI and Ppy) thin films using an easy, binder-free, and inexpensive chemical methods. The optimization of several preparative parameters resulted in a highly porous structure with a larger specific surface area, which significantly enhanced the electrochemical characteristics of PANI and Ppy thin films. The composite thin films showed better supercapacitor performance than PANI and Ppy thin films. As a result, for developing the flexible

solid-state ASC device, positive electrodes were composed of composite thin films exhibiting excellent electrochemical characteristics. Furthermore, WO_3 was utilized as a wide potential window negative electrode. The work was divided into VI chapters.

Chapter I provides an overview and literature review of several CPs electrode materials for supercapacitor application. It presents details on the methods used to extract energy from various energy sources. It emphasizes the importance of storing energy through renewable sources. This article describes the basics of energy storage devices, including capacitors, batteries, and supercapacitors. There are descriptions of the advantages of supercapacitors over batteries and capacitors based on power and energy densities. The importance of thin films and nanostructures in materials is briefly described.

The section provides a detailed explanation of the supercapacitor mechanism. This covers the essential requirements of supercapacitors, including the active electrode material. CPs play a significant role in supercapacitor application is described including contributions from non-faradaic and faradaic processes. Additionally, an overview of the literature on PANI and Ppy based electrode materials for use in supercapacitors. Also, the literature review on rGO based CPs electrodes for supercapacitors and their properties are included and lastly, the thesis purpose and orientation are addressed.

Chapter II covers the introduction to thin films, a brief classification of thin film deposition methods, the theoretical basis of CBD and SILAR methods, and related preparative parameters. Additionally, a variety of characterisation techniques are used in thin film structural and surface textural studies. Several characterisation techniques, including XRD, Raman spectroscopy, XPS, FE-SEM, BET, and contact angle measurement were utilized to assess the structural, morphological, and elemental compositional characteristics. Last section of this chapter addresses supercapacitors. It discusses the many types of supercapacitors, including symmetric, asymmetric, and hybrid capacitors. There includes a detailed explanation of the supercapacitive characteristics, such as cyclic voltammetry, galvanostatic charge-discharge and electrochemical impedance analysis.

In **Chapter III**, the effect of temperature on the physico-chemical characteristics and electrochemical properties of PANI thin films are studied. Chapter III covers the synthesis and characterisation of PANI thin films utilizing CBD method for evaluating electrochemical properties. The PANI films deposited at temperatures

of 263, 273, 303, and 323 K. PANI film thickness increases with temperature, achieving a maximum of 1.0 μm at 303 K. Additionally, the modified Hummer's method for rGO synthesis is discussed. This chapter also covers the composition of rGO with optimized PANI electrode using CBD method. The impact of rGO concentration on rGO/PANI thin film electrochemical properties was studied. The XRD and Raman analysis showed the formation of a rGO, PANI, and rGO/PANI thin films. The FE-SEM analysis revealed PANI spike-like surface morphology and composite film shows PANI spikes anchoring on rGO sheets. The PANI electrode synthesized at 303 K showed a maximum C_s of 816 F g^{-1} at a scan rate of 50 mV s^{-1}, and 85% capacitive retention after 3,000 GCD cycles. The introduction of rGO nanosheets into PANI material efficiently enhances surface area of composite thin films. Due to this, rGO/PANI composite electrode showed a highest C_s of 1130 F g^{-1} at a 5 mV s^{-1} scan rate in 1 M H_2SO_4 electrolyte and 92% cyclic stability after 3,000 GCD cycles. For P3 electrode, R_s and R_{ct} values were 0.2 and 0.80 Ω cm^{-2}, whereas rGO/PANI electrode were 0.13 and 0.41 Ω cm^{-2}, respectively. Therefore, by combining rGO and PANI in an appropriate ratio, it is possible to modify the structural and morphological characteristics and enhance C_s. In comparison with PANI and rGO thin films, this chapter highlights the advantages of rGO/PANI thin films.

Chapter IV addresses the synthesis and characterisation of Ppy and rGO/Ppy thin films using SILAR method. In rGO/Ppy thin films, the concentration of rGO in the composite film affects the electrochemical characteristics. Therefore, the effect of rGO concentration was examined. The effects of rGO on composition of chemical, crystal structure, appearance, surface, and electrochemical characteristics were examined. The rGO/Ppy thin films surface morphology varies based on rGO concentration. The spherical shaped particles of Ppy thin film modified to large voids and gaps randomly interlinked particles over rGO sheets. The rGO/Ppy thin film showed a significant number of spherical Ppy particles deposited over rGO sheets. The addition of 1 mg mL^{-1} rGO to rGO/Ppy composite resulted in larger pore size (21.3 nm), resulting in a porous structure with a remarkable specific surface area of 41 m^2 g^{-1}.

The supercapacitive characteristics of Ppy thin film were evaluated using CV, GCD, EIS, and cyclic stability study. The highest C_s of Ppy electrode was 331 F g^{-1} obtained at a scan rate of 5 mV s^{-1}. The quasi-triangular charge-discharge curves

indicate a faradic transformation, confirming the pseudocapacitive nature of Ppy material. The innate redox properties of rGO and Ppy, as well as their synergy, give enhanced electrochemical properties with the highest C_s of RP1.0 electrode was 803 F g^{-1} at a scan rate of 5 mV s^{-1}. The Ppy thin film stability significantly improved after rGO composition, increasing from 83 to 92% after 5,000 cycles. The rGO/Ppy composite electrode exhibited lower R_s and R_{ct} values of 0.15 and 98 Ω cm^{-2}, respectively as compared to Ppy electrode (0.90 and 209 Ω cm^{-2}). In conclusion, the highest specific surface area of rGO/Ppy material reduces ion diffusion resistance, and the greatest number of active sites exposed to the electrolyte improves penetration of electrolyte ion into electrode.

In **Chapter V**, WO_3 thin films are synthesized using CBD method and evaluating their electrochemical properties in 1 M H_2SO_4 electrolyte. The WO_3 thin film showed an average pore diameter of 9.64 nm and 54 m^2 g^{-1} specific surface area, which exhibited hydrophilic properties. Furthermore, WO_3 thin film demonstrated C_s of 620 F g^{-1} at a scan rate of 5 mV s^{-1}. The WO_3 thin film electrode nanostructured morphology, which consists of nanoflakes, is responsible for its low resistive properties, including R_s and R_{ct} (0.6 and 29 Ω cm^{-2}), and its cyclic stability of 86% over 3,000 GCD cycles.

Chapter VI describes the fabrication process and electrochemical analysis of rGO/PANI/PVA-H_2SO_4/WO_3 and rGO/Ppy/PVA-H_2SO_4/WO_3 flexible solid-state ASC devices. For the fabrication of ASC device, negative electrode material with excellent electrochemical properties is needed. Moreover, the production of solid-state PVA-H_2SO_4 gel electrolyte is discussed in this chapter. The rGO/PANI/PVA-H_2SO_4/WO_3 flexible solid-state ASC device exhibited an operational voltage of +1.4 V because to the distinct working potential windows of rGO/PANI and WO_3 electrodes. It achieved a C_s of 117 F g^{-1} and showed maximal S_E of 32 Wh kg^{-1} at S_P of 1152 W kg^{-1}. The rGO/PANI/PVA-H_2SO_4/WO_3 device obtained 82% capacitive retention after 5,000 CV cycles and high mechanical flexibility, sustaining 93% capacitance at a bending angle of 160°.

Likewise, a rGO/Ppy/PVA-H_2SO_4/WO_3 flexible solid-state ASC device working at potential window +1.3 V exhibited C_s of 56 F g^{-1} at a 5 mV s^{-1} scan rate. The device remarkable S_E (12 Wh kg^{-1}) and S_P (881 W kg^{-1}) show its capability for practical uses. The rGO/Ppy/PVA-H_2SO_4/WO_3 device showed 79% of capacitive retention over 5,000 GCD cycles and 91% after bending at an angle of 160°.

In conclusion, we have synthesized thin film electrodes of PANI, rGO/PANI, Ppy, rGO/Ppy, and WO_3 using binder-free, cost-effective chemical methods and examined their properties. **Table 7.1** summarizes the electrochemical characteristics of PANI, rGO/PANI, Ppy, rGO/Ppy, and WO_3. This table includes the material preparation method, surface morphology, C_s, electrolytes, R_s, R_{ct}, and cyclic stability of electrodes. Among the all electrodes, rGO/PANI electrode deposited by CBD method showed maximum C_s values of 1130 F g^{-1} than rGO/Ppy electrodes deposited by SILAR method. According to the EIS study, the extremely porous rGO/PANI electrode offers a lower R_{ct}, facilitating simple access for intercalation and deintercalation of ions. These results show that CBD deposited rGO/PANI electrode exhibited better supercapacitive performance than SILAR deposited rGO/Ppy electrodes.

Flexible solid-state ASC devices were built based on the excellent electrochemical characteristics of rGO/PANI, rGO/Ppy, and WO_3 film electrodes, and their supercapacitor characteristics were examined using CV, GCD, and EIS techniques. **Table 7.2** summarizes the electrochemical characteristics of rGO/PANI/PVA-H_2SO_4/WO_3 and rGO/Ppy/PVA-H_2SO_4/WO_3 flexible solid-state ASC devices. The flexible solid-state rGO/PANI/PVA-H_2SO_4/WO_3 ASC device exhibited maximum C_s of 117 F g^{-1} at a scan rate of 5 mV s^{-1}. The cost effective rGO/PANI and WO_3 electrodes based supercapacitors can be useful for various commercial applications in portable and foldable devices.

Table 7.1: The electrochemical properties of PANI, rGO/PANI, Ppy, rGO/Ppy, and WO_3 thin film electrodes deposited using CBD and SILAR methods in three-electrode system.

Material	**Method**	**Surface morphology**	**Electrolyte**	**Potential window (V/SCE)**	**C_s (F g^{-1})**	**R_s (Ω cm^{-2})**	**R_{ct} (Ω cm^{-2})**	**Stability (%) @ cycles**
P1	CBD	Spikes	1M H_2SO_4	-0.2 to +0.8	369	0.5	0.89	-
P2		Spikes		-0.2 to +0.8	376	0.5	0.88	-
P3		Spikes		-0.2 to +0.8	816	0.2	0.80	85@3,000
P4		Spikes		-0.2 to +0.8	242	0.6	1.3	-
rGO/PANI		Spikes on sheet-like structure		-0.2 to +0.8	1130	0.13	0.41	92@3,000
Ppy	SILAR	Spherical particles	1M H_2SO_4	-0.4 to +0.6	331	0.90	209	83@5,000
RP0.5		Spherical particles on sheet-like structure		-0.4 to +0.6	586	0.72	145	-
RP1.0		Spherical particles on sheet-like structure		-0.4 to +0.6	803	0.15	98	90@5,000
RP1.5		Spherical particles on sheet-like structure		-0.4 to +0.6	629	0.36	130	-
WO_3	CBD	Interconnected nanoflakes	1M H_2SO_4	-0.6 to 0	620	0.6	29	86@3,000

Table 7.2: The electrochemical parameters of flexible solid-state ASC devices evaluated using two-electrode system.

Configuration of flexible solid-state ASC device	**C_s (F g^{-1})**	**S_E (Wh kg^{-1}) at S_P (W kg^{-1})**	**R_s (Ω)**	**R_{ct} (Ω)**	**Stability (%) @ cycles**	**Flexibility (%) @160°**
rGO/PANI/PVA-H_2SO_4/WO_3	117	32 at 1152	0.12	47	82@5,000	93@160°
rGO/Ppy/PVA-H_2SO_4/WO_3	56	12 at 881	0.3	240	79@5,000	91@160°

CHAPTER – VIII

80-Recommendations

80-Recommendations

8.1 Recommendations:

In this study, CPs thin films particularly PANI and Ppy were synthesized using CBD and SILAR methods. The enhancement of surface area led to an improvement in these thin films ability to store charge. To achieve this, rGO was composited with PANI using CBD and Ppy using SILAR methods. In comparison to bare materials, the composite electrode was developed with the aim of increasing its stability and specific capacitance. The incorporation of rGO into the composite electrodes played a key role in enhancing their electrical conductivity and providing additional active sites for electrochemical reactions. This addition not only increased the charge storage capacity but also improved the cycling stability of the electrodes, making them more suitable for long-term energy storage applications. The flexible solid-state supercapacitor that was developed using these thin films possesses 32 Wh kg^{-1} energy density at 1152 W kg^{-1} power density.

Finally, it is recommended that PANI thin films exhibited superior electrochemical performance by CBD method, and Ppy thin films at 50 SILAR cycles. An optimum 1.0 mg mL^{-1} rGO concentration is for the best electrochemical properties. It concludes that CBD is a useful chemical method to improve rGO/PANI thin films supercapacitor properties. Furthermore, CBD offer expedient method for resulting nanofibers with a large surface area and good electrical conductivity, which have been useful for monitoring the porous surface morphology of rGO/PANI thin film. Additionally, CBD provides an easy method to produce nanofibers with a significant amount of surface area and high electrical conductivity, which have proved helpful for controlling rGO/PANI thin films porous surface morphology. The deposition methods simplicity and scalability make it suitable for industrial applications with few modifications.

8.2 Future findings:

This work used CBD and SILAR methods to synthesis CPs thin films and their composites with rGO. The addition of rGO enhances the pristine material entire electrochemical properties, specific surface area, and electrical conductivity. The future work is proposed as following:

- There are various carbon allotropes that may be utilized in place of rGO in the composition, such as fullerene, carbon nanotubes, carbon aerogel, and carbon foam.
- Furthermore, the addition of other transition metals (Ni, Co, and Cr) to produce a bimetallic compound may improve the electrochemical energy storage capabilities of CPs based electrode material.
- To better understand energy storage in CPs based materials, physical characterization techniques including XRD, FE-SEM, BET, and XPS may be used to examine changes in crystal structure, chemical composition, and surface morphology.
- Moreover, TEM and NMR in situ characterisation of ASC devices may provide more understanding of the actual charge storage mechanisms.

Patent

INTELLECTUAL PROPERTY INDIA
PATENTS | DESIGNS | TRADE MARKS
GEOGRAPHICAL INDICATIONS

सत्यमेव जयते

क्रम सं/SL No :022145459

पेटेंट कार्यालय,भारत सरकार | The Patent Office, Government Of India

पेटेंट प्रमाण पत्र | Patent Certificate

(पेटेंट नियमावली का नियम 74) | (Rule 74 of The Patents Rules)

पेटेंट सं. / Patent No.	:	542485
आवेदन सं. / Application No.	:	202321016608
फाइल करने की तारीख / Date of Filing	:	13/03/2023
पेटेंटी / Patentee	:	D.Y.PATIL EDUCATION SOCIETY (DEEMED TO BE UNIVERSITY)
आविष्कारकों का नाम /Name of Inventor(s)	:	1.PROF.CHANDRAKANT DNYANDEV LOKHANDE 2.MS.DIVYA CHANDRAKANT PAWAR 3.MR.AJINKYA GOVINDRAO BAGDE 4.MR.SURAJ RAVASAHEB SANKAPAL

प्रमाणित किया जाता है कि पेटेंटी को, उपरोक्त आवेदन में यथाप्रकटित *"METHOD OF SYNTHESIZING REDUCED GRAPHENE OXIDE/POLYANILINE COATING FOR ENERGY STORAGE APPLICATION THEREOF'* नामक आविष्कार के लिए, पेटेंट अधिनियम, 1970 के उपबंधों के अनुसार आज तारीख मार्च 2023 के तेरहवें दिन से बीस वर्ष की अवधि के लिए पेटेंट अनुदत्त किया गया है।

It is hereby certified that a patent has been granted to the patentee for an invention entitled *"METHOD OF SYNTHESIZING REDUCED GRAPHENE OXIDE/POLYANILINE COATING FOR ENERGY STORAGE APPLICATION THEREOF'* as disclosed in the above mentioned application for the term of 20 years from the 13th day of March 2023 in accordance with the provisions of the Patents Act,1970.

अनुदान की तारीख : 21/06/2024
Date of Grant :

पेटेंट नियंत्रक
Controller of Patents

टिप्पणी - इस पेटेंट के नवीकरण के लिए फीस, यदि इसे बनाए रखा जाना है, मार्च 2025 के तेरहवें दिन को और उसके पश्चात प्रत्येक वर्ष मे उसी दिन देय होगी।

Note. - The fees for renewal of this patent, if it is to be maintained, will fall / has fallen due on 13th day of March 2025 and on the same day in every year thereafter.

Publications

Journal of Energy Storage 79 (2024) 110154

Contents lists available at ScienceDirect

Journal of Energy Storage

journal homepage: www.elsevier.com/locate/est

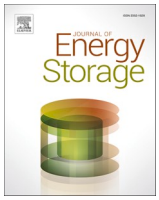

Research Papers

Facile synthesis of layered reduced graphene oxide/polyaniline (rGO/PANI) composite electrode for flexible asymmetric solid-state supercapacitor

D.C. Pawar [a], D.B. Malavekar [b], A.C. Lokhande [c], C.D. Lokhande [a,*]

[a] Centre for Interdisciplinary Research, D.Y. Patil Education Society, Kolhapur 416 003, India
[b] Optoelectronic Convergence Research Center, Department of Materials Science and Engineering, Chonnam National University, Gwangju 61186, South Korea
[c] Applied Quantum Materials Laboratory (AQML), Department of Physics, Khalifa University of Science and Technology, P.O. Box 127788, Abu Dhabi, United Arab Emirates

ARTICLE INFO

Keywords:
Asymmetric solid-state supercapacitor
Polyaniline
Reduced graphene oxide
Successive ionic layer adsorption and reaction method

ABSTRACT

For supercapacitors, composite electrodes with a combination of reduced graphene oxide and polyaniline (rGO/PANI) have gained a lot of attention due to their synergistic effects. In this study, rGO-PANI composite thin films were deposited on a stainless steel substrate with various mass loadings by successive ionic layer adsorption and reaction (SILAR) method. The specific surface area rises from 13 $m^2\ g^{-1}$ to 30 $m^2\ g^{-1}$ with the introduction of rGO. Due to the composition modification and specific surface area enhancement, the specific capacitance (capacity) of 1348 F g^{-1} (1255C g^{-1}) was obtained at 0.89 mg cm^{-2} mass deposition. Additionally, rGO/PANI/PVA-H_2SO_4/AC flexible asymmetric solid-state supercapacitor (ASSS) showed specific energy of 20 Wh kg^{-1} at specific power of 1198 W kg^{-1}. The device maintained almost 96 % of C_s at bending angle of 160° and 75 % over 5000 cycles. This work illustrates a simple way to improve the capacity and stability of PANI via rGO composition for supercapacitor applications.

1. Introduction

Production of a wide range of electronic devices that are helpful in several fields, including aircraft, military, business, agriculture, medicine, information technology, and others, highlights the significance of effective energy storage devices like Lithium-ion batteries and supercapacitors. Lithium-ion batteries enable our electronic devices to function throughout the day because they have a high energy density, but they might take hours to recharge if they run out. Electrochemical capacitors, also called supercapacitors, are used for quick power supply and recharging (i.e., high power density) [1]. Among the various energy storage technologies, supercapacitors have gained a lot of interest, especially because of their noteworthy qualities, including substantial power density, the ability to charge and discharge quickly, and an extended cycle life. The flexible supercapacitor has received considerable interest due to its mechanical flexibility and bending tolerance required in modern wearable electronic devices [2].

Based on the methods used for charge storage, supercapacitor materials are divided into electric double-layer capacitors (EDLC), and pseudocapacitor materials. The charge is stored in EDLC by electrolyte ions adhering to the electrode material surfaces. The pseudocapacitor charge-storage device primarily relies on transferring charge through redox reactions on the electrode surface and in the electrolyte. Hence, the term pseudocapacitance has been used to characterize the properties of an electrode that exhibits capacitor-like behavior in its electrochemical properties [3]. Only carbon-based materials consisting of graphene [4,5], carbon fibers [6], carbon aerogel [7], etc. have demonstrated desirable flexibility; as a result, they have been extensively explored for flexible supercapacitors. Conducting polymers (CPs) involve polyaniline (PANI), polypyrrole (Ppy), and polythiophene (PT), and transition metal compounds have also been largely composited and studied for supercapacitor applications due to their prominent energy storage properties [8–10].

In emerging materials, the two-dimensional and sp^2 hybridized carbon material known as graphene has emerged as a promising choice for next-generation flexible electrode materials. This is because graphene sheets have a huge accessible surface area (2630 $m^2\ g^{-1}$), facilitating large double-layer capacitance. In addition, covalent sp^2 bonds

* Corresponding author.
E-mail address: l_chandrakant@yahoo.com (C.D. Lokhande).

https://doi.org/10.1016/j.est.2023.110154
Received 19 July 2023; Received in revised form 21 November 2023; Accepted 13 December 2023

European Polymer Journal 218 (2024) 113366

Contents lists available at ScienceDirect

European Polymer Journal

journal homepage: www.elsevier.com/locate/europolj

Synthesis of reduced graphene oxide (rGO)/polyaniline (PANI) composite electrode for energy storage: Aqueous asymmetric supercapacitor

D.C. Pawar, A.G. Bagde, J.P. Thorat, C.D. Lokhande *

Centre for Interdisciplinary Research, D.Y. Patil Education Society, Kolhapur 416 003, India

ARTICLE INFO

Keywords:
Asymmetric supercapacitor
Chemical bath deposition
Composite electrodes
Polyaniline
Reduced graphene oxide

ABSTRACT

Composite materials have gained significant interest for energy storage applications due to their possible synergistic effects. This work describes the synthesis of reduced graphene oxide (rGO)/polyaniline (PANI) composite thin films using chemical bath deposition (CBD) method. A field-emission scanning electron microscope revealed that PANI spikes coated on rGO sheets in rGO/PANI composite. The electrochemical studies of a rGO/PANI composite electrode showed a specific capacitance (C_s) of 1130F/g C_s at a scan rate of 5 mV/s in 1 M H_2SO_4 electrolyte. The combined effect of rGO with PANI, a aqueous asymmetric supercapacitor device (ASC) with configuration of rGO/PANI/H_2SO_4/WO_3 produced 97F/g C_s at a 5 mV/s scan rate and retained 82 % capacitance after 5,000 galvanostatic charge–discharge cycles. The ASC achieved a high specific energy of 23 Wh kg^{-1} at a specific power of 732 W kg^{-1}. The electrochemical properties of rGO/PANI composite indicate a feasible method for creating asymmetric supercapacitors.

1. Introduction

Excessive use of non-renewable energy has raised global worries about energy consumption and ecological balance. Thus, there is a tremendous interest in the extraction and use of renewable but erratic energy sources like wind, tidal, and solar energy [1]. To accomplish this goal, significant progress needs to be achieved in the creation of energy storage and conversion technologies that are highly efficient, environmentally friendly, and affordable [2]. In term of new energy storage technologies, supercapacitors are often used in mobile phones, electric cars and laptops because of their quick charging, extended lifespans, high specific capacitance, and safety [3–5]. Supercapacitors (SCs) may be categorised into three groups based on the materials used for their electrodes: electrical double layer capacitors (EDLCs), pseudocapacitors, and hybrid supercapacitors. The value of specific capacitance for pseudocapacitor materials, resulting from the faraday charge storage process, is several times greater than that of an EDLCs [6,7]. Pseudocapacitor materials involves conductive polymers and transition metal oxides. Conducive polymers are considered as one of the best materials for flexible supercapacitor electrodes due to its remarkable benefits of excellent redox activity, electrical conductivity, and flexible mechanical properties [8]. Among the several conductive polymers, including polyaniline (PANI), polythiophene (PTh), polycarbazole and their derivatives, PANI is widely recognized as one of the most economically valuable materials due to its benefits including simple production, simple doping and dedoping, high electrical conductivity, and strong environmental stability [9]. Although PANI molecular chain undergoes repetitive contraction and expansion throughout the charging and discharging process, which damages its conjugated structure and results in the electrode materials weak cyclic stability [10].

In EDLCs, charges are accumulated at the electrode–electrolyte contact and there is no charge transfer between them. Since no chemical reactions involved in the charge storage process, it provides high reversibility with improved cycle stability of SCs. [11]. Due to this, graphene, a two-dimensional material is essential in EDLC as an electrode material. Theoretically, graphene shows a large specific surface area (2630 m^2/g), superior chemical stability, a relatively wide potential range, and rapid electron mobility [12]. The stacking of π-π bond between graphene sheets causes agglomeration in graphene, which changes its functionality and decrease the specific capacitance. Due to these inherent limitations, there is a relatively low energy density [13]. As a consequence, the drawbacks of PANI and graphene can be solved by combining them to create composite material for SCs. By adding reduced graphene oxide (rGO) sheets in PANI matrix to improve their surface area, electrochemical processes, diffusion route, and increasing energy and power density. The non-covalent bonding of rGO sheets and PANI

* Corresponding author.
E-mail address: l_chandrakant@yahoo.com (C.D. Lokhande).

https://doi.org/10.1016/j.eurpolymj.2024.113366
Received 28 March 2024; Received in revised form 30 May 2024; Accepted 31 July 2024
Available online 2 August 2024

Electrochimica Acta 514 (2025) 145671

Contents lists available at ScienceDirect

Electrochimica Acta

journal homepage: www.journals.elsevier.com/electrochimica-acta

Chemically deposited reduced graphene oxide/polypyrrole (rGO/Ppy) composite thin films for flexible solid-state supercapacitor: Effect of rGO composition

D.C. Pawar [a], D.B. Malavekar [b], J.H. Kim [b], C.D. Lokhande [a,*]

[a] Centre for Interdisciplinary Research, D.Y. Patil Education Society, Kolhapur, 416 003, India
[b] Optoelectronic Convergence Research Center, Department of Materials Science and Engineering, Chonnam National University, Gwangju 61186, South Korea

ARTICLE INFO

Keywords:
Composite electrodes
Layered structure
Polypyrrole
Reduced graphene oxide
Solid-state supercapacitor

ABSTRACT

As electrochemical energy storage systems become more prevalent, there is a growing imperative to investigate electrode materials that offer both flexibility and superior capacitive performance. In this research, a stainless steel substrate was used to synthesize a composite of reduced graphene oxide/polypyrrole (rGO/Ppy) by simple successive ionic layer adsorption and reaction (SILAR) method. The various rGO concentrations were used to improve the material electrochemical characteristics. Field emission scanning electron microscopy images revealed that Ppy particles were sandwiched between rGO sheets. At a 1 mg mL^{-1} of rGO concentration, the highest specific capacitance of rGO/Ppy composite was 803 F g^{-1}, greater than Ppy (331 F g^{-1}). The rGO/Ppy composite exhibited remarkable cycling stability, retaining over 92 % of its initial capacitance over 5,000 cycles. Furthermore, rGO/Ppy/PVA-H_2SO_4/WO_3 flexible solid- state supercapacitor device revealed a specific capacitance of 49 F g^{-1} at 5 mV s^{-1} scan rate and showed a maximum specific energy (S_E) of 12 Wh kg^{-1} at a 881 W kg^{-1} specific power (S_P). This indicates that the optimized concentration of rGO in Ppy composite led to an improvement in capacitive performance, and SILAR proved to be an effective method for preparing composite electrodes.

1. Introduction

Improvements in renewable energy production are driving rapid growth in the utilization of energy storage devices. In order to meet the ever-growing requirements, supercapacitors have received substantial interest because they have a longer lifespan than batteries and the ability to provide significant specific power (S_P). Moreover, it has quick charge and discharge times. The majority of commercial supercapacitors are composed of carbon allotropes, which results in a low specific capacitance (C_s) and specific energy (S_E) [1,2]. In contrast to solely carbon-based materials, pseudocapacitive electroactive materials include conductive polymers (CPs), like polyaniline (PANI), polypyrrole (Ppy), etc., and transition metal compounds [3,4]. These materials significantly increase the supercapacitors S_E by electrochemical reversible redox processes across the electrode and electrolyte interface. An abundance of electro-active sites for reversible faradic redox reactions is provided by electrode materials with porous structures and excellent conductivity [5]. The carbon-based materials offer superior conductivity, reduced thermal expansion coefficient, excellent electrolyte stability, larger surface area to mass ratio, and low cost. [6]. Due to these properties, recently, carbon-based materials especially graphene derivatives have been the preferred supercapacitors electrode material. In addition, the poor electrochemical stability of pseudocapacitive materials can be effectively compensated using reduced graphene oxide (rGO) to improve cycle life of supercapacitors [7].

Among the different pseudocapacitive materials used in supercapacitors, CPs have attracted much attention, either individually or as a composite because of its unique characteristics, which include high redox activity, electrical conductivity, and mechanical flexibility. While CPs molecular chain is repeatedly contracted and expanded throughout the charging and discharging process, causing damage to its conjugated structure and weakening the cyclic stability of the electrode material [8]. As a result, improving the electrochemical properties of CPs can be achieved by incorporating graphene, specifically rGO nanosheets, into an efficient composite structure. Further, numerous studies have shown that this combination is significantly useful, enhancing the C_s and

* Corresponding author.
E-mail address: l_chandrakant@yahoo.com (C.D. Lokhande).

https://doi.org/10.1016/j.electacta.2025.145671
Received 14 November 2024; Received in revised form 5 January 2025; Accepted 7 January 2025
Available online 8 January 2025

Materials Science and Engineering B 292 (2023) 116432

Contents lists available at ScienceDirect

Materials Science & Engineering B

journal homepage: www.elsevier.com/locate/mseb

Performance of chemically synthesized polyaniline film based asymmetric supercapacitor: Effect of reaction bath temperature

D.C. Pawar [a], D.B. Malavekar [b], S.D. Khot [a], A.G. Bagde [a], C.D. Lokhande [a,*]

[a] Centre for Interdisciplinary Research, D.Y. Patil Education Society, Kolhapur 416 006, India
[b] School of Materials Science and Engineering, Chonnam National University, Gwangju 500757, South Korea

ARTICLE INFO

Keywords:
Asymmetric supercapacitor
Chemical bath deposition
Hybrid supercapacitor
Polyaniline
Tungsten oxide

ABSTRACT

Polyaniline (PANI) electrodes were prepared using chemical bath deposition method at various reaction bath temperatures ranging from 263 to 323 K. The specific surface area and wettability of films are significantly impacted by the polymerization temperature, which influences the electrochemical performance of electrodes. The electrode synthesized at 303 K showed a maximum specific surface area of 25 $m^2\ g^{-1}$, specific capacitance (C_s) of 816F g^{-1} (0.11F cm^{-2}) at a scan rate of 0.005 V s^{-1}, and 89% capacitive retention after 1,000 cyclic voltammetry (CV) cycles. An aqueous asymmetric supercapacitor device was fabricated using PANI as a cathode and tungsten oxide (WO_3) as an anode in 1 M H_2SO_4 electrolyte. The fabricated PANI/H_2SO_4/WO_3 device achieved a maximum C_s of 43 F g^{-1} with an energy density of 12 Wh kg^{-1} at a power density of 0.88 kW kg^{-1} and 72 % capacitive retention after 10,000 CV cycles.

1. Introduction:

In response to the fast growth of the global economy, the depletion of fossil fuels, and the degradation of ecosystems, there is a critical need to improve extremely effective, inexhaustible, and environment friendly methods for the conversion and storage of energy. This has animated advances in converting renewable energy through greenways and innovations related to electrochemical energy storage, i.e., supercapacitors and batteries [1,2]. Because of their inherent electrochemical properties, such as fast charge–discharge, long cycle stability, greater energy density compared to capacitors, and larger power density than ordinary batteries, supercapacitors have been explored as key enabler for the next generation energy storage device. Supercapacitor materials are split into three groups based on charge storage mechanisms: electric double-layer capacitors (EDLC), pseudocapacitors, and battery-type supercapacitors [3].

In EDLC capacitors, charge storage is caused by an electrostatic process at the electrode/electrolyte interface. EDLC materials are carbon-based, such as carbon nanotubes (CNT), activated carbon, and carbon aerogel, etc. [4-6]. The pseudocapacitor charge-storage system essentially depends on exchanging charge through the electrolyte and electrode surface redox reactions. Pseudocapacitor materials include transition metal chalcogenides and conducting polymers such as polyaniline (PANI) [7], polypyrrole (Ppy), and polythiophene (PT) [8,9]. The charge storage mechanism is based on strongly electrochemical redox reactions in battery-type materials, like Ni-based materials. Conducting polymers have unique and important properties, such as high electrical conductivity like metals and the capability to transition between redox states. PANI is an excellent material among conducting polymers and has been studied recently due to its easy synthesis process, low price, and interesting redox properties applicable in supercapacitor devices [10].

A convenient method for significant deposition on many substrates is the chemical bath deposition (CBD) method. It is quite an easy and cheap method compared to other methods. The development of nucleation is essential for the formation of precipitates. The result of nucleation in solution is that the molecular clusters produced quickly decompose, and particles combine to grow the film to a particular thickness. The controlled precipitation of the desired compound from a solution of its constituents is the fundamental principle of the CBD method [11,12].

The reaction temperature is more important in thin film preparation since it impacts the rate of reaction, morphology, thickness, surface wettability, and pore size, which determine the ions transport kinetics [13]. However, a complete understanding of its impact on electrode electrochemical activity is still lacking. The specific surface area of the

* Corresponding author.
E-mail address: l_chandrakant@yahoo.com (C.D. Lokhande).

https://doi.org/10.1016/j.mseb.2023.116432
Received 22 December 2022; Received in revised form 22 February 2023; Accepted 5 March 2023
Available online 14 March 2023

Journal of Physics and Chemistry of Solids 179 (2023) 111386

Contents lists available at ScienceDirect

Journal of Physics and Chemistry of Solids

journal homepage: www.elsevier.com/locate/jpcs

Pseudocapacitive performance of amorphous ruthenium oxide deposited by successive ionic layer adsorption and reaction (SILAR): Effect of thickness

A.G. Bagde [a], D.B. Malavekar [b], D.C. Pawar [a], S.D. Khot [a], C.D. Lokhande [a,*]

[a] Centre for Interdisciplinary Research, D. Y. Patil Education Society, Kolhapur, 416 006, India
[b] School of Materials Science and Engineering, Chonnam National University, Gwangju, 500757, South Korea

ARTICLE INFO

Keywords:
Ruthenium oxide
Successive ionic layer adsorption and reaction (SILAR)
Supercapacitor
Thin film

ABSTRACT

Developing and fabricating effective, affordable electrode materials for supercapacitors is still a challenge. Electrical conductivity, a large surface area, dynamic faster electron transport, and other customizable qualities are present in metal oxide materials while being inexpensive to manufacture. In this work, successive ionic layer adsorption and reaction (SILAR) method was employed for deposition of amorphous ruthenium oxide (RuO_2) thin films of different thicknesses on a stainless steel substrate. At 1.56 mg cm^{-2} thickness amorphous RuO_2 achieved a maximum specific capacitance (C_s) of 1146 F g^{-1} at a scan rate of 5 mV s^{-1} with 87% capacitance retention up to 5000 cycles. These findings bolster the idea of cost effective deposition of amorphous RuO_2 material for supercapacitor applications.

1. Introduction

Enhancing the capacity of energy storage systems has certainly been the subject of significant study worldwide because of growing need for large-capacity power storage for use in hybrid electric cars, armed forces gears, lightweight and versatile digital devices, and designate biomedical gear [1–4]. However, the more accomplished energy that is sustainable is not suitable to meet the energy storage demands. Hence, this energy storage transformation is important for research as well as industries. Supercapacitor (SC) signifies a rising energy storage system category that has drawn interest because it offers a greater energy density than conventional capacitors. The SCs possess a higher capacity for rapid charging and discharging and longer cycle life than rechargeable batteries [5]. The electrode material is crucial in the design of SC. It is effectively tuneable for the crucial electrochemical performances of the SC. The taxonomy of SCs is classified in three kinds, such as electric double layer capacitor (EDLC), pseudocapacitor, and hybrid capacitor, based on their charge storage techniques. In EDLCs, energy storage mechanisms arise from electronic and ionic charge processes that are separated at the interfaces between electrode and electrolyte. The EDLC-type behaviour has been shown by carbon-based materials, like activated carbon, carbon nanotubes, graphene, diamond, carbon aerogel, etc. [6]. On the other hand, metal oxides/sulfides and conducting polymers store charge mostly by a quick, reversible redox process that results in pseudocapacitance [7–9]. Here, electron transport takes place chemically, producing the excess pseudocapacitance at a certain potential. Here, charge storage is carried out by bulk of material, enhancing the specific energy density and device capacitance [10]. Both methods of charge storage reveal both beneficial and undesirable electrochemical qualities. The efficiency of a single-charge storage method is insufficient to compete with batteries. In this sense, the deployment of a performance-oriented energy storage system requires the development of a hybrid strategy. Both types of charge storage methods are included in the hybrid strategy. The capacitive method increases device stability and electronic conductivity by having a large surface area and an efficient charge transportation path [11].

Ruthenium oxide (RuO_2), one of the most popular metal oxide has been extensively researched due to its enormous surface area, excellent reversibility, and relatively high capacitance [12]. Recently, it has also been revealed that RuO_2 has excellent electrocatalytic activity in a wide range of electrochemical processes [13]. The stable RuO_2 mainly adopts the “rutile structure” of RuO_2, even though it is observed in other variations with respect to liquid hydrate. Its molecular orbital theory effectively explained the thermodynamic stability and large isotropic charge transportation characteristics of RuO_2. Additionally, RuO_2 has a long cycle life with tunable-metallic conductivity, multiple oxidation states, and durable stability across a broad potential range. In fact, these characteristics have greatly aided SC research. However, a few

* Corresponding author.
E-mail address: l_chandrakant@yahoo.com (C.D. Lokhande).

https://doi.org/10.1016/j.jpcs.2023.111386
Received 15 February 2023; Received in revised form 6 April 2023; Accepted 17 April 2023
Available online 17 April 2023

Chemical Engineering Journal 501 (2024) 157533

Contents lists available at ScienceDirect

Chemical Engineering Journal

journal homepage: www.elsevier.com/locate/cej

Review

Advancements in graphene and its derivatives based composite Materials: A comprehensive review on Synthesis, Characterization, and supercapacitive charge storage

Dhanaji Malavekar [a], Divya Pawar [b], Ajinkya Bagde [b], Sambhaji Khot [b], Suraj Sankapal [b], Shital Bachankar [c], Sharadchandra Patil [d], Chandrakant D. Lokhande [b,*], Jin Hyeok Kim [a,*]

[a] Optoelectronics Convergence Research Center and Department of Materials Science and Engineering, Chonnam National University, 300, Yongbong-Dong, Buk-Gu, Gwangju 61186, South Korea
[b] Centre for Interdisciplinary Research, D. Y. Patil Education Society, Kolhapur 416003, India
[c] Department of Intelligent Electronics and Computer Engineering, Chonnam National University, Gwangju, 61186, South Korea
[d] Department of Physics, Shivaji University, Kolhapur 416004, India

ARTICLE INFO

Keywords:
Composite materials
Graphene
Pseudocapacitor
Specific energy and power
Supercapacitor

ABSTRACT

Composite materials incorporating graphene have emerged as promising candidates for enhancing both energy and power density in supercapacitors, owing to graphene's exceptional electrical, mechanical, and chemical properties. These graphene properties enable the maintenance of cyclability without compromising performance. Over the last two decades, research on graphene and its derivatives has shifted from synthesis and applications to exploring their compositional blends with various materials for broader applications. Graphene and its derivatives like graphene oxide and reduced graphene oxide primarily consist of carbon, interconnected through σ bonds, responsible for impressive conductivity. This review presents a comprehensive overview of recent advancements in two dimensional (2D) graphene and its derivatives' composites with pseudocapacitive materials like transition metal compounds (hydroxides, oxides, chalcogenides, metalorganic frameworks, and MXenes), conducting polymers, metal nanoparticles, and other organic materials for supercapacitor applications. We highlight the evolution of synthesis and characterization methods for composite electrode materials, emphasizing their relevance to practical applications. Key compositions and the underlying charge storage mechanisms are also discussed. Finally, we explore the opportunities and challenges in using graphene and its derivatives' composites for practical energy storage in supercapacitors.

Abbreviations: **ACNRs**, Activated polyaniline-derived hollow carbon nanorods; **AgNPs**, Ag nanoparticles; **ASC**, Asymmetric supercapacitors; **ALD**, Atomic layer deposition; **BPMW**, Bi-pyrene-terminated molecular wires; **BN**, Boron nitride; **CBD**, Chemical bath deposition; **CC**, Carbon cloth; **CWCC**, Carbonized wood cell chamber; **CVD**, Chemical vapor deposition; **Co_3O_4**, Cobalt oxide; **CV**, Cyclic voltammetry; **DHAQ**, Dihydroxyanthraquinone; **EDL**, Electric double-layer; **EDLC**, Electrochemical double-layer capacitor; **EES**, Electrochemical energy storage; **EIS**, Electrochemical impedance spectroscopy; **FTIR**, Fourier transform infrared; **Au**, Gold; **G/AC**, Graphene/activated carbon; **G/SC**, Graphene/soft carbon; **GA**, Graphene aerogel; **GCD**, Galvanostatic charge discharge; **GO-CMC**, Graphene-carboxy methylcellulose; **GO**, Graphene oxide; **GQD**, Graphene quantum dots; **hrGO**, Holy reduced graphene oxide; **HSC**, Hybrid supercapacitor; **IrO_2**, Iridium oxide; **$FeCoS_2$**, Iron cobalt sulphide; **LDH**, Layered double hydroxide; **LICs**, Li-ion capacitor; **LIMCs**, Li-ion micro capacitors; **MnO_2**, Manganese oxide; **MVO**, Manganese vanadate; **MOFs**, Metal-organic frameworks; **CH_4**, Methane; **MSCs**, Micro-supercapacitors; **MoS_2**, Molybdenum disulphide; **$MoSe_2$**, Molybdenum diselenide; **MWCNT**, Multi-walled carbon nanotubes; **NiO/NLIG**, N-doped laser-induced graphene; **NiCo-P**, Nickel cobalt phosphate; **NiV-LDH**, Nickel–vanadium LDH; **NSC**, Nitrogen and sulfur in carbon mircosheets; **OCC**, Oxidized carbon cloth; **PANI**, Polyaniline; **PEDOT**, Poly 3,4-ethylenedioxythiophene; **PI**, Polyimide; **PPy**, Polypyrrole; **PTh**, Polythiophene; **PGF**, Porous graphene skeleton; **rGO**, Reduced graphene oxide; **RuO2**, Ruthenium oxide; **SEM**, Scanning electron microscopy; **SiC**, Silicon carbide; **SILAR**, Successive ionic layer adsorption and reaction; **S-rGO**, Sulfur doped graphene; **SSC**, Symmetric supercapacitors; **TGA**, Thermogravimetric analysis; **3D**, Three-dimensional; **TEM**, Transmission electron microscopy; **TMCs**, Transition metal chalcogenides; **2D**, Two-dimensional; **UCNG**, Ultrafine Co_3O_4 nanoparticles/graphene; **XRD**, X-ray diffraction; **XPS**, X-ray photoelectron spectroscopy; **ZIFs**, Zeolitic imidazolate frameworks.

* Corresponding authors at: Centre for Interdisciplinary Research, D. Y. Patil Education Society, Kolhapur 416003, India (C.D. Lokhande). Optoelectronics Convergence Research Center and Department of Materials Science and Engineering, Chonnam National University, 300, Yongbong-Dong, Buk-Gu, Gwangju 61186, South Korea (Jin Hyeok Kim).

E-mail addresses: l_chandrakant@yahoo.com (C.D. Lokhande), jinhyeok@chonnam.ac.kr (J. Hyeok Kim).

https://doi.org/10.1016/j.cej.2024.157533
Received 14 August 2024; Received in revised form 30 October 2024; Accepted 7 November 2024
Available online 9 November 2024

Conferences

DEPARTMENT OF PHYSICS
AMSCA MAVERICK - 2022
PUNE-07
SAVITRIBAI PHULE PUNE UNIVERSITY

DEPARTMENT OF PHYSICS

Certificate of Participation

This is to certify that

Divya Pawar

Centre for Interdisciplinary Research, D. Y. Patil Education Society, Kolhapur, India

Participated and presented the **Poster paper** entitled **Performance of Chemically --------Effect of Reaction Bath Temperature** from the **Energy Storage Materials** Theme made in the **International Conference on Advanced Materials Synthesis, Characterization and Applications (AMSCA Maverick-2022)** With Special Topic: New Education Policy held at the Department of Physics, Savitribai Phule Pune University, Pune- 07, Maharashtra, India during **18th -20th October, 2022.**

Convener
(AMSCA Maverick-2022)

Co-Convener
(AMSCA Maverick-2022)

Chairperson
(AMSCA Maverick-2022)

Three days International Conference on

Nano Composites for Aerospace Applications

Hybrid Mode

02nd to 04th February 2023

CERTIFICATE

Best Paper Award

presented to

Ms. Divya Pawar

Centre for Interdisciplinary Research, D.Y. Patil Education Society, Kolhapur.

for presenting the Research Paper Entitled on

Effect of temperature on polyaniline thin film electrodes for asymmetric supercapacitor.

in Three days International Conference on Nano Composites for Aerospace Applications (ICNCAS - 2023) held at the Department of Basic Sciences and Electronics & Communication Engineering, Cambridge Institute of Technology, Bengaluru, India.

Dr. Ravi Shankar	Dr. G. Indumathi	Shri. Nithin Mohan	Shri. D.K. Mohan
Assoc. Professor, Dept. of Basic Sciences	Principal	CEO	Chairman
Cambridge Institute of Technology	Cambridge Institute of Technology	Cambridge Institute of Technology	Cambridge Institute of Technology
Bangalore	Bangalore	Bangalore	Bangalore

Sponsored by

AICTE

ICNCAS - 2023

CAMBRIDGE INSTITUTE OF TECHNOLOGY

Organized by

Department of Basic Sciences and Electronics & Communication Engineering

D. Y. PATIL EDUCATION SOCIETY
(Deemed to be University), KOLHAPUR
NAAC 'A+' Grade in 3rd Cycle

Certificate of Best Poster Presentation

This is to certify that **Mr/Ms.** Divya Pawar of CIR, DYPES, Kolhapur got the ~~First~~/~~Second~~/ Third prize in best poster presentation in **Materials Science** in the **International Conference on Nanotechnology Addressing the Convergence of Materials Science, Biotechnology and Medical Sciences (IC-NACMBM-2024)** held at the Centre for Interdisciplinary Research, D. Y. Patil Education Society (Deemed to be University), Kolhapur, Maharashtra, India during 12th to 14th February 2024. His/Her contribution to the conference is highly appreciated.

Dr. Jayavant L. Gunjakar	**Prof. Meghnad G. Joshi**	**Prof. Chandrakant D. Lokhande**
Convener	Convener	Chairman

SHIVAJI UNIVERSITY, KOLHAPUR

SOPHISTICATED ANALYTICAL INSTRUMENT FACILITY (SAIF)– COMMON FACILITY CENTRE (CFC)
WORKSHOP & HANDS-ON TRAINING ON BIO-ATOMIC FORCE MICROSCOPY (BIO-AFM) ORGANISED BY SAIF-CFC UNDER MAHARASHTRA ACADEMY OF SCIENCE AND STRIDE PROGRAMME

Certificate of Participation

This is certify that Ms. DIVYA PAWAR has successfully participated in the workshop & hands-on training on BIO-ATOMIC FORCE MICROSCOPY (BIO-AFM) organised by SAIF (CFC), Shivaji University, Kolhapur held during 04-05 Jan, 2022 under the Maharashtra Academy of Science and STRIDE (Scheme for Trans-disciplinary Research for India's Developing Economy) programme.

Prof. R. G. Sonkawade
Co-ordinator : SAIF, Head (i/c) : CFC
Shivaji University, Kolhapur.
Chairman

|| Tewo Sada Dnyanamay Pradeep ||

Shikshan Prasarak Mandal's

Shankarrao Mohite Mahavidyalaya, Akluj

Tal. Malshiras, Dist. Solapur, 413101 (Maharashtra State)

Affiliated to Punyashlok Ahilyadevi Holkar Solapur University, Solapur

Department of Chemistry & IQAC

organized

One Day Online National Conference on "Emerging Trends in Chemistry"

This is to certify that ***Divya Pawar*** of **D Y Patil Education Society Deemed University Kolhapur** has actively participated in one Day Online National Conference on " Emerging Trends in Chemistry"(NCETC-2022) organized by Department of Chemistry & IQAC, Shankarrao Mohite Mahavidyalaya, Akluj held on 10th February 2022.

Dr. S.S.Deokar
Convener & Head of Department

Mrs. D.R.Kamble
Organizing Secretary

Prof. Dr.D.S. Bagade
I/C Principal

INTELLECTUAL PROPERTY INDIA
PATENTS | DESIGNS | TRADE MARKS
GEOGRAPHICAL INDICATIONS

सत्यमेव जयते

NIPAM
NATIONAL IP AWARENESS MISSION

Government of India
Ministry of Commerce and Industry
Department for Promotion of Industry and Internal Trade
Office of the Controller General of Patents, Designs and Trade Marks

CERTIFICATE

This is to certify that, **MISS. DIVYA CHANDRAKANT PAWAR** has successfully participated in IP Awareness/Training program under

NATIONAL INTELLECTUAL PROPERTY AWARENESS MISSION

on August 12,2022

Azadi Ka Amrit Mahotsav

Organized by

Intellectual Property Office, India

Date:August 22,2022

(Prof. (Dr) Unnat P. Pandit)
CONTROLLER GENERAL OF
PATENTS, DESIGNS & TRADE MARKS

Rayat Shikshan Sanstha's

D. P. Bhosale College, Koregaon, District- Satara

International Conference on

Emerging Trends in Material Science

e-Certificate

This is to certify that **Miss.Divya Chandrakant Pawar** of **D. Y. Patil Education Society, Kolhapur** has participated in **International Conference on "Emerging Trends in Material Science"** dated 9th & 10th November, 2022 jointly organized by Department of Physics & Chemistry in association with IQAC, D. P. Bhosale College, Koregaon, District- Satara, Maharashtra, India.

Certificate ID: ETMS-IC-085

Prof. Dr. S. D. Jadhav	Dr. V. S. Jamadade	Dr. B. S. Lokde	Dr. V. S. Sawant
Convener	Co-Convener	IQAC Coordinator	Principal

SANJAY GHODAWAT UNIVERSITY Kolhapur

Empowering Lives Globally !

(Approved by UGC & Govt.of Maharashtra)

Certificate

This is to certify that

Prof. / Dr. / Mr. / Ms. Divya Chandrakant Pawar, Ph.D. Scholar

of D Y Patil University Kolhapur has participated in National Seminar on

"Emerging Nano Materials for Renewable Energy"

held on Monday, 26th December, 2022 and organized by Sanjay Ghodawat University, Kolhapur.

Dr. Sambhaji M. Pawar	Dr. Pallavi D. Bhange	Dr. Sarita P. Patil	Prof. Dr. Arun S. Patil
Convener	Convener	Co-ordinator	Vice-Chancellor

Madha Taluka Shikshan Prasarak mandal's

K. N. BHISE ARTS, COMMERCE AND VINAYAKRAO PATIL SCIENCE COLLEGE,

VIDYANAGAR, Bhosare, Tal-Madha, Dist- Solapur (M.S.) (NAAC A Grade 3.10 CGPA)

Faculty of Science and I.Q. A. C.

Organized

One Day National Conference on Physical, Chemical and Biological Strategies, Tools and Ideas for Promising Future

(Sponsored by P. A. H. Solapur University, Solapur)

(10-03-2023)

Certificate

This is to certify that Prof./ Dr./Mr./Ms. DIVYA CHANDRAKANT PAWAR of K. N. Bhise Arts, Commerce and Vinayakrao Patil Science College Vidyanagar Bhosare. **has participated in One Day National Conference on Physical, Chemical and Biological Strategies, Tools and Ideas for Promising Future organized by Faculty of Science and I. Q. A. C. of K. N. Bhise Arts, Commerce and Vinayakrao Patil Science College, Vidyanagar, Bhosare (Kurduwadi), Solapur, Maharashtra.**

Dr. N. D. Deshmukh
Convener
Head, Dept of Microbiology

Prof. M. M. Patil
Organizing Secretary
Coordinator, Faculty of Science

Prof. Dr. P. S. Kamble
Director
I/C Principal

"Education through self-help is our motto."- Karmaveer

Rayat Shikshan Sanstha's

RAJARSHI CHHATRAPATI SHAHU COLLEGE, KOLHAPUR

(Reaccredited 3rd Cycle by NAAC at 'A' Grade with CGPA 3.07)

DEPARTMENT OF PHYSICS and IQAC

Organizes Under G20 University Connect Program

One Day International Conference on

"Recent Trends in Fabrication of Nanomaterials and Their Applications (ICRTFNA-2023) "

Certificate

This is to certify that, Dr. /Prof./Mr./Ms./Mrs. Divya Chandrakant Pawar of D.Y. Patil Edu. Society Kolhapur has participated /~~worked as Resource Person~~/~~Chairperson~~/~~Organizing committee member~~ in **One Day International Conference on 'Recent Trends in Fabrication of Nanomaterials and Their Applications (ICRTFNA-2023)** ' Organized by **Department of Physics** and **IQAC held on March 15, 2023.** He/She has presented paper entitled _____

Dr. A. R. Patil	**Dr. V. V. Killedar**	**Dr. L. D. Kadam**
Coordinator	Organizing secretary	Principal

SWAMI RAMANAND TEERTH MARATHWADA UNIVERSITY, NANDED

Sponsored

One Day National Conference on

EMERGING TRENDS IN BASIC SCIENCES (NCETBS-2023)

Organized by

Faculty of Science

Madhavrao Patil Arts, Commerce & Science College, Palam

Dist. Parbhani (M.S.) - 431720

Certificate

This is to certify that **Ms. Divya Chandrakant Pawar** of **D. Y. Patil University, Kolhapur** has actively participated in One Day National Confernce on **"EMERGING TRENDS IN BASIC SCIENCES (NCETBS-2023)"** held on 20 March, 2023. He/She has presented research paper /poster presentation/delivered keynote adress / invited talk / chaired the session entitled _____

Chief Organizer
Dr. H. T. Satpute
(Principal)

Convenor
Dr. A. D. Arsule
(Vice - Principal)